

AD-A092 874

CIVIL SYSTEMS INC ALBUQUERQUE NM
MISERS BLUFF PHASE II, GROUND SHOCK DATA ANALYSIS.(U)

F/G 18/3

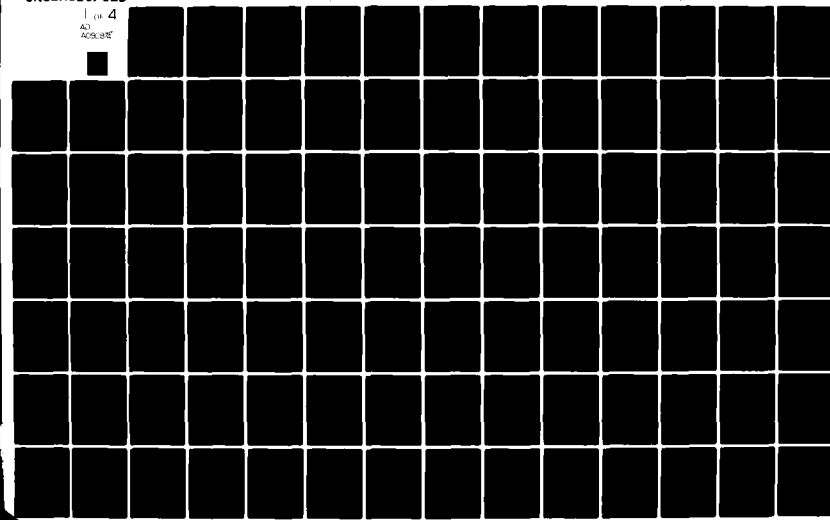
OCT 79 J S PHILLIPS, L S MELZER, J L BRATTON DNA001-79-C-0168

DNA-51352

NL

UNCLASSIFIED

1 (u) 4
A2
ACBSE



1

AD A092874

LEVEL 2

DNA 5135Z

MISERS BLUFF PHASE II

Ground Shock Data Analysis

James S. Phillips

Lawrence S. Melzer

Jimmie L. Bratton

Civil Systems, Incorporated

2201 San Pedro, N.E.

Albuquerque, N.M. 87110

DTIC
DEC 10 1980

31 October 1979

Interim Report for Period 1 November 1978-1 October 1979

CONTRACT No. DNA 001-79-C-0168

APPROVED FOR PUBLIC RELEASE;
DISTRIBUTION UNLIMITED.

THIS WORK SPONSORED BY THE DEFENSE NUCLEAR AGENCY
UNDER RDT&E RMSS CODE B344079462 H53BAXSX37712 H2590D.

Prepared for
Director
DEFENSE NUCLEAR AGENCY
Washington, D.C. 20305

DDC FILE COPY

80 12 10 061

Destroy this report when it is no longer needed. Do not return to sender.

PLEASE NOTIFY THE DEFENSE NUCLEAR AGENCY,
ATTN: STTI, WASHINGTON, D.C. 20305, IF
YOUR ADDRESS IS INCORRECT, IF YOU WISH TO
BE DELETED FROM THE DISTRIBUTION LIST, OR
IF THE ADDRESSEE IS NO LONGER EMPLOYED BY
YOUR ORGANIZATION.



UNCLASSIFIED

SECURITY CLASSIFICATION OF THIS PAGE (When Data Entered)

(17) X377
READ INSTRUCTIONS
BEFORE COMPLETING FORM

REPORT DOCUMENTATION PAGE		
1. REPORT NUMBER 18	2. GOVT ACCESSION NO. AD-A092874	3. RECIPIENT'S CATALOG NUMBER
4. TITLE (and Subtitle) MISERS BLUFF PHASE II, Ground Shock Data Analysis.	5. TYPE OF REPORT & PERIOD COVERED Interim Report For Period 1 Nov 78—1 Oct 79	6. PERFORMING ORG. REPORT NUMBER
7. AUTHOR(s) 10 James S. Phillips Lawrence S. Melzer Jimmie L. Bratton	8. CONTRACT OR GRANT NUMBER(s) 15 DNA 001-79-C-0168	9. PROGRAM ELEMENT, PROJECT, TASK AREA & WORK UNIT NUMBERS 16 H53BAXSK377-12
11. CONTROLLING OFFICE NAME AND ADDRESS Director Defense Nuclear Agency Washington, D.C. 20305	12. REPORT DATE 11 31 October 1979	13. NUMBER OF PAGES 330
14. MONITORING AGENCY NAME & ADDRESS (if different from Controlling Office)	15. SECURITY CLASS. (of this report) 12 331 UNCLASSIFIED	
16. DISTRIBUTION STATEMENT (of this Report) Approved for public release; distribution unlimited	15a. DECLASSIFICATION/DOWNGRADING SCHEDULE	
17. DISTRIBUTION STATEMENT (of the abstract entered in Block 20, if different from Report)		
18. SUPPLEMENTARY NOTES This work sponsored by the Defense Nuclear Agency under RDT&E RMSS Code B344079462 H53BAXSX37712 H2590D		
19. KEY WORDS (Continue on reverse side if necessary and identify by block number) Misers Bluff Phase II Prediction Methods High Explosive Test Wave Propagation Ground Shock Data Multiple Burst Effects		
20. ABSTRACT (Continue on reverse side if necessary and identify by block number) Phase II of the Misers Bluff high explosive experimental program had as a primary objective, the collection of multiple burst ground motion data in a scaled MX valley, against which the Waveform Synthesis Model (WSM) developed in Phase I could be evaluated.		

UNCLASSIFIED

SECURITY CLASSIFICATION OF THIS PAGE(When Data Entered)

20. ABSTRACT (Continued)

Phenomenology in single and multiple burst environments is examined and its effect on the WSM discussed. The end result of the study is a modified WSM for both single and multiple bursts. Example waveforms from the WSM are compared with Misers Bluff data. Limitations on the WSM are discussed and recommendations for further study are made.

A

Accession For	
NTIS GRA&I	<input checked="" type="checkbox"/>
DTIC TAR	<input type="checkbox"/>
Unannounced	<input type="checkbox"/>
Justification	
By _____	
Distribution/ _____	
Availability Codes	
Avail and/or	
Dist	Special

UNCLASSIFIED

SECURITY CLASSIFICATION OF THIS PAGE(When Data Entered)

SUMMARY

Misers Bluff Phase II consisted of 2 experiments, a single 100 Ton TNT burst and 6 100 Ton TNT charges arranged in a hexagonal pattern and fixed simultaneously. The primary purpose of the experiments was to evaluate the Waveform Synthesis Model (WSM) for scaled MX conditions. The WSM was developed during Misers Bluff Phase I as a procedure for predicting ground motions for the multiple burst attacks which might result because of the MX deployment pattern.

The fundamental assumption underlying the WSM is that the principle of superposition may be used to combine the effects of individual bursts to predict the ground motions for multiple detonations. It was recognized from the outset that the known nonlinearities in soil response could lead to failure of this assumption in which case the multiple burst experimental data would be used to construct algorithms to account for the nonlinearities. The Waveform Synthesis Model contains the following seven elements:

- (a) A statistical package that allows Monte Carlo treatment of CEP, time-on-target errors, and height-of-burst uncertainties
- (b) An air-slap-induced vertical ground motion prediction procedure that uses the LAMB code to predict the

multiple burst overpressure waveforms at points of interest and a one-dimensional finite difference code, PLID, that includes the no-flow pore-air expansion model, to calculate the air-slap-induced vertical ground motions

- (c) An analytical estimate of the horizontal air slap motion
- (d) A WES-developed empirical prediction procedure for the low frequency upstream-induced motions, based on a compilation of high explosive and nuclear data, and groundroll frequencies calculated by computer code
- (e) A routine for calculating the proper time phasing and vector components for each individual burst, of the motions at designated target points and linearly combining these effects
- (f) Algorithms for adjusting the linear combinations to account for the nonlinearities
- (g) An input/output routine to plot and list pertinent data.

The Misers Bluff Phase I results had demonstrated that the superposition assumption was not valid for all locations of interest for the hexagonal array. Because of this the major thrust of the Phase II data analysis was to evaluate predictions based on superposition of waveforms measured on the single burst event

and identification of the nonlinearities causing the failure of superposition.

The single burst predictions which are superimposed for multiple burst cases are based on state-of-the-art empirical procedures. Evaluation of these procedures for the MB-II single burst event resulted in the following observations:

- The vertical air-slap component of motion is well predicted by the 1-D finite difference code, PLID, used in the WSM. This code includes a first-order, no flow model of the pore-air expansion phenomenon which results due to the negative (gage) phase of the surface airblast.
- The horizontal air-slap component of motion is reasonably well predicted by the AFDM procedure used in the WSM except for the air-slap induced shear wave contribution.
- The low frequency components (crater-related, upstream-induced, and oscillatory motions) are reasonably well predicted by the modified WES prediction procedure.

Analysis of the data from the multiple-burst event (MBII-2) and comparison with the Phase I results led to the following results:

- Superposition fails as a predictor of the local airblast related signal. This occurred on Phase I also and was anticipated because of the nonlinear response of the air. The WSM does not use superposition for this component. Instead the LAMB code is used to predict the airblast environment and the PLID code is used to predict the vertical airblast induced particle velocity. This procedure resulted in good predictions where LAMB gave airblast results consistant with the airblast data.
- The near surface horizontal motions were not predicted satisfactorily by superposition inside the explosive array. These motions do not appear to be significantly affected by the pore-air expansion phenomenon, but indicate, as do the deeper horizontal motions, that the geometry of the experiment (wave convergence) is resulting in larger motions than predicted by superposition due to the high stresses generated by the wave interactions and nonlinear stress-strain behavior of the soil.
- The "late time" low frequency (Raleigh Wave) motions and the total waveform for stations outside the explosive array are well predicted by superposition.

- The relationship derived by Murphy and Auld concerning the effect of bedrock on the period of the low frequency motions is consistent with the Misers Bluff data.
- The principle nonlinearities causing the failure of superposition were the nonlinear equation of state of air, the pore-air expansion phenomenon, the geometry leading to the wave convergence effects (related to the constitutive equations of the soil) and the nonlinearities associated with free fall after spall.

Theoretical analysis of the first two of these are reasonably well in hand, but pretest evaluation of the in-situ soil properties controlling the pore-air expansion represent a problem in practice. Material stress-strain nonlinearities and spall can be treated theoretically, however the empirical predictions procedures used in the Waveform Synthesis Model do not treat these explicitly, therefore, simplified algorithms must be developed for the WSM.

The Waveform Synthesis Model has been significantly improved as a result of the Misers Bluff II-2 experiment. It now does a credible job of predicting nuclear multiple burst events.

PREFACE

This work is a continuation of the research begun under Contract DNA001-77-C-0301. The present research spans the period of November 78 - October 79 and was performed under Contract DNA001-79-C-0168, Program element NWE T 62710H, Project H53BAXS, Task Area X377, Work Unit 12. The Technical Monitor for this work was Dr. George W. Ullrich, DNA. We thank Dr. Ullrich for his helpful suggestions and coordination with other agencies.

The authors wish to express their appreciation to the CSI staff for a job well done. A special thanks goes to Mrs. M. V. Vivian, Mr. V. F. Jojola, and Ms. C. P. Childs without whose help and cooperation the preparation of the reports prepared under these contracts would have been immensely more difficult.

PERTINENT CONVERSION FACTORS - SI TO U. S. CUSTOMARY UNITS OF MEASUREMENT

<u>PARAMETERS</u>	<u>TO CONVERT FROM</u>	<u>TO</u>	<u>MULTIPLY BY</u>
Length	Meters (m)	Feet	3.281
Velocity	Meters/Second (mps)	Feet/Second	3.281
Unit Weight	Grams/Cubic Centimeter (G/cc)	Pounds/Cubic Foot	62.427
Yield	Terra Joules (TJ)	Kilotons	2.391×10^{-1}
Volume	Cubic Meters (m^3)	Cubic Feet	35.315
Cratering Efficiency	Cubic Meters/Terra Joule (m^3/TJ)	Cubic Feet/Ton	6.770
Pressure	Mega Pascals (MPa)	Pounds/Square Inch	145
Impulse	Mega Pascals-Sec (MPa-sec)	Pounds/Square Inch-Sec	145
Area	Hectares	Acres	2.47

TABLE OF CONTENTS

	<u>Page No.</u>
SUMMARY	1
PREFACE	6
CONVERSION TABLE	7
LIST OF ILLUSTRATIONS	11
LIST OF TABLES	27
1. Introduction	29
2. Experimental Plan	33
2.1 Location	33
2.2 Geology	33
2.2.1 Description	35
2.2.2 Seismic Properties	35
2.2.3 Material Properties	38
2.3 Instrumentation Plan	40
3. Discussion of Data	49
3.1 Review of Phase I Results	49
3.2 MBII-1	54
3.2.1 Previous 100T High Explosive Experiments	54
3.2.2 Phenomenology	59
3.2.3 Airblast Results	73
3.2.4 Air-Slap Component of Ground Motion	77
3.2.4.1 Prediction Procedure	77
3.2.4.2 Predictions vs Data	81
a) Waveforms	81
b) Peaks	83
c) Negative Phase Effects	91
d) Evaluation	100

TABLE OF CONTENTS

	<u>Page No.</u>
3.2.5 Crater Related Component of Ground Motion	109
3.2.5.1 Prediction Procedure	109
3.2.5.2 Predictions vs Data	113
a) Waveforms	113
b) Peaks	113
c) Evaluation	120
3.2.6 Oscillatory Component of Ground Motion	131
3.2.6.1 Prediction Procedure	131
3.2.6.2 Data vs Prediction	133
3.2.6.3 Evaluation	138
3.2.7 Summary Observations of MBII-1 Analysis	144
3.3 MBII-2	144
3.3.1 Introduction	144
3.3.2 Phenomenology	145
3.3.3 Airblast Results	167
3.3.4 Ground Motion	170
3.3.4.1 Air-Slap Component of Ground Motion	172
a) Peaks	172
b) Waveforms	178
c) Evaluation	182
3.3.4.2 Crater Related Component	184
a) Peaks	184
b) Waveforms	186
c) Evaluation	186
3.3.4.3 Oscillatory Component	188
a) Peaks	188
b) Waveforms	191
c) Evaluation	192
3.3.4.4 Multiple Burst Nonlinear Effects	194
3.3.5 Results of MBII-2 Analysis	219

TABLE OF CONTENTS (continued)

	<u>Page No.</u>
4. Recommended Prediction Procedures	222
4.1 Air-Slap Component	222
4.1.1 Single Burst	222
4.1.2 Multiple Burst	223
4.2 Crater-Related and Oscillatory Components . .	224
4.2.1 Single Burst	224
4.2.2 Multiple Burst	224
4.3 Waveforms Synthesis Model	225
5. Conclusions and Recommendations	238
5.1 Conclusions	238
5.1.1 Event II-1	238
5.1.2 Event II-2	239
5.2 Recommendations	242
References	244
APPENDIX A Superposition vs Data Waveform Comparisons	247
APPENDIX B Superposition vs Data Shock Spectra Comparisons	303

LIST OF ILLUSTRATIONS

<u>Figure</u>		<u>Page No.</u>
1	Misers Bluff Phase II Test Bed Location . . .	34
2	P-Wave Velocity Profile Interpreted from Crosshole and Refraction Surveys Near MBII-1 (Ref. 7)	36
3	S-Wave Velocity Profile Interpreted from Crosshole Survey Near MBII-1 (Ref. 7) . . .	37
4	P-Wave and S-Wave Velocity Profiles Interpreted from Crosshole Survey Near MBII-2 (Ref. 10)	39
5	Site Profile of MBII-1 (Ref. 12)	41
6	Site Profile Along Main Gage Line MBII-2 (Ref. 7)	42
7	Profile and Computation Parameters Used for MBII Predictions	43
8	Three-Dimensional Projection of the Bedrock Contact at Misers Bluff II (Ref. 7) . . .	44
9	Instrumentation Layout for MBII-1 (Ref. 13)	45
10	Plan View of MBII-2 Experiment	46
11	Profiles Along Main Ground Motion Measurement Radials - MBII-2	47
12	Typical Gage Layout for Multiple Burst Experiments in Phase I (MBI-4)	50
13	Accuracy of Superposition on Misers Bluff Phase I	51
14	Comparison of Superposition and Data in Phase I (MBI-4)	53
15	Modulus (compressibility) of Soil with Enclosed Air for a Sandy Soil with a Void Ratio of 0.46 (Ref. 15)	58
16	Vertical Velocity Waveforms at the 0.5 m Depth MBII-1	60

LIST OF ILLUSTRATIONS (continued)

<u>Figure</u>		<u>Page No.</u>
17	Horizontal Velocity Waveforms at the 0.5 m Depth - MBII-1	61
18	Vertical Velocity Waveforms at the 0.5 m Depth - MBII-1	62
19	Horizontal Velocity Waveforms at the 0.5 m Depth - MBII-1	63
20	Vertical Velocity Waveforms at the 3.0 m Depth - MBII-1	67
21	Horizontal Velocity Waveforms at the 3.0 m Depth - MBII-1	68
22	Horizontal Velocity Waveforms at the 3.0 m Depth - MBII-1	69
23	Extent of "Spall" in MBII-1	74
24	Comparison of Measured and Predicted Over-pressure and Impulse - MBII-1	75
25	Comparison of Measured and Predicted Positive Phase Duration MBII-1	76
26	Airblast Arrival Time Curve for MBII-1 . . .	78
27	Comparison of Measured and Predicted Vertical Air-Slap Waveforms - MBII-1	82
28	Comparison of Measured and Predicted Horizontal Air-Slap Waveforms - MBII-1	84
29	Comparison of Measured and Predicted Air-Slap Velocities; 0.5 m \leq Z \leq 3 m - MBII-1	85

LIST OF ILLUSTRATIONS (continued)

<u>Figure</u>		<u>Page No.</u>
30	Comparison of Measured and Predicted Air-Slap Velocities; $Z \geq 9$ m - MBII-2	87
31	Attenuation of Vertical Velocity w/Depth	89
32	Comparison of Measured and Predicted Air-Slap Acceleration; $0.5 \leq Z \leq 3.0$ m; MBII-1	90
33	Comparison of Measured and Predicted Air-Slap Accelerations; $Z \geq 9$ - MBII-1	92
34	Comparison of Pore-Air Model Calculations and MBII-1 Data @ R=25 m; Z=0.5 m	93
35	Comparison of Pore-Air Model Calculations and MBII-1 Data @ R=25 m; Z=1.5 m	94
36	Comparison of Pore-Air Model Calculations and MBII-1 Data @ R=25 m; Z=3 m	95
37	Comparison of Pore-Air Model Calculations and MBII-1 Data @ R=50 m; Z=0.5 m	97
38	Comparison of Pore-Air Model Calculations and MBII-1 Data @ R=50 m; Z=1.5 m	98
39	Comparison of Pore-Air Model Calculations and MBII-1 Data @ R=50 m; Z=3 m	99
40	Comparison of Pore-Air Model Calculations and MBII-1 Data @ R=100 m; Z=0.5 m	101
41	Comparison of Pore-Air Model Calculations and MBII-1 Data @ R=100 m; Z=1.5 m	102
42	Near Surface Downward Acceleration for Misers Bluff and Similar Experiments	104
43	Peak Downward Velocity vs Range for Misers Bluff and Similar Experiments	105
44	Peak Downward Displacement (Airblast-Induced) vs Range for Misers Bluff II-1 and Similar Experiments	106

LIST OF ILLUSTRATIONS (continued)

<u>Figure</u>		<u>Page No.</u>
45	MIDDLE GUST III Vertical Velocities Measured at the 24.4 Meter Range of the 240° Azimuth .	107
46	Attenuation Coefficients for Crater- Related Displacements	110
47	Crater-Related Waveform	111
48	Comparison of Measured and Predicted Crater- Related Components @ 12.5-0.5	114
49	Comparison of Measured and Predicted Crater- Related Components @ 33.5-0.5	115
50	Comparison of Measured and Predicted Crater- Related Components @ 50-0.5	116
51	Crater-Related Velocities - MBII-1	118
52	Crater-Related Displacements for $z < 0.1V_a^{1/3}$; MBII-1	119
53	Crater-Related Displacements for $0.1V_a^{1/3} \leq z \leq 0.5V_a^{1/3}$; MBII-1	121
54	Crater-Related Displacements for $z > 0.5V_a^{1/3}$; MBII-1	122
55	Peak Upward Particle Velocity vs Range for Misers Bluff II-1 and Similar Experiments . .	124
56	Peak Upward Displacements vs Range for Misers Bluff II-1 and Similar Experiments	125
57	Peak Upward Displacement vs Soil Air Voids for Misers Bluff II-1 and Similar Experiments	126
58	Displacement Time Histories at 25 m Ground Range, 0.5 m Depth from Surface 100 Ton HE Tests	127
59	Peak Outward Particle Velocity vs Range for Misers Bluff II-1 and Similar Experiments . .	129

LIST OF ILLUSTRATIONS (continued)

<u>Figure</u>		<u>Page No.</u>
60	Peak Outward Displacement vs Range for Misers Bluff II-1 and Similar Experiments	130
61	Comparison of WES Low Frequency Prediction Procedure and MBII-1 Data @ R=25 m; Z=1.5 m . . .	134
62	Comparison of WES Low Frequency Prediction Procedure and MBII-1 Data @ R=50 m; Z=0.5 m . . .	135
63	Comparison of WES Low Frequency Prediction Procedure and MBII-1 Data @ R=100 m; Z=0.5 m . . .	136
64	Comparison of WES Low Frequency Prediction Procedure and MBII-1 Data @ R=150 m; R=0.5 m . . .	137
65	Idealized Layering Characteristics of 100-ton Test Sites	139
66	Outrunning Velocity Waveforms (Ground Range ~ 120m) for 100-ton Surface H.E. Tests	142
67	Vertical Velocity Waveforms on a Charge Radial @ Z=0.5 m	146
68	Vertical Velocity Waveforms on a Bisector @ Z=0.5 m	147
69	Horizontal Velocity Waveforms on a Charge Radial @ Z=0.5 m	149
70	Horizontal Velocity Waveforms on a Bisector @ Z=0.5 m	150
71	Vertical Velocity Waveforms at 25 m Range on a Charge Line	152
72	Horizontal Velocity Waveforms at the 25 m Range on the Charge Line	153
73	Definition of Time and Peak Values of "800 msec Signal" MBII-2	155

LIST OF ILLUSTRATIONS (continued)

<u>Figure</u>		<u>Page No.</u>
74	Azimuthal Variation of Times of Peak for "800 msec Signal" MBII-2 - Z=12.5 m	156
75	Time-of-Peak vs Depth - "800 msec Signal" MBII-2	158
76	Timing of "800 msec Signal" - Vertical Velocity	159
77	Time-of-Peak of "800 msec Signal" - Horizontal Velocity	160
78	Peak-to-Peak Magnitude of "800 msec Signal" - Vertical Velocities	162
79	Peak-to-Peak Magnitude of "800 msec Signal" - Horizontal Velocities	163
80	Vertical Velocity at the 25 m Depth - Charge Radial MBII-2	164
81	Vertical Velocity at the 25 m Depth - Bisector MBII-2	165
82	Motions at and Below 25 m Depth	166
83	Peak Pressure vs Range for MBII-2	169
84	Peak Impulse vs Range for MBII-2	171
85	Vertical Velocity Associated with Passage of the First Compressive Phase of the Airblast - Superposition vs Data	173
86	Vertical Velocities Associated with Passage of Second and Third Compressive Phases of the Airblast	175
87	Horizontal Velocities Associated with Passage of the First and Second Compressive Phases of the Airblast	177

LIST OF ILLUSTRATIONS (continued)

<u>Figure</u>		<u>Page No.</u>
88	Comparison of Large Upward, Long Duration Vertical Motion and Superposition (0.5m Depth)	179
89	Comparison of Superposition and MBII-2 for Vertical Velocity Air-Slap Component	180
90	Comparison of Superposition and MBII-2 for Horizontal Velocity Air-Slap Component	181
91	Evaluation Plot of Superposition for Horizontal Crater-Related Velocities	185
92	Comparison of Superposition and MBII-2 for Horizontal Velocity - Crater-Related Component	187
93	Identification of Peak Oscillatory Motion for Comparison Purposes R=12.5 m; Z=12.5 m, Bisector	189
94	Evaluation Plot of Superposition for Oscillatory Component Peak-to-Peak Velocities	190
95	Correction of Superposition for Differing Rock Elevations of MBII-1 and MBII-2	193
96	Large Upward Signal - MBII-2 vs Superposition .	195
97	Magnitude of Negative Phase - MBII-2	197
98	Timing Aspects of the Positive Phase and Negative Phase Air Pressure and the Large Upward Vertical Particle Velocity	198
99	Comparison of Pore-Air Calculation and MBII-2 Data @ the Array Center	200
100	Comparison of the Pore-Air Calculation and MBII-2 Data @ R=25 m, Z=0.5 m, on a Bisector . . .	201
101	Comparison of the Pore-Air Calculation and MBII-2 Data @ R=25 m, Z=0.5 m, on a Charge Line .	202

LIST OF ILLUSTRATIONS (continued)

<u>Figure</u>		<u>Page No.</u>
102	Comparison of the Pore-Air Calculation and MBII-2 Data @ R=50 m, Z=0.5 m, on a Bi-sector	204
103	Comparison of the Pore-Air Calculation and MBII-2 @ R=50 m, Z=1.5 m on a Bisector	205
104	Comparison of Pore-Air Calculation and MBII-2 Data @ R=50 m; Z=3 m on a Bisector	206
105	Comparison of Pore-Air Calculation and MBII-2 Data @ R=50 m, Z=0.5 m, on a Charge Line	207
106	Comparison of Pore-Air Calculation and MBII-2 Data @ R=50 m, Z=1.5 m, on a Charge Line	208
107	Comparison of Pore-Air Calculation and MBII-2 Data @ R=50 m, Z=3 m on a Charge Line	209
108	Comparison of Pore-Air Calculation and MBII-2 Data @ R=86.6 m; Z=0.5 m, on a Bisector	211
109	Comparison of Pore-Air Calculation and MBII-2 Data @ R=86.6 m; Z=1.5 m on a Bisector	212
110	Comparison of Pore-Air Calculation and MBII-2 Data @ R=86.6 m; Z=3 m on a Bisector	213
111	Horizontal and Vertical Waveforms Measured @ R=50 m; Z=3 m on a Charge Line	215
112	Behavior of Direct Wave Interior to the Charge Array @ the 3 m Depth	217
113	Differences in the Air Pressure and Stress Waveforms Near the Array Center - MBII-2 vs Superposition	218
114	Generalized Flow Diagram of WSM	227
115	Comparison of MBII-1 Data and the Waveform Synthesis Model @ R=25 m; Z=0.5 m	228

LIST OF ILLUSTRATIONS (continued)

<u>Figure</u>		<u>Page No.</u>
116	Comparison of MBII-1 Data and the Waveforms Synthesis Model @ R=25 m; Z=0.5 m	229
117	Comparison of MBII-1 Data and the Waveforms Synthesis Model @ R=50 m; Z=0.5 m	230
118	Comparison of MBII-1 Data and the Waveforms Synthesis Model @ R=50 m; Z=0.5 m	231
119	Comparison of MBII-2 Data and the Waveforms Synthesis Model @ R=0.5 m; Z=0.5 m	232
120	Comparison of MBII-2 Data and the Waveforms Synthesis Model @ R=25 m; Z=0.5 m, Charge Line	233
121	Comparison of MBII-2 Data and the Waveforms Synthesis Model @ R=25 m; Z=0.5 m; Charge Line	234
122	Comparison of MBII-2 Data and the Waveforms Synthesis Model @ R=50 m; Z=0.5 m, Bisector . .	235
123	Comparison of MBII-2 Data and the Waveforms Synthesis Model @ R=50 m; Z=0.5 m; Bisector . .	236

APPENDIX A

LIST OF ILLUSTRATIONS

<u>Figure</u>		<u>Page No.</u>
A.1	Comparison of MBII-2 Data and Super-imposed MBII-1 Data @ 0-0.5 - Vertical Velocity	248
A.2	Comparison of MBII-2 Data and Super-imposed MBII-1 Data @ 0-9 - Vertical Velocity	249
A.3	Comparison of MBII-2 Data and Super-imposed MBII-1 Data @ 0-12.5 - Vertical Velocity	250
A.4	Comparison of MBII-2 Data and Super-imposed MBII-1 Data @ 0-25 - Vertical Velocity	251
A.5	Comparison of MBII-2 Data and Super-imposed MBII-1 Data @ 6-3 - Charge Line-Vertical Velocity	252
A.6	Comparison of MBII-2 Data and Super-imposed MBII-1 Data @ 6-3 - Charge Line-Horizontal Velocity	253
A.7	Comparison of MBII-2 Data and Super-imposed MBII-1 Data @ 12.5-3 - Bisector-Vertical Velocity	254
A.8	Comparison of MBII-2 Data and Super-imposed MBII-1 Data @ 12.5-3 - Bisector-Horizontal Velocity	255
A.9	Comparison of MBII-2 Data and Super-imposed MBII-1 Data @ 12.5-9 - Bisector-Vertical Velocity	256
A.10	Comparison of MBII-2 Data and Super-imposed MBII-1 Data @ 12.5-9 - Bisector-Horizontal Velocity	257
A.11	Comparison of MBII-2 Data and Super-imposed MBII-1 Data @ 12.5-12.5 - Bisector - Vertical Velocity	258

APPENDIX A

LIST OF ILLUSTRATIONS (Continued)

<u>Figure</u>		<u>Page No.</u>
A.12	Comparison of MBII-2 Data and Super-imposed MBII-1 Data @ 12.5-12.5 - Bisector - Horizontal Velocity	259
A.13	Comparison of MBII-2 Data and Super-imposed MBII-1 Data @ 12.5-25 - Bisector - Vertical Velocity	260
A.14	Comparison of MBII-2 Data and Super-imposed MBII-1 Data @ 12.5-25 - Bisector - Horizontal Velocity	261
A.15	Comparison of MBII-2 Data and Super-imposed MBII-1 Data @ 25-0.5 - Charge Line and 25-0.5-Bisector - Vertical Velocity	262
A.16	Comparison of MBII-2 Data and Super-imposed MBII-1 Data @ 25-0.5 - Charge Line and 25-0.5-Bisector - Horizontal Velocity	263
A.17	Comparison of MBII-2 Data and Super-imposed MBII-1 Data @ 25-9-Bisector - Vertical Velocity	264
A.18	Comparison of MBII-2 Data and Super-imposed MBII-1 Data @ 25-9-Bisector - Horizontal Velocity	265
A.19	Comparison of MBII-2 Data and Super-imposed MBII-1 Data @ 25-12.5-Bisector - Vertical Velocity	266
A.20	Comparison of MBII-2 Data and Super-imposed MBII-1 Data @ 25-12.5-Bisector - Horizontal Velocity	267
A.21	Comparison of MBII-2 Data and Super-imposed MBII-1 Data @ 25-25-Bisector - Vertical Velocity	268
A.22	Comparison of MBII-2 Data and Super-imposed MBII-1 Data @ 25-25-Bisector - Horizontal Velocity	269

APPENDIX A

LIST OF ILLUSTRATIONS (Continued)

<u>Figure</u>		
		<u>Page No.</u>
A.23	Comparison of MBII-2 Data and Super-imposed MBII-1 Data @ 50-0.5-Chargeline - Vertical Velocity	270
A.24	Comparison of MBII-2 Data and Super-imposed MBII-1 Data @ 50-0.5-Bisector - Vertical Velocity	271
A.25	Comparison of MBII-2 Data and Super-imposed MBII-1 Data @ 50-0.5 Charge Line and 50-0.5-Bisector - Horizontal Velocity	272
A.26	Comparison of MBII-2 Data and Super-imposed MBII-1 Data @ 50-1.5-Charge Line - Horizontal Velocity	273
A.27	Comparison of MBII-2 Data and Super-imposed MBII-1 Data @ 50-3 Charge Line - Vertical Velocity	274
A.28	Comparison of MBII-2 Data and Super-imposed MBII-1 Data @ 50-3-Charge Line - Horizontal Velocity	275
A.29	Comparison of MBII-2 Data and Super-imposed MBII-1 Data @ 50-3-Bisector - Vertical Velocity	276
A.30	Comparison of MBII-2 Data and Super-imposed MBII-1 Data @ 50-3-Bisector - Horizontal Velocity	277
A.31	Comparison of MBII-2 Data and Super-imposed MBII-1 Data @ 50-9-Charge Line - Vertical Velocity	278
A.32	Comparison of MBII-2 Data and Super-imposed MBII-1 Data @ 50-9-Charge Line - Horizontal Velocity	279
A.33	Comparison of MBII-2 Data and Super-imposed MBII-1 Data @ 50-9-Bisector - Vertical Velocity	280

APPENDIX A

LIST OF ILLUSTRATIONS (Continued)

<u>Figure</u>		<u>Page No.</u>
A.34	Comparison of MBII-2 Data and Super-imposed MBII-1 Data @ 50-9-Bisector - Horizontal Velocity	281
A.35	Comparison of MBII-2 Data and Super-imposed MBII-1 Data @ 50-12.5-Charge Line - Vertical Velocity.	282
A.36	Comparison of MBII-2 Data and Super-imposed MBII-1 Data @ 50-12.5-Bisector - Vertical Velocity	283
A.37	Comparison of MBII-2 Data and Super-imposed MBII-1 Data @ 50-12.5-Bisector - Horizontal Velocity	284
A.38	Comparison of MBII-2 Data and Super-imposed MBII-1 Data @ 50-25-Bisector - Vertical Velocity	285
A.39	Comparison of MBII-2 Data and Super-imposed MBII-1 Data @ 50-25-Bisector - Horizontal Velocity	286
A.40	Comparison of MBII-2 Data and Super-imposed MBII-1 Data @ 75-0.5-Charge Line and 125-0.5 Charge Line Vertical Velocity.	287
A.41	Comparison of MBII-2 Data and Super-imposed MBII-1 Data @ 86.6-0.45-Bisector - Vertical Velocity	288
A.42	Comparison of MBII-2 Data and Super-imposed MBII-1 Data @ 86.6-0.5-Bisector - Horizontal Velocity	289
A.43	Comparison of MBII-2 Data and Super-imposed MBII-1 Data @ 86.6-3-Bisector - Vertical Velocity	290
A.44	Comparison of MBII-2 Data and Super-imposed MBII-1 Data @ 86.6-3-Bisector - Horizontal Velocity	291

APPENDIX A

LIST OF ILLUSTRATIONS (Concluded)

<u>Figure</u>		<u>Page No.</u>
A.45	Comparison of MBII-2 Data and Super-imposed MBII-1 Data @ 86.6-9-Bisector - Vertical Velocity	292
A.46	Comparison of MBII-2 Data and Super-imposed MBII-1 Data @ 86.6-9-Bisector - Horizontal Velocity	293
A.47	Comparison of MBII-2 Data and Super-imposed MBII-1 Data @ 86.6-12.5-Bisector - Horizontal Velocity.	294
A.48	Comparison of MBII-2 Data and Super-imposed MBII-1 Data @ 86.6-12.5-Bisector - Vertical Velocity	295
A.49	Comparison of MBII-2 Data and Super-imposed MBII-1 Data @ 86.6-25-Bisector - Vertical Velocity	296
A.50	Comparison of MBII-2 Data and Super-imposed MBII-1 Data @ 129.9-0.5-Bisector - Vertical Velocity	297
A.51	Comparison of MBII-2 Data and Super-imposed MBII-1 Data @ 129.9-0.5-Bisector - Horizontal Velocity	298
A.52	Comparison of MBII-2 Data and Super-imposed MBII-1 Data @ 133.5-0.5-Charge Line - Vertical Velocity.	299
A.53	Comparison of MBII-2 Data and Super-imposed MBII-1 Data @ 188-0.5-Charge Line - Vertical Velocity.	300
A.54	Comparison of MBII-2 Data and Super-imposed MBII-1 Data @ 188-0.5-Charge Line - Horizontal Velocity.	301
A.55	Comparison of MBII-2 Data and Super-imposed MBII-1 Data @ 188-0.5-Charge Line - Horizontal Velocity.	302

APPENDIX B

LIST OF ILLUSTRATIONS

<u>Figure</u>		<u>Page No.</u>
B.1	Shock Spectra Comparisons of MBII-2 Data and Superposition @ R=0	304
B.2	Shock Spectra Comparisons of MBII-2 Data and Superposition @ R=6 Bisector .	305
B.3	Shock Spectra Comparisons of MBII-2 Data and Superposition @ R=6 Charge Line	306
B.4	Shock Spectra Comparisons of MBII-2 Data and Superposition @ R=12.5-0.5 - Bisector and Charge Line	307
B.5	Shock Spectra Comparisons of MBII-2 Data and Superposition @ R=12.5-3 - Bisector and Charge Line	308
B.6	Shock Spectra Comparisons of MBII-2 Data and Superposition @ R=12.5-9 - Bisector and Charge Line	309
B.7	Shock Spectra Comparisons of MBII-2 Data and Superposition @ R=12.5-12.5 and 12.5-25 - Bisector and Charge Line	310
B.8	Shock Spectra Comparisons of MBII-2 Data and Superposition @ R=25-0.5 - Bisector and Charge Line	311
B.9	Shock Spectra Comparisons of MBII-2 Data and Superposition @ R=25-9 - Bi- sector and Charge Line	312
B.10	Shock Spectra Comparisons of MBII-2 Data and Superposition @ R=12.5-12.5 - Bisector and Charge Line	313
B.11	Shock Spectra Comparisons of MBII-2 Data and Superposition @ R=25-25 - Bisector and Charge Line	314

APPENDIX B

LIST OF ILLUSTRATIONS (CONCLUDED)

<u>Figure</u>		<u>Page No.</u>
B.12	Shock Spectra Comparisons of MBII-2 Data and Superposition @ R=50-0.5 - Bisection and Charge Line	315
B.13	Shock Spectra Comparisons of MBII-2 Data and Superposition @ R=50-3 - Bisection and Charge Line	316
B.14	Shock Spectra Comparisons of MBII-2 Data and Superposition @ R=50-9 - Bisection and Charge Line	317
B.15	Shock Spectra Comparisons of MBII-2 Data and Superposition @ R = 75, 125, and 90.1-0.5 Charge Line	318
B.16	Shock Spectra Comparisons of MBII-2 Data and Superposition @ R=86.6-0.5 and 3 - Bisection	319
B.17	Shock Spectra Comparisons of MBII-2 Data and Superposition @ R=86.6-9, 12.5 and 25 Bisection	320
B.18	Shock Spectra Comparisons of MBII-2 Data and Superposition @ R=129.9-0.5 Bisection and 133.5-0.5 Charge Line . . .	321
B.19	Shock Spectra Comparisons of MBII-2 Data and Superposition @ R=188-0.5 Charge Line	322
B.20	Shock Spectra Comparisons of MBII-2 Data and Superposition @ R=50-12.5 Bisection and Charge Line	323
B.21	Shock Spectra Comparisons of MBII-2 Data and Superposition @ R=50-25 Bisection and Charge Line	324

LIST OF TABLES

<u>Table No.</u>		<u>Page No.</u>
1	Misers Bluff Test Program	32
2	100 Ton Tangent-Above High Explosive Test Events.	55
3	Summary of Ground Roll Frequencies for Misers Bluff II-1 and Similarly Configured Experiments	140

1. Introduction

The Multiple Protective Structure basing concept for the MX system, currently under development by the Air Force, derives its survivability by creating more potential launch points than can be attacked one-on-one. This basing mode results in a large number of hardened launch sites only a few of which are occupied by missiles at any point in time. The missiles are covertly shuttled among the protective structures in a random manner such that each potential launch point is an equally appropriate target.

The land requirements and system operating costs favor close spacing of the launch points while survivability considerations favor a large spacing to prevent the accumulation of weapons effects on unattacked launch points from the attack of neighboring launch points. Evaluation of this trade-off requires predictions of the ground motions which result from multiple detonations in the vicinity of the unattacked launch point.

The Misers Bluff Test Program was a two phase series of experiments designed to study the multiple burst phenomena pertinent to the MX system concept. The overall objective of the program was the development of a Waveforms Synthesis Model (WSM) which could be used for the prediction of the multiple burst ground motion environment. The point of departure for the WSM was a superposition of the empirically predicted waveforms for the individual bursts.

Phase I of the test program consisted of eight small scale experiments (see Table 1 for configurations, yields and individual objectives). The single burst experiments served two purposes:

- To evaluate the accuracy of the state-of-the-art single burst prediction procedures,
- To provide a data base for preparation of superposition predictions for the multiple-burst experiments.

This allowed an independent evaluation of the two major assumptions of the Waveform Synthesis Model. The primary purposes of the multiburst experiments were to:

- Evaluate the superposition assumption.
- Provide a data base to identify the possible nonlinearities in the waveform accumulation.

The analysis of the Phase I experiments is reported in References 3 and 4.

Phase II of the Misers Bluff program consisted of two larger yield experiments in a geology more representative of the MX siting region. The objective of these experiments was to test the predictive model (WSM) for both single and multiple burst events. This broadened the limited multiple burst

data base, and allowed more confidence in generalizing the prediction procedure. The analysis of the Phase II experiments is the subject of this report.

Section 2 of this report presents a description of the site geology and the experimental configurations. The data are analyzed, compared to previous experiments and the pre-test predictions are evaluated in Section 3. Section 4 presents the resulting recommended prediction procedures for both single and multiple burst events and describes the Waveform Synthesis Model. Conclusions and recommendations are presented in Section 5.

Event	# of Charges	Yield/Charge	Charge Configuration	Date	Objective
MBl-1	1	2.09x10 ⁻³ TJ	Half Buried	2Aug77	Provide Single Burst Data for Multiburst Waveform Synthesis
MBl-2	1	2.09x10 ⁻³ TJ	Surface Tangent	15Aug77	Identify depth of burst phenomena differences in oscillatory ground motion region; provide data for scaling comparisons with Pre-Dice Throw 100 ton event
MBl-3	1	2.09x10 ⁻³ TJ	Half Buried	23Aug77	Repeat of MBl-1 to obtain data on reproducability and emphasize definitions of motions in the plateau region
MBl-4	6	2.09x10 ⁻³ TJ	Surface Tangent	7Sep77	Provide data for waveforms synthesis model and identification of height of burst phenomena differences in multiple burst configurations
MBl-5	1	2.09x10 ⁻³ TJ	Tangent Below	22Sep77	Identify depth of burst phenomena differences in oscillatory ground motion region
MBl-6	b	2.09x10 ⁻³ TJ	Half Buried	13Oct77	Provide data for the waveforms synthesis model
MBl-7	1	5.35x10 ⁻⁴	Half Buried	26Oct77	Provide data on scaling between 2.09x10 ⁻³ TJ and 5.35x10 ⁻⁴ TJ
MBl-8	24	2.09x10 ⁻³ TJ	Surface Tangent	7Dec77	Resolve importance of more distant charges on "local" multiple burst phenomena; provide data for assuming reproducability symmetry, etc. because configuration contains seven identical 6 charge arrays
MBl-1	1	.418TJ			Provide single burst data for multiburst waveform comparison, provide test of single burst prediction ability
MBl-2	6	.418TJ	Surface Tangent	28Jun78	Provide test of multiple burst synthesis model for yield & geology differences. Provide excitation of "Minature" Valley

NOTE: RTJ = .2391 kilotons

2. Experimental Plan

2.1 Location

Misers Bluff Phase II was conducted on a privately owned ranch known as the Planet Ranch. The ranch is located approximately 25 km east of Parker Dam near the Arizona-California border. The nearest cities are Parker and Lake Havasu, Arizona located at a distance of approximately 48 km (insert on Figure 4) from the test site.

The 95 hectare test site (Figure 4) was located near the eastern edge of the Planet Ranch in a valley at the confluence of a major arroya and the Bill Williams River. The valley is bordered on the east by a 15.2 m to 91.4 m cliff, to the north and west by low lying hills, and to the south by the Bill Williams River. (References 5 and 6)

2.2 Geology

Geotechnical studies of the Phase II test site were performed by AFWL, Fugro National Inc., and the U.S. Army Engineer Waterways Experiment Station (WES). Results of the studies that relate to the data analysis will be summarized herein. For a more detailed discussion, the reader is referred to References 7 through 12.

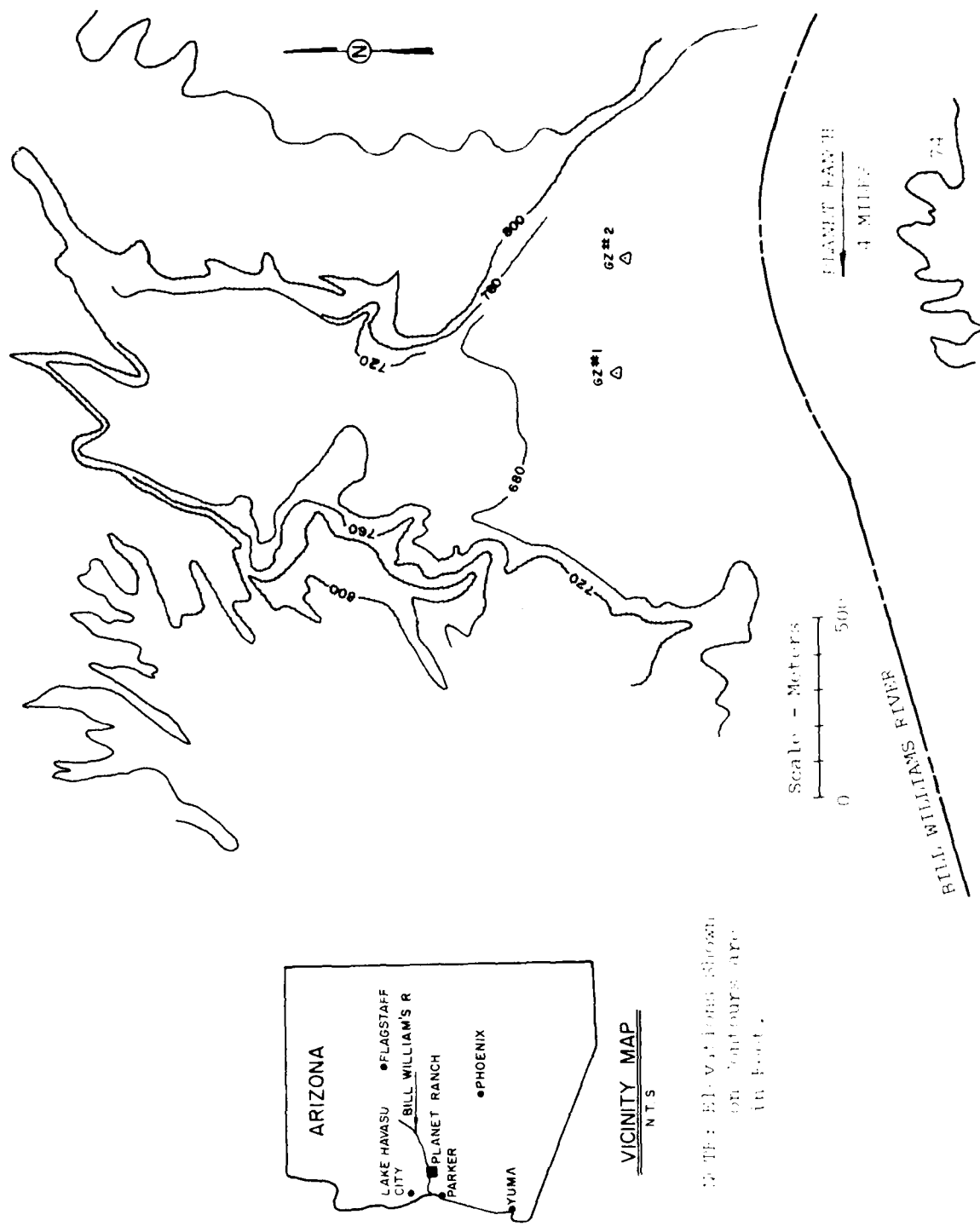


Figure 1. Misers Bluff Phase II Test Bed Location

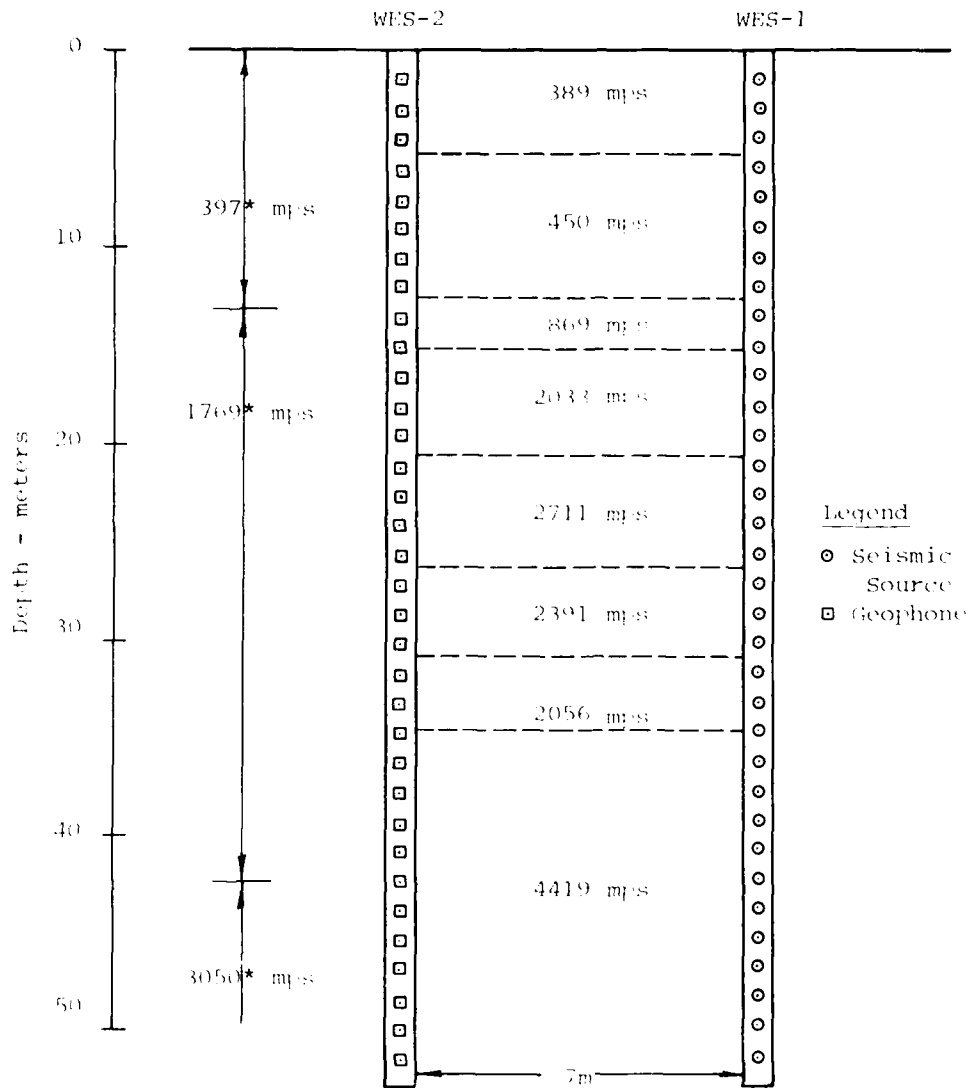
2.2.1 Description

The Phase II test site is characterized by a variable thickness (0 to 2 meters) of dry, highly compressible silt overlying a fine-to-coarse sand strata with gravel contents varying between 0% and 40% by weight. At most locations in the test bed area, clays and silts were encountered below the sands at depths that ranged between 8 m and 11 m. Below these fine grained deposits was a second sequence of sands with gravel that in turn overlie a few meters of gravels, cobbles, and boulders. Conglomeritic sandstone was the bedrock at the site; the soil/bedrock contact ranged between about 20 m and 70 m below the surface in the area of interest. The ground water table was at about the 4.5 m and 6.5 m depths at the time of MBII-1 and -2 respectively (Reference 7).

2.2.2 Seismic Properties

An extensive geophysical program was conducted at the Phase II test site. This included down-hole, uphole, crosshole, and seismic refraction surveys. The specific methods and analyses used in determining the properties of the site are presented in References 7 through 12.

True p-wave and s-wave velocity profiles determined from the crosshole and p-waves from the refraction surveys by WES near MBII-1 are shown in Figures 5 and 6. The p-wave profile indicates that the 100% saturation zone was around 15 meters below the surface. Bedrock, as determined



*From Seismic Refraction Survey

Figure 2. P-Wave Velocity Profile Interpreted from Crosshole and Refraction Surveys Near MBII-1 (Ref. 7)

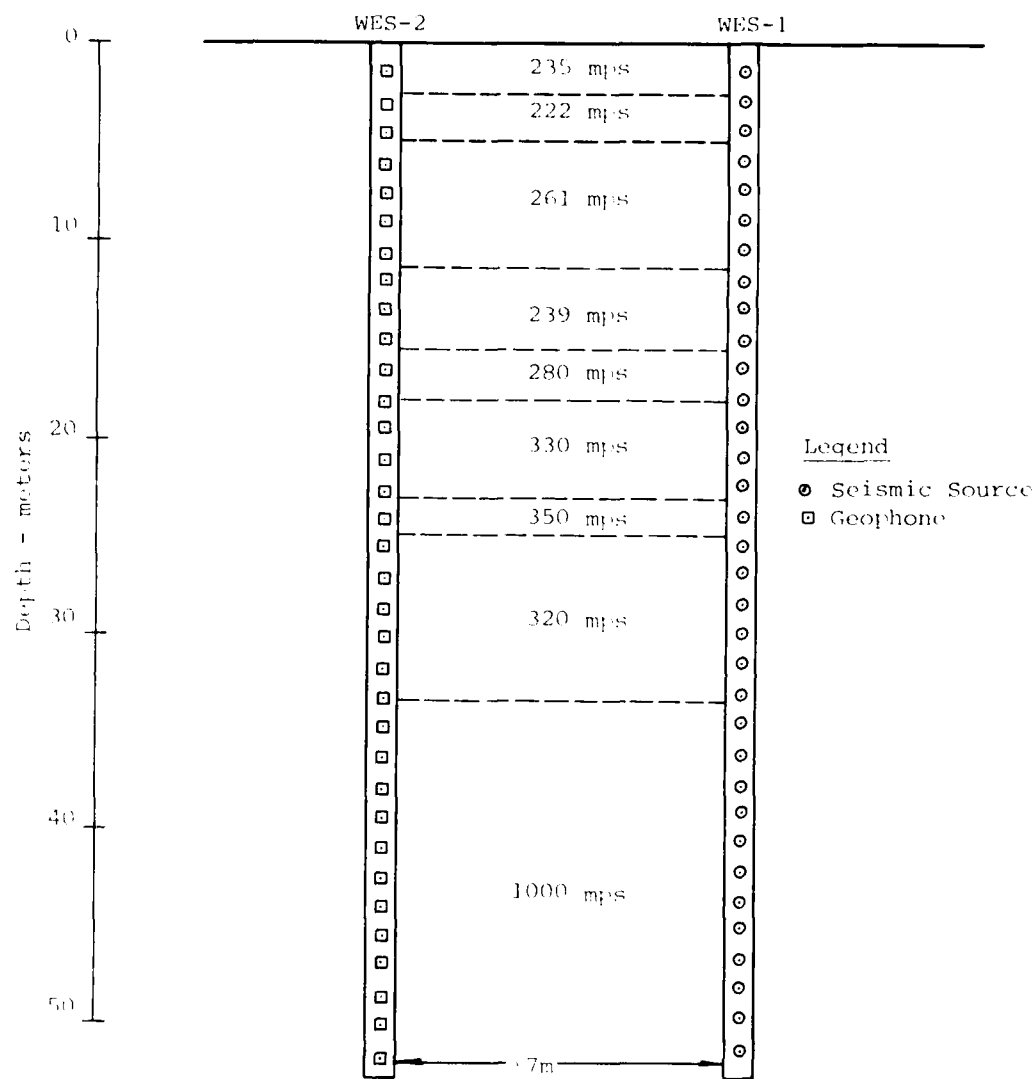


Figure 3. S-Wave Velocity Profile Interpreted from Crosshole Survey Near MBII-1 (Ref. 7)

from the p-wave profile, was at a depth of 34.7 m. The s-wave profile shows minor changes until rock is encountered around 33.5 m. The reversals seen in these profiles indicate varying percentages of gravels in the layers and differing degrees of cementation.

True p-wave and s-wave profiles determined from the crosshole survey by Fugro near the MBII-2 ground zero are presented in Figure 7. The seismic properties around Event 2 are similar to those at Event 1, however, there are differences in the depths of the major layers. The 100% saturation zone was between 10.7 m and 12.2 m and bedrock was encountered at about 52 m. Comparison of the p-wave velocities of the bedrock indicates that at MBII-2 it is slightly less competent than around MBII-1.

2.2.3 Material Properties

Site exploration and laboratory testing programs were carried out to characterize the materials at the Misers Bluff test site. Index, properties tests, consolidated-undrained triaxial shear tests, compaction, and relative density tests were performed by Fugro. Results from these tests are reported in Reference 8. Standard penetration, classification, and composition properties were determined by WES and the results are reported in Reference 7. Dynamic UX tests performed by WES and recommended material properties are reported in Reference 12. In addition to laboratory testing, CIST 19 (Ref. 11) was conducted at the site to determine insitu properties.

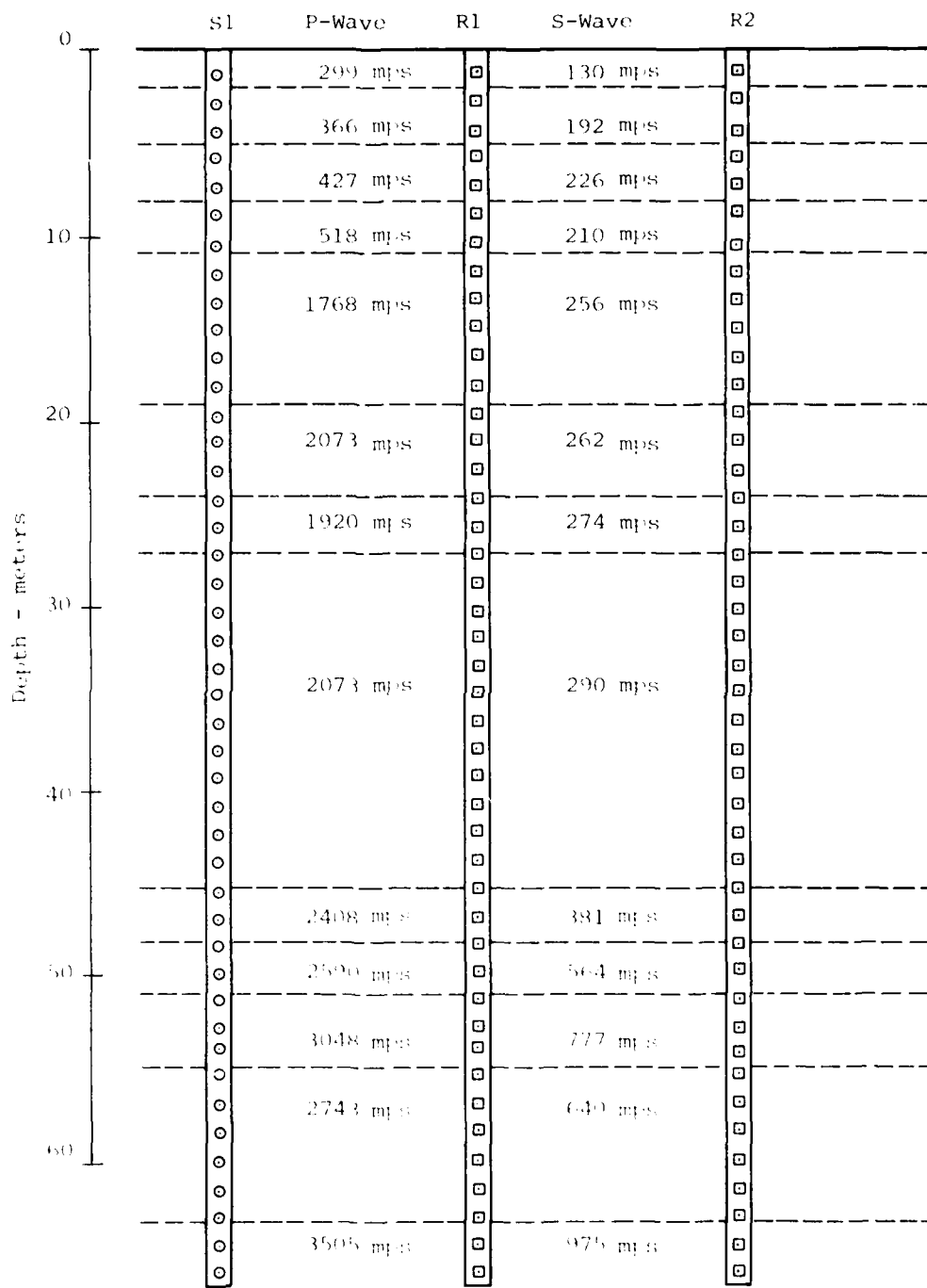


Figure 4. P-Wave and S-Wave Velocity Profiles
Interpreted from Crosshole Survey
Near MBII-2 (Ref. 10)

The results of the material property investigation and the geophysical studies are shown in Figures 8 and 9 for MBII-1 and MBII-2 respectively. These are the site profiles used in analysis of the MBII data. Figure 10 shows the idealized calculational site profile (determined from CIST 19) that was used for the pretest predictions of MBII-1 and MBII-2. This is slightly different from Figures 8 and 9 because it was based on preliminary geophysical information. Figure 11 shows a three dimensional projection of the bedrock surface which illustrates the nonlevel nature of bedrock over the valley.

2.3 Instrumentation Plan

The instrumentation layouts for the experiments in Misers Bluff Phase II are shown in Figures 12 through 14. Motion sensors used on these experiments were Endevco model 2262 and 2264 accelerometers, Sandia model DX velocity gages, WES SE stress gages, LVDT soil strain gages, and Kulite model HKS-375 and XTS-1-190 airblast gages. Ranging, installation, and recording of the data was performed by WES. A more detailed discussion of the instruments used may be found in Reference 13.

Initial data reduction for Phase II was done by WES. They provided corrected data plots at scales of 1"-400 msec to a total time of 2 seconds with amplitude scales automatically set by the plot program. WES then provided corrected data tapes to AFWL who made additional plots at

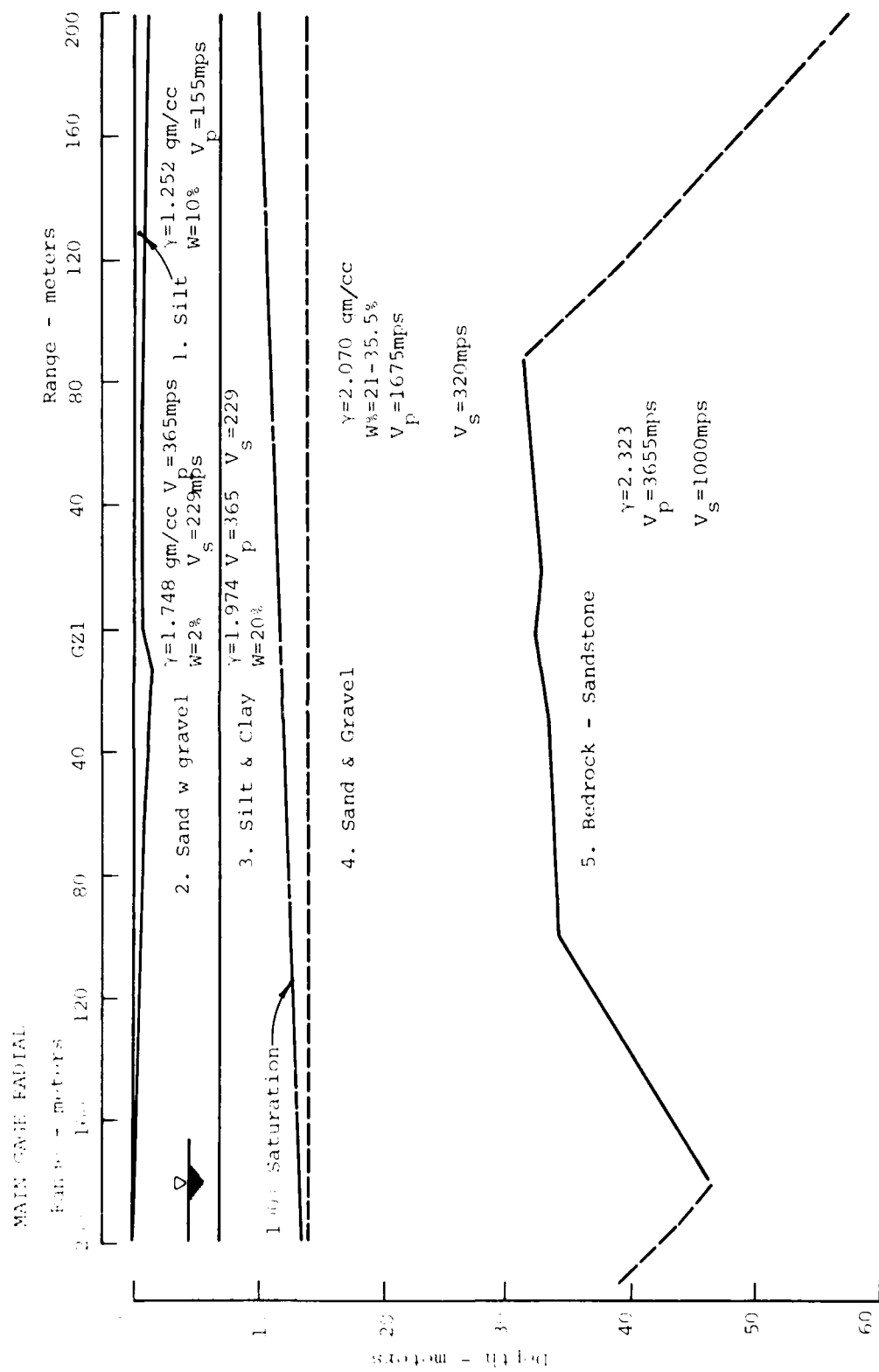


Figure 5 . Site Profile of MBII-1 (Ref. 12)

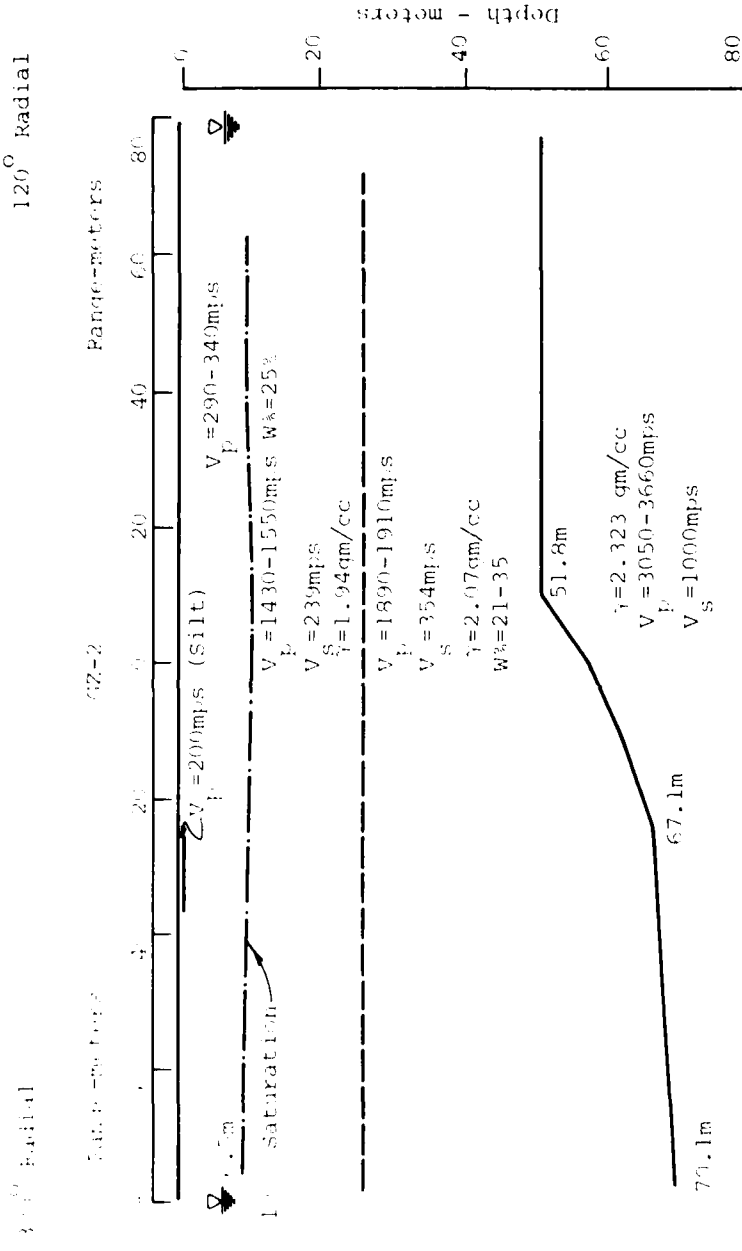
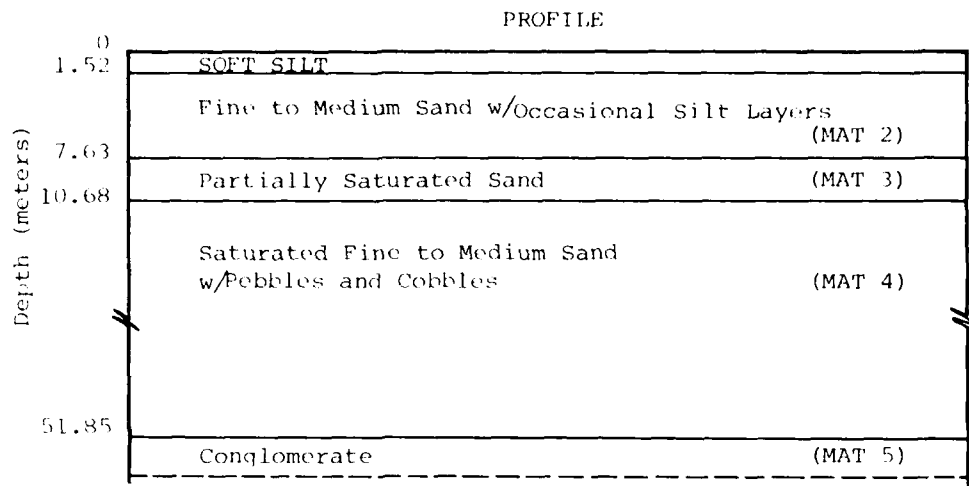


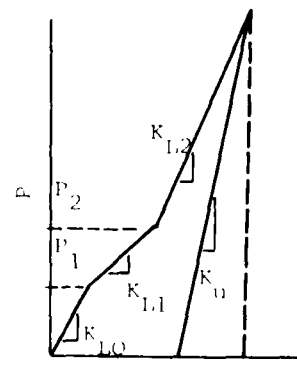
Figure 6 . Site profile Along Main Gage Line MBII-2 (Ref. 7)



Prop	Units	MAT. 1*	MAT. 2	MAT. 3	MAT. 4	MAT. 5
ρ	g/cc	1.22	1.85	1.90	2.0	2.3
C_{LO}	mps	0.35	0.30	0.40	0.45	0.2
C_{L1}	mps	168	214	366	2135	2745
C_{L2}	mps	336	305	366	2135	1830
C_{L3}	mps	-	549	366	2135	1830
C_{L4}	mps	2306	549	1525	2135	2745
C_{L5}	mps	-	549	1525	2135	2745
P_1	Mpa	-	3.4	.069	.069	.345
P_2	Mpa	1.4	13.8	.69	.69	.69
α		.7	0.4	0.1	0.04	.03

* Not used in MBII-1
Pretest Predictions

HYDROSTAT USED IN PLID



$$E_x = \frac{P_2 - P_1}{x} \cdot \frac{\left(1 + V_x\right)}{\left(1 - V_x\right)}$$

Figure 7. Profile and Computation Parameters Used for MBII Predictions

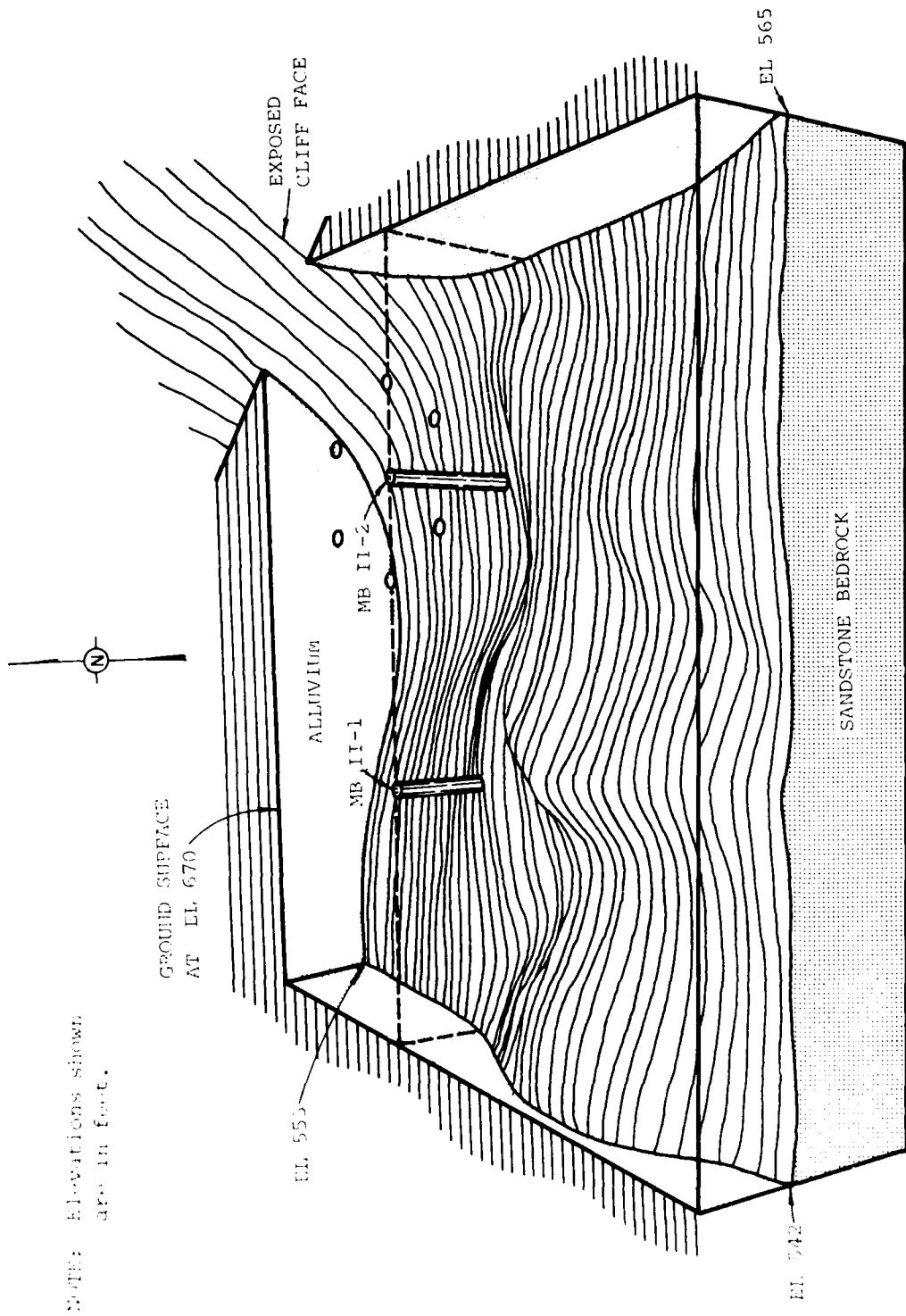


Figure 8 . Three-Dimensional Projection of the Bedrock Contact at Misers Bluff (Ref. 7)

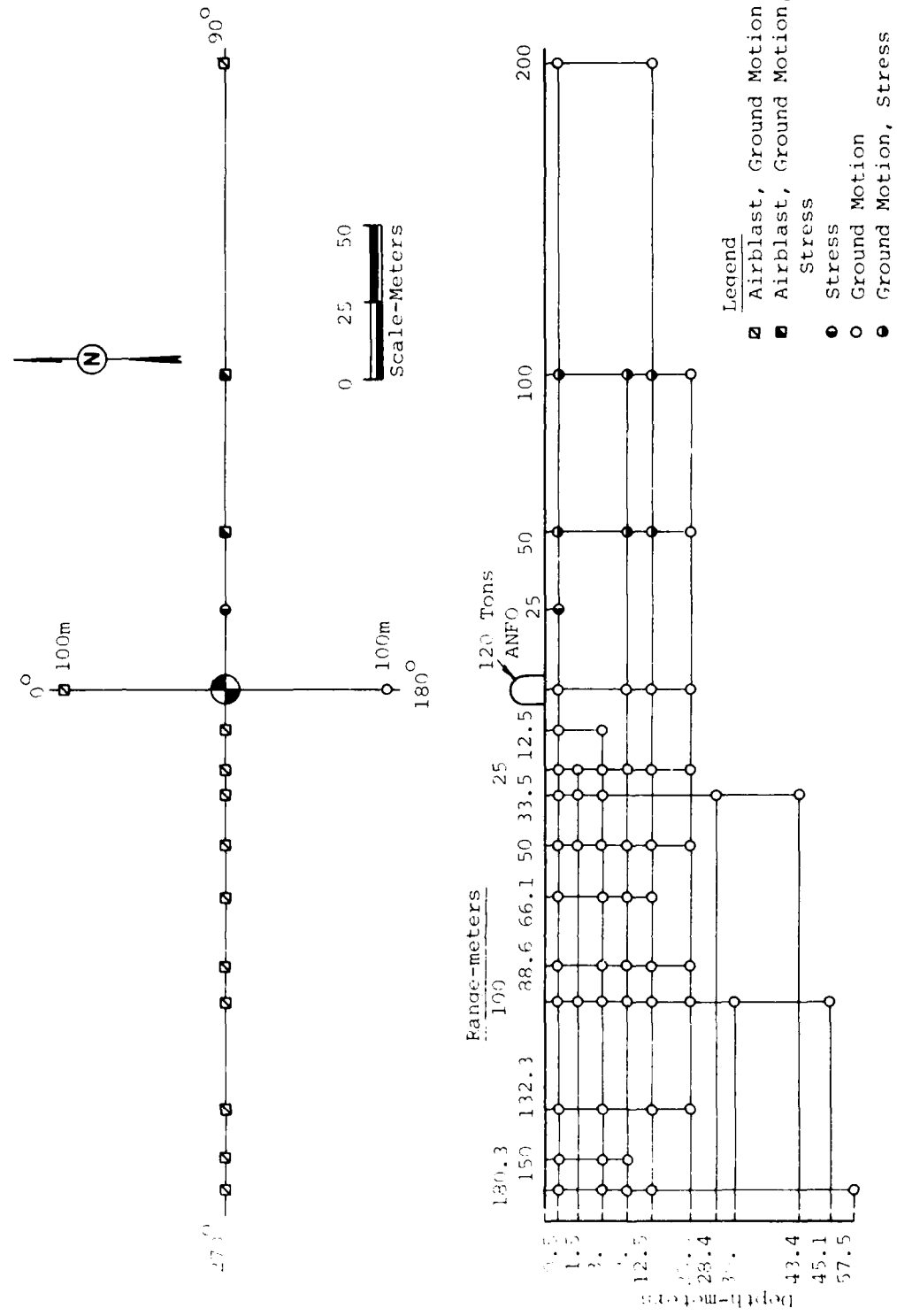


Figure 9. Instrumentation Layout for MBII-1 (Ref. 13)

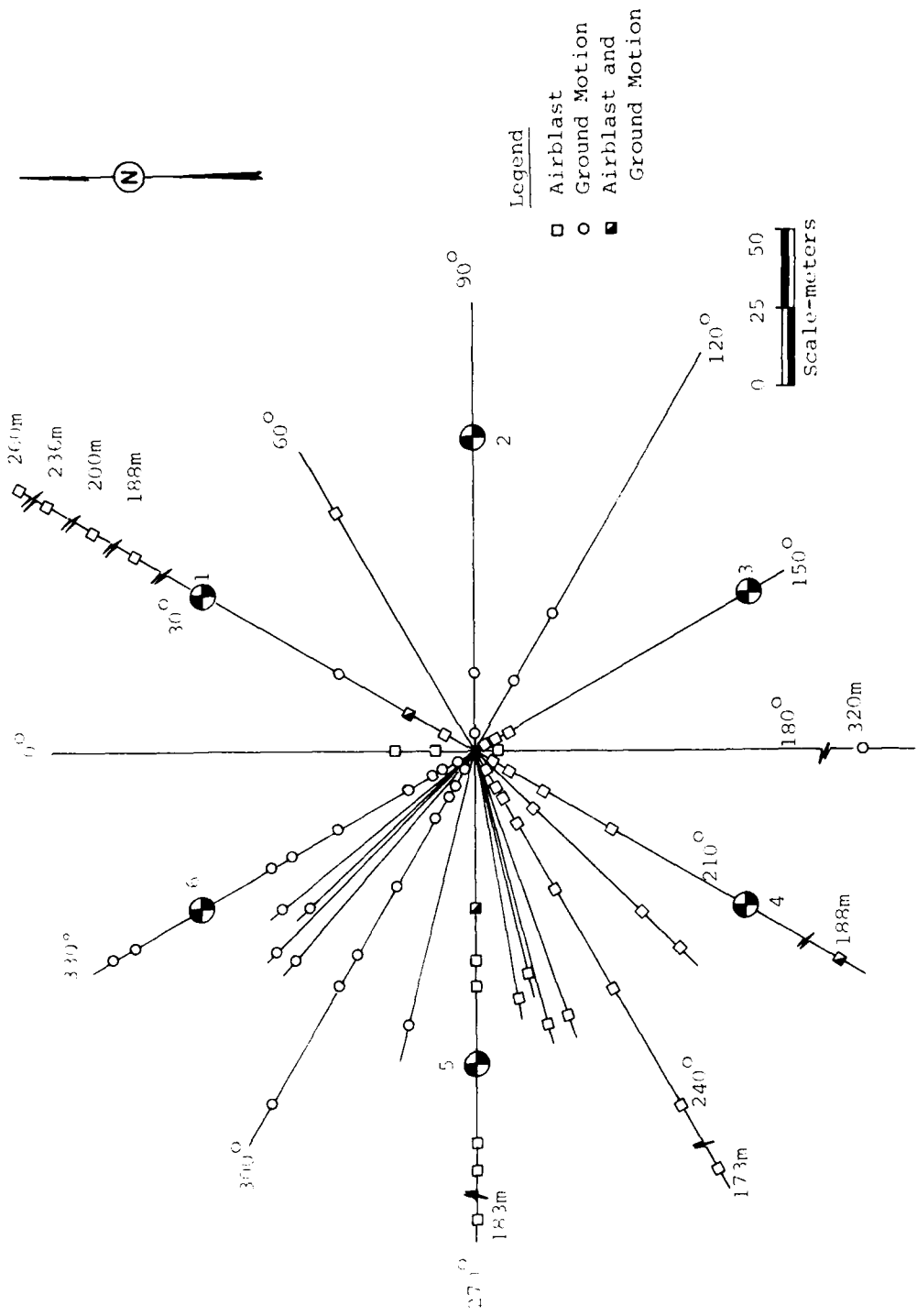


Figure 10 . Plan View of MBII-2 Experiment

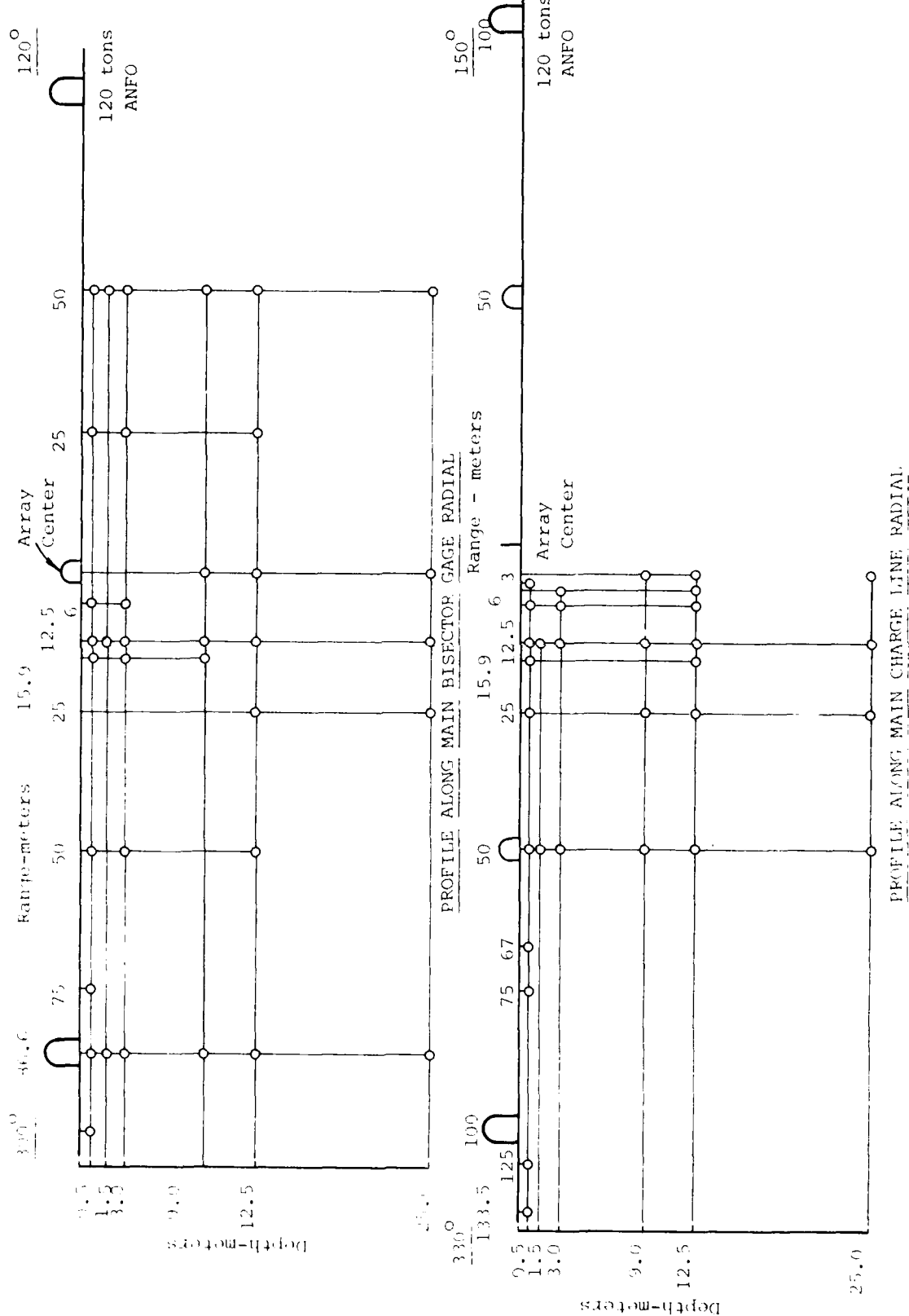


Figure 11. Profiles Along Main Ground Motion Measurement Radials - MBII-2

expanded time and amplitude scales. Frequency domain data were also provided by WES for selected measurements of MBII-2.

3. Discussion of Data

3.1 Review of Phase I Results

In order to discuss the Phase II experiments, it is helpful to review the major multiple burst results, from Phase I. A typical multiple burst experiment (MBI-4) is shown in Figure 12. Shown on Figure 13 are the areas in which the superposition assumption was accurate and inaccurate.

Superposition failed as a predictive model interior to the charge array above the water table. Examples of the waveforms measured in this region are shown in Figures 14a and 14c. The failure was apparent in both horizontal and vertical waveforms, but was more dramatic in the vertical motions. The major difference observed was the long duration, large amplitude upward motion following the downward air slap (Figure 14a). Two hypotheses concerning the origin of this signal resulted from the data analysis. The first hypothesis is that the upward motion is due to the expansion of the pore air in the soil caused by the passage of the negative pressure of the airblast, which dilates the material and produces significant upward motions. The second hypothesis is that these large upward motions are due to free surface spall which results from high stress levels created by the interaction of direct and reflected (from the center) waves. The interactions are the result of the convergent nature of the geometry. Calculations modeling both phenomena were made for comparison of

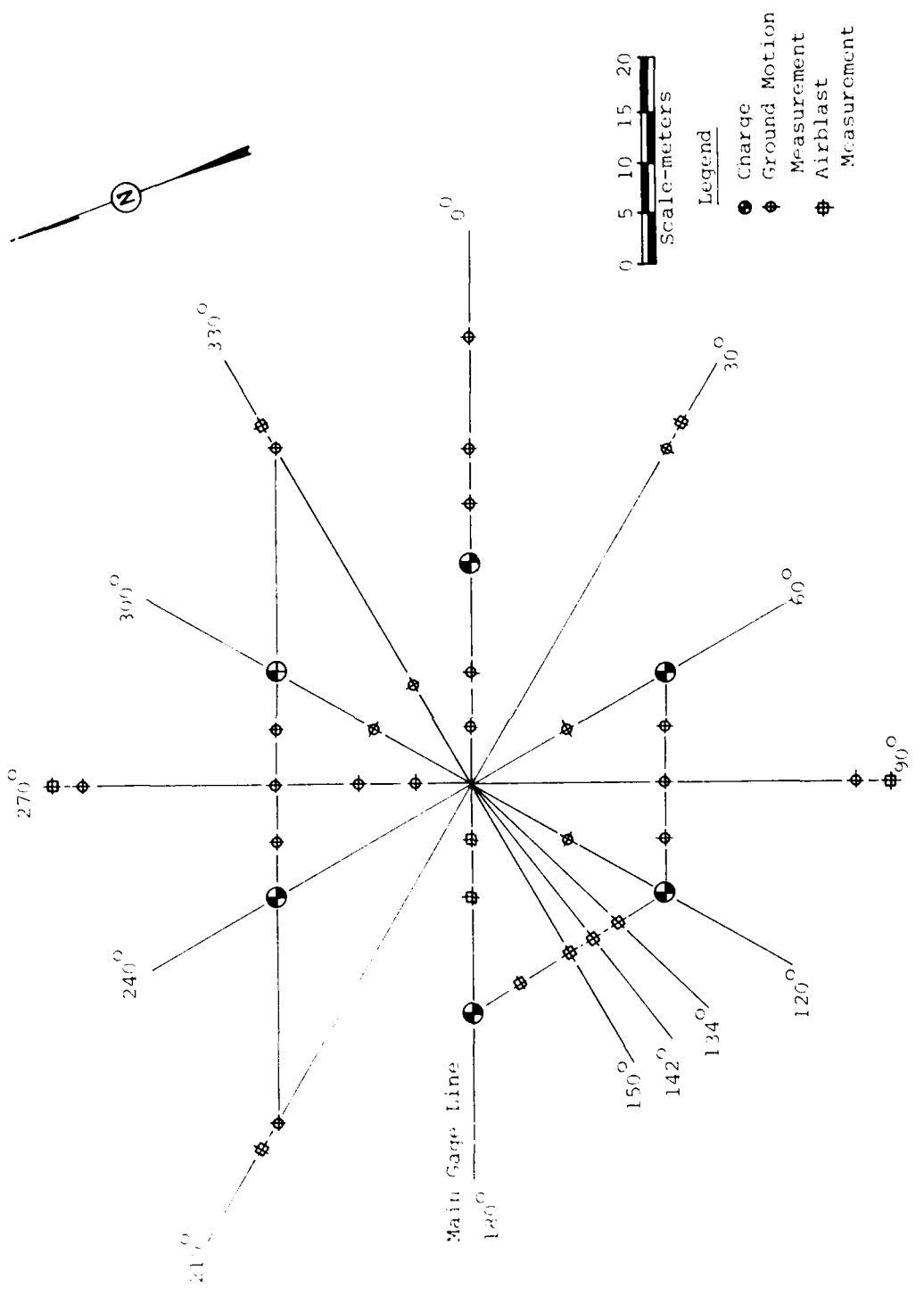


Figure 12. Typical Gage Layout for Multiple Burst Experiments in Phase I (MBI-4)

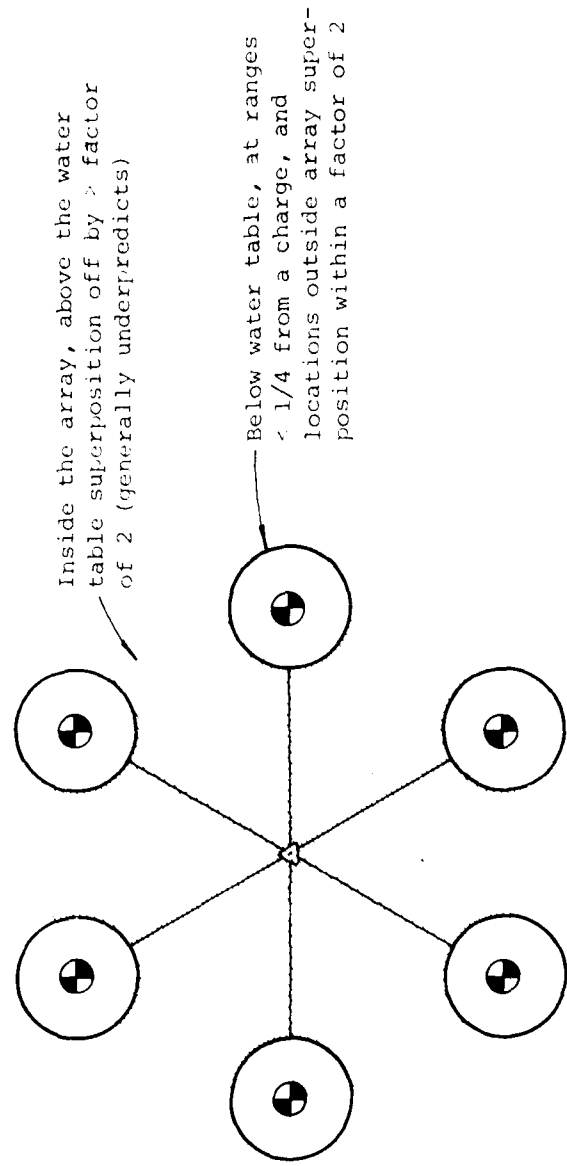


Figure 13. Accuracy of Superposition on Misers Bluff Phase T

the Phase I experiments and the pore air expansion mechanism appeared to be more influential than wave convergence.

Based on the results from Phase I the waveform synthesis model was updated and used to predict the Phase II experiments. The objective of this report is to evaluate and refine this model based on the new data.

The process of developing a prediction procedure naturally involves the prudent utilization of theory adjusted for experimental data. In developing prediction procedures for ground shock phenomena, simple theory has proven inadequate and prediction procedures are heavily biased to experimental data. The unfortunate aspect to a heavy emphasis upon empiricism in making predictions is that the predictions are only as good as the data base from which they are derived. Since the data base is quite limited and predominately from high explosive events, theoretical guidance is required in extrapolating to the high yield nuclear events of interest.

For the above reason it is imperative that each new data group added to the data base be checked for consistency and anomalies, thereby validating or revising the prediction procedures based upon the previous data set. Therefore, within this report comparisons of Misers Bluff II-1 data to the preexisting data are made.

The MBII-2 event data will be used to evaluate the superposition assumption and to study in greater detail

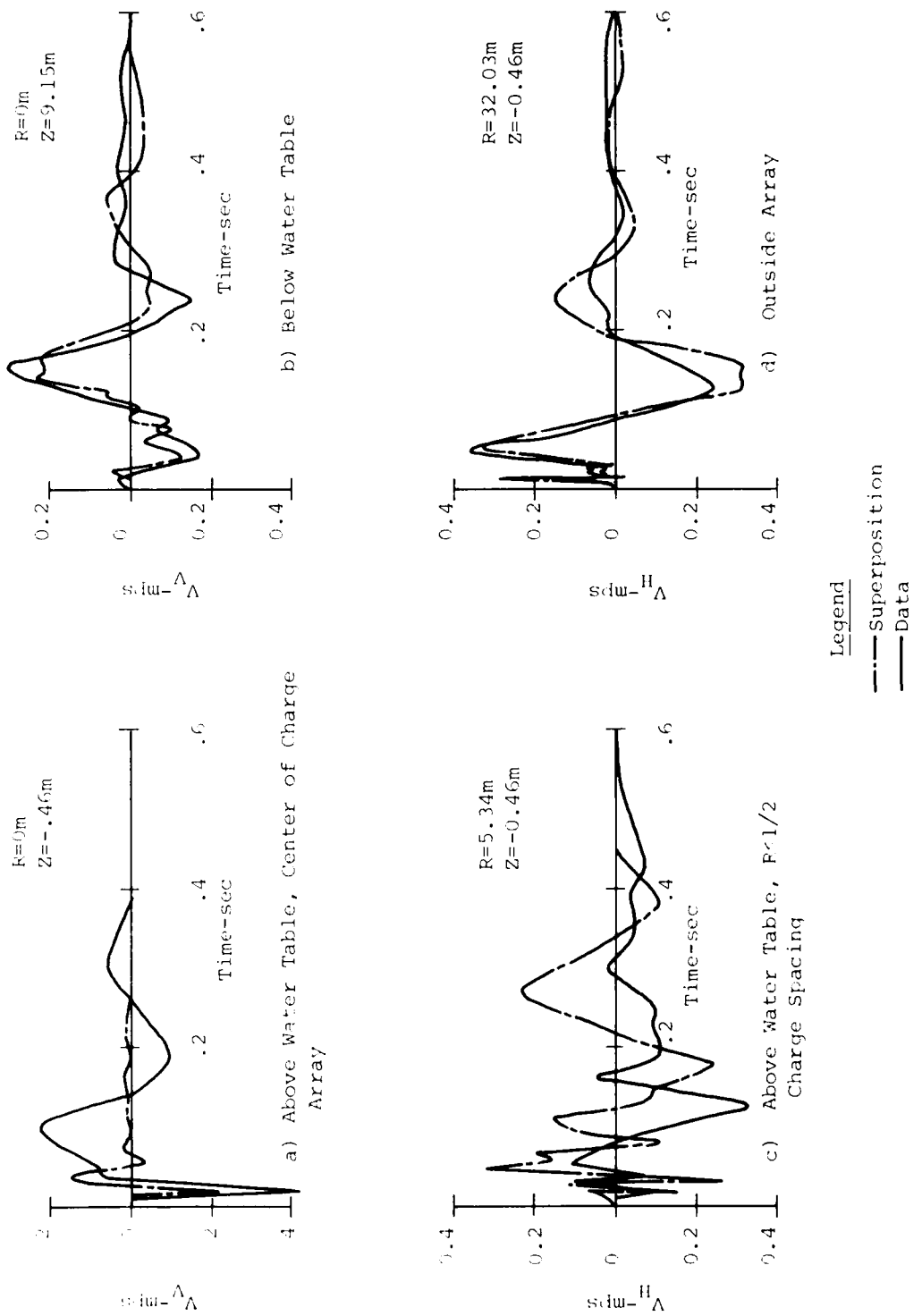


Figure 14. Comparison of Superposition and Data in Phase I (MBI-4)

the nonlinearities which were hypothesized from the results of Phase I. The end result of this study will be a Waveform Synthesis Model for predicting waveforms from either single or multiple burst detonations.

3.2 MBII-1

3.2.1 Previous 100T High Explosive Experiments

Misers Bluff II-1 is identical in explosive yield and configuration to eight previously conducted tests. Small variations in explosive charge and/or configuration were present in some of these tests, however, the effect of those small changes are felt to be minor when making comparisons for determination of site effects. For example, the MINERAL ROCK and MINE ORE events were 1/10th buried, that is to say the center of the TNT charge was at a height of 2.20 meters rather than at the standard surface tangent height of 2.4 meters. Other charge variations including the PRE MINE THROW IV 102-ton Nitromethane charge and the more recent AN/FO capped cylinders have proven similar to the surface tangent 100-ton TNT charges in the PRE DICE THROW series of tests (Ref. 14).

Table 2 presents a brief review of the 100-ton explosion site data. The spectrum of sites tested covers a wide range of earth material properties from the low strength saturated silts, sands, and clays of the PRE DICE THROW Site on the White Sands Missile Range, New Mexico to the high strength properties of the quartz diorite at the MINE SHAFT

TABLE 2. 100-TON TANGENT-ABOVE HIGH EXPLOSIVE TEST EVENTS

EVENT	YIELD (tons)	CHARGE	TEST MEDIUM	D _{WT} (m)	D _{BR} (m)
DISTANT PLAIN 6	100	TNT	Silty clay and fine sand	7.63	>60
MINE ORE	100	TNT	Quartz diorite	>150	0
MINERAL ROCK	100	TNT	Quartz diorite	>150	0
MIDDLE GUST III	100	TNT	Wet clay/shale	1.22	3.05
MIDDLE GUST IV	100	TNT	Dry clay/shale	>150	5
PRE MINE THROW	102	Nitromethane	Dry silt and clay	>150	>150
PRE DICE THROW III-1	100	TNT	Clayey silt and sand	2.14	>150
PRE DICE THROW III-2	120	AN/FO	Clayey silt and sand	2.14	>150
Misers Bluff III-1	120	AN/FO	Gravelly sand	10.68	30.5

Site near Cedar City, Utah. The depth of water table varies from 1.2 meters at the MIDDLE GUST Wet Site to a depth of over 150 m at the PRE MINE THROW and MIDDLE GUST Dry Site. The depth to rock also covers a wide range of variation from the surface rock at the MINE ORE and MINERAL ROCK events (MINE SHAFT site) to the 3 meter depth shale at the MIDDLE GUST Wet Site to a depth greater than 150 meters at the PRE MINE THROW and PRE DICE THROW Sites.

There are three site characteristics present at the Misers Bluff Site which were not present in any of the previous events. The first of these is the presence of an extremely soft and compactible near-surface layer. This characteristic will be discussed in the following sections of this chapter since special emphasis was placed in estimating the effect of this layer on pretest predictions. This characteristic will be shown to cause significant differences in downward air slap and upward motions from those motions observed in the past test on other geologies.

The second difference in the Misers Bluff II site has to do with a zone of near-complete water saturation above the 15 meter depth, but below what is generally referred to as the water table. Material below the water table is most generally and commonly assumed to be saturated, i.e., all voids are completely filled with water. The effect of small amounts

of air within the voids is known to cause significant differences in material compressibility in the laboratory (Ref. 15) and is believed to cause the significant differences in both compressibility, and wave speeds in the field, however, measurements of percent saturations in the field are nearly impossible to make within a few percent. Figure 15 illustrates an example of the significance of a small amount of air filled voids on soil compressibility. The effect of this layer upon the Misers Bluff field of motion will be addressed in Section 3.1.5.

The third site characteristic of Misers Bluff significantly different from previous tests is the presence of bedrock at a depth within the range of 20-60 meters. All previous test event geologies can be characterized as one or two-layer systems. Misers Bluff is a distinct three layer geology with the near-surface dry soil underlain with saturated sand and gravel at a depth of 10.6 meters and bedrock shallow enough to affect motions within the conventional outrunning ground motion regime (typically 100-200 meters).

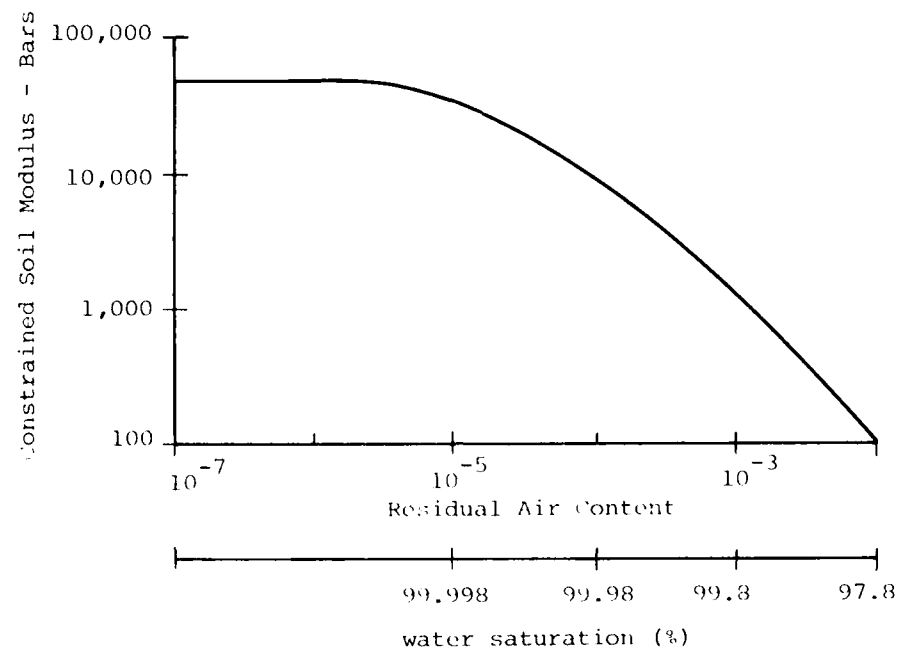


Figure 15. Modulus (Compressibility) of Soil with Entrapped Air for a Sandy Soil with a Void Ratio of 0.46 (Ref. 15)

The theoretical techniques being used presently for prediction of surface waves (oscillatory component) indicate that stiffer material at depths on the order of 1/2 to 1/3 of the ground ranges involved have a significant effect on the motion. This site has the stiff layer shallow enough to evaluate this effect. This subject is addressed in Section 3.1.6

3.2.2 Phenomenology

Near surface (0.5m) vertical and horizontal velocity waveforms are shown in Figures 16 through 19. There are three distinct regions of ground motion categorized according to range from ground zero, and similar to the zonation used in Reference 16. The first includes the 12.5 m range to the 33.5 m range measurements. The next region includes those gages from the 50 m range to the 100 m range. The final region extends from the 132.3 m range out to the farthest measurement stations.

The ground motion observed in these regions appears to reflect the variable thickness near surface silt (Refer to Fig. 8). In the first region the depth of silt is greater than the gage depth. As the second region is approached the silt is tapering up to a depth approximately the same as the gage. In the third region the gages are deeper than the bottom of the silt layer.

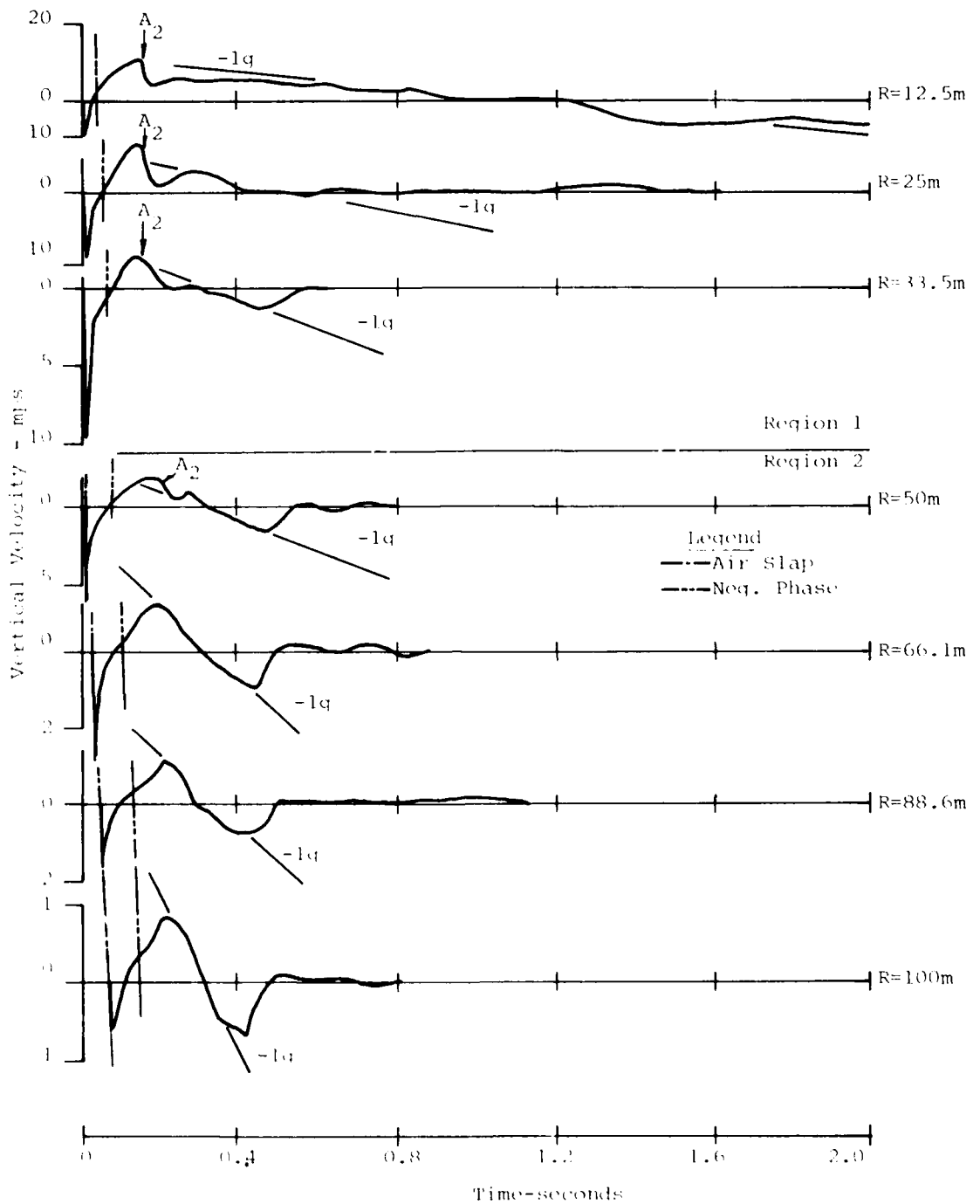


Figure 16. Vertical Velocity Waveforms at the 0.5 m Depth - MBII-1

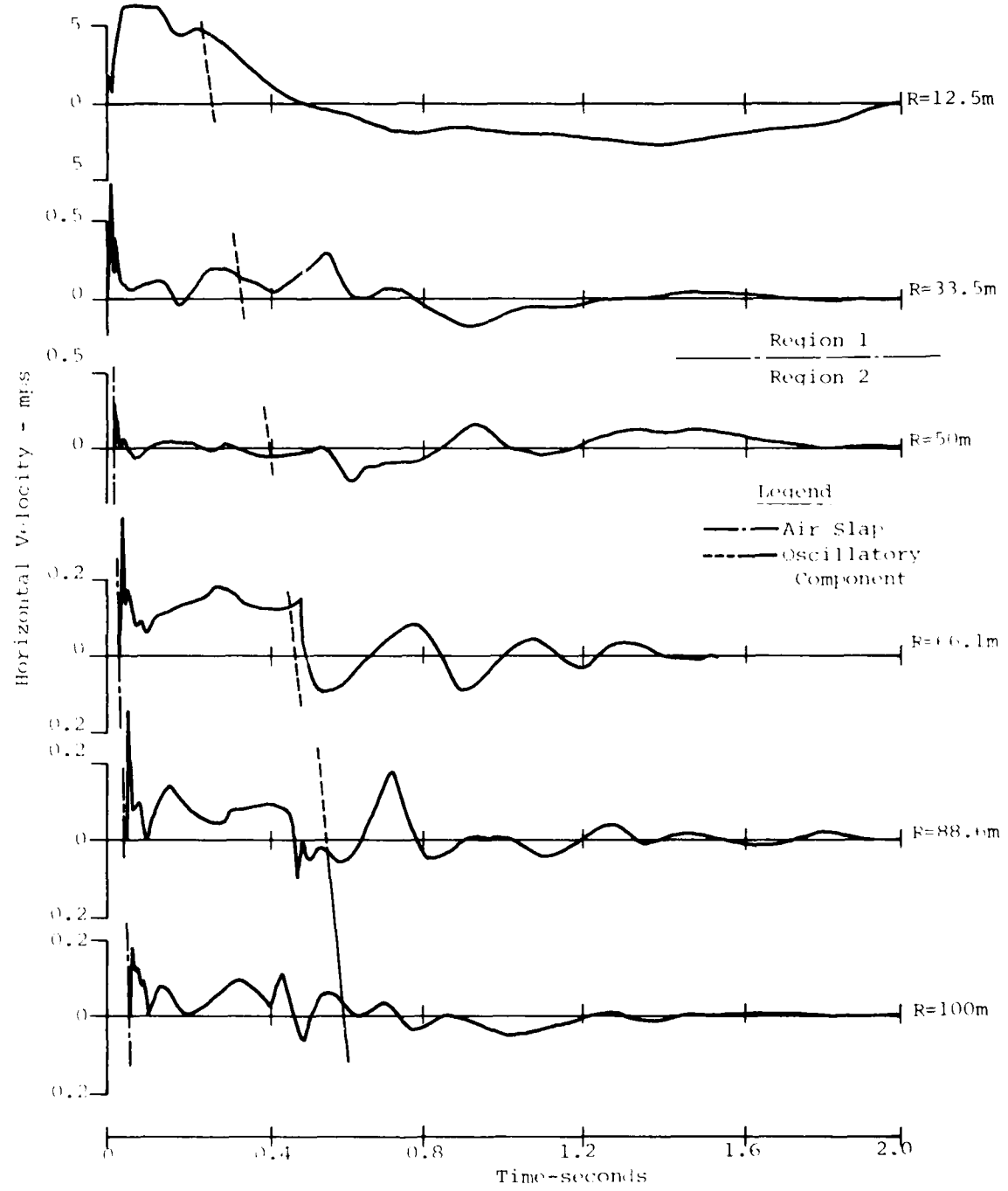


Figure 17. Horizontal Velocity Waveforms at the
0.5 m Depth - MBII-1

Region 3

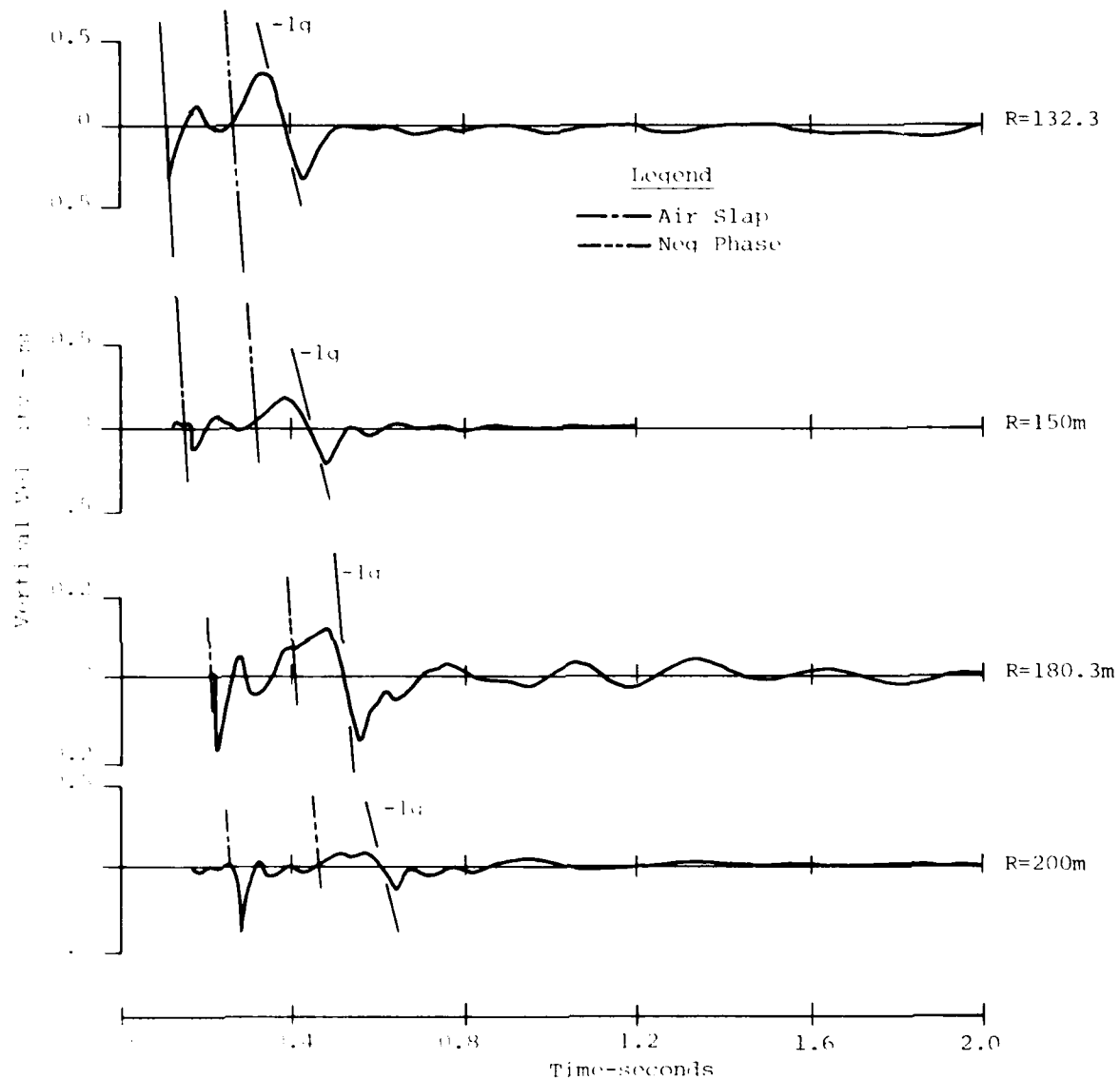


Figure 13. Vertical Velocity Waveforms at the
0.5 m Depth - MBII-1

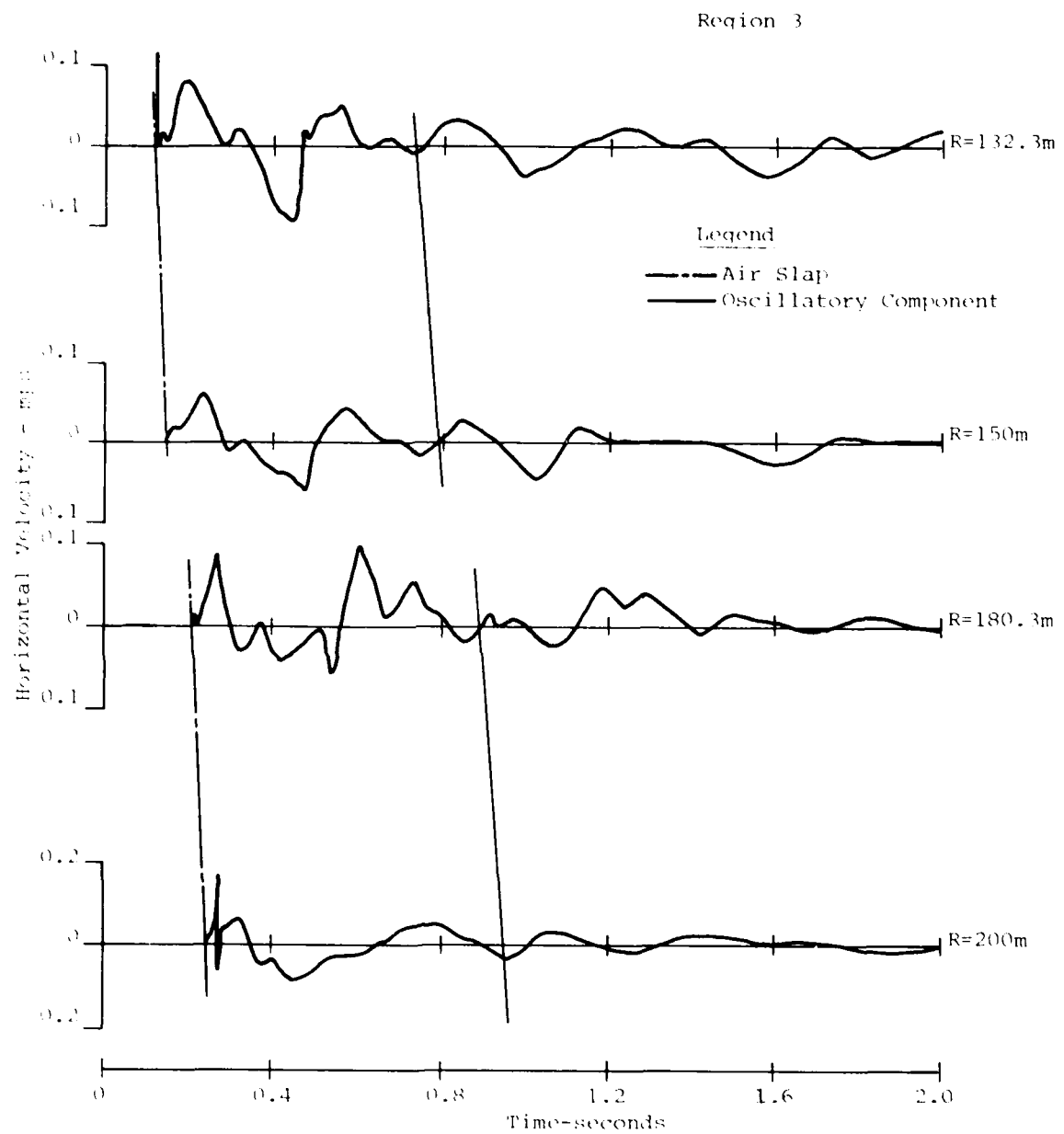


Figure 19. Horizontal Velocity Waveforms at the
0.5 m Depth - MBII-1

Vertical motion in the first group (Fig. 16) is initiated by the passage of the overhead airblast which creates a downward velocity. This is immediately followed by a large upward motion which is related to the formation of the crater and the negative phase of the airblast. The upward motion is interrupted by a small secondary compressive phase in the airblast (indicated by A₂'s on Fig. 16). This secondary compressive phase is of short duration and terminates before the material can return to its initial position. The material then begins to free-fall (signified by the -lg slope in Fig. 16). This free-fall ranges in duration from approximately 1.8 seconds (the extent of the data plot) at the 12.5 m range to about 0.3 seconds at the 33.5 m range. This group of waveforms is characterized by little or no motions at later times.

Horizontal motions in this region (Fig. 17) exhibit the same behavior as the vertical motions described above. The overhead airblast initiates the motion with an outward signal. This signal is followed by the airblast induced shear wave which clips the outward air slap and drives the motion inward (toward the charge). This is not seen in the vertical records. Then a large outward signal attributable to the formation of the crater occurs during the time frame of negative phase effects seen in the verticals. Late time motions vary from little motion at the 12.5 m range to oscillatory in nature at the 33.5 m range.

Beginning with the 50 m range a slight change in character is developing in the vertical motions (Fig. 16). The initial motions are as described above, but the free-fall signal is followed by an abrupt reversal in motion. This reversal is due to the material reaching its initial position (transient displacements are zero) and rejoining the lower material. Following this rejoin an oscillatory motion is observed. At the 50 m range this oscillatory motion is of small magnitude and short duration, but at increasing ranges this component becomes more significant.

Again, horizontal motions (Fig. 17) correlate reasonably well with the verticals. Crater-related (upstream air induced) effects are occurring in the time frame of the negative phase effects seen in vertical motions. The abrupt outward signal visible at approximately 450 msec is the result of the material rejoining in the vertical motions. Horizontal motions are completed in this region by oscillatory motions. These oscillatory motions are much larger in magnitude relative to early time horizontal motions than was observed for the vertical motions. Comparison of this oscillatory signal between the vertical motion and horizontal motion however revealed that the peak values were of the same order of magnitude.

The final group of vertical waveforms (Fig. 18) is in the outrunning region so the air slap is preceded by, and superimposed upon the low frequency oscillatory motion. Following the air slap there is an upward signal related to the recovery of the material and reflections from deeper layers and upstream air-induced effects (see Fig. 8). Motion is then directed downward as the upward momentum of the material is overcome by the tail of the initial compressive phase of the airblast. Following the downward motion comes the upward motion attributable to the overhead passage of the negative phase of the airblast. This second upward peak is reached as the recompression phase of the airblast arrives. Subsequently the material begins free-fall (signified by the -1g slope on Fig. 18). Rejoin (impact) then takes place, reversing the motion and a continuation of the oscillatory component completes the motion.

Horizontal motions measured in this region are shown in Figure 19. Again the correlation in phenomenology is good between the horizontal and vertical motions.

Figures 20 through 22 present the vertical and horizontal waveforms measured at the 3 m depth. Again these waveforms may be placed into three categories. The first is of the classical superseismic nature (33.5m to 66.1m). Region 2 (88.6m to 132.3m) is transitioning from the superseismic zone of region 1 to the outrunning zone of region 3.

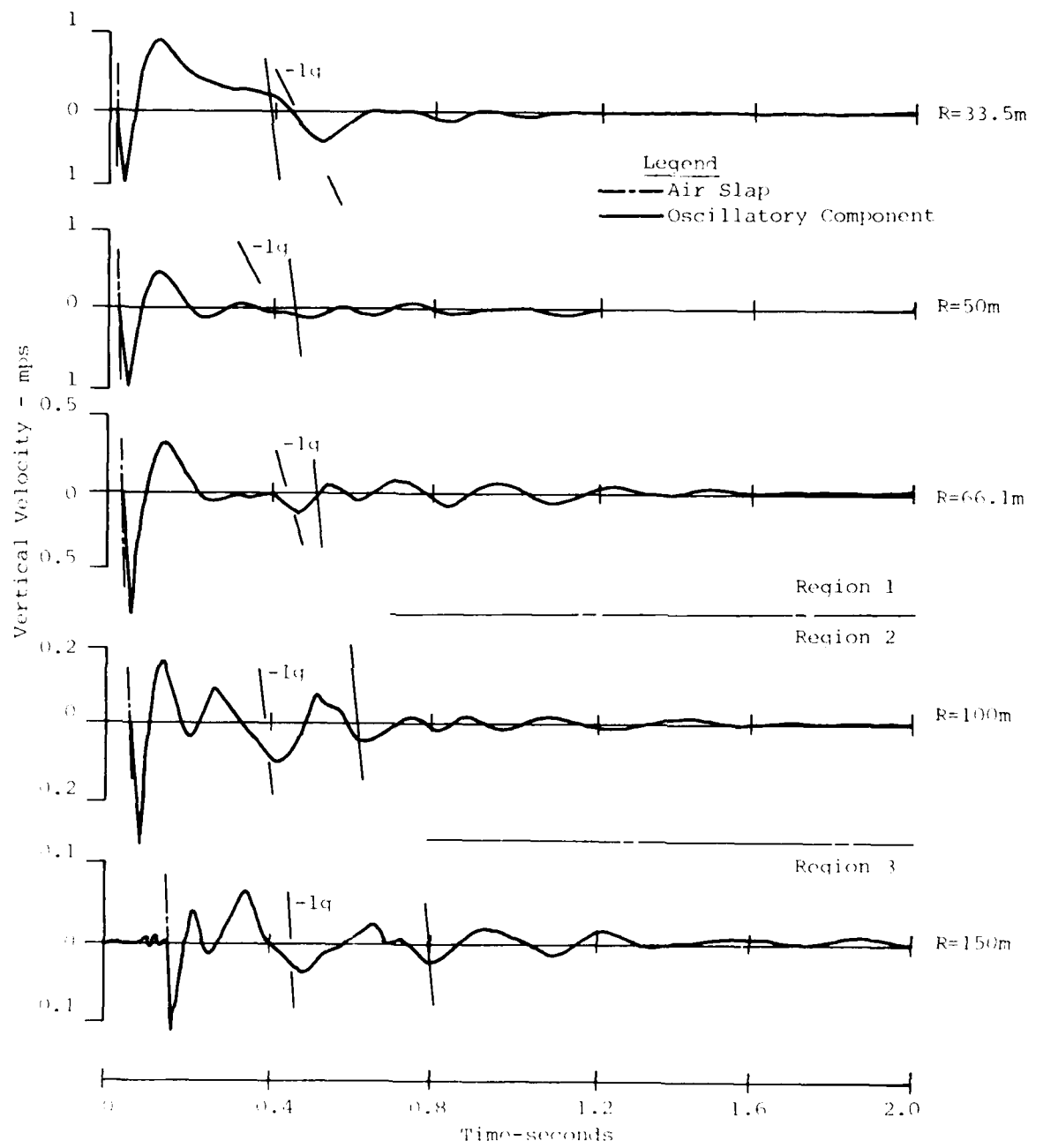


Figure 20. Vertical Velocity Waveforms at the 3.0 m Depth - MBII-1

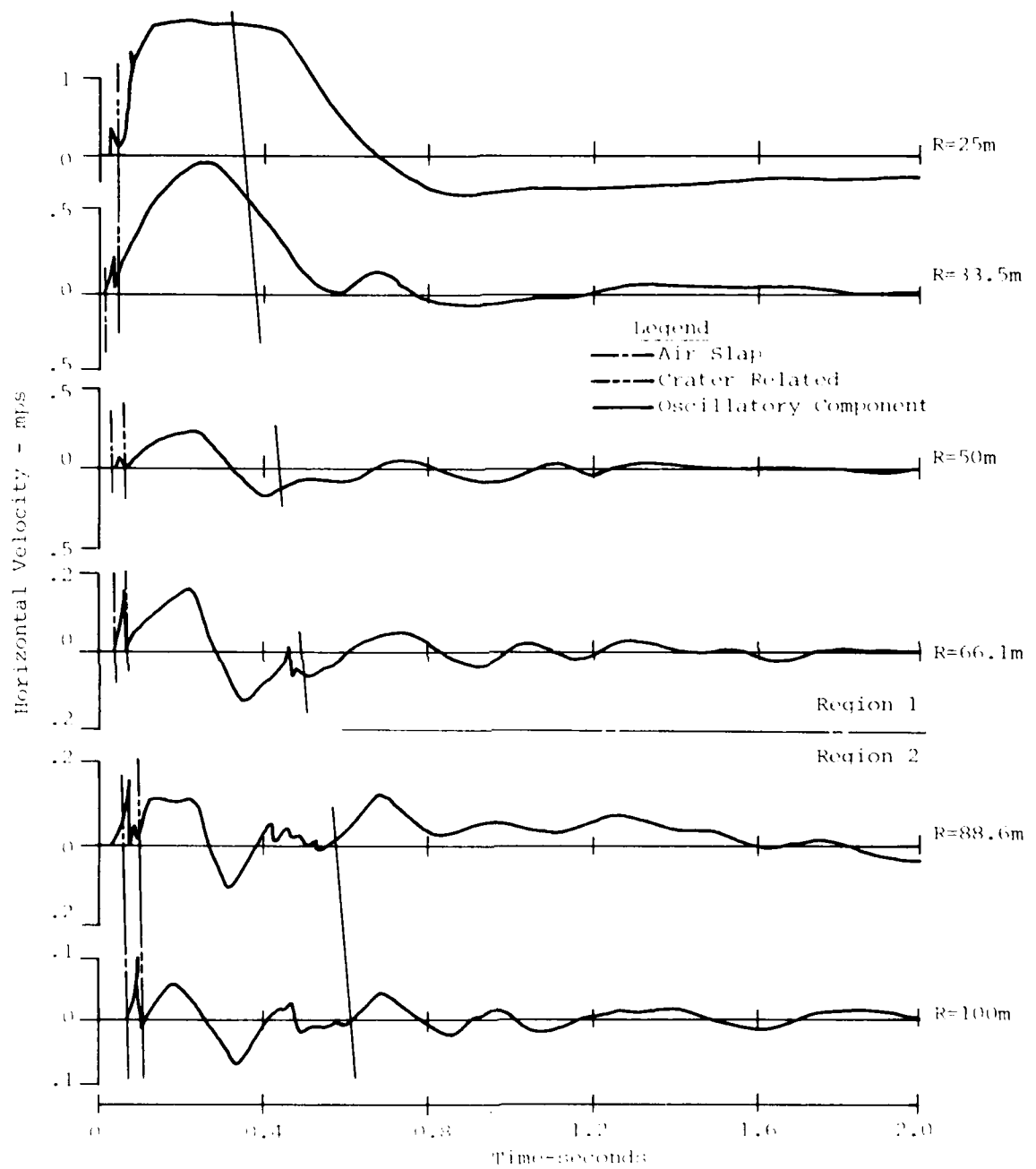


Figure 21. Horizontal Velocity Waveforms at the 3.0 m Depth MBII-1

Region 3

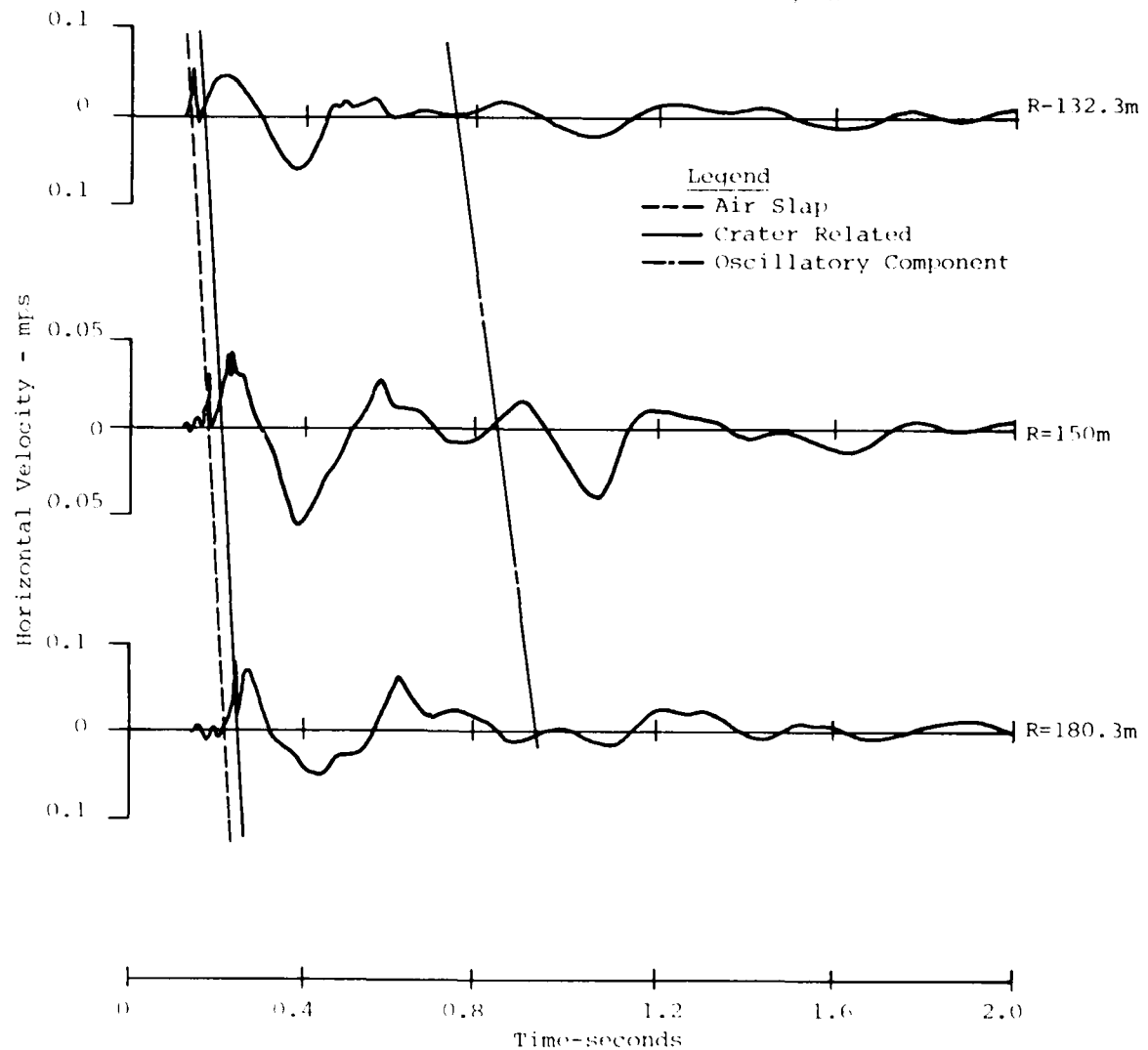


Figure 22. Horizontal Velocity Waveforms at the
3.0 m Depth - MBII-1

Vertical motions in the first region (Fig. 20) is characterized by the initial high frequency downward air slap. Immediately following this is a long duration upward motion. This signal originates from a combination of the crater-related motion (that impulse causing crater excavation closer-in), reflections of the air slap from deeper layers and direct-induced and upstream airblast induced refracted motion. Calculations indicate that the negative phase effect does not affect these depths. The material then begins to fall only under the influence of gravity. This downward motion is decelerated and reversed as the upper material rejoins the lower material. This is then followed by an oscillatory motion that becomes more significant as distance from the source increases.

Horizontal motions measured in this region are shown on Figure 21. As was the case for the data measured at the 0.5 m depth, there is good correlation of phenomenology between horizontal and vertical velocities, i.e., motions described in the vertical waveforms are identifiable in the horizontal waveforms.

The intermediate range record (region 2 on Fig. 20) for vertical motions shows transition from the classical superseismic waveforms with strong crater related motions, to waveforms that have reduced crater related (upstream induced) motions, and have more significant oscillatory

motions. This waveform also exhibits a second upward motion in the time frame that the preceding group was quiescent. This may be due to second and third reflections imparting upward momentum while the overburden stresses above are reduced due to zero or negative air pressure (gage) at the surface. At this time, the oscillatory component arrives and completes the motion.

The horizontal motions in this region (Region 2, Fig. 21) are similar, however the upstream induced signal has a longer duration than in the vertical waveform. This indicates that this signal is more dominant in the horizontal direction. Following this cycle of motion the oscillatory component arrives and completes the waveform.

The final region of vertical motion (region 3 on Fig. 20) is similar to those described above with the exception that the air slap is superimposed on the outrunning waveform. Also a signal similar to a free-fall rejoin signal is apparent, however, the rate of motion is less than free fall and timing is such that it appears to be propagating from the 100 m range.

Again the horizontal motions (Region 3, Fig. 22) correlate well with the vertical motions.

This single burst experiment was phenomenologically different from those in Phase I in one very important respect. This was the range to which the long duration upward motion followed by the free-fall slope of -1 g and the abrupt reversal of motion extended. The Phase I single burst experiments experienced the phenomena to ranges not greater than 1/2 the multiburst charge spacing, whereas on Phase II it extended to greater than the charge spacing. In the near surface (0.5 m depth) waveforms this signal is due to the dilation of the near surface material by the passage of the negative phase of the overhead airblast. The surface silt layer, which was reported to have 47 percent air voids (Ref. 7), is very susceptible to the pore air expansion mechanism. As the dilated material returns to the lower more competent material, it falls only under the influence of gravity which produces the -1 g slope on the velocity records. The abrupt reversal is due to the upper material rejoining the lower material much like the dropping of a spring, i.e., the dilated material hits the lower material and goes through a period of compression and then rebounds causing reversal of the motion in an abrupt fashion.

The upward motion and associated free-fall rejoin signal at the 3 m depth is believed to be caused by a mechanism other than pore-air expansion. The increased density (and a consequently smaller volume of air) and greater overburden stresses of this deeper material would have a tendency to resist the pore-air mechanism.

The hypothesis is that the apparent spall is the result of compression waves striking a free surface and reflecting back into the soil as tensile waves. Separation occurs because the constructive interference of these two waves produces a net tensile stress greater than the strength of the material and overburden stress. As this separation occurs another free surface is formed. The spall will then propagate downward as compressive waves below from below impinge on the downward propagating free surface. This process continues until the magnitude of reflected tensile wave is insufficient to overcome the tensile strength of the material and overburden stress. This separation can be identified at the 3 m depth to about the 100 m range. A similar signal at greater depths and ranges is apparently the transmission of the impact from the rejoin of the material. Figure 23 shows the extent of spall. The gages in the silt layer separated as a result of the pore-air expansion mechanism whereas those below the silt spalled as a result of the free surface.

3.2.3 Airblast Results

Peak values of overpressure, overpressure impulse, and positive phase duration are shown in Figures 24 and 25. The predictions were taken from the Misers Bluff Test Plan Volume II (Ref. 6). As is seen from the figure, the predictions of all three parameters are quite acceptable.

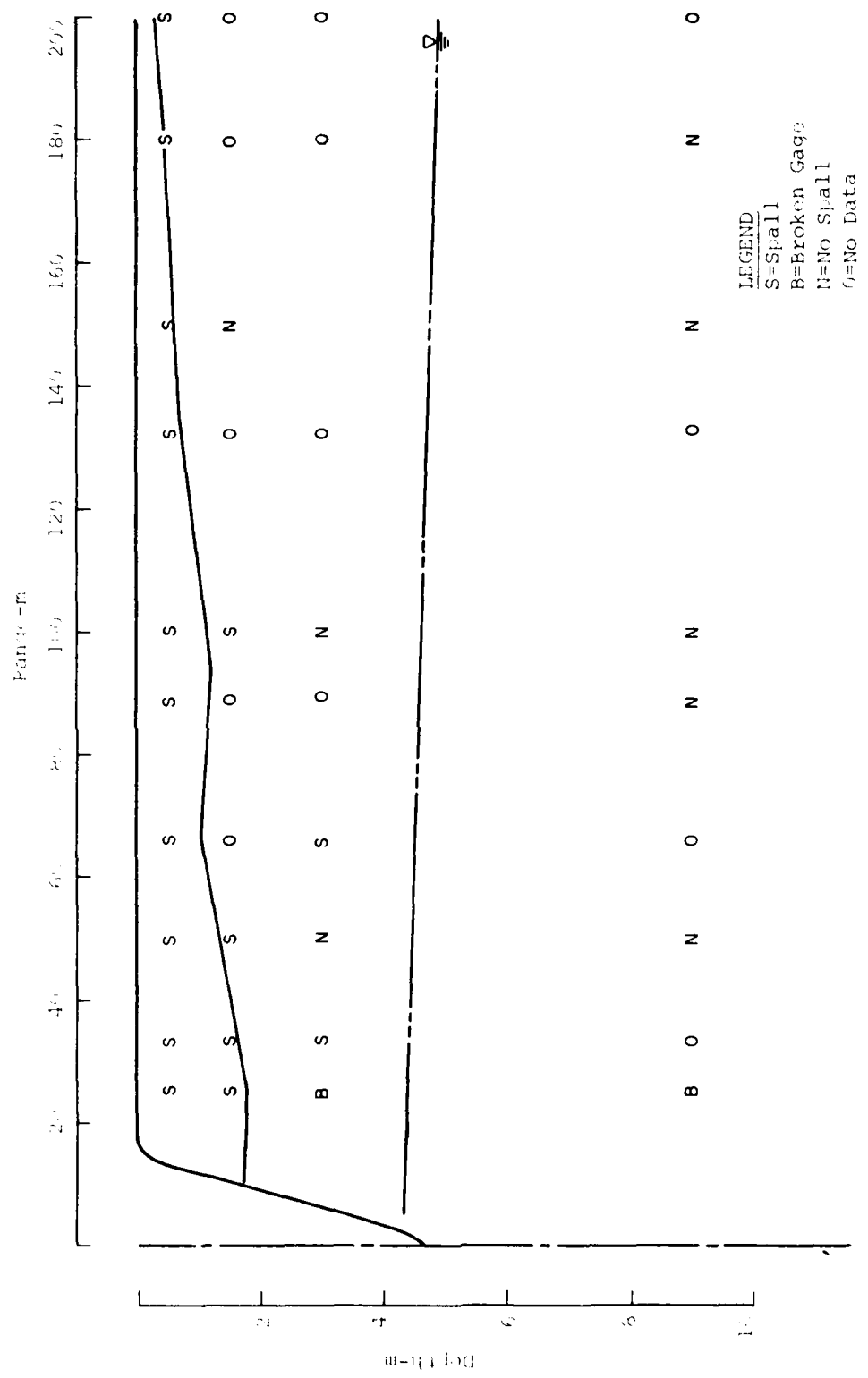


Figure 23. Extent of "Spall" in MBII-1

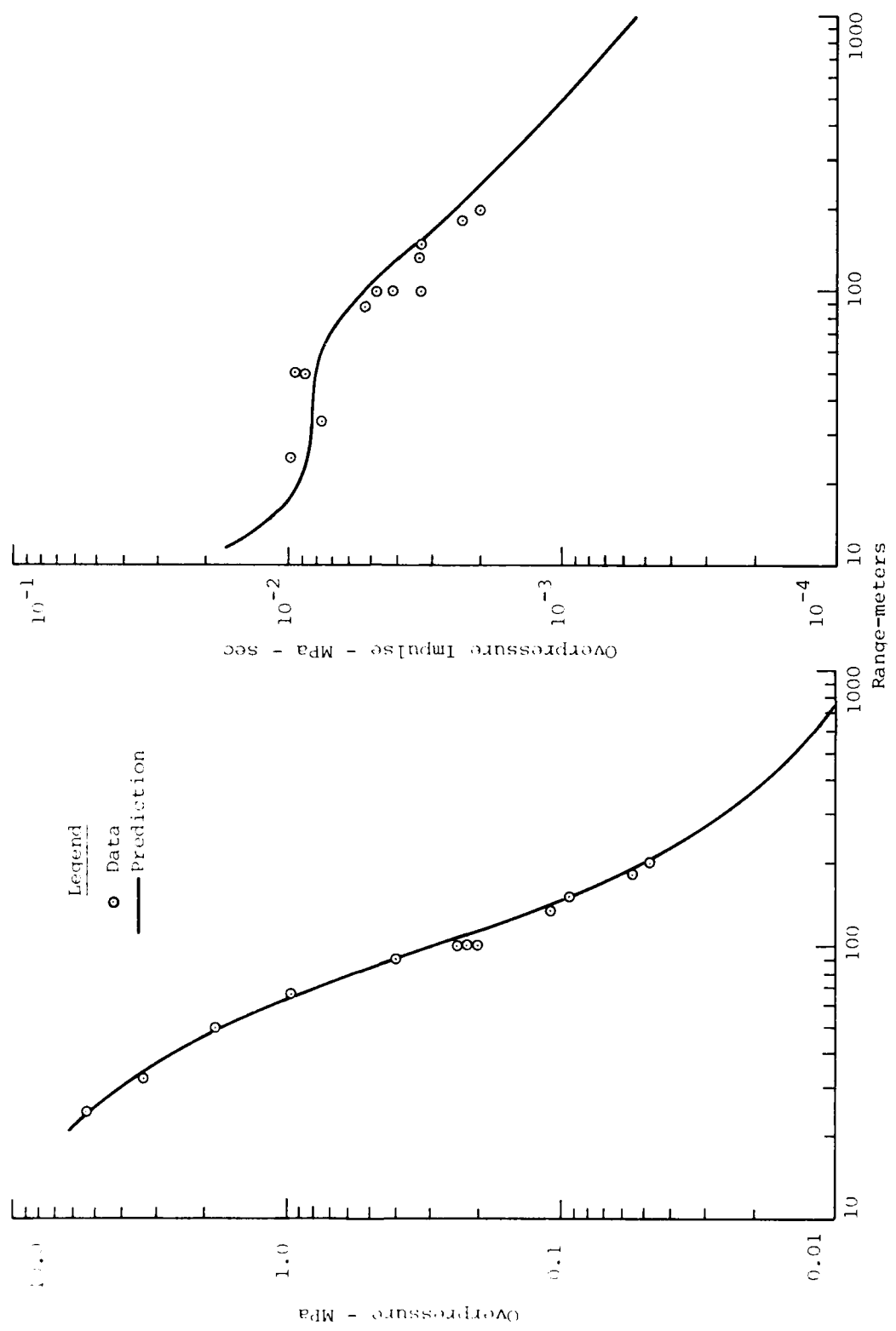


Figure 24. Comparison of Measured and Predicted Overpressure and Impulse - MBII-1

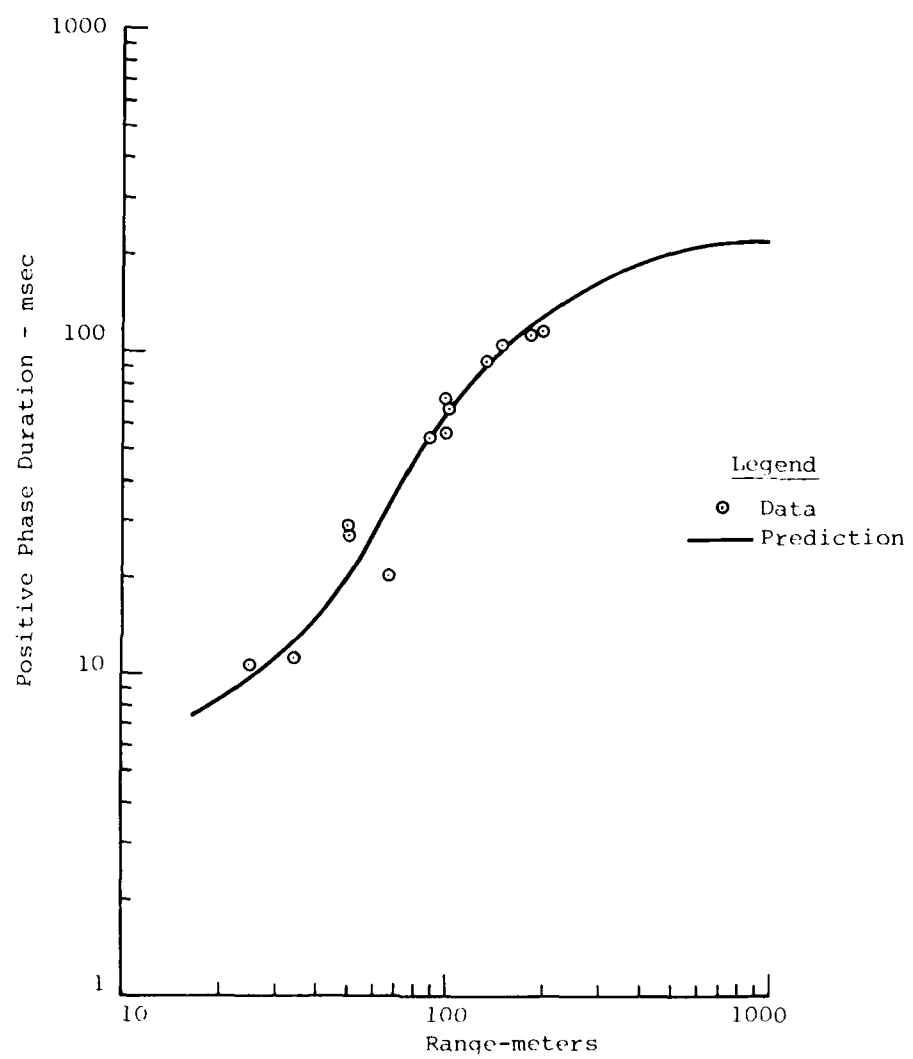


Figure 25. Comparison of Measured and Predicted Positive Phase Duration MBII-1

Airblast arrival times are shown in Figure 26. This curve shown was taken from Reference 6. Again the prediction of arrival times was good.

3.2.4 Air Slap Component of Ground Motion

For the purposes of this report, the air slap component of ground motion will be defined as that component of ground motion that is directly attributable to the passage of the overhead airblast.

3.2.4.1 Prediction Procedure

Prediction of the air slap component was accomplished using PLID, a one-dimensional finite difference code. Use of this code requires specification of the overhead airblast at the location in question and a uniaxial material model.

Airblast parameters necessary for specification in PLID are peak overpressure, positive phase duration, and impulse. These parameters were obtained from Reference 6. The overpressure waveform was described by an exponential function of the form:

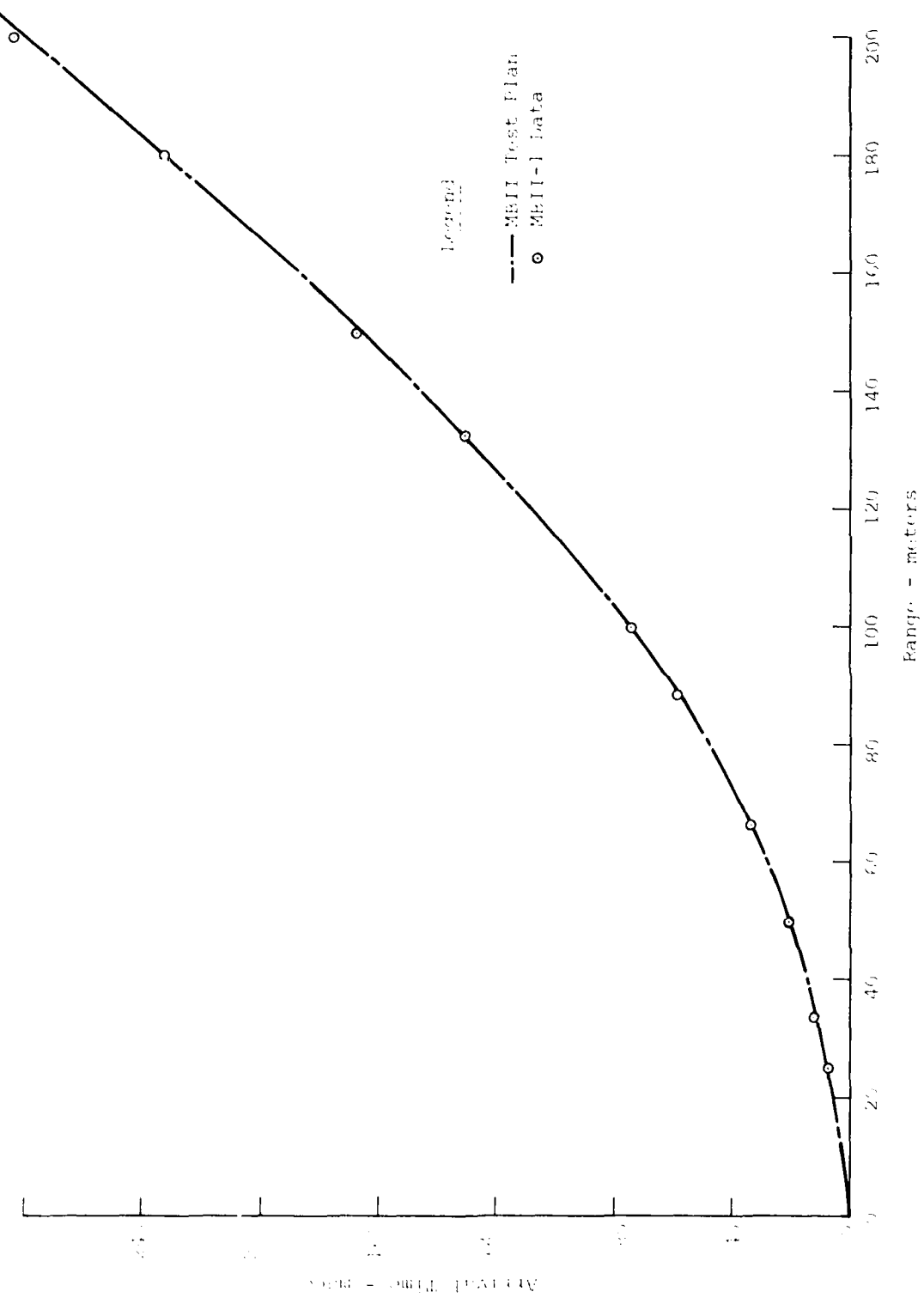
$$P(t) = \Lambda e^{-\alpha t}$$

where $P(t)$ = overpressure at time t

Λ = peak overpressure

α = decay coefficient developed from iteration

t = time



A curve fitting procedure was used in developing the decay coefficient α . After determining α , the function was integrated over the positive phase duration to check the calculated impulse and the predicted impulse. This process was repeated until the two impulses were approximately the same. (This procedure rather than LAMB was used pretest because the LAMB/PLID code combination was unavailable at that time.)

The material model, material parameters, and profile used in the pretest predictions were shown in Figure 10. These material properties are essentially those discussed in Section 2.2.3. There are some differences because the properties shown here were developed early in Phase II before the complete geotechnical investigation had been completed. In fact, the soft silt layer which had a large influence on the near surface motions had not been identified when these pretest predictions were made.

PLID calculates velocity, displacement, acceleration and stress. Values of velocity, displacement and stress were taken directly from the calculation. Due to the high sensitivity of acceleration on artificial viscosity, time step, and zone size, acceleration was calculated separately. The following empirical equation from the Air Force Design Manual (Ref. 17) was used:

$$a = \left(\frac{2v}{t_r} \right) \left(\frac{1}{9.8} \right)$$

where,

a = acceleration -g's

t_r = rise time of velocity-seconds

v = velocity from PLID -mps.

Horizontal motions were then calculated from the vertical values by the following equations (Ref. 17) :

$$\text{Acceleration } \frac{a_H}{a_v} = \tan \left(\arcsin \frac{c_i}{u} \right)$$

$$\text{Velocity } \frac{v_H}{v_v} = \tan \left(\arcsin \frac{c_L}{u} \right)$$

$$\text{Displacement } \frac{d_H}{d_v} = \tan \left(\arcsin \frac{c_L}{u} \right)$$

where

c_i = seismic velocity

c_L = velocity associated with loading modulus

u = airblast shock front velocity

Peak values and waveforms predicted in this manner are compared with measured data in the following section.

3.2.4.2 Predictions vs Data

a) Waveforms

Comparison of the vertical air slap portion of the waveform at 0.5 m depth is shown in Figure 27. In general, the downward portion of the waveform was underpredicted. This underprediction is due to the highly compressible silt layer in the near surface region, which was not modeled.

The upward portion of the vertical waveforms shown in Figure 27 was underpredicted by as much as a factor of 9. This portion of the signal was not modeled in the prediction. This particular signal has traditionally been attributed to a combination of rebound reflections off layers and the crater-related signal, but in light of recent studies it appears that at least some (and more than likely, most) of this magnitude is due to the negative phase of the overhead airblast. This mechanism is known as pore air expansion and a first-order calculational model is described by Ullrich in Reference 18. Since this model was not included in the pretest predictions, additional calculations were run post-test to evaluate it. The results of these additional calculations will be shown and discussed shortly.

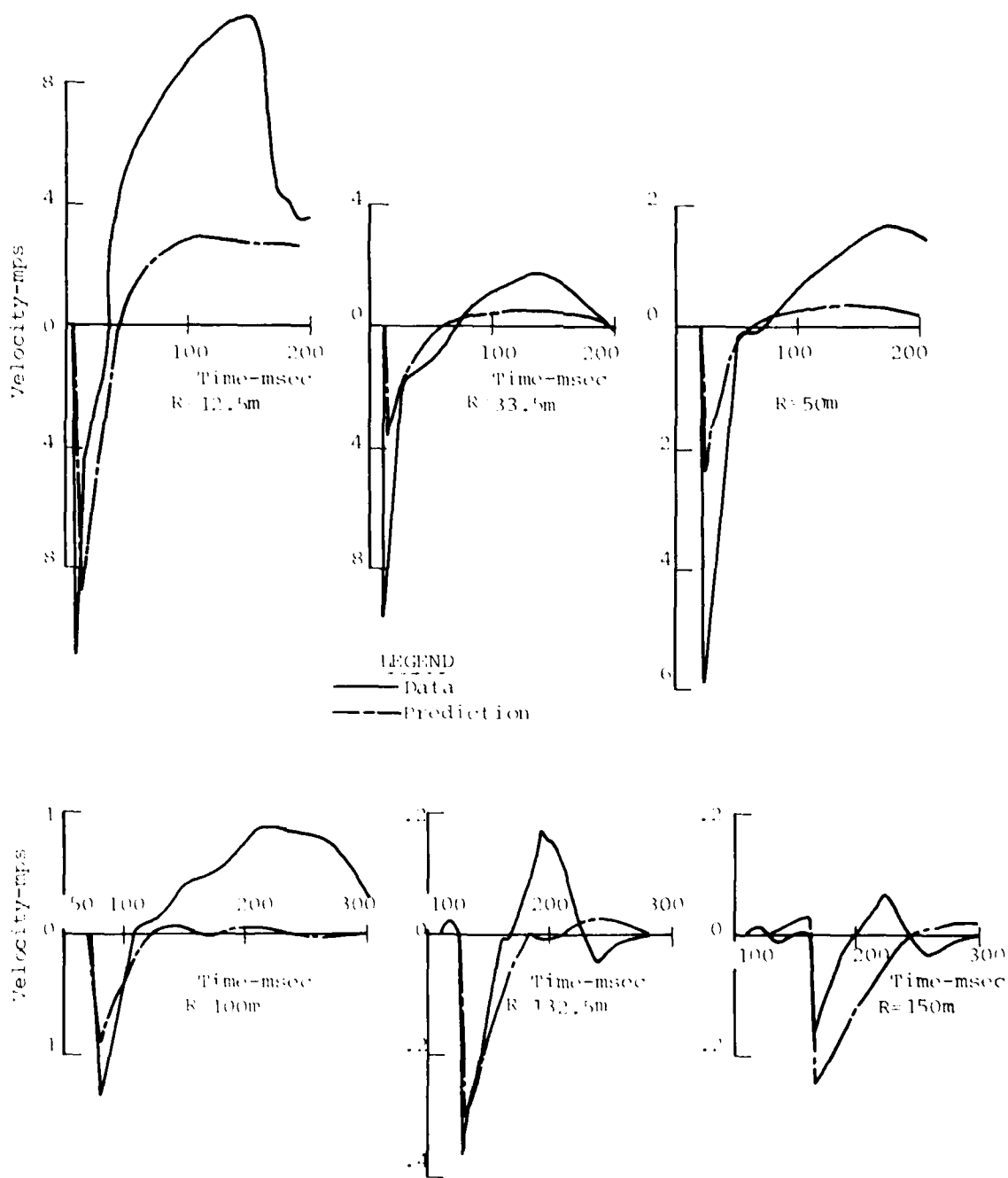


Figure 27. Comparison of Measured and Predicted Vertical Air-Slap Waveforms at the 0.5 m Depth - MBI 1-1

The horizontal waveforms

are compared in Figure 28. In general, for the waveforms measured at ranges from 12.5 m to approximately 50 m, the magnitude of the initial outward signal was fairly well predicted. Pulse widths are somewhat greater because the 1-D vertical prediction procedure does not have the capability to predict the airblast-induced shear wave. At ranges greater than 50 m, the magnitude of this first outward peak became much greater than the data. Pulse widths of the prediction were significantly greater than the data. The second (and much greater) outward peak seen in the data is the signal referred to as crater-related. It is not clear at this point whether motion here is due entirely to crater-related motions or whether, as in the verticals, the negative phase has an effect.

b) Peaks

Comparison of peak predicted and measured air slap vertical downward and horizontal outward air slap induced particle velocities for locations above the water table are shown in Figure 29. Vertical velocities at the 0.5 m depth were underpredicted by as much as a factor of 3 close-in, but as distance from the source increased, the prediction improves significantly. The reason for this is that the high air void material was not modeled in the prediction.

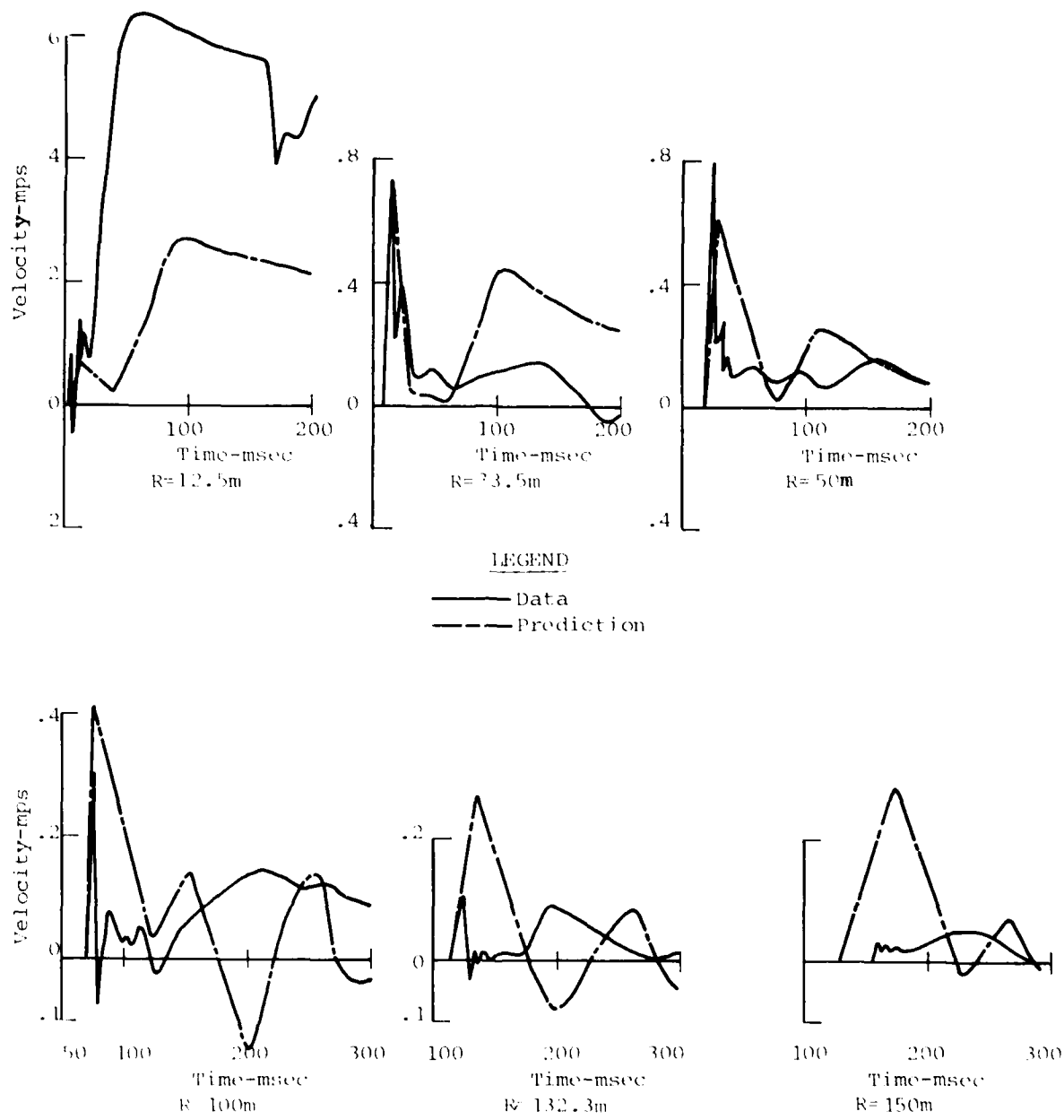


Figure 28. Comparison of Measured and Predicted Horizontal Air-Slap Waveforms at the 0.5 m Depth - MBII-1

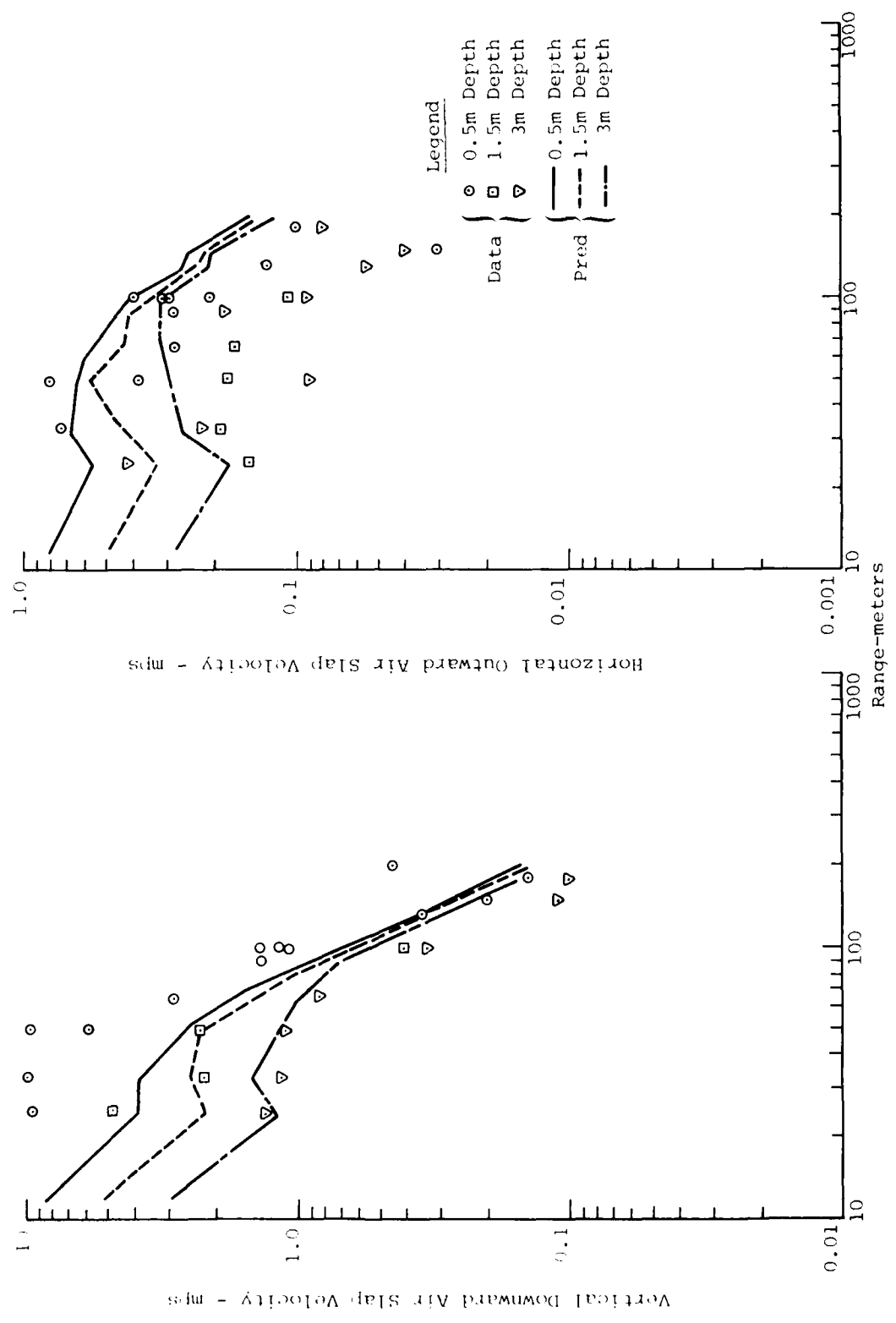


Figure 29. Comparison of Measured and Predicted Air-Slap Velocities; $0.5 \text{m} \leq z \leq 3 \text{m}$ - MBI-1

As range increased along the main gage radial, the silt became thinner and the gage measured the response of the sand. Prediction of the vertical velocities at the greater depths above the water table appear to be better predicted than those near the surface. Horizontal velocities were not as successfully predicted as the verticals. Generally magnitudes were overpredicted at all depths, and the tendency is for the predictions to worsen with depth.

The comparison of vertical and horizontal, air slap particle velocities are shown in Figure 30. For the vertical motions the predictions generally bound the data. The measured data at the 9 m depth is generally less than the data at the two greater depths. This could be the result of upstream effects arriving at these depths at about the same as the air slap which add to the magnitude. These effects are virtually impossible to separate from the air slap. Another observation made is that the prediction for the 12.5 m and 25 m depths are shown as a single line. In actuality, the prediction produced two lines, but the separation was so slight that only one line was used. The reason for the "closeness" of these two prediction lines was that the material at this depth was modeled to be essentially elastic.

Horizontal air slap velocities for depths below the water table (Fig. 30) were not predicted as successfully as the verticals. In general, the predictions for horizontal motion were an order of magnitude lower than the

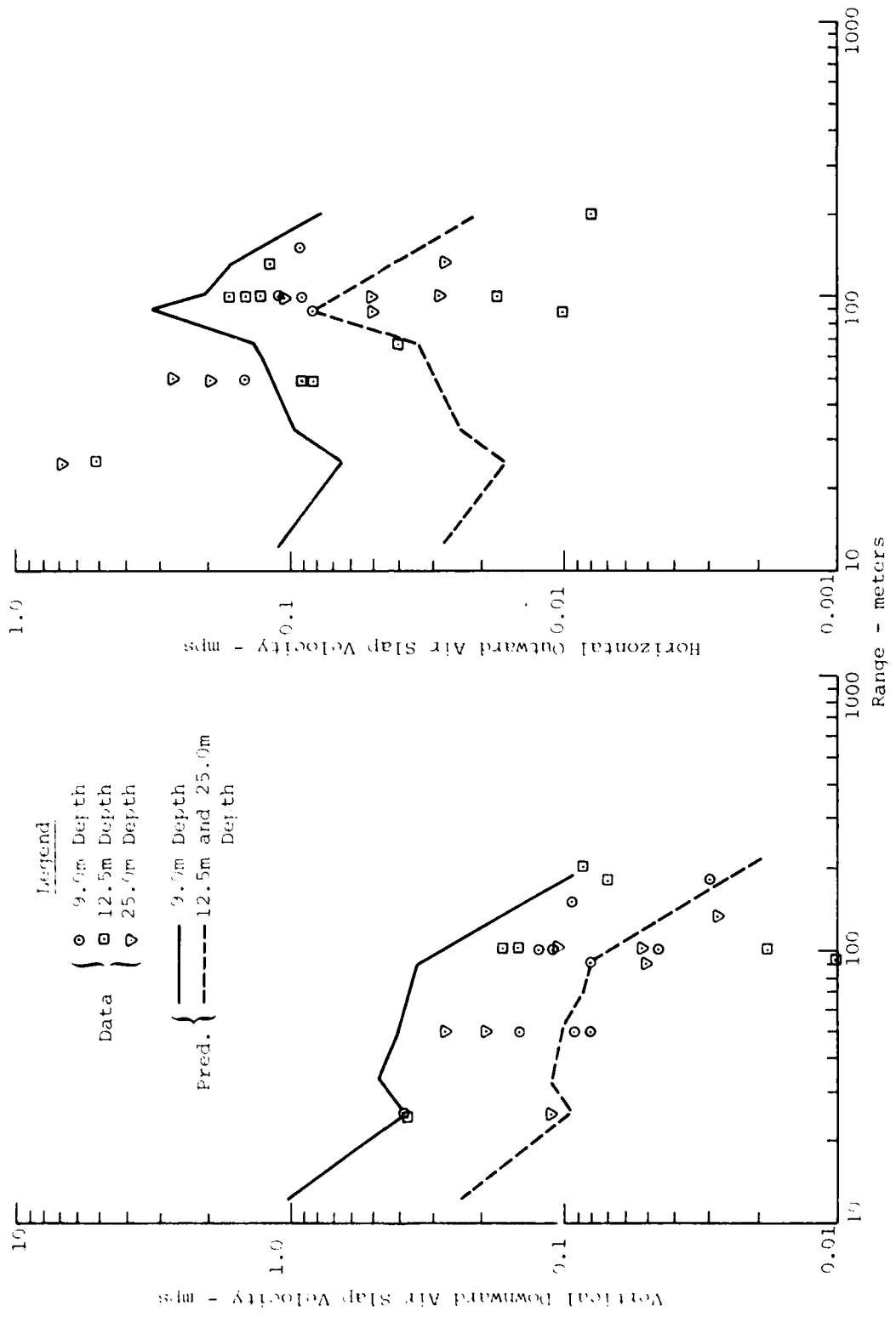


Figure 30. Comparison of Measured and Predicted Air-Slap Velocities;
 $Z = 9\text{m} - \text{MBII-2}$

vertical prediction. The horizontal data, however, is of the same order of magnitude as the vertical data.

Attenuation of vertical velocity with depth is shown in Figure 31 for the 100 m and 33.5 m ranges. At the 33.5 m range the data and the prediction are fairly close. The 0.5 m depth gage produced data higher than the prediction but this is felt to be due to the silt. As depth increased however the prediction was accurate. There is some scatter in the data at the 100 m range. It appears however that the general tendency at this range was to underpredict at most depths.

Comparison of peak predicted and measured air slap vertical downward and horizontal outward accelerations for locations above the water table are shown in Figure 32. The same general comments made for the vertical velocities may be made for the vertical accelerations. The reason for this is the fact that the vertical velocity was used to determine the vertical acceleration (see section 3.1.4.1).

Horizontal air slap acceleration above the water table were generally overpredicted. This is due to the fact that the airblast induced shear wave is not modeled in the prediction and, therefore, does not "clip" the magnitude of the prediction as it does in the data. This overprediction was evident at the greater depths on this figure also.

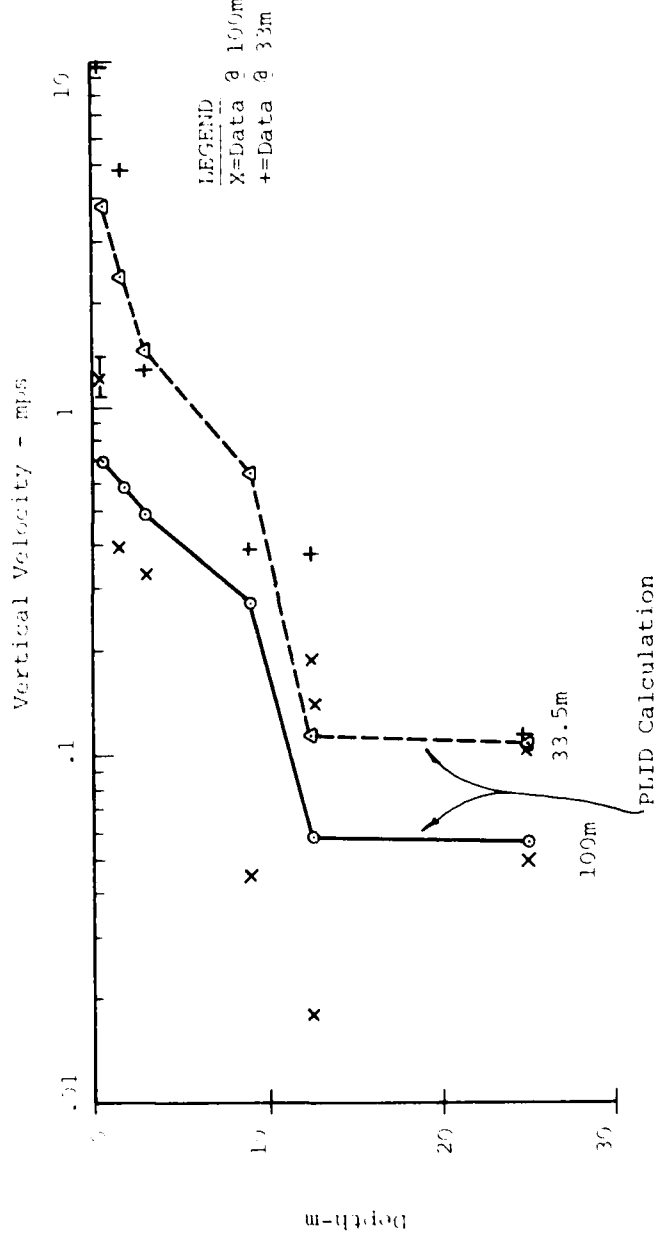


Figure 31. Attenuation of Vertical Velocity w/Depth

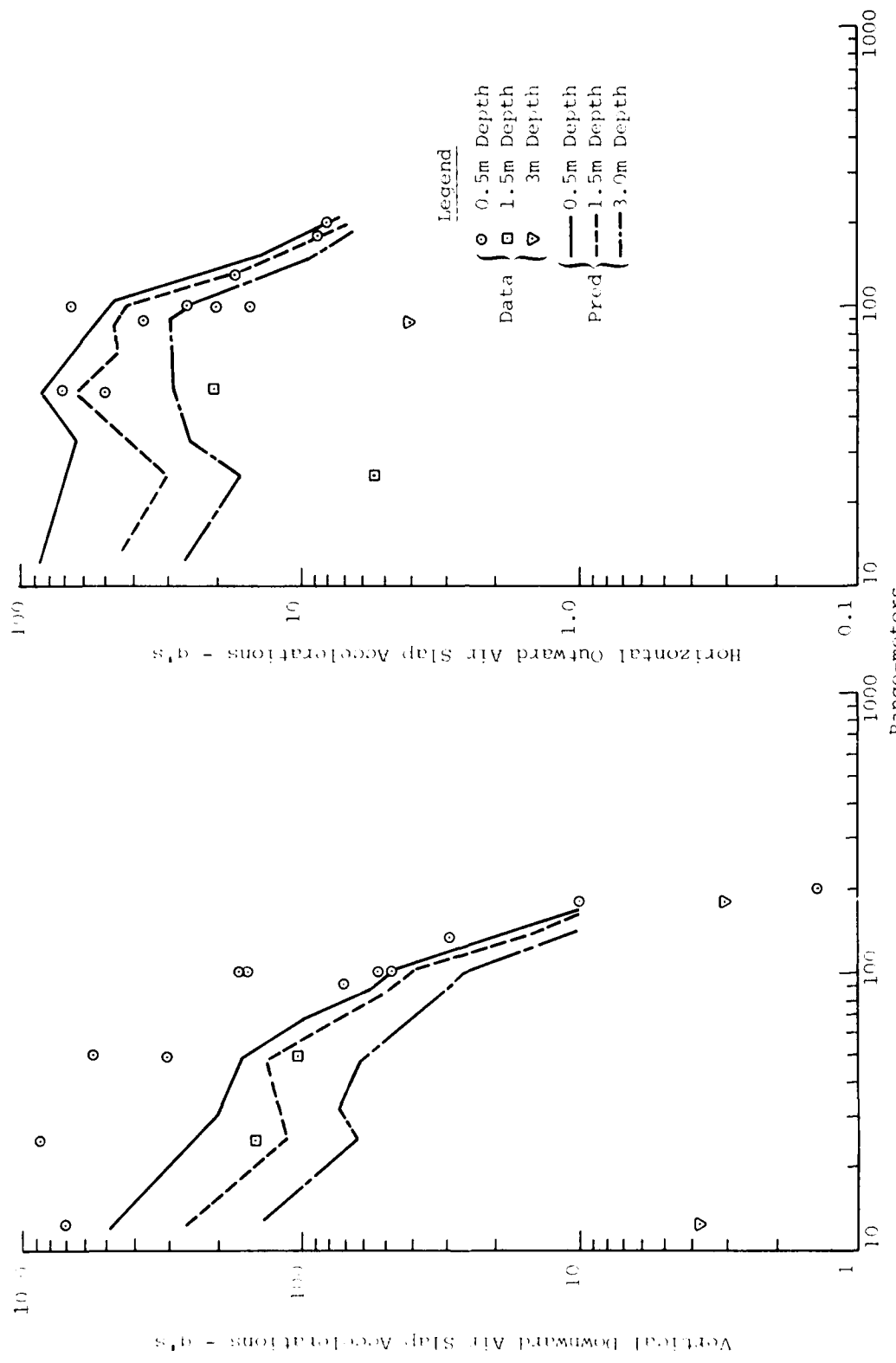


Figure 32. Comparison of Measured and Predicted Air-Slap Acceleration;
 $0.5m \leq z \leq 3.0m$; MBII-1

Figure 33 shows the vertical and horizontal air slap accelerations for depths below the water table. Again much the same comments may be made for these data as has been made previously because all these predictions were derived from the calculation of the vertical velocity.

c) Negative Phase Effects

Calculations utilizing the pore-air model were run post-test to evaluate the model and to also determine if inclusion of the silt layer in the calculation would produce acceptable predictions in the compressive phase. To do these calculations the PLID code was used. The driver for this code was the measured overpressure from MBII-1. Results of these calculations are shown in Figures 34 through 41.

Figures 34 through 36 show the calculations versus the measured data at the 25 m range to a depth of 3 m. For the near-surface location (Fig. 34) the compressive phase of the air slap is fairly close to the measured value. The large upward motion is almost identical to the data (in character). The magnitude is somewhat lower than the data, but not to the extent the pretest predictions were. As depth is increased to 1.5 m, the compressive and negative phases are both somewhat underpredicted. But the inclusion of the pore air

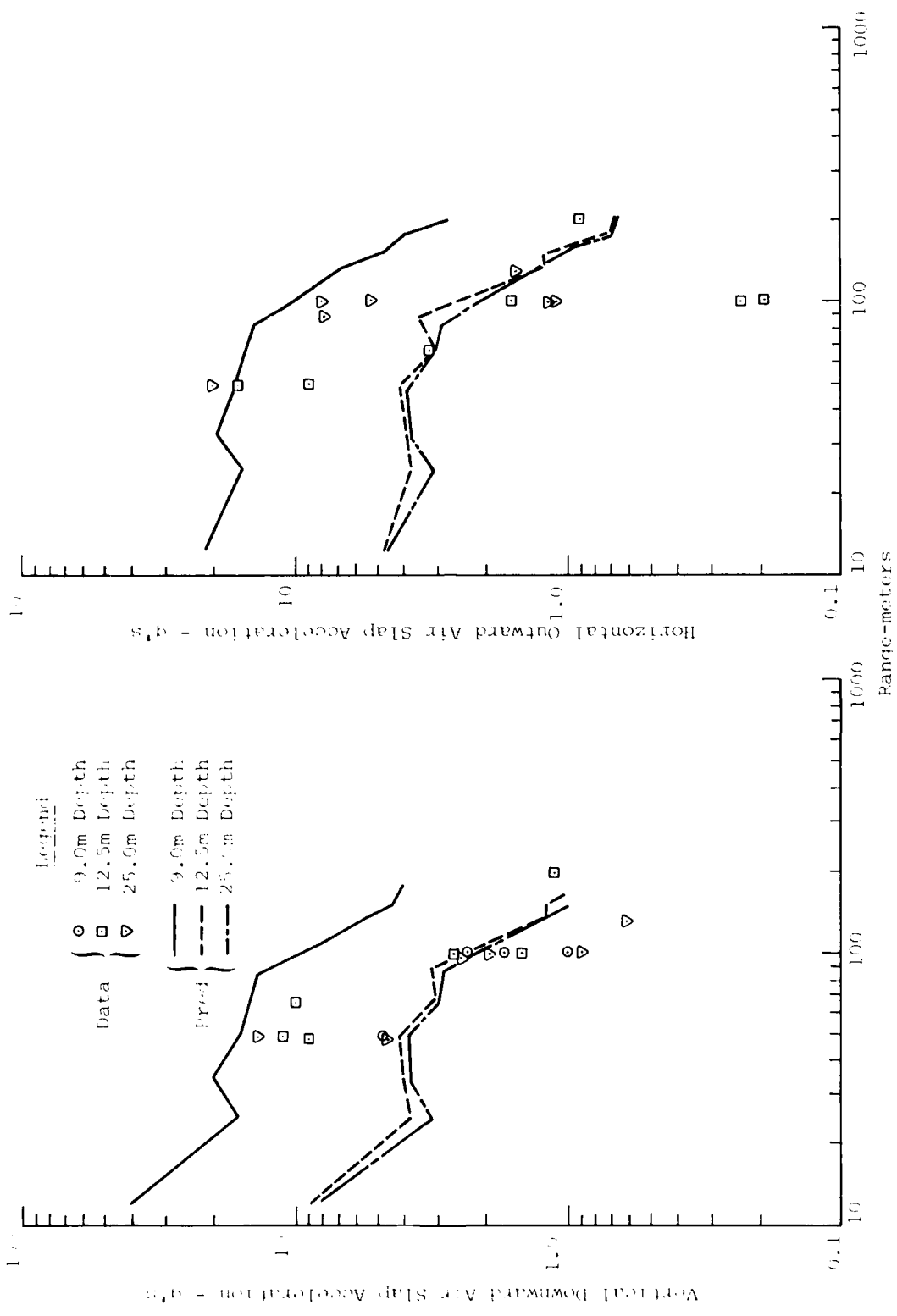


Figure 33. Comparison of Measured and Predicted Air-Slap Accelerations; Z = 9m - MBI-1

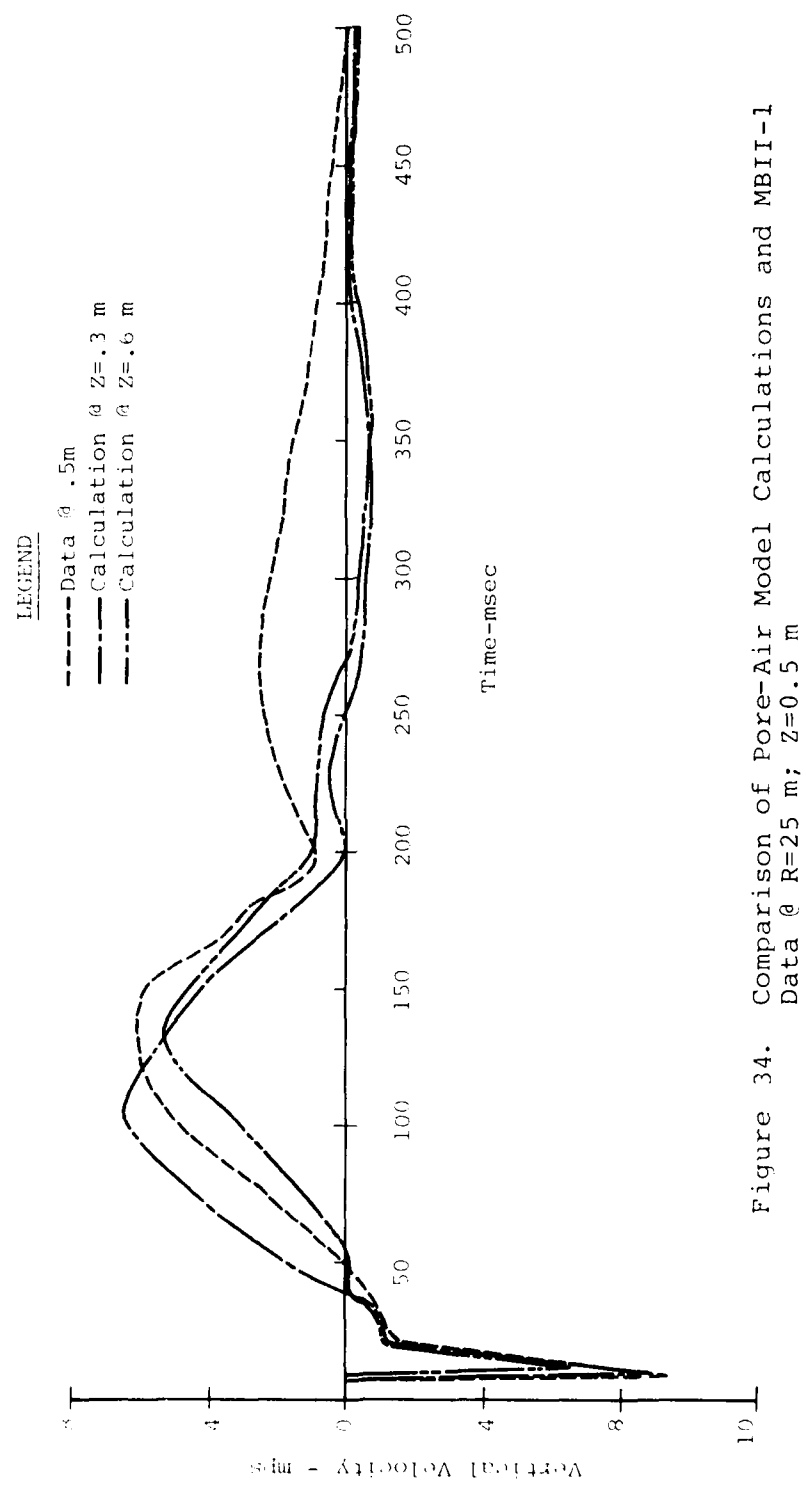


Figure 34. Comparison of Pore-Air Model Calculations and MBII-1 Data @ R=25 m; Z=0.5 m

AD-A092 874

CIVIL SYSTEMS INC ALBUQUERQUE NM
MISERS BLUFF PHASE II, GROUND SHOCK DATA ANALYSIS. (U)
OCT 79 J S PHILLIPS, L S MELZER, J L BRATTON DNA001-79-C-0168

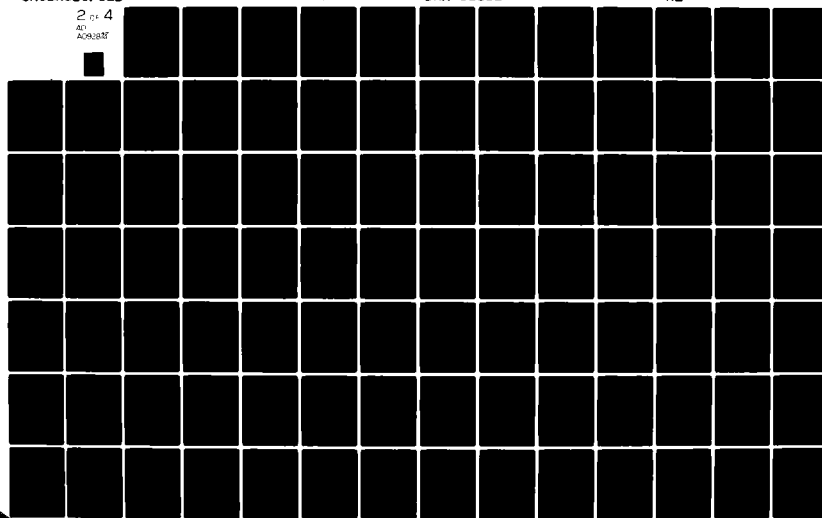
F/G 18/3

UNCLASSIFIED

DNA-51352

NL

2 of 4
AD
A09284T



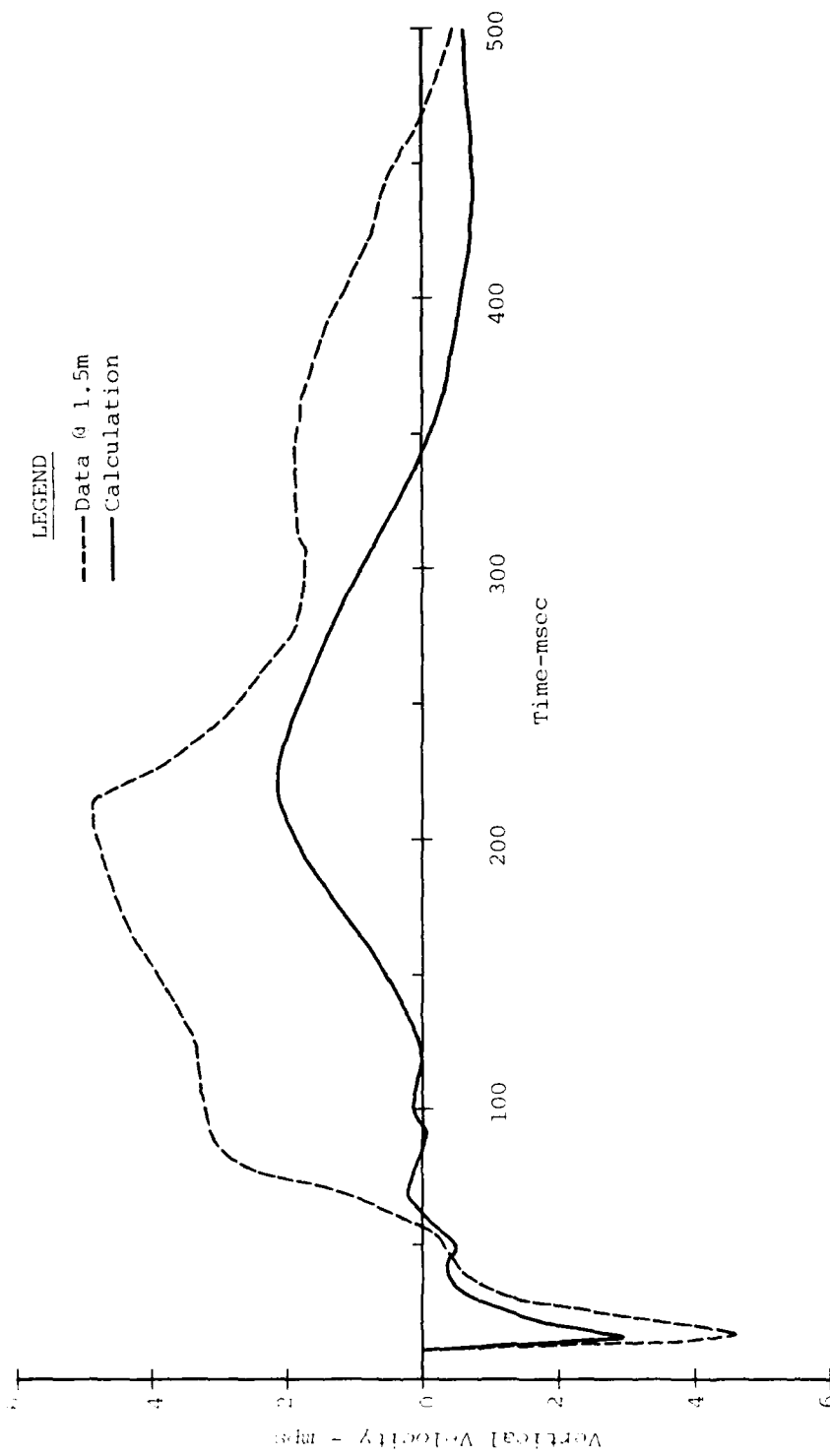


Figure 35. Comparison of Pore-Air Model Calculations and MBII-1 Data @ $R=25$ m;
 $Z=1.5$ m

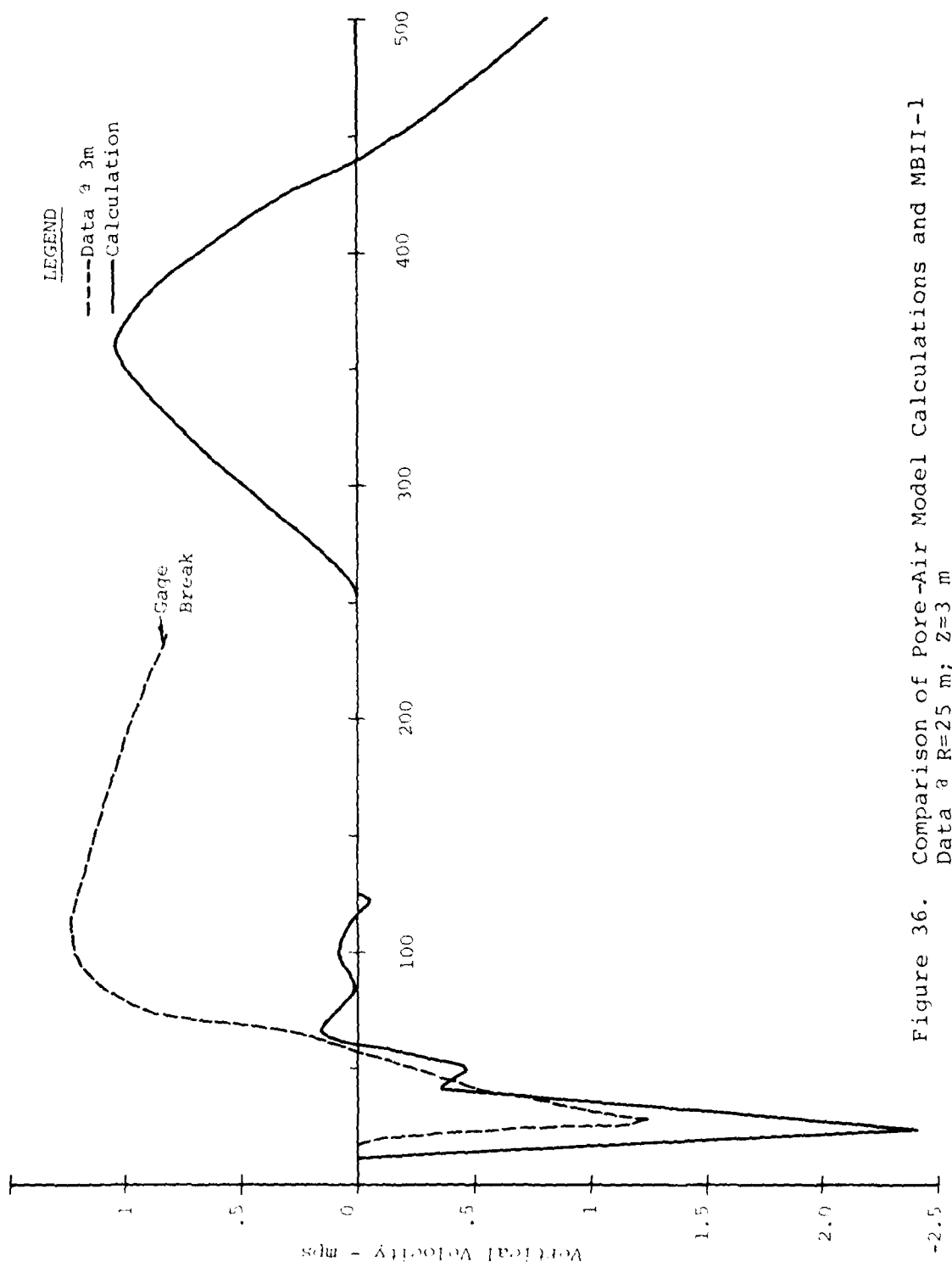


Figure 36. Comparison of Pore-Air Model Calculations and MBI-1
Data at R=25 m; z=3 m

model provides an improved prediction of ground motion during the negative phase over the pretest prediction. The gage at the 3 m (Fig. 35) depth broke at about 250 msec so the data previous to this may be questionable. In comparison with the data, the compressive air slap is greatly overcalculated and the negative phase arrives in the calculation after the gage failure.

Figures 37 through 39 show the comparisons for the 50 m range to the 3 m depth. Near surface (Fig. 37) the comparison looks good. The compressive air slap is fairly close in duration and magnitude. The upward signal is somewhat shorter in duration and lower in magnitude than the data, but the character is almost identical. Again, the improvement over the pretest calculations is significant. As depth is increased, the calculations are not quite as good as the near surface (Figs. 38 and 39). At the 1.5 m depth (Fig. 38) compressive peak and pulse width values are still accurately calculated. Upward peak magnitudes are about the same in the calculation as they are in the data in this time frame, but the character of the signal is somewhat different. One of the largest character differences is that the calculation shows the material reaching its initial position much sooner than seen in the data. The calculation at the 3 m depth (Fig. 39) overcalculates the compressive signal in magnitude but duration is still good. The pore-air effect is not calculated for this depth. The upward

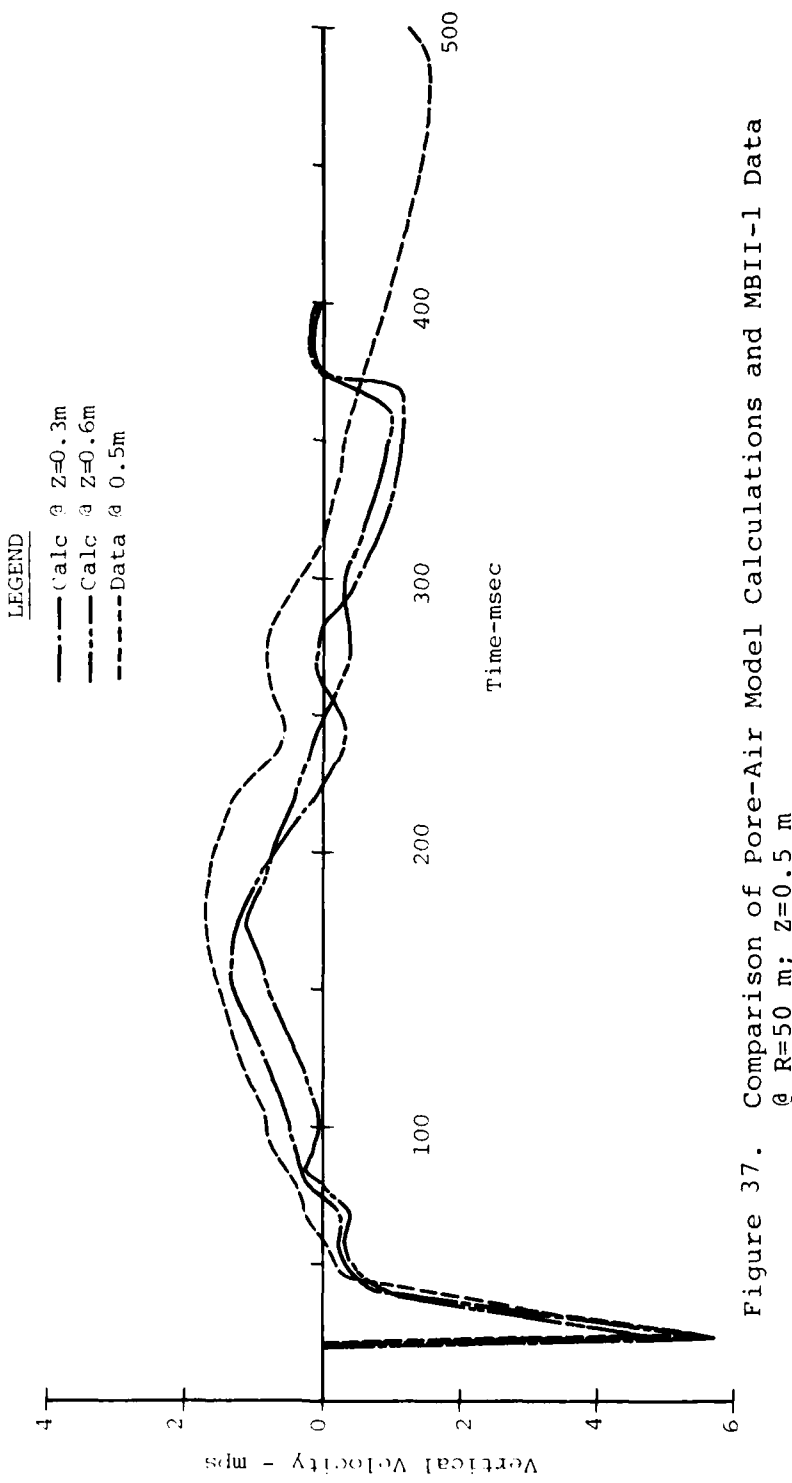


Figure 37. Comparison of Pore-Air Model Calculations and MBII-1 Data
 $\vartheta R=50$ m; $Z=0.5$ m

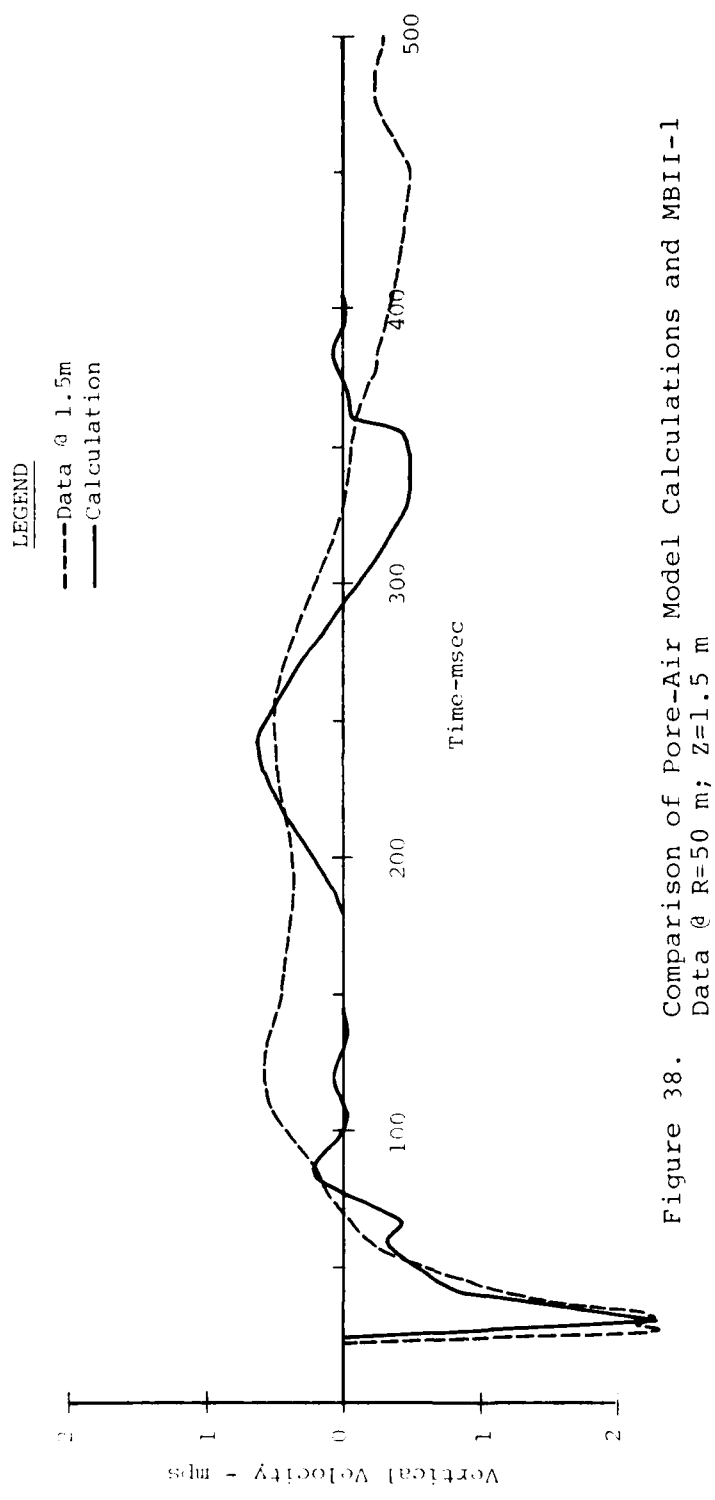


Figure 38. Comparison of Pore-Air Model Calculations and MBII-1
Data @ R=50 m; Z=1.5 m

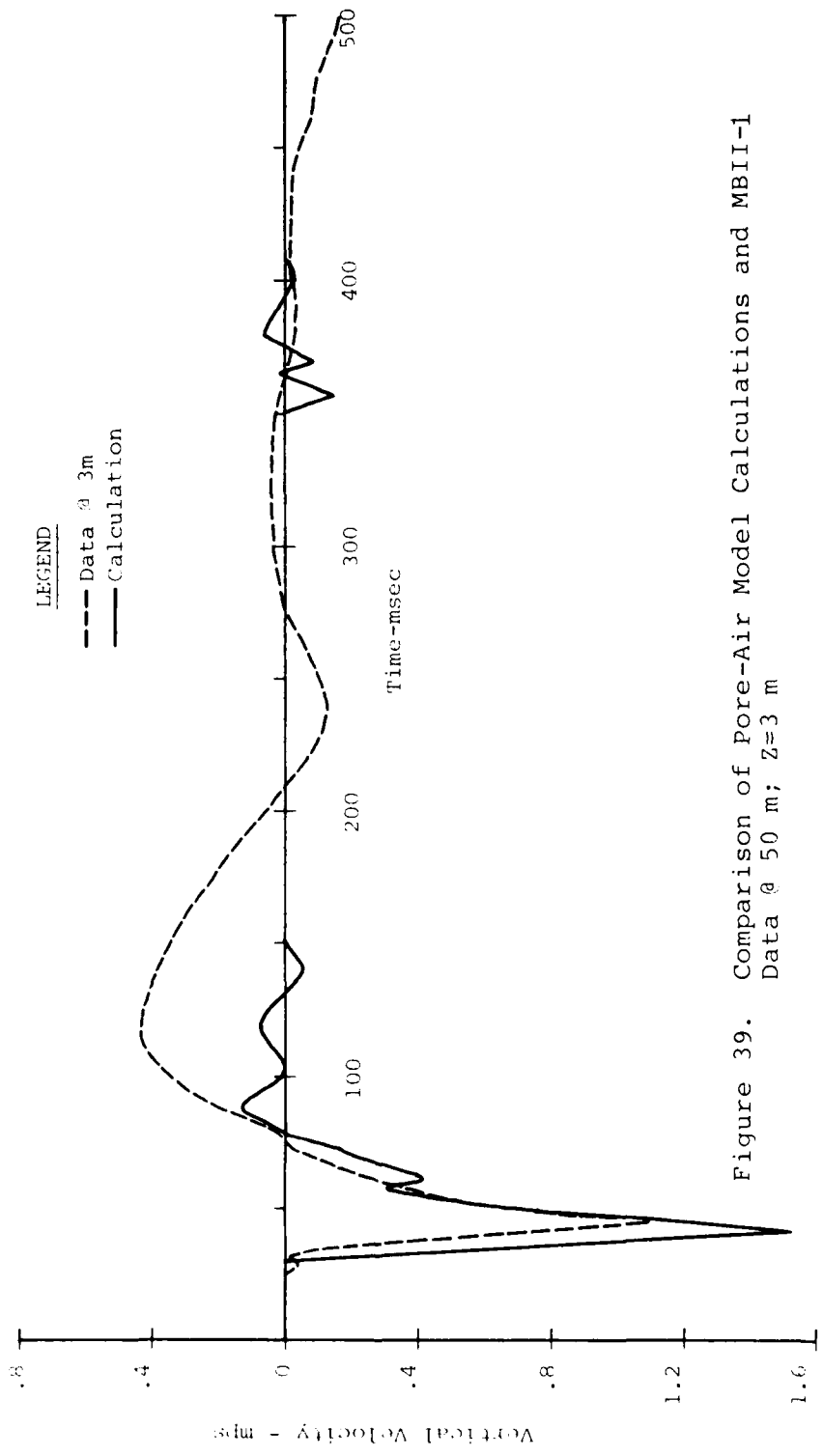


Figure 39. Comparison of Pore-Air Model Calculations and MBI-1
Data @ 50 m; $Z=3$ m

signal seen at approximately 100 msec in the calculation is due to recovery of the material and reflections from below. The signal seen in the calculation at approximately 350 msec is the transmission of the rejoin signal from above. This calculation supports the earlier comment that the upward motion at this depth is not directly attributable to the pore-air mechanism.

The calculations for the 100 m range are shown in Figures 40 and 41. At this range the calculations appear to break down. Magnitudes are lower than the measured values and the character of the waveforms are inaccurate. The duration of the upward signal in the calculation was somewhat reduced by the secondary compressive phase in the air pressure. This large effect was not seen in the data possibly due to two dimensional effects occurring within this time frame. As was the case for the 50 m range, the calculations for the deeper material did not show the pore-air effect. The upward motion seen in the early time is due to recovery of the material and reflections from below and in the late time frame the motion is the transmission of the rejoin signal from above.

d) Evaluation

The most dominant influence on the air-slap component of ground motion at the Misers Bluff II-1 site was the near-surface, soft and compactible silt layer.

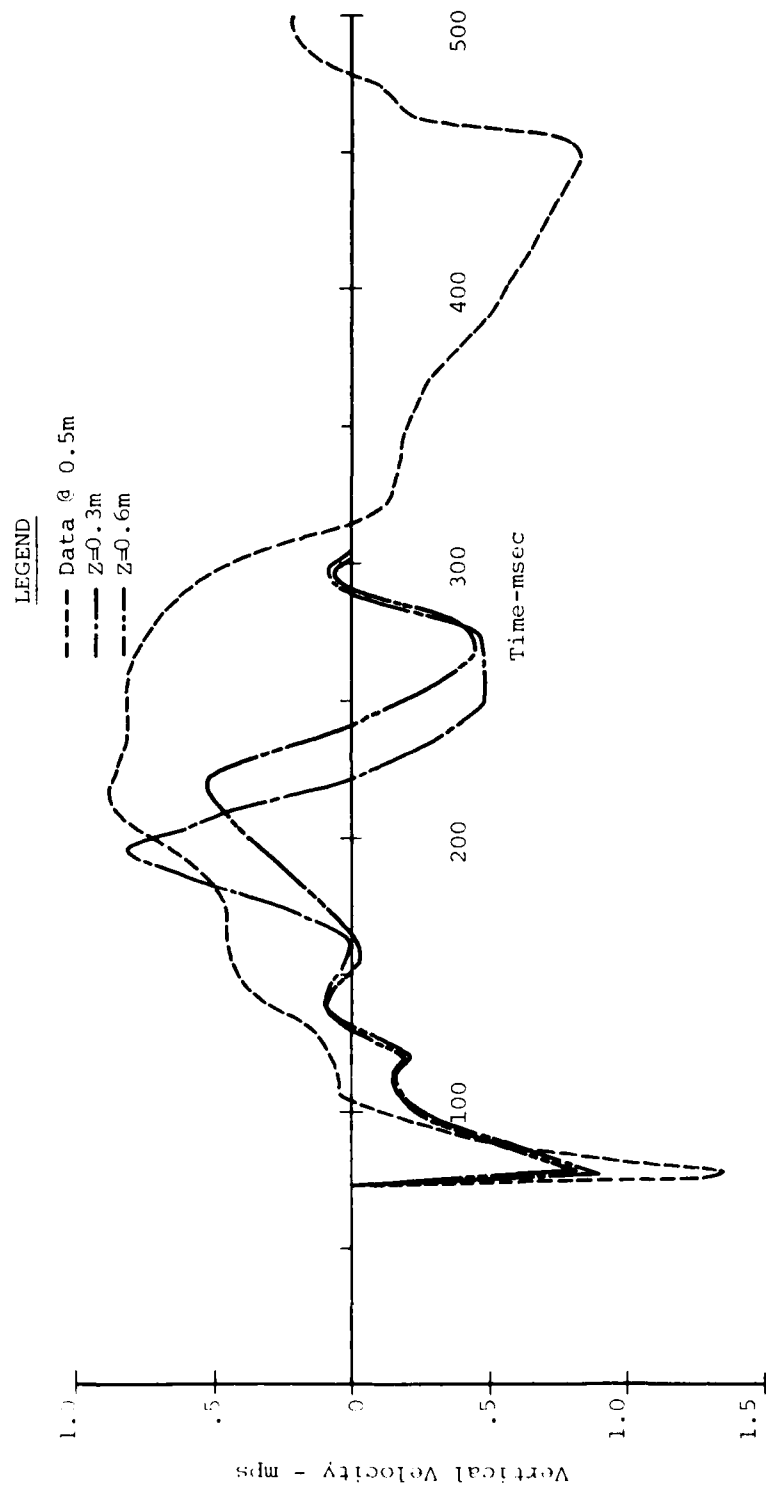


Figure 40. Comparison of Pore-Air Model Calculations and MBII-1 Data
@ R=100 m; Z=0.5 m

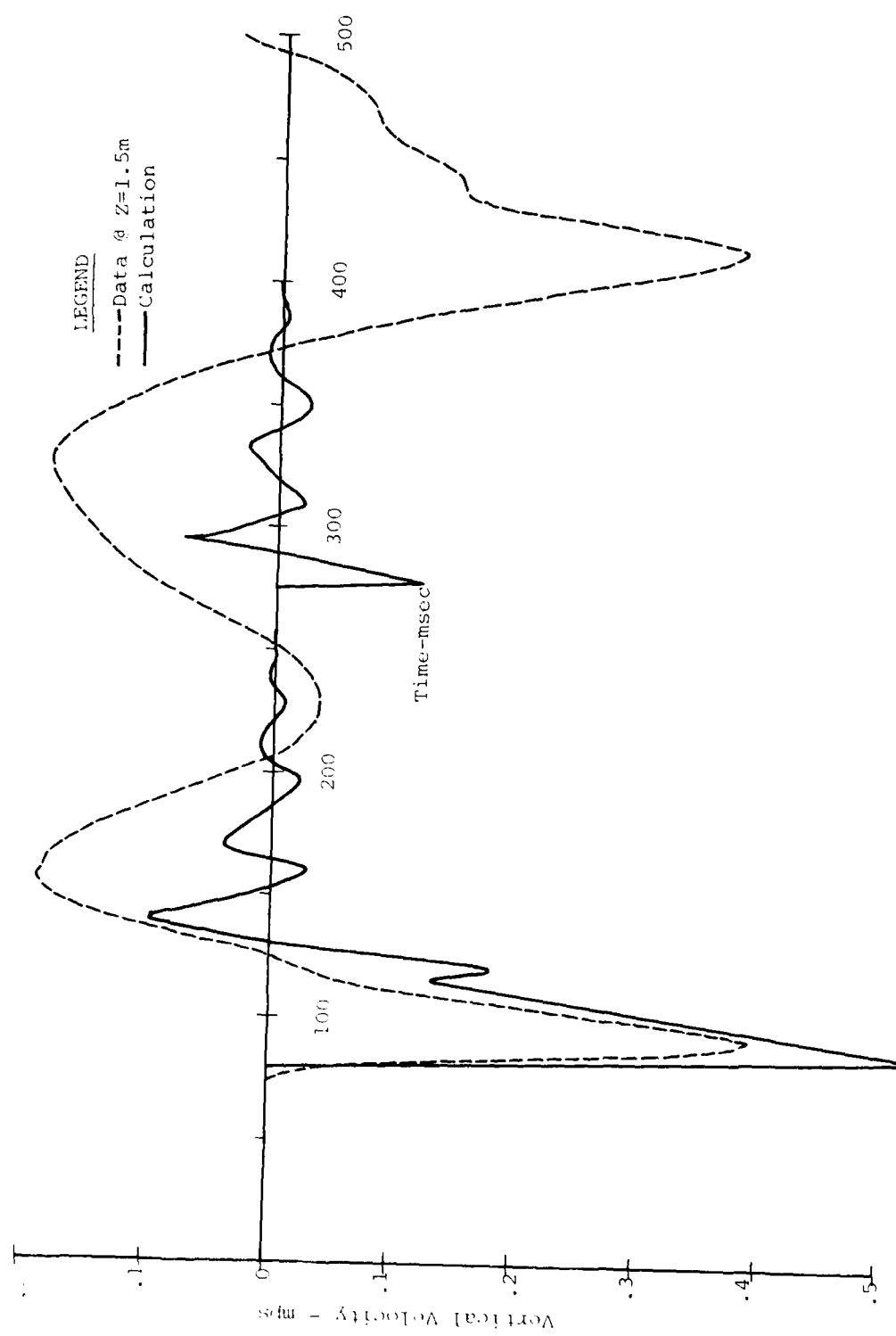


Figure 41. Comparison of Pore-Air Model Calculations and MBII-1 Data
@ R=100 m, Z=1.5 m

No site previously tested has had a layer as thick or as soft as this site and considerable effort was applied to account for the possible effect of this layer in adjusting predictions for the test.

Figure 42 shows the near surface (~0.5m depth), vertical, downward accelerations for the Misers Bluff II-1 in comparison to previous tests. Note that the acceleration measured on Misers Bluff fall on the high side but generally within the band of data from previous tests.

The peak downward velocities are shown in Figure 43. This plot shows that the Misers Bluff data forms the upper bound to all data indicating a significant effect of the silt layer. This trend shows up even greater in Figure 44. It must be noted here, however, that air slap displacements are often truncated by upward directed upstream effects reflections and/or refractions prior to completion of peak downward airblast-induced motion. Figure 45 from MIDDLE GUST III shows an example of such truncation. In any case, however, the compactible nature of the near-surface silt had a substantial effect upon the air-slap motions observed on Misers Bluff II-1, and provide a new upper bound for peak airblast-induced motions.

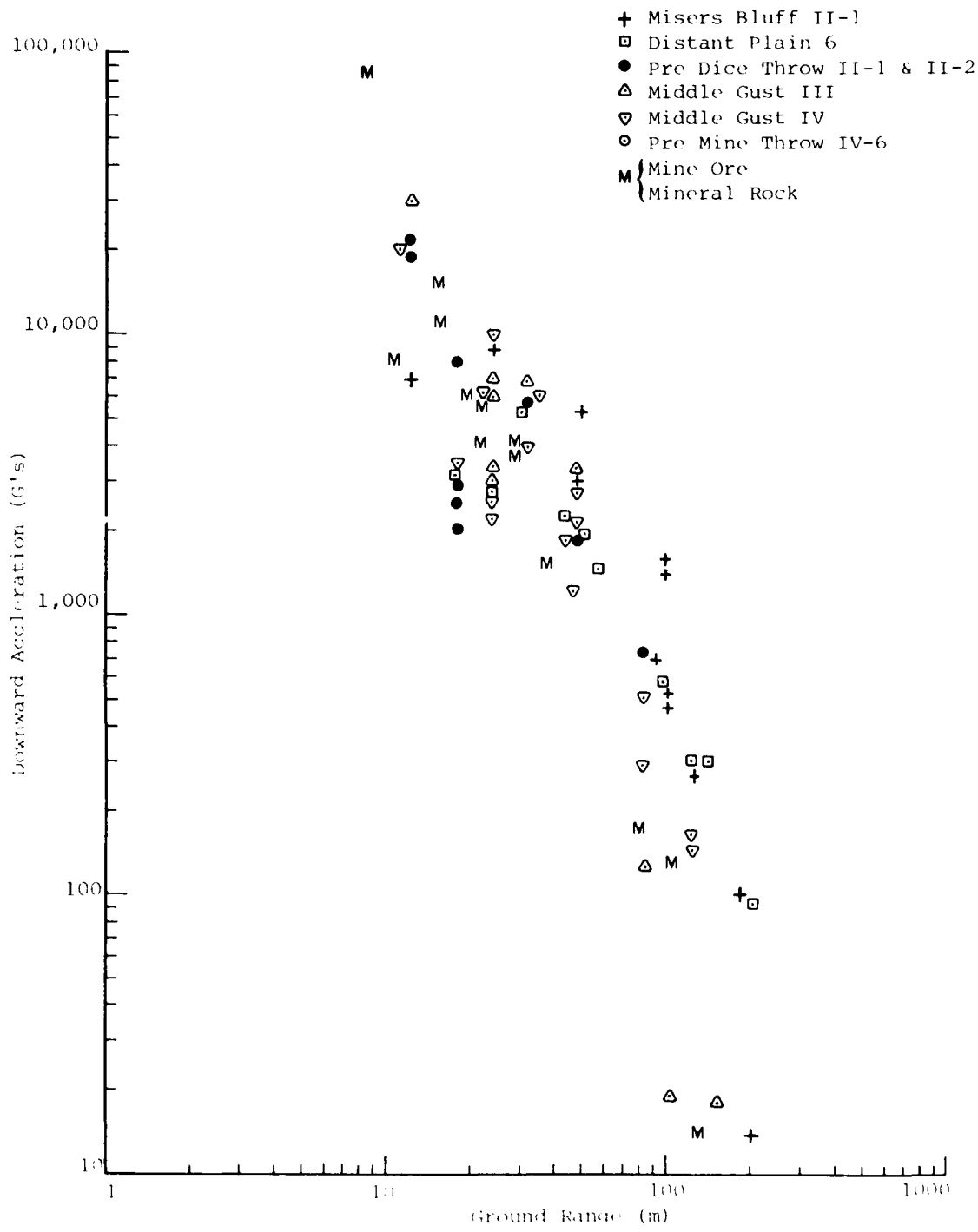


Figure 42. Near-Surface Downward Acceleration for Misers Bluff and Similar Experiments

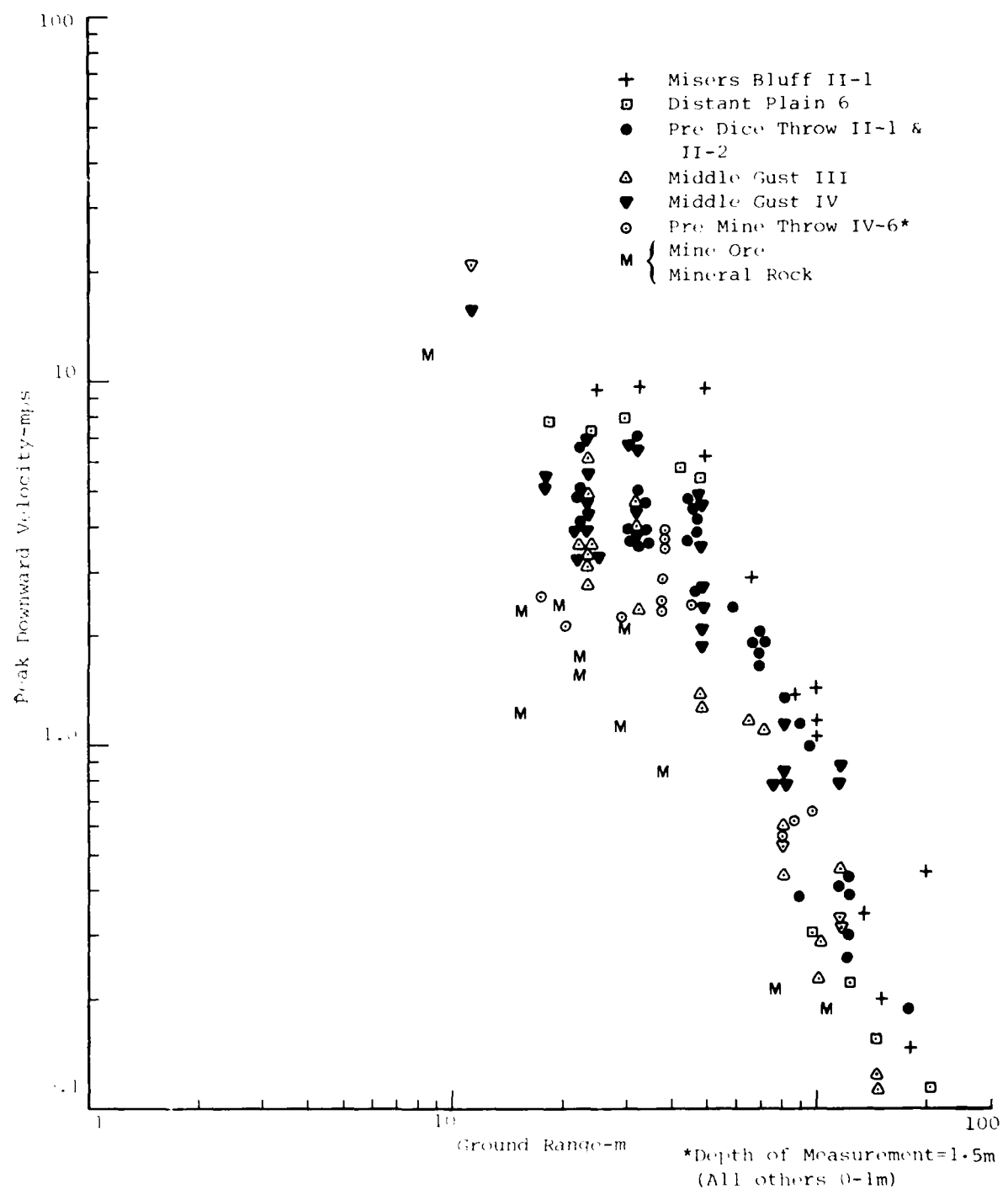


Figure 43. Peak Downward Velocity vs Range for Misers Bluff and Similar Experiments

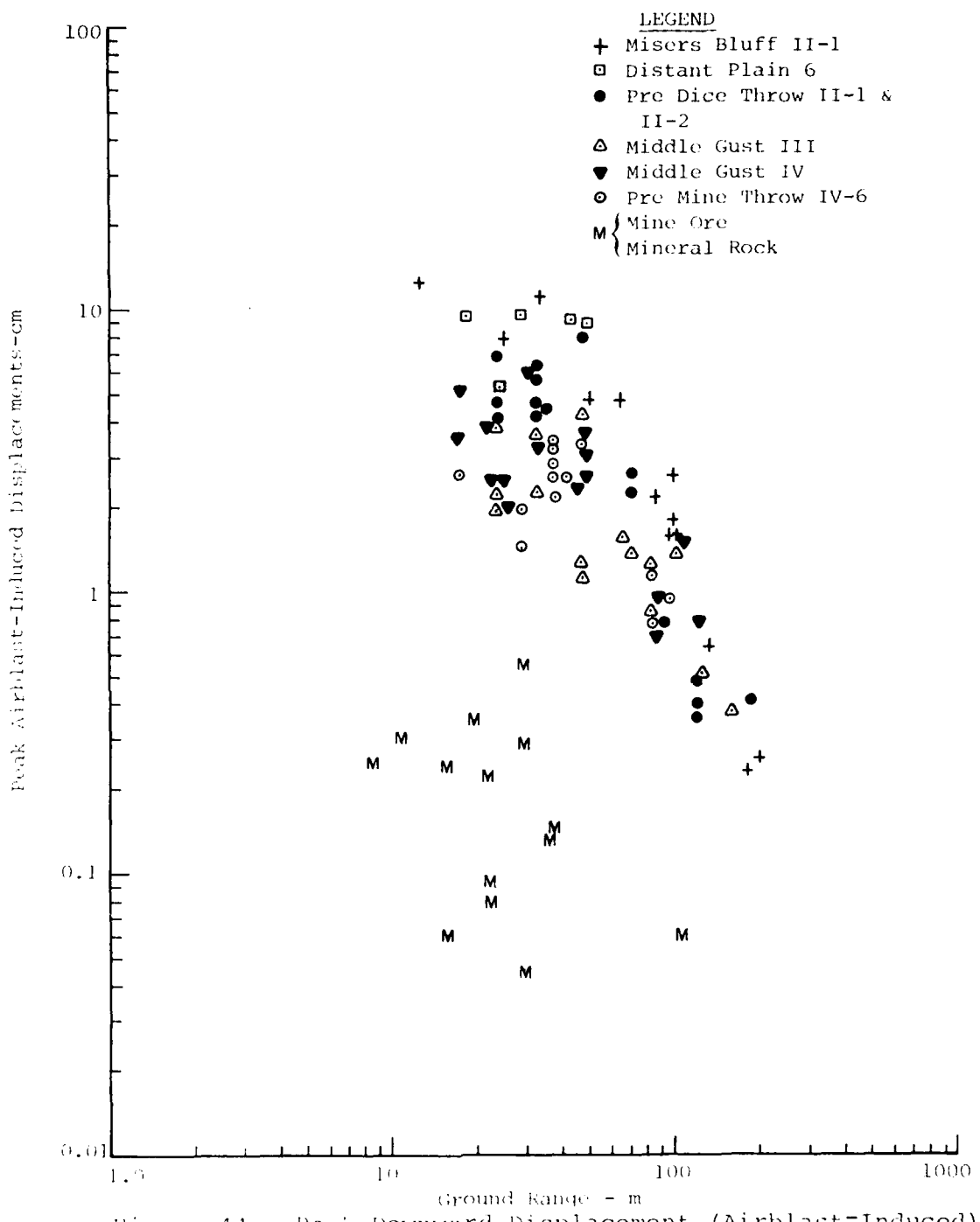


Figure 44. Peak Downward Displacement (Airblast-Induced) vs Range for Misers Bluff II-1 and Similar Experiments

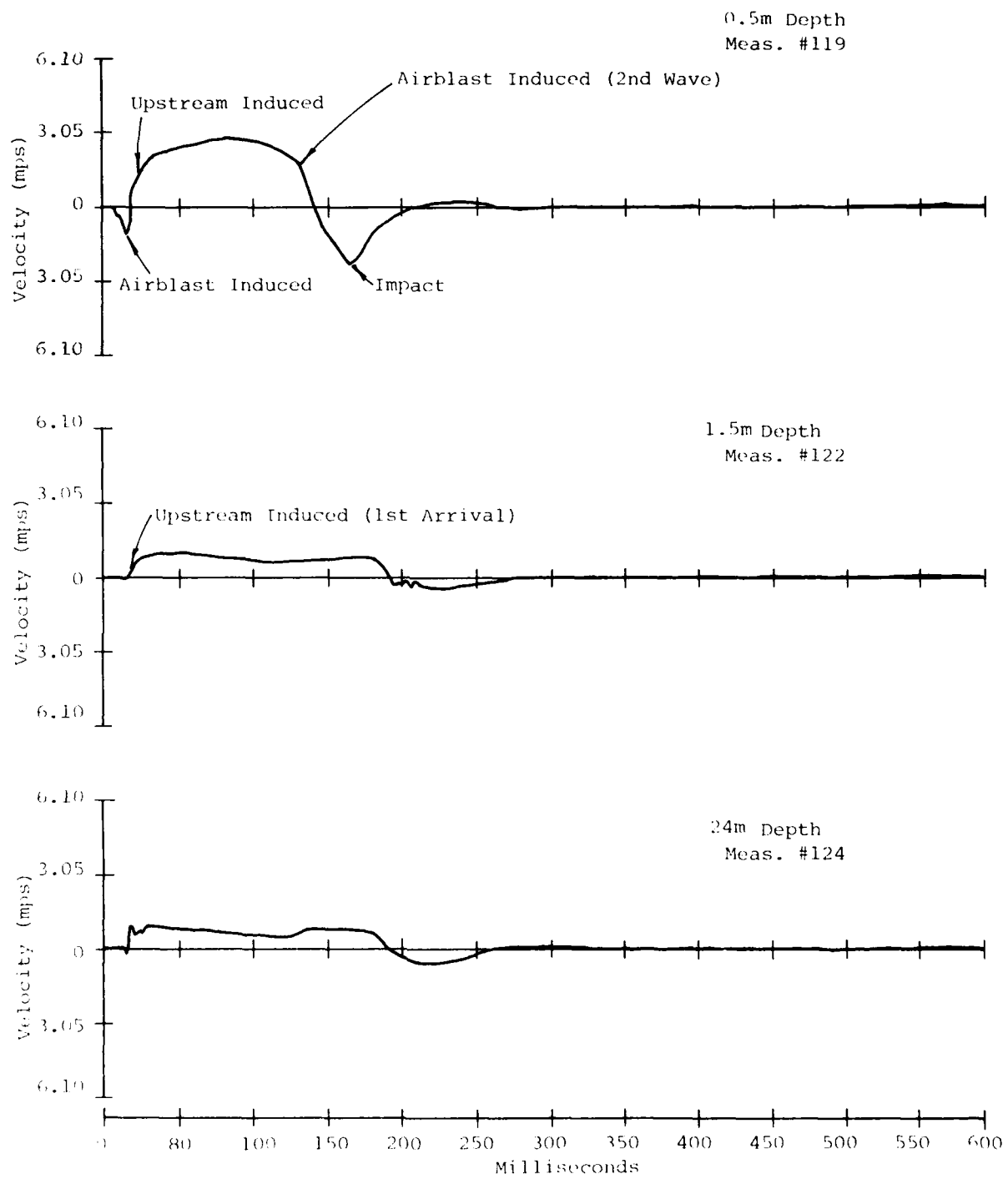


Figure 45. MIDDLE GUST III Vertical Velocities Measured at the 24.4 Meter Range of the 240° Azimuth

As far as the prediction procedure is concerned, the PLID code coupled with the pore-air model is probably the best tool at this point for the vertical air-slap component for near-surface predictions. The accuracy of this tool is dependent upon the ability to determine the material properties of the media in question. These include compressive properties as well as tensile properties. Tensile properties are the hardest to quantify especially for the very low values of these types of soils and therefore provide the "weakest link" for the prediction of this component. The procedure appears to break down rather quickly with increasing depth. This may be due to two-dimensional effects not included in the one-dimensional PLID code calculations. It may also be due to inadequacy in the pore-air model currently being used. Two-dimensional calculations utilizing a pore-air model should be run to evaluate these 2-D effects and the effect of the pore air model on horizontal motions.

For horizontal air-slap motions the prediction procedure was based on the AFDM. This represents a first-order estimate. As was seen in the comparisons in this section it provided results somewhat greater than the data so it is at least design conservative. At this point it is felt that the AFDM procedure should be applied only to the compressive portion of the vertical air slap because of the uncertainty with regard to the pore-air expansion effect on horizontal motions.

3.2.5 Crater-Related Component of Ground Motion

For the purposes of this report the crater-related (or direct-induced) component is motion that is due to the ground stresses and motions caused by the initial stress wave that results from energy coupled at the burst point. The prediction procedure is based upon crater-volume scaling and does not differentiate between upstream-airblast and crater-related motions, therefore, upstream-airblast effects are not predicted independently.

3.2.5.1 Prediction Procedure

The prediction of crater related motions require first an estimate of the crater volume. The procedures for predicting the crater volume are given in References 3 and 17. Once the crater volume has been determined, the following equations may be used to calculate near surface peak particle velocities and displacements:

velocity: $v = C_e (.01) \left(\frac{R}{V_a^{1/3}} \right)^{-2}$

displacement: $d = \frac{\alpha V_a^{4/3}}{R^3}$

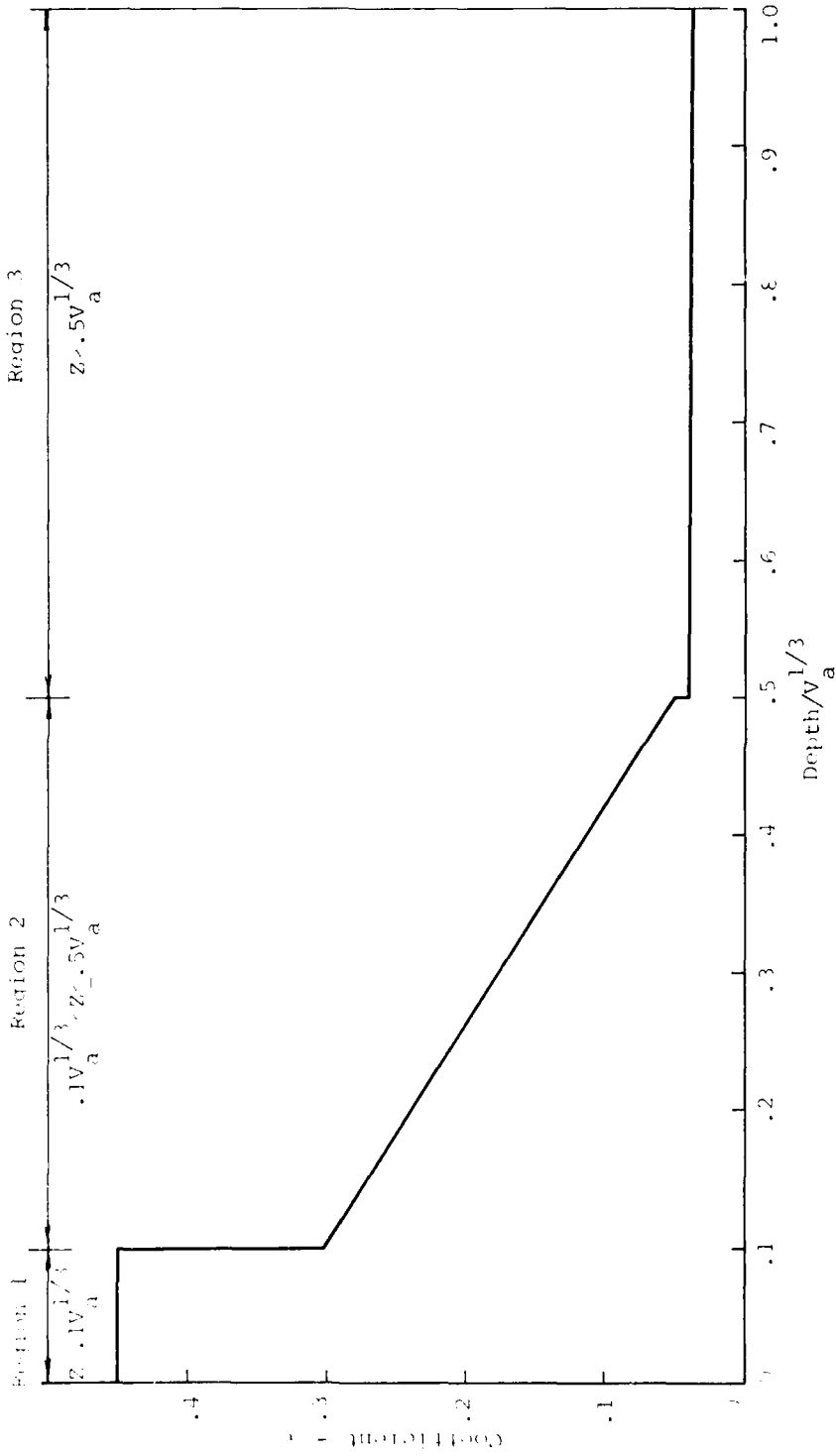


Figure 46. Attenuation Coefficients for Crater Related Displacements

where: v = velocity

R = range of interest

V_a = apparent crater volume

c_e = effective wave velocity $\left(\frac{\text{range of interest}}{\text{time of direct wave arrival}} \right)$

d = displacement

α = attenuation coefficient from Figure 46.

The crater related waveform was predicted in a fashion similar to that shown in Reference 3, with the modifications described below.

Figure 47 shows the waveform with important parameters marked. The half cycle of the waveform is calculated from the following equation:

$$t_p = \frac{50}{c_e} \frac{v_a^{2/3}}{R} \quad (\text{variables are as defined previously}).$$

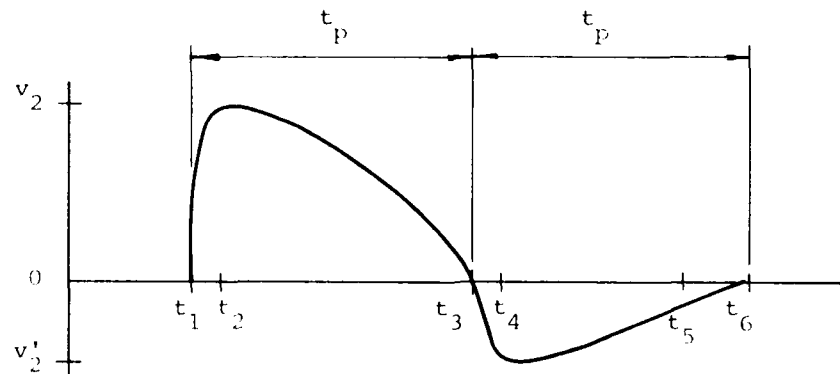


Figure 47. Crater-Related Waveform

The waveform is defined mathematically as follows: (Ref. 19)

<u>Region</u>	<u>Equation</u>
$t_1 \leq t \leq t_2$	$v = +v_2 \sin \frac{\pi}{2} \left(\frac{t - t_1}{t_2 - t_1} \right)$
$t_2 \leq t \leq t_3$	$v = -v_2 \cos \frac{\pi}{2} \left(\frac{t - t_2 + t_1}{t_3 - t_2} \right)$
$t_3 \leq t \leq t_4$	$v = v'_2 \sin \frac{\pi}{2} \left(\frac{t - t_3 + t_1}{t_4 - t_3} \right)$
$t_4 \leq t \leq t_5$	$v = v'_2 \left[\left(1 - \frac{2}{\pi} \right) \cos \frac{\pi}{2} \left(\frac{t - t_4 + t_1}{t_5 - t_4} \right) + \frac{2}{\pi} \right]$
$t_5 \leq t \leq t_6$	$v = \frac{2}{\pi} \left[1 - \sin \frac{\pi}{2} \left(\frac{t - t_5 - t_1}{t_6 - t_5} \right) \right]$

Where the times are defined as:

t_1 = time of arrival of direct wave

$t_2 = .1 tp + t_1$

$t_3 = tp + t_1$

$t_4 = .1tp + t_1 + tp$

$t_5 = \left| \frac{2}{\pi} (t_6 - t_4) + t_4 \right| + t_1$

$t_6 = 2 tp$

The velocities v_2 and v'_2 are the peak velocity determined from the equation given previously and half of the peak velocity respectively.

3.2.5.2 Predictions vs Data

a) Waveforms

Waveform comparisons for the 12.5 m, 33.5 m, and the 50 m ranges are shown in Figures 48 through 50 (the compressive portion of the air-slap component has been removed from the data on these comparisons). The predictions for the 12.5 m range (Fig. 48) are consistently low. In the vertical waveform this underprediction was almost a factor of 4 and in the horizontal waveforms the underprediction was a little greater than a factor of 2. The character of the prediction is similar to the data. This is especially true in the horizontal motions. At the 33.5 m range (Fig. 49) the vertical waveform is again underpredicted by about a factor of 4. The horizontal waveform on the other hand was overpredicted. The character of the predictions are somewhat different than that seen in the data. At the 50 m ranges (Fig. 50) vertical motions are still underpredicted and horizontal motions are overpredicted.

b) Peaks

In discussing the peak upward and outward crater-related motions in the data compared with predictions, it is convenient to work in terms of scaled values. Ranges and displacements are scaled by the cube root of the measured crater volume and velocities are scaled by the effective wave velocity. Depths at which the measurements were made

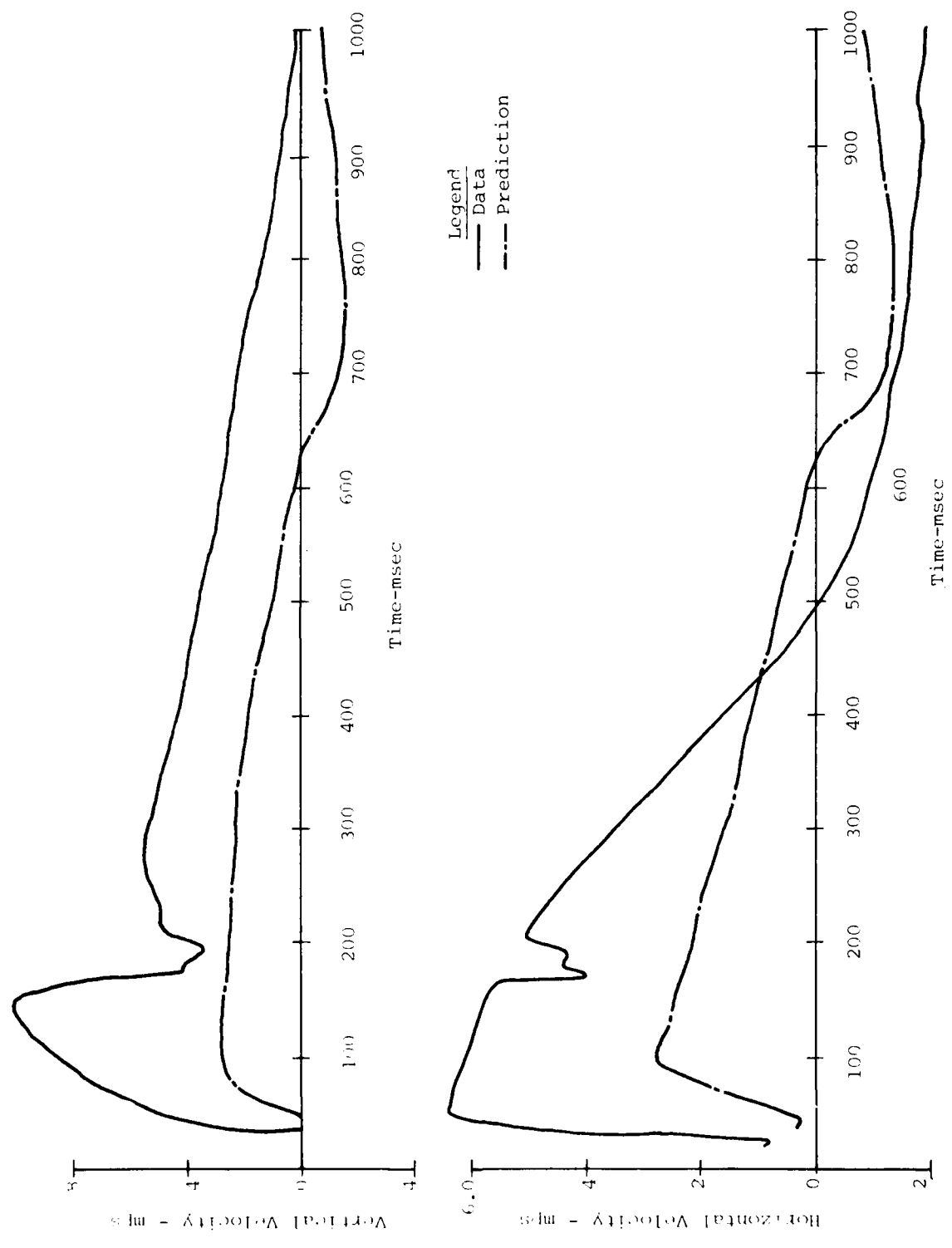


Figure 48. Comparison of Measured and Predicted Crater-Frelated Components @
12.5-0.5

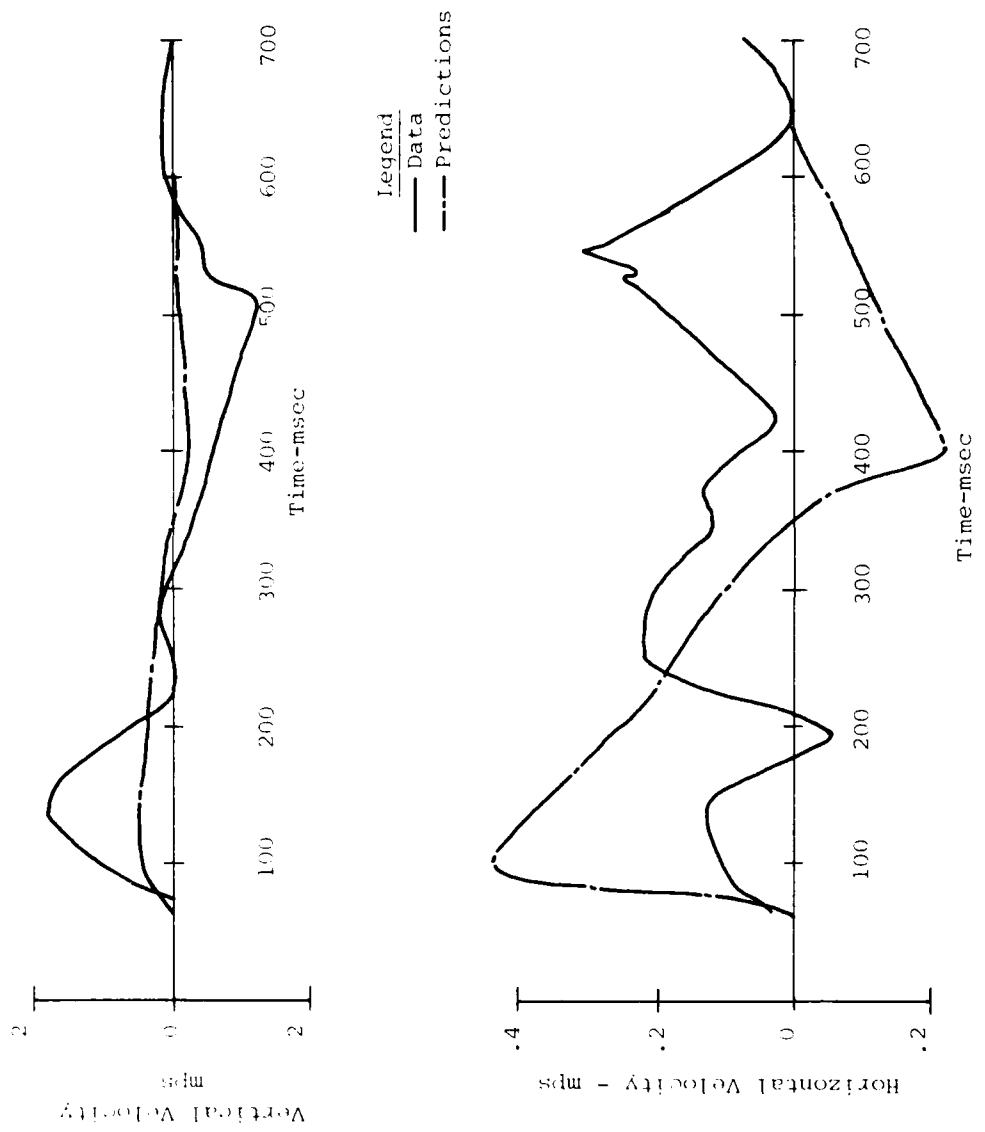


Figure 49. Comparison of Measured and Predicted Crater-Related Components @ 33.5-0.5

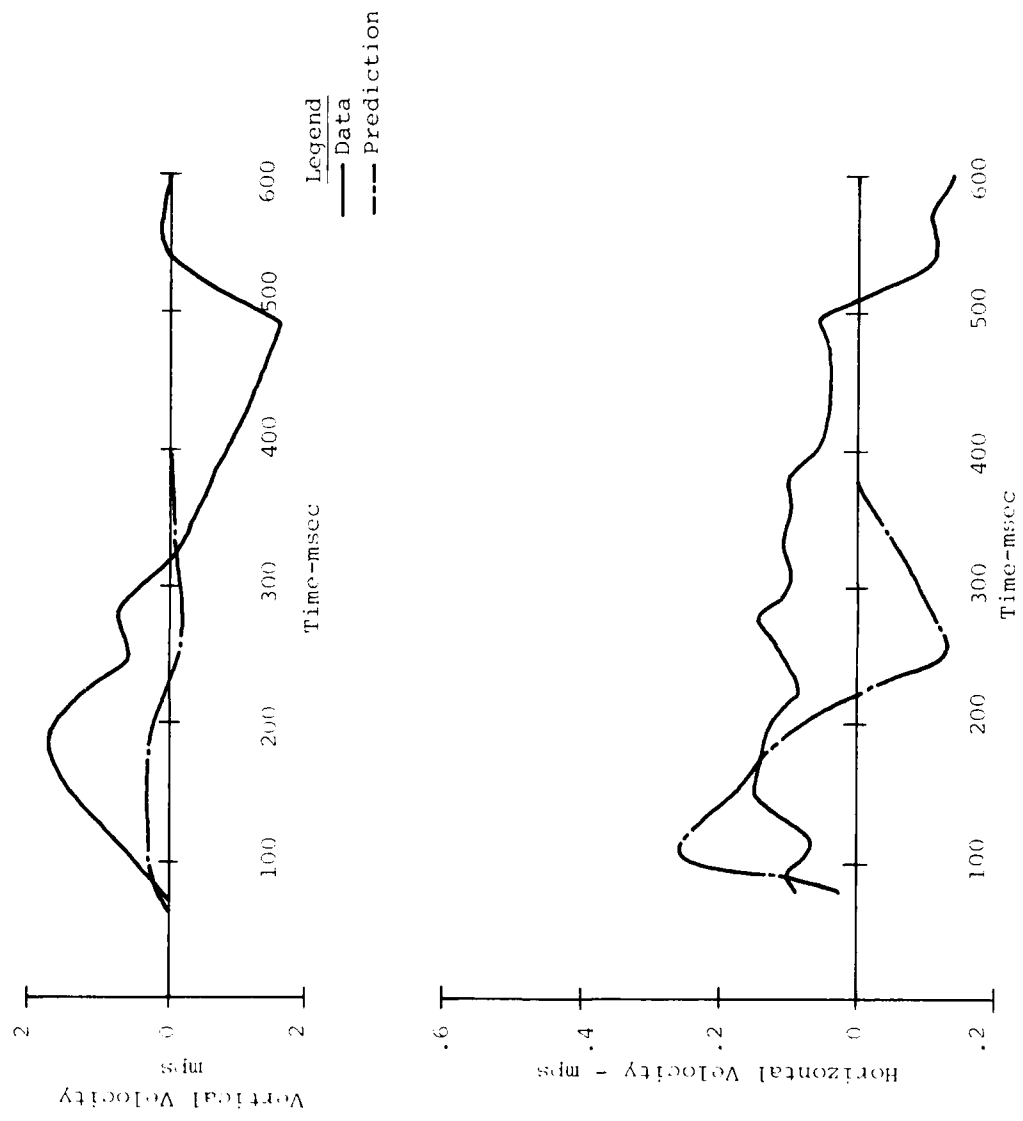


Figure 50. Comparison of Measured and Predicted Crater-Related Components at 50-0.5

are classified in three regions. The first are those depths less than $0.1V_a^{1/3}$; secondly the region between $.1V_a^{1/3}$ and $0.5V_a^{1/3}$; and finally depths greater than $0.5V_a^{1/3}$. The reader is reminded that the prediction procedure does not separate the crater-related from the upstream-airblast effects.

Upward and outward velocities are shown in Figure 51. Vertical velocities scatter about the prediction line by about a factor of ± 4 . This is within the accuracy published for this prediction in the AFDM. Attenuation of the data appears to be fairly well described by the predicted rate of R^{-2} . Horizontal velocities were fairly well predicted, and were within the factor of 4 accuracy, published in the AFDM. Again it appears that the data is attenuating at the rate of R^{-2} . The vertical data show a definite attenuation with depth whereas the horizontal magnitudes appear independent of depth. This could reflect the influence of the pore-air expansion on the near-surface vertical motions. The measurements from the intermediate depths, which are below the effect of the pore-air expansion, agree reasonably well with the prediction.

Upward and outward displacements for $z \leq 0.1V_a^{1/3}$ are shown in Figure 52. Vertical displacements were underpredicted by about a factor of 6. This is within the scatter of displacement data published in the AFDM. The attenuation rate of the data appears to be about the R^{-3} predicted. Horizontal displacements were also underpredicted,

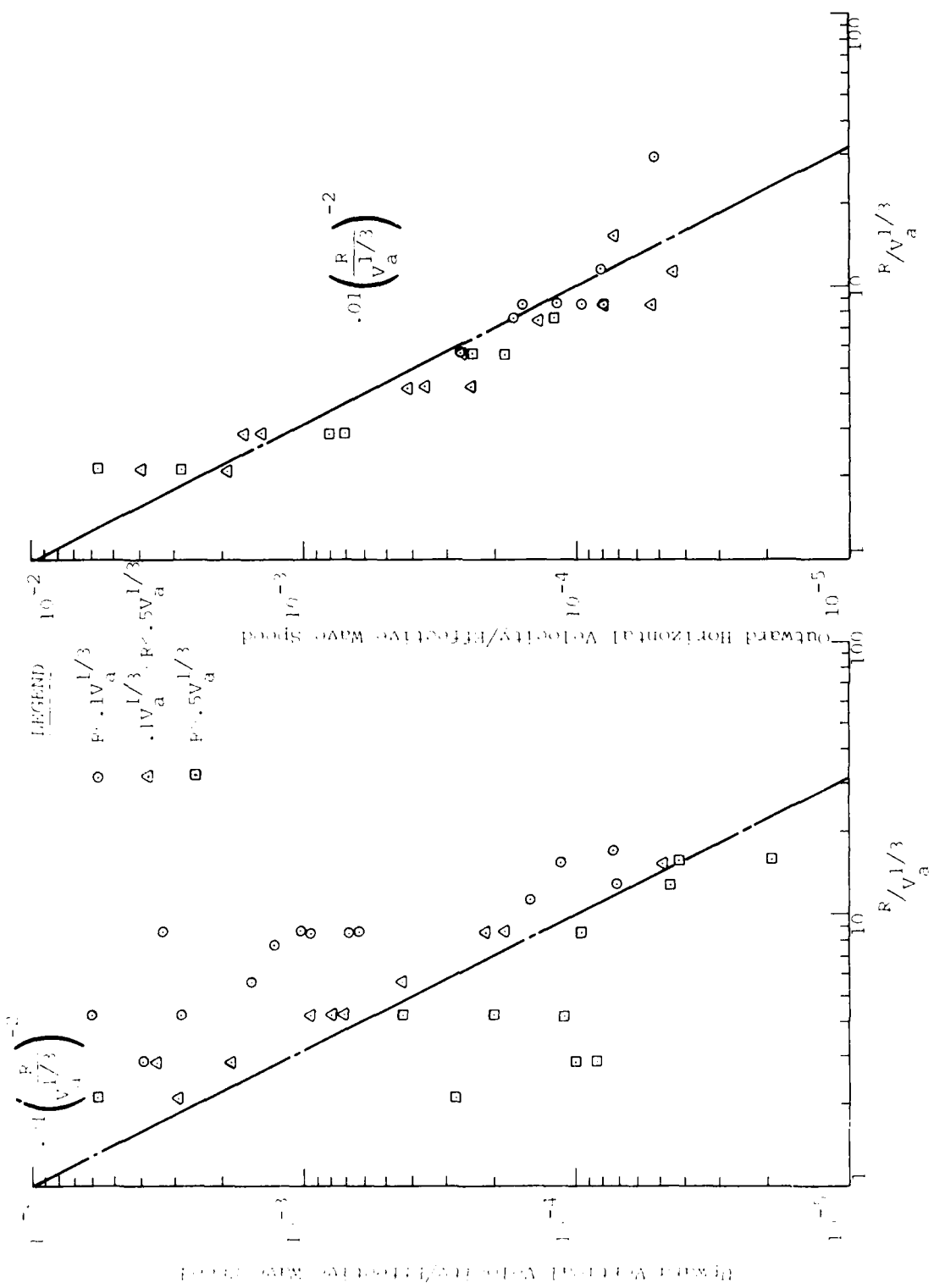


Figure 51. Crater-Related Velocities - MBII-1

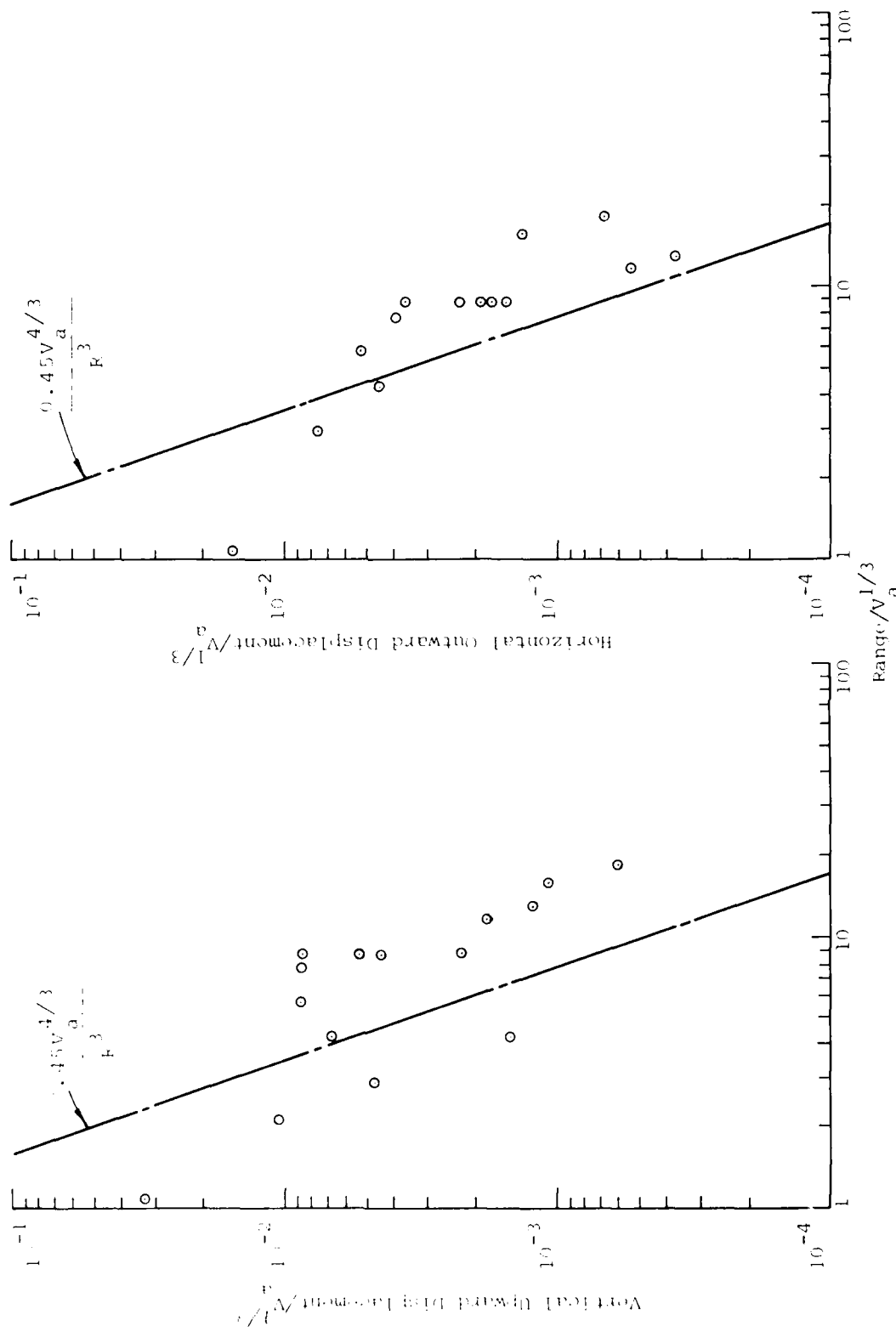


Figure 52. Crater-Related Displacements for $Z \cdot 0.1V_a^{1/3}$; MBII-1

but not as much as the verticals. Again the predicted attenuation rate appears to be reasonably accurate.

Upward and outward displacements for $0.1V_a^{1/3} < z < 0.5V_a^{1/3}$ are shown in Figure 53. On this plot are two prediction curves. The first is the curve for the near-surface displacement and the second is the curve with the coefficient determined from Figure 46. The vertical displacements in this region appear to lie more on the near surface displacement curve, although the differences in the two curves is not large. The predicted attenuation rate appears to be accurate. The horizontal velocity also lies more on the near-surface prediction curve than the lower curve with attenuation rates of the data and prediction about the same.

Displacements for the greater depths are shown in Figure 54. Again the near surface displacement line is shown with the prediction curve for this region. The vertical data lie generally below the near-surface line and above the second line. Attenuation of the data is about what was predicted. Horizontal displacements lie closer to the near-surface line, but are generally bounded by the two lines shown. It appears that the attenuation rates of the data and predictions are about the same.

c) Evaluation

As the reader is aware by now, the identification and prediction of crater related motion is

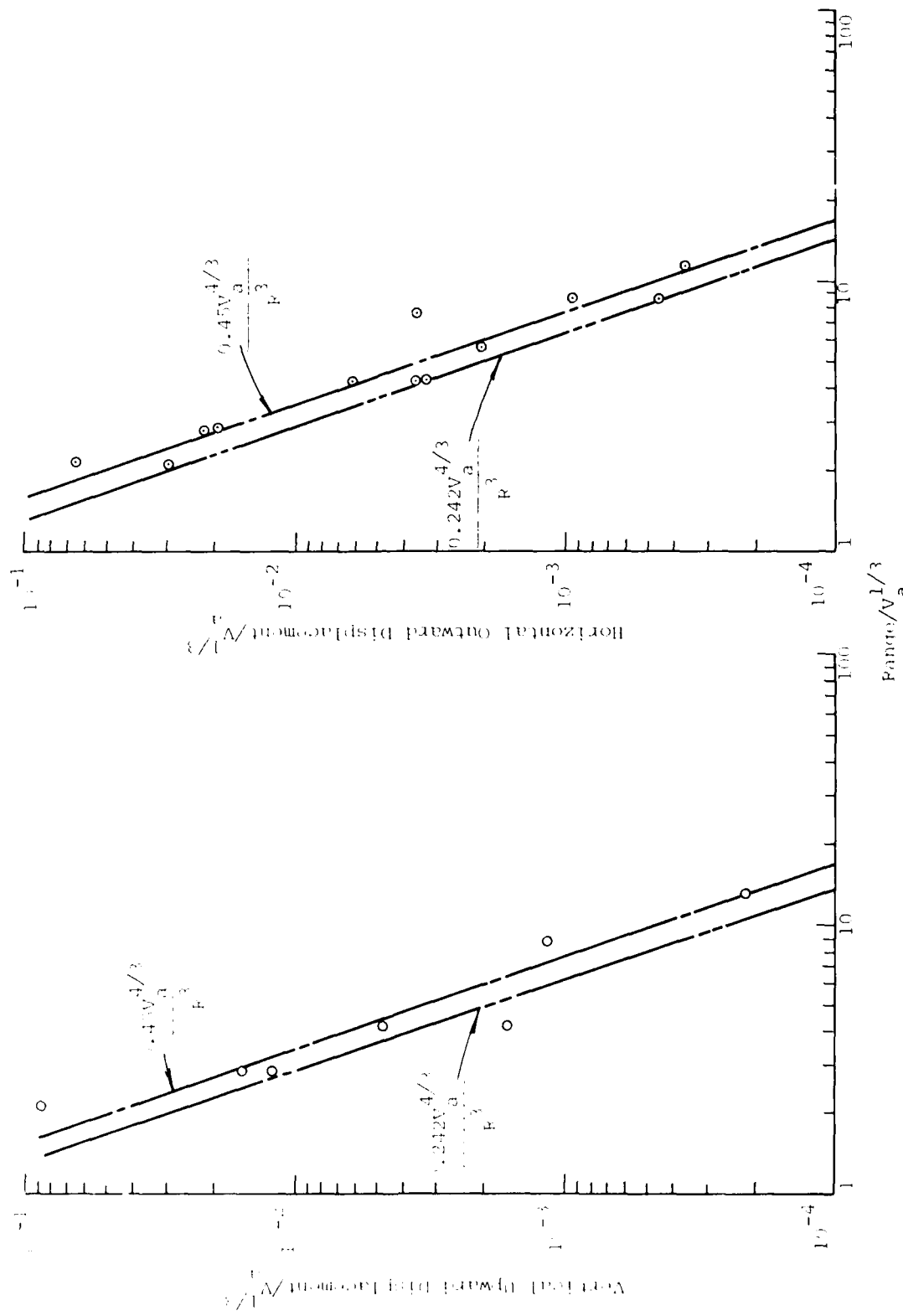


Figure 53. Crater-Related Displacements for $0.1V_a^{1/3} \leq z \leq 0.5V_a^{1/3}$; MBIT-1

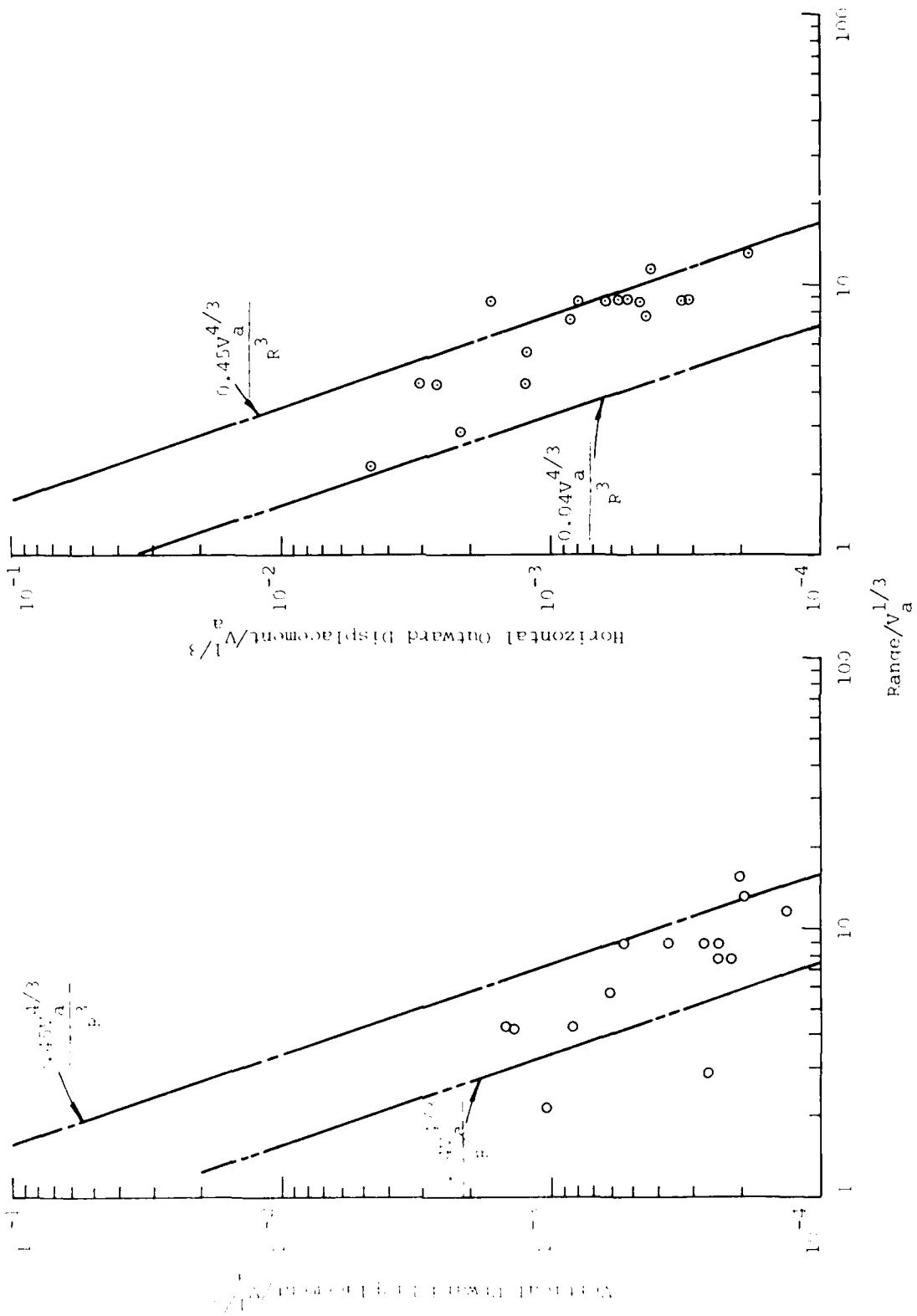


Figure 54. Crater-Related Displacements for $z = 0.5 V_a^{1/3}$; MBII-1

a difficult if not impossible proposition. Recent studies (Ref. 18) have shown that vertical motions, called crater related in the past, have been identified in part, as motions caused by the negative phase of the airblast. In addition, separation of direct and upstream airblast-induced from crater-induced has been difficult and even arbitrary. However, as discussed earlier, the motions described and compared in this chapter are those low frequency motions most often directed upward. However, since theory of origin and some data has been collected on the negative phase component, an attempt has been made here to account for its effect on the upward motions at each of the pertinent sites.

Figure 55 presents comparison of vertical (upward) motions from tests similar in yield and charge configuration to the Misers Bluff II-1 Event. The first observation that can be made on the vertical motion is that a wide range of particle velocities is present. The sites showing smallest upward motions are those with the smallest air void contents near the surface.

The upward displacement from these experiments are the subject of Figures 56 through 58. Figure 56 shows the upward displacements for these experiments. The trend is the same as was evidenced for the velocities but even more pronounced. That is sites with the largest air void

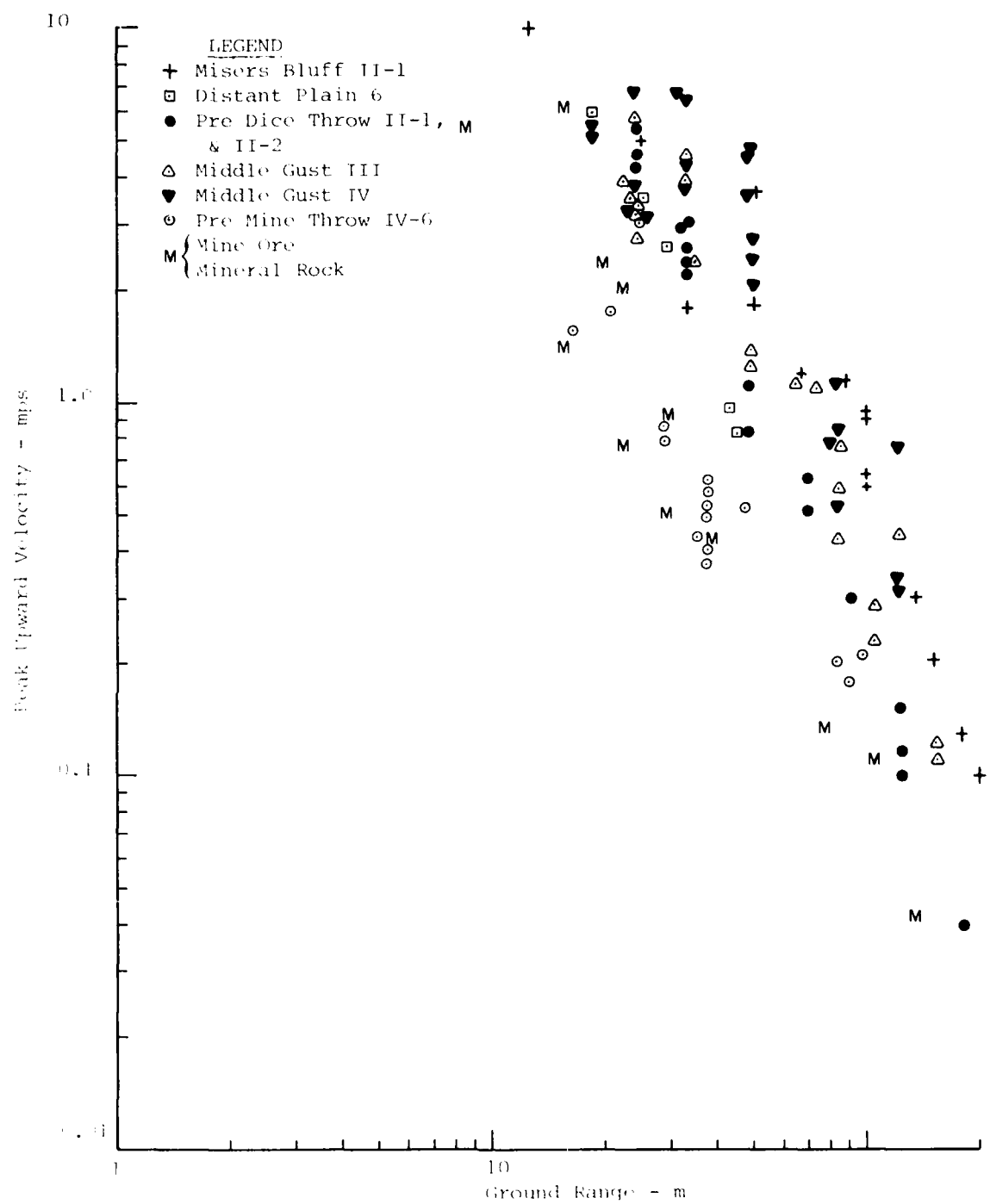


Figure 55. Peak Upward Particle Velocity vs Range for Misers Bluff II-1 and Similar Experiments

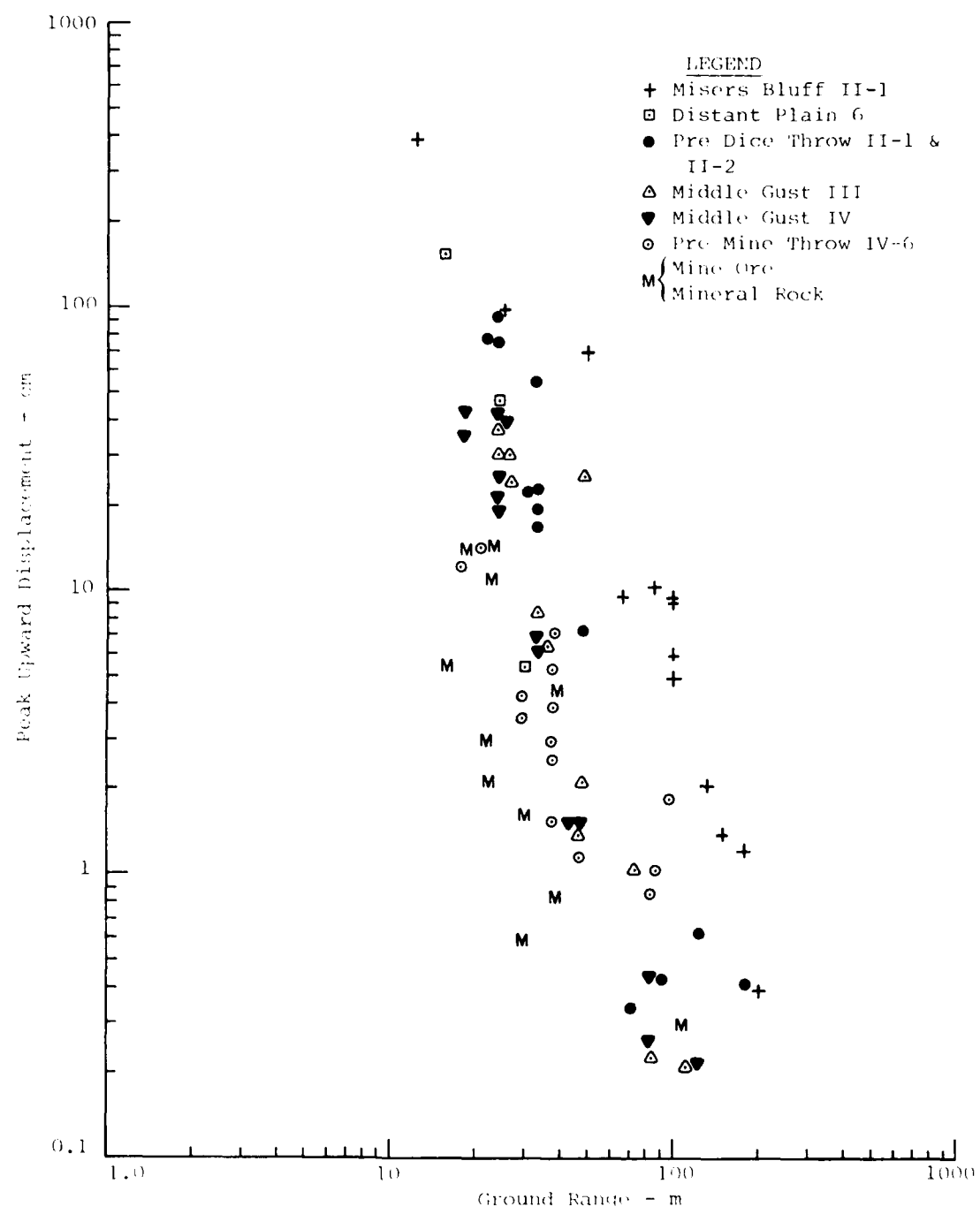


Figure 56. Peak Upward Displacement vs Range for Misers Bluff II-1 and Similar Experiments

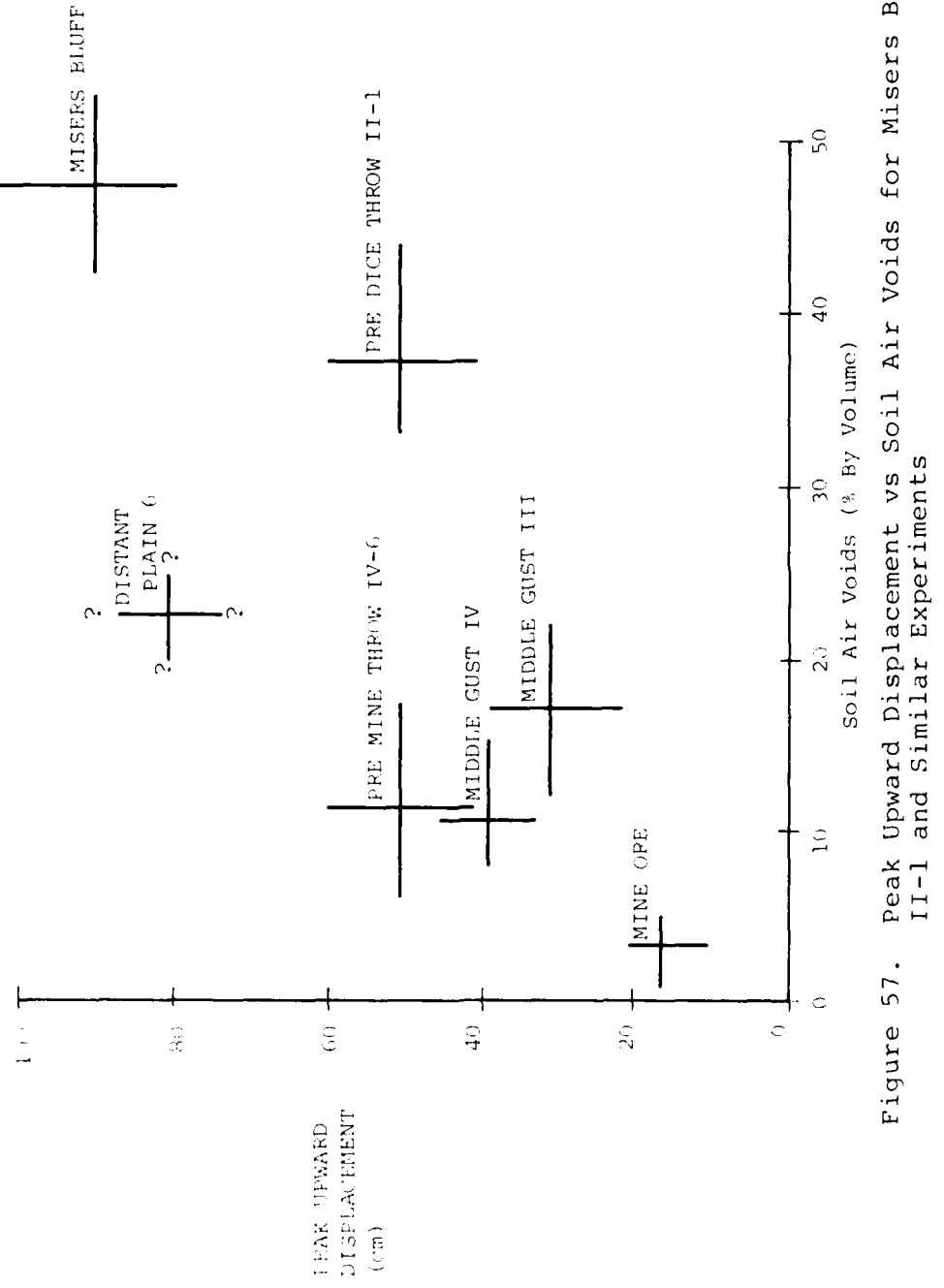


Figure 57. Peak Upward Displacement vs Soil Air Voids for Misers Bluff II-1 and Similar Experiments

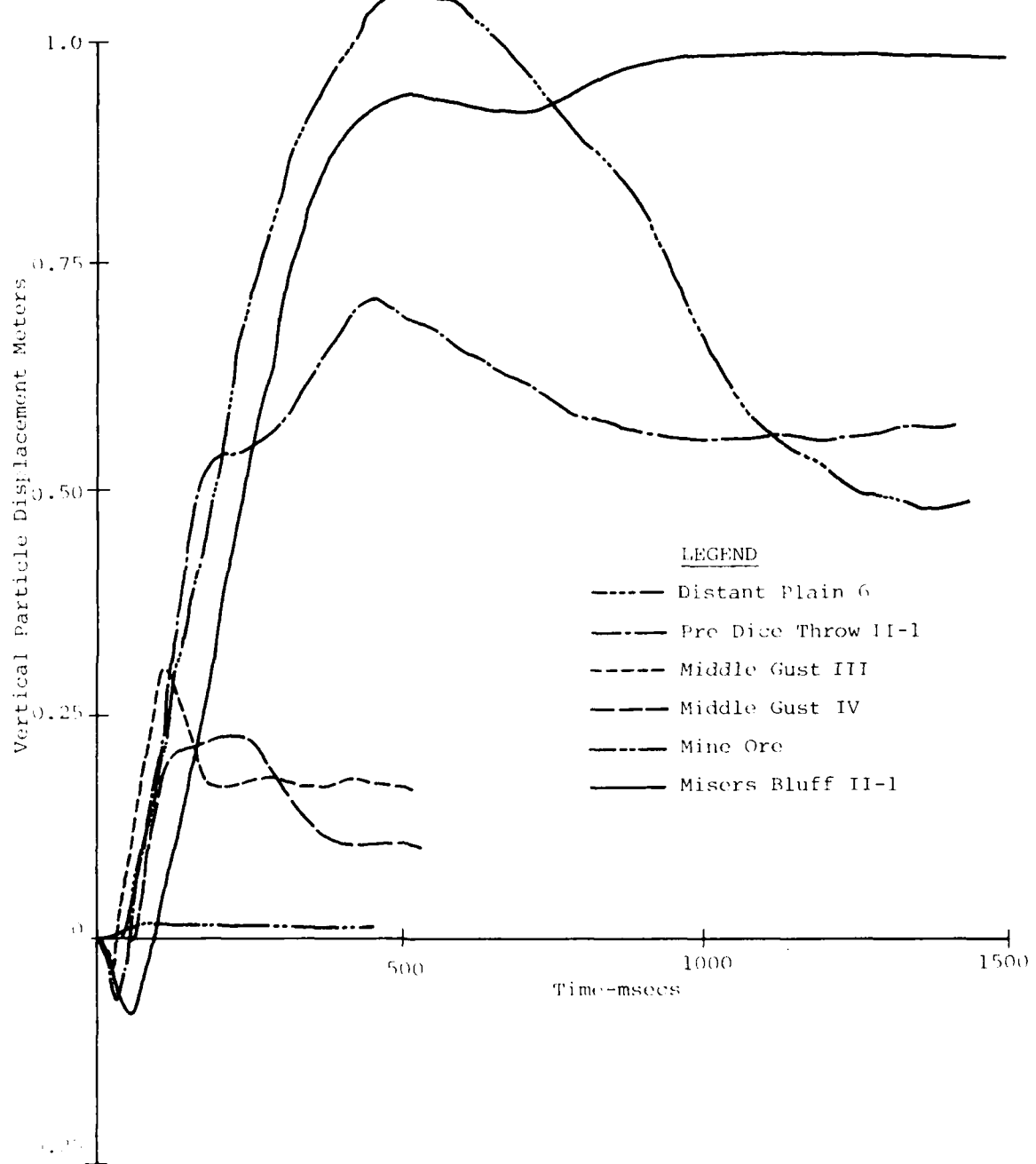


Figure 58. Displacement Time Histories at 25 m Ground Range,
0.5 m Depth from Surface 100 Ton H-E Tests

contents had the largest upward displacements. Figure 57 is a plot of air void and upward displacement data for these different sites. The displacement data is taken at the 24.4 m range and depths ranged from 0.5 m to 1.5 m. The air void data was taken at the depth of the measurement. Again the trend is that the greater air void contents produce the largest upward displacement. This same trend is seen in the displacement time histories shown in Figure 58.

Horizontal velocities (Fig. 59) show a different story. The Misers Bluff data falls within the small spread of data from past shots. Horizontal particle velocities appear to show very little site dependence for the surface tangent explosions.

Horizontal displacements are not so simple (Fig. 60); however, and illustrate significant site dependence. With the trend following an apparent dependency upon craterability. Since the Misers Bluff crater falls within the band of crater sizes from previous experiments, the horizontal displacements fall within this band also.

In summary, horizontal crater-related motions on Misers Bluff II-1 fall within expected trends and the upward velocities and displacements form a bound to previous data. These upward motions seem to be controlled by the pore-air expansion phenomenon related to the negative phase effect of the airblast and the presence of the near surface soft, porous silt layer at the site.

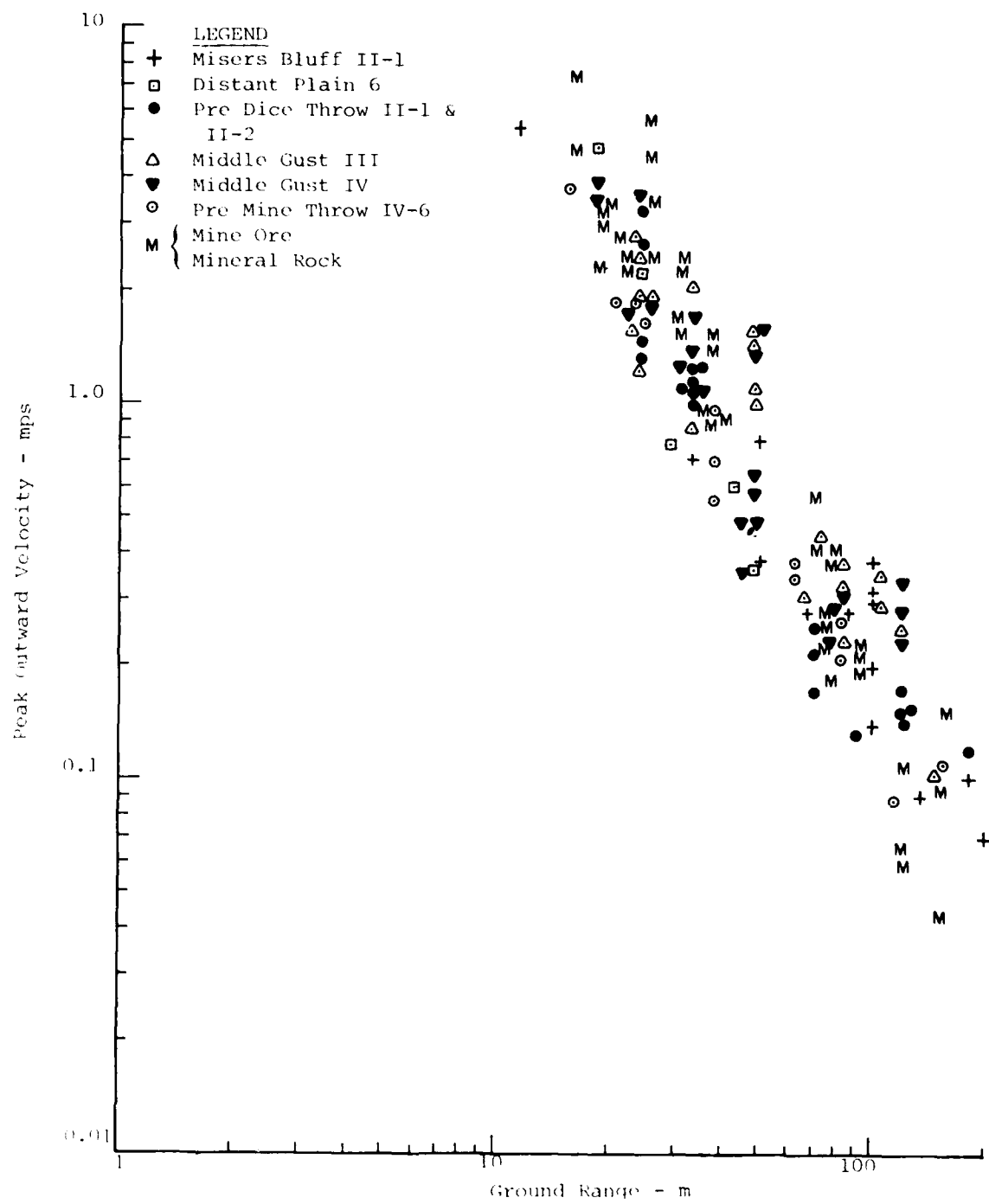


Figure 59. Peak Outward Particle Velocity vs Range for Misers Bluff II-1 and Similar Experiments

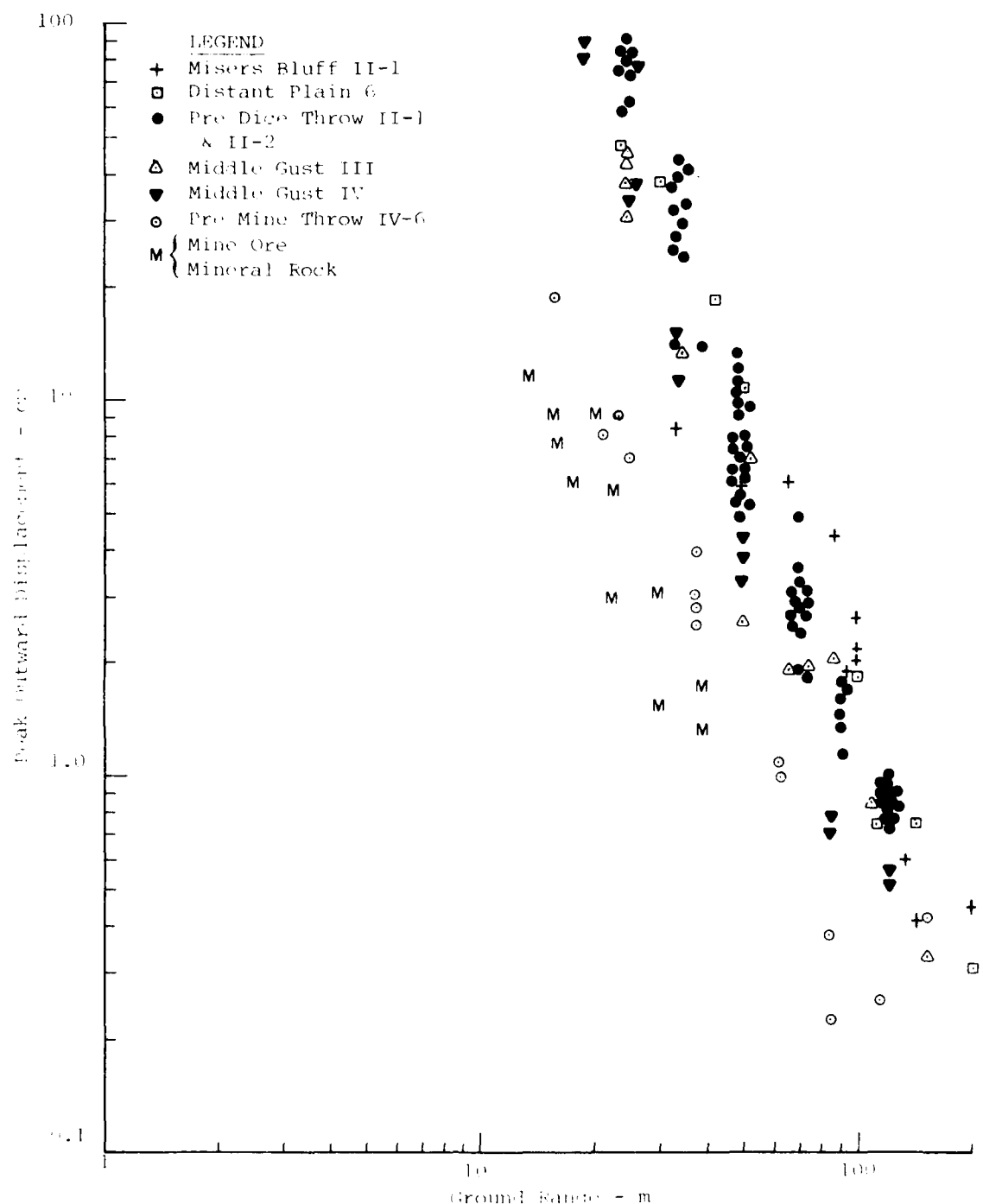


Figure 60. Peak Outward Displacement vs Range for Misers Bluff II-1 and Similar Experiments

3.2.6 Oscillatory Component of Ground Motion

The oscillatory component is defined for the purposes of this report as the motion attributable to the head wave and surface wave phenomena.

3.2.6.1 Prediction Procedure

The pretest prediction procedure used for this component was the Higgins method used in Phase I (Ref. 20). This method, which was based on 100T experiments provided adequate prediction of magnitudes for the motion and the periods observed were reasonably close in the vertical motions. Horizontal periods were poorly predicted but the magnitudes were reasonably accurate.

Considerable work during the conduct of this research has resulted in a new oscillatory component prediction procedure which is based on a procedure developed by WES (Ref. 21). This procedure has been endorsed by the DAWG as the state-of-the-art technique. Since this WES procedure will be used in the waveform synthesis procedure it will be evaluated rather than the procedure used for the pretest predictions.

The main features of the WES procedure include:

1) A uniform transition from crater related motions close-in, to oscillatory ground roll in the far field;

2) Frequency of far field motions are determined on the basis of the shear wave profile and layer thickness;

3) Motion periods close-in are dependent upon depth to water table;

4) Yield scaling ($NE=0.5HE$) of maximum particle velocities in all but the transition region, and in the transition region velocities are dependent upon depth to rock;

5) Peak velocities for the horizontal and vertical components are set equal.

In the upstream airblast dominated region these are given by the equation:

$$V_{\max} \text{ (mps)} = 0.340 \left(\frac{R \text{ (km)}}{Mt^{1/3}} \right)^{-2}$$

in the transition region the equation becomes:

$$V_{\max} \text{ (mps)} = 0.229 \left(\frac{304.8}{H} \right)^{1/3}$$

and in the final region the equation is:

$$V_{\max} \text{ (mps)} = 0.811 \left(\frac{R \text{ (km)}}{Mt^{1/3}} \right)^{-3/2}$$

Where;

V_{\max} = peak velocity, meters per second

R = range, kilometers

Mt = yield, megatons NE

H = depth to rock, meters.

The waveforms are calculated from an exponentially damped sine wave with a variable period. The general waveshape is fit in intervals to match the first three velocity peaks and the time occurrence of the peaks. Periods of the waveforms in the far field (beyond the transition region, where the

attenuation rate is $R^{-3/2}$) are calculated from the equation (developed by Auld & Murphy) :

$$T = \frac{2H}{\beta}$$

where

T = period, seconds

H = rock depth, meters

β = depth weighted shear
wave velocity, meters per
second

3.2.6.2 Data vs Predictions

Comparisons of the prediction of this component and data for some key locations on MBII-1 are shown in Figures 61 through 64. The airblast-related motion has been deleted from the data on these figures.

Figure 61 shows this comparison at the 25 m range. In general the prediction has too long a period of oscillation, in the vertical waveform. Generally, the magnitude of the prediction is reasonably close to the data.

Comparisons at the 50 m range are shown in Figure 62. The vertical waveform was somewhat underpredicted, out of phase and the periods are too long. The horizontal waveform on the other hand appears to overpredict the magnitude and the timing is incorrect.

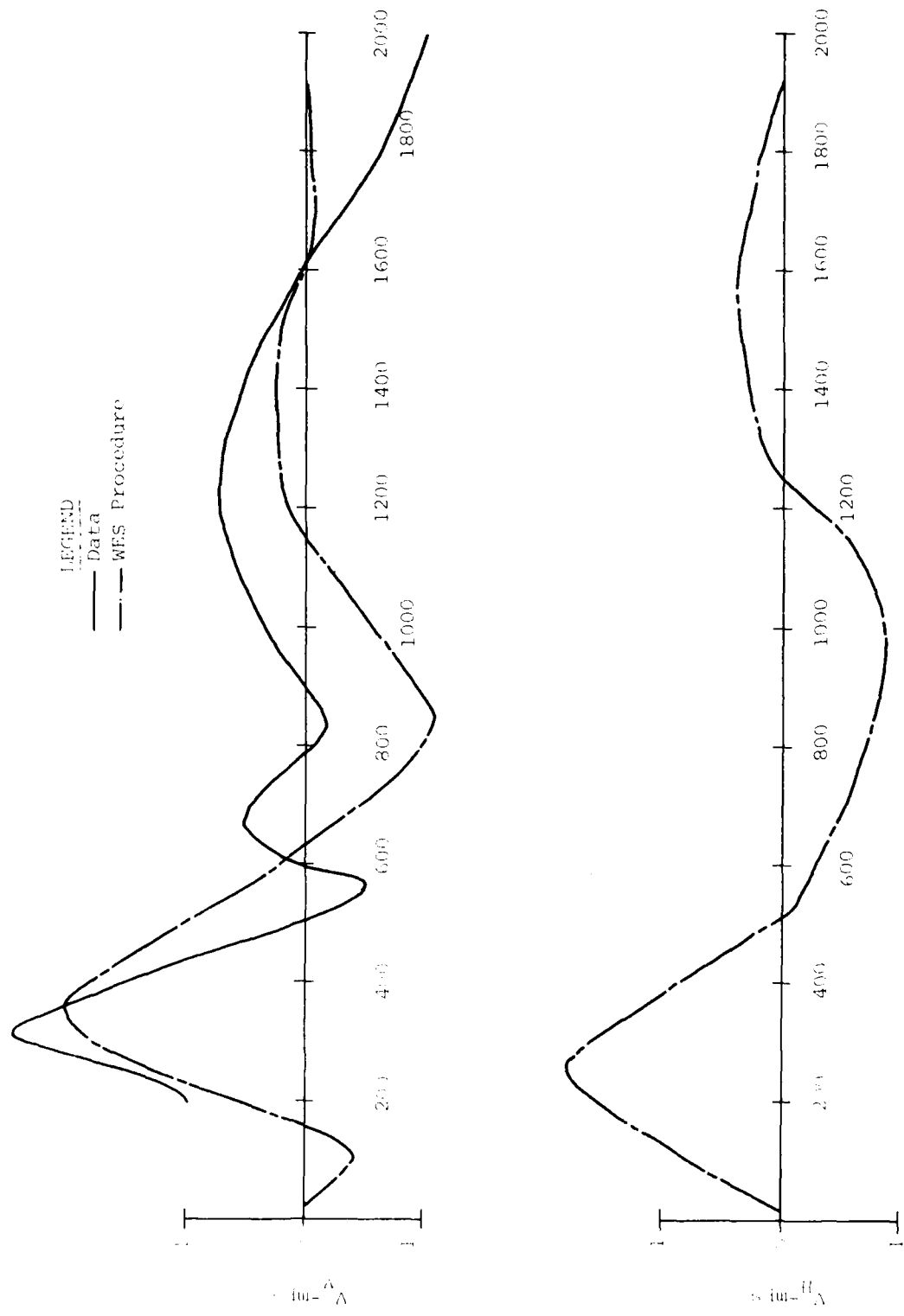


Figure 61. Comparison of WES Low Frequency Prediction Procedure and MBII-1 Data at R=25 m; Z=1.5 m

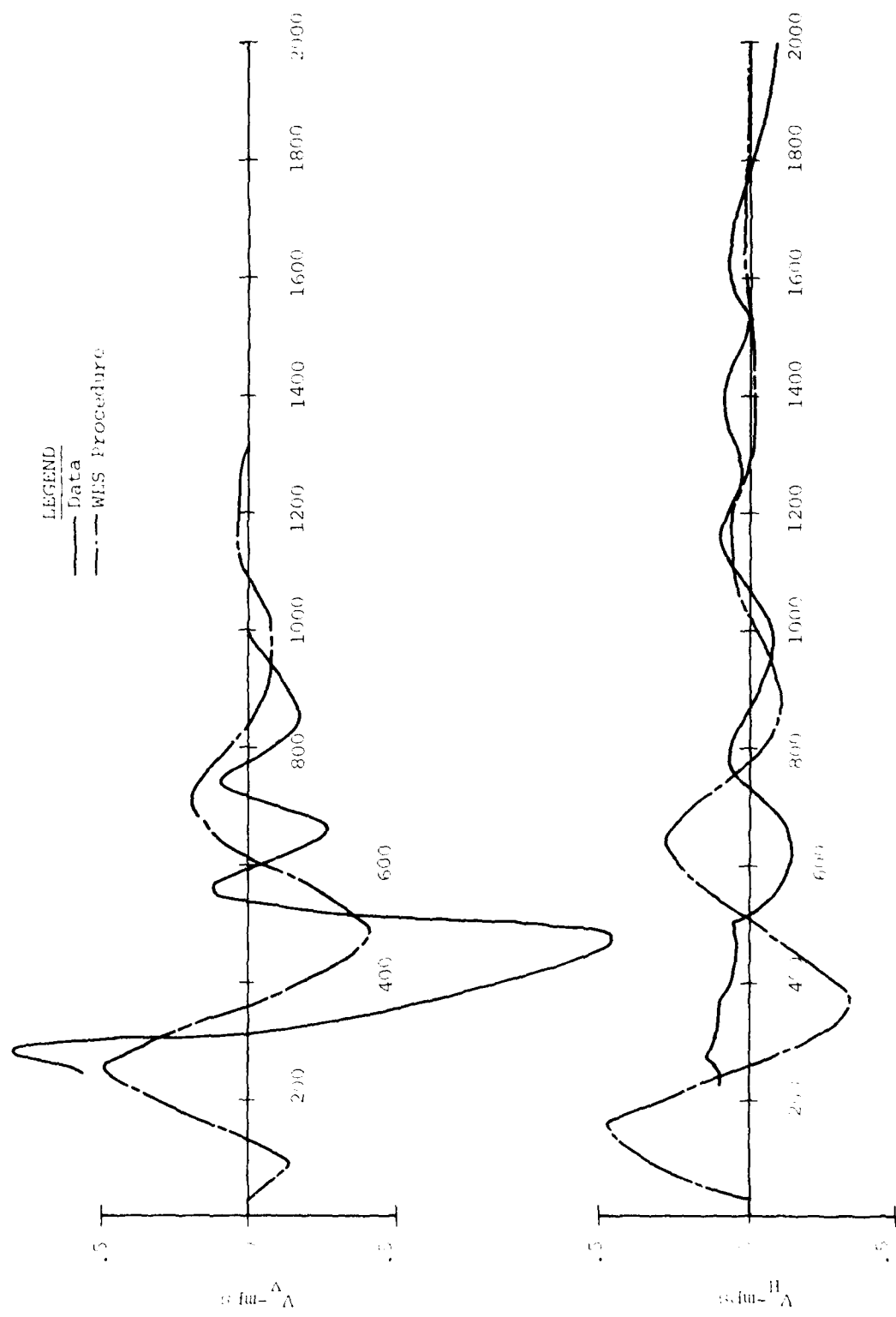


Figure 62. Comparison of WES Low Frequency Prediction Procedure and MBII-1 Data; $R=50$; $Z=0.5$ m

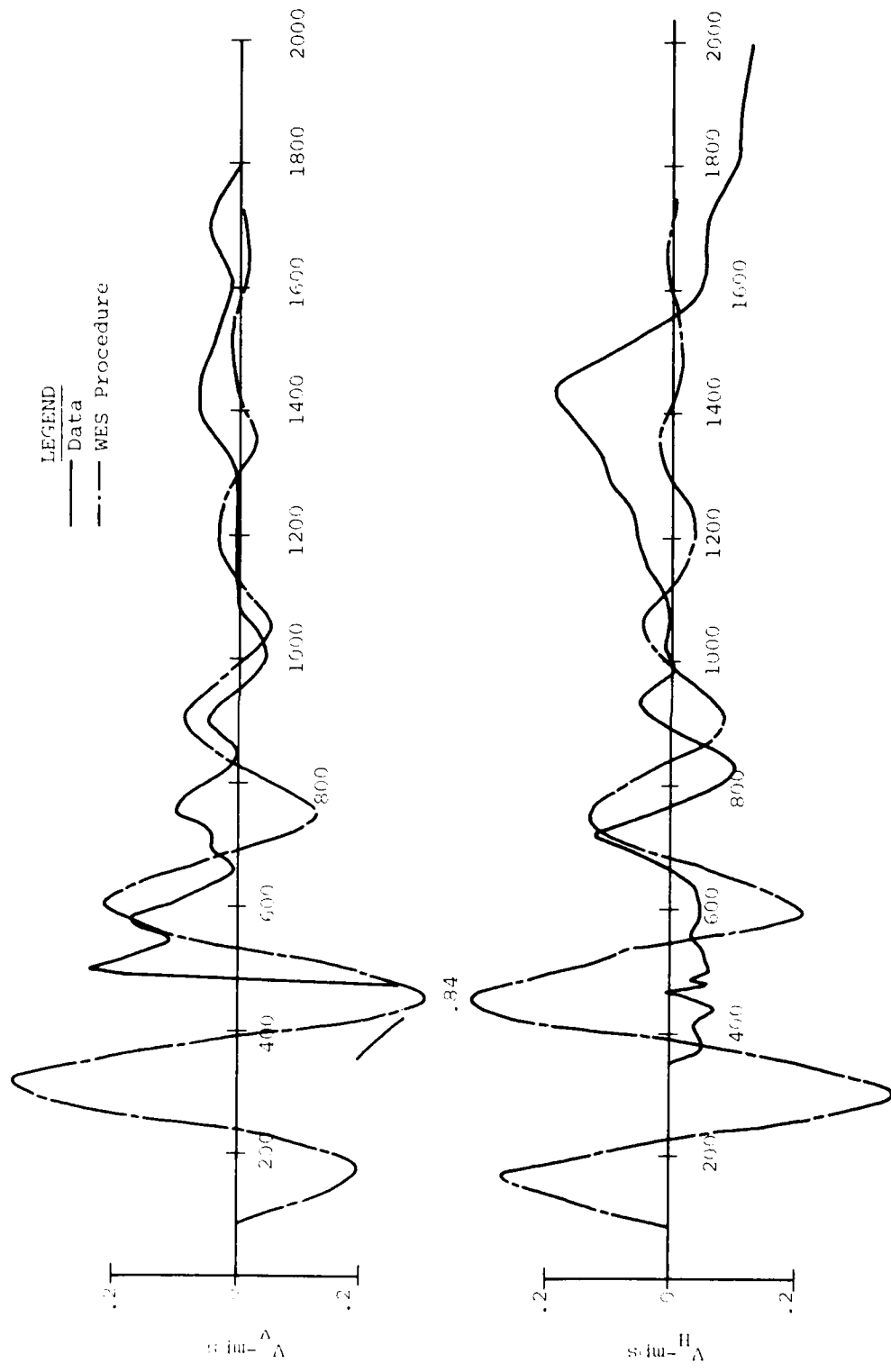


Figure 63. Comparison of WES Low Frequency Prediction Procedure and MBII-1 Data at R=100 m; z=0.5 m

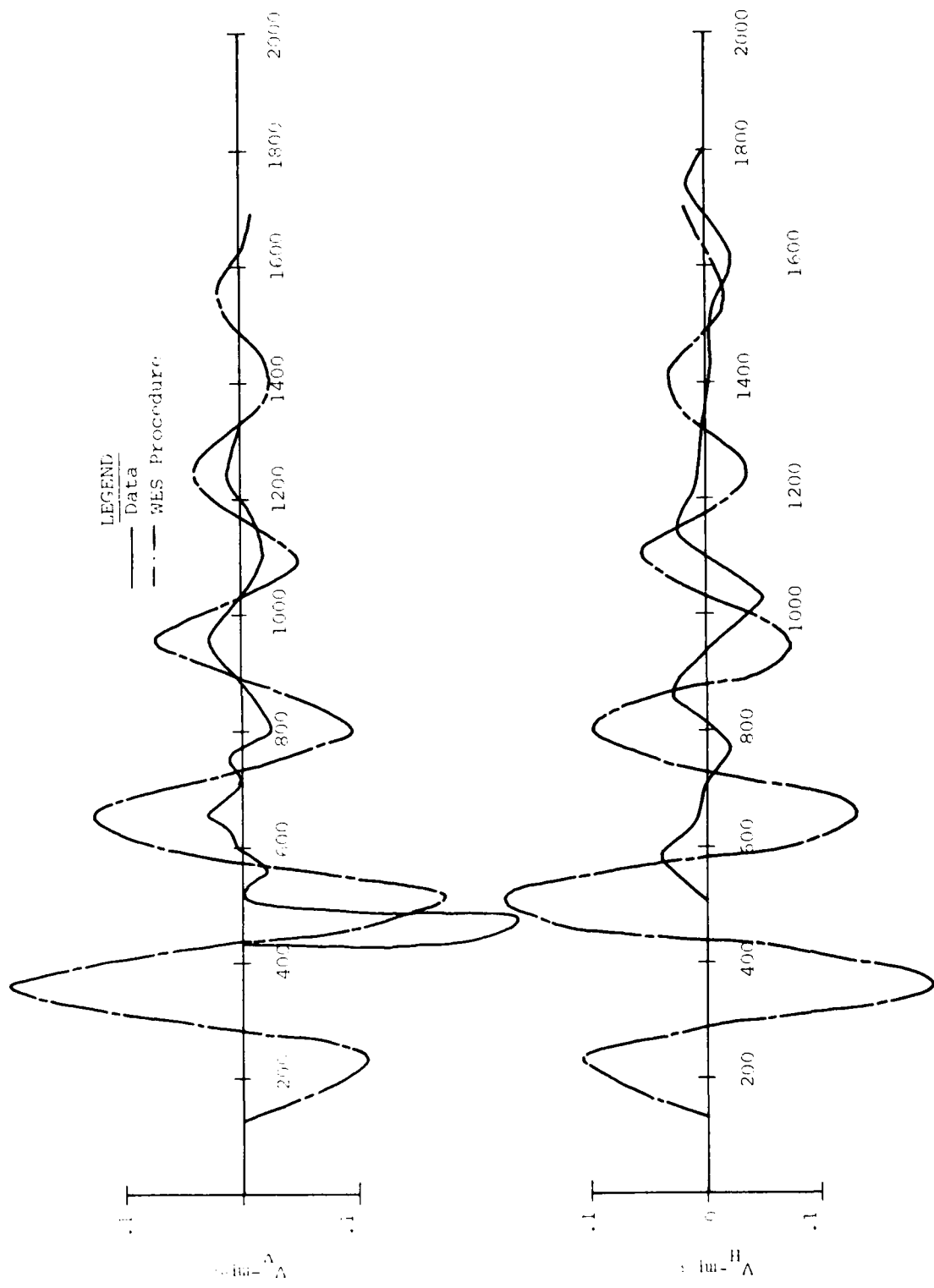


Figure 64. Comparison of WES Low Frequency Prediction Procedure and MBII-1 Data @ R=150 m; Z=0.5 m

At 100 m (Fig. 63), the prediction improves. Periods of oscillation in both the vertical and horizontal are improved from the previous two comparisons. The magnitudes of the waveforms were somewhat overpredicted, however. At the 150 m range (Fig. 64) the vertical motion is significantly overpredicted. Frequencies appear to be fairly accurate at times later than 800 msec. Horizontal motions are also overpredicted. Frequencies are about right, but the data timing is shifted somewhat from the prediction.

3.2.6.3 Evaluation

In general, this procedure is an improvement over past techniques, and is still under development at WES. The main problem with this procedure is in the close-in region. As distance from the source increases the frequencies and magnitudes improve, and the character of the waveforms are similar to the data.

As mentioned previously, the site layering (and material properties) is the controlling variable affecting the frequency of outrunning motions. Figure 65 displays in graphical form the layering characteristics of previous tests, showing the "void" filled by the Misers Bluff Phase II testing. Table 3 provides the frequency summary of these past tests. Some interpretation is required, of course, to select a single representative frequency from each event,

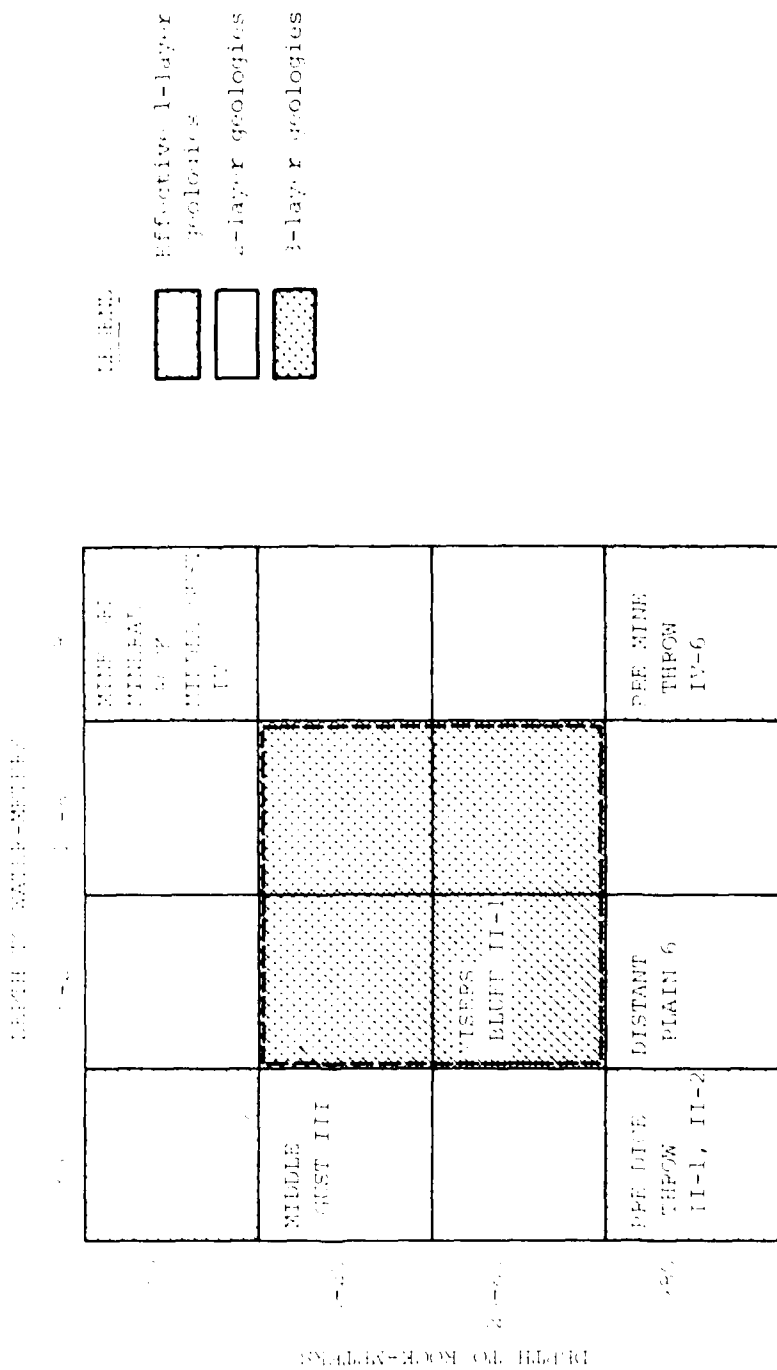


Figure 65. Idealized Layering Characteristics of 100-ton Test Sites

Table 3: Summary of Ground Roll Frequencies for Misers Bluff II-1 and Similarly Configured Experiments

<u>Test Event</u>	<u>Ground Roll Frequency</u>
Pre Dice Throw II-1, II-2	2
Distant Plain 6	2
Misers Bluff II-1	5
Pre Mine Throw IV-6	8,5
Middle Gust III	8
Middle Gust IV	7
Mine Ore	20

however, these frequencies are believed to be good to \pm 10%. Note that the only hard rock site, MINE-SHAFT and the MINE ORE tests, provide the upper bound frequency, 15-17 Hz. The low frequency bound is the PRE DICE THROW II and DISTANT PLAIN 6 sites, those which have the lowest site shear wave velocity profile.

Finally, Figure 66 is a plot of vertical and horizontal velocities at the 400' ground range and 0.5-1.5 meter depth for the HE surface tests. No data is shown for the hard rock tests, MINE ORE and MINERAL ROCK because no quality shallow measurements were taken near 120 meters ground range. Measurements from both smaller and greater ranges, as well as from greater depths form the basis of the 15-17 hertz frequency attributed to ground roll at this site.

Several observations may be made concerning the data shown in the figure. Two of the tests have relatively weak materials composing the bulk of the profiles from near-surface to depths greater than 80 m. These tests, DISTANT PLAIN 6 and PRE DICE THROW II-1, give the smallest frequency for outrunning (2-3Hz). Misers Bluff II-1 has similar soil properties as DISTANT PLAIN 6 to about the 30 m depth. At this point the Misers Bluff stiffens relative to the DISTANT PLAIN 6 material because of relatively shallow

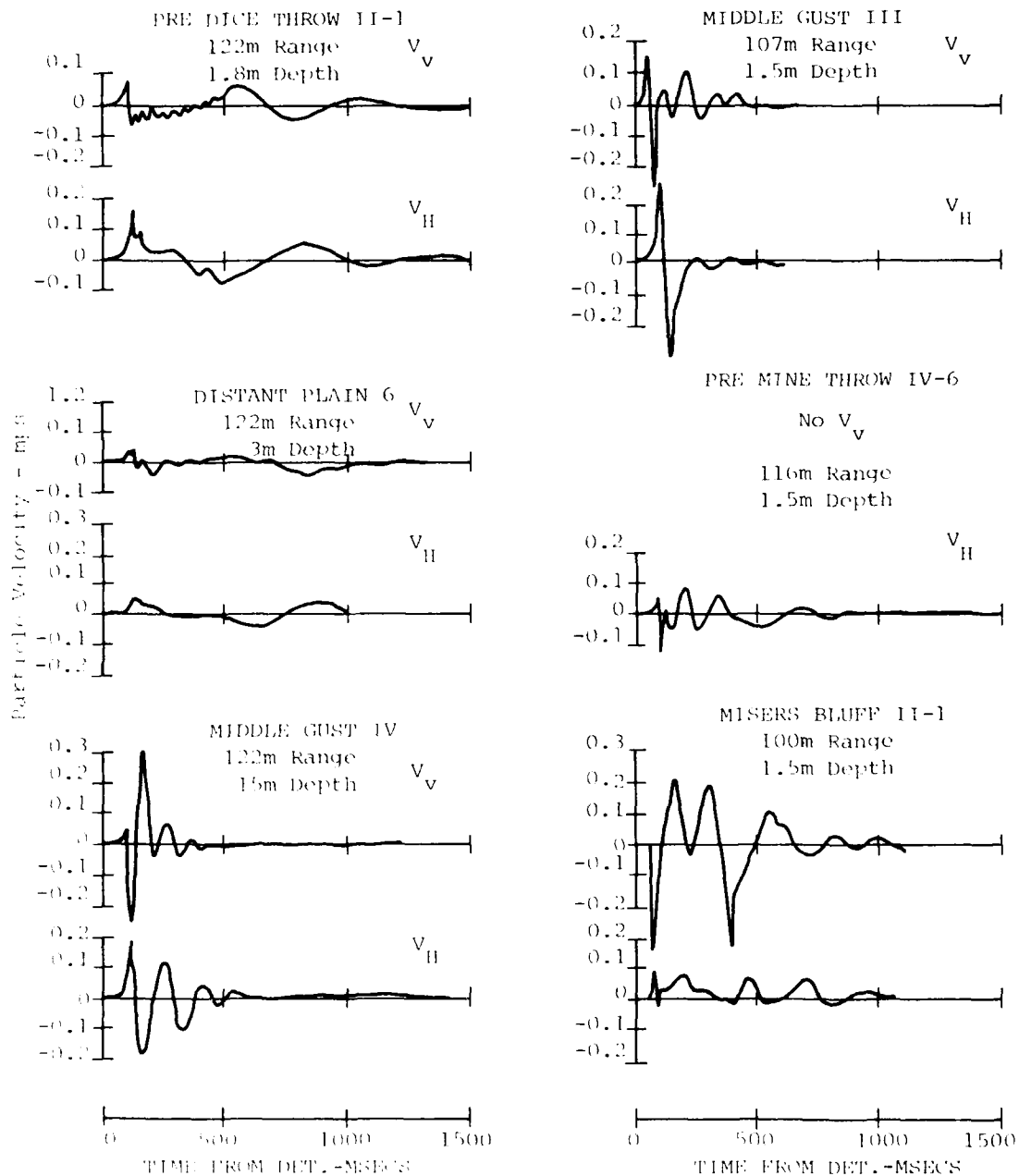


Figure 66. Outrunning Velocity Waveforms (Ground Range = 120m) for 100-ton Surface H.E. Tests

bedrock. The observation that the outrunning frequency is higher at Misers Bluff than in DISTANT PLAIN (5Hz vs 2Hz) suggests that the material at depths greater than 30 m play a role in the determination of the frequency of outrunning motions at ranges on the order of 120 m and beyond. Waveforms measured in MIDDLE GUST III and IV also support this observation. While the shallow materials (<6m) at the two sites are considerably different, the shales from 6 m and deeper are quite similar in properties. The frequency of outrunning motions also appear nearly equivalent indicating the effect of deep materials on the outrunning frequencies. The stiffest (and strongest) of sites, MINE SHAFT, yields the highest frequency of the oscillatory component (15Hz to 17Hz). Thus the spectrum of frequencies varies from the 2-3 Hz at PRE DICE THROW and DISTANT PLAIN sites, through the Misers Bluff II site (like DISTANT PLAIN but with rock at approximately 30 m depth), through the PRE MINE THROW dry playa site (5-8Hz), to the 15-17Hz at the MINE SHAFT site.

Since this signal has been identified as a shear wave the material property most likely to correlate with these observations would be a depth weighted shear-wave velocity.

3.2.7 Summary Observations of MBII-1 Analysis

The purpose of MBII-1 was to test the state-of-the-art prediction procedures for the single burst case. These procedures were extensively discussed on a component-by-component basis in the previous sections. The net result of this study is the recommendation of the following prediction procedures for ground motion due to a single burst:

- The vertical air slap component (for both positive and negative phases of the airblast) is well predicted by 1-D finite differences codes such as PLID with a first order model of pore-air expansion.
- The horizontal air slap component is estimated by modifying the compressive portion of the vertical air-slap signal as recommended in the AFDM.
- Low frequency motions (crater-related, upstream-induced, and oscillatory components) are reasonably well determined by the WES prediction procedure.

3.3 MBII-2

3.3.1 Introduction

The multiple burst experiment of Phase II consisted of six 120T AN/FO charges. The configuration of the experiment was shown in Figures 9 and 10.

The approach taken in the development of a Waveform Synthesis Model was, to use the single burst event to evaluate the theoretical and empirical state-of-the-art prediction procedures. Data from the single burst experiment would then be used to prepare superposition predictions for the multiple burst environment. These superposition prediction predictions would then be compared with data to determine where the major multiple burst related nonlinearities occurred. Analysis of the test data and supporting studies would then be used to model these nonlinearities. These analysis efforts would ultimately be meshed together to yield the Waveform Synthesis Model. The single burst analysis was presented in the previous sections of this chapter. The multiple burst analysis and evaluation of superposition will be discussed in the remaining sections of this chapter.

3.3.2 Phenomenology

Figures 67 and 68 show the 0.5 m depth vertical waveforms measured on the main bisector and charge line radials inside the charge array of MBII-2.

In general, the waveforms from the array center out to the 12.5 m range are characterized by a single downward air-slap peak. This is followed by a rebound peak and then crater-related and negative phase effects. As was the case in the MBII-1 data, it is felt that the negative phase effect is dominating this upward motion. The upward

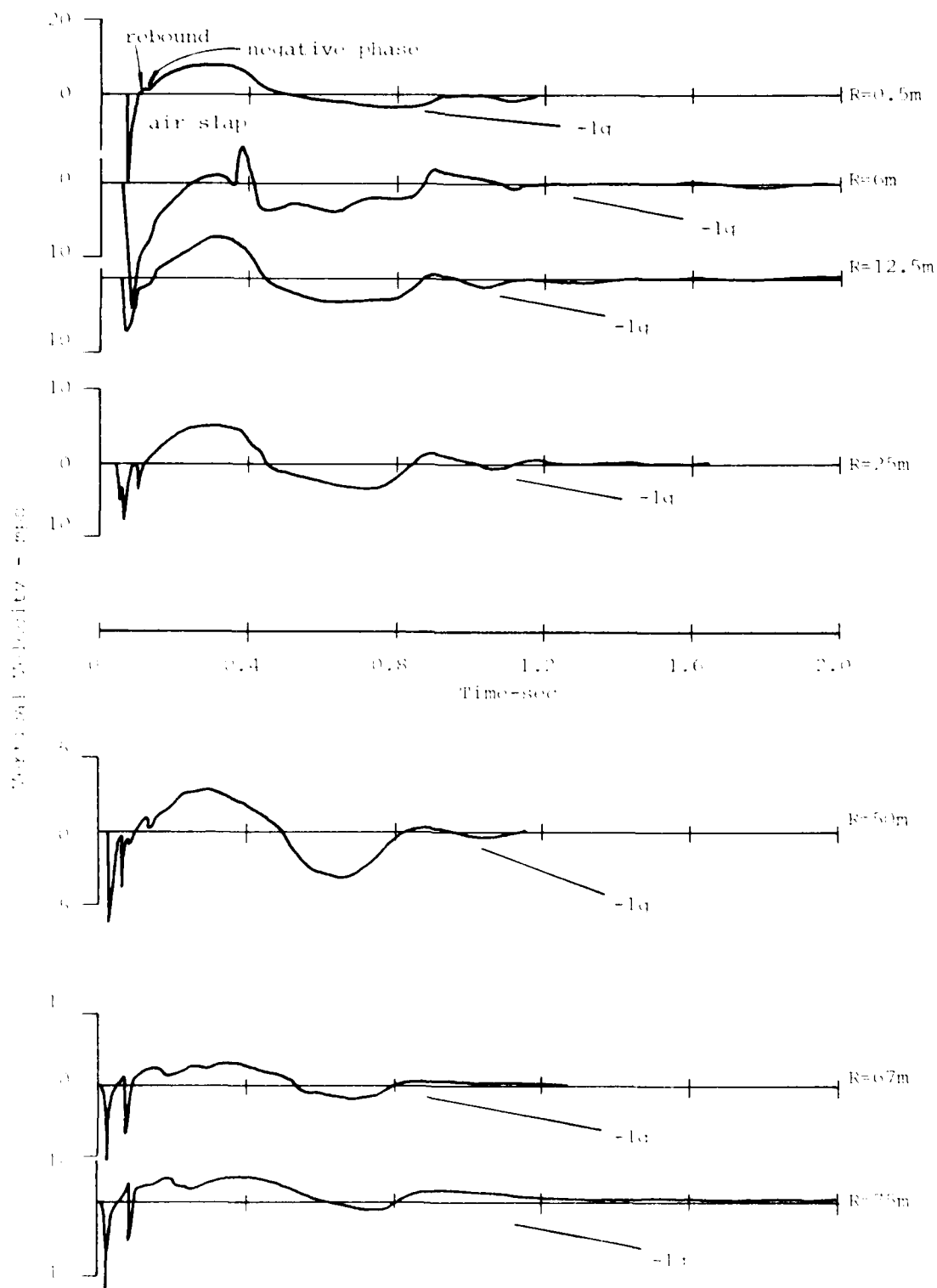


Figure 67. Vertical Velocity Waveforms on a Charge Radial
 $z = 0.5\text{m}$

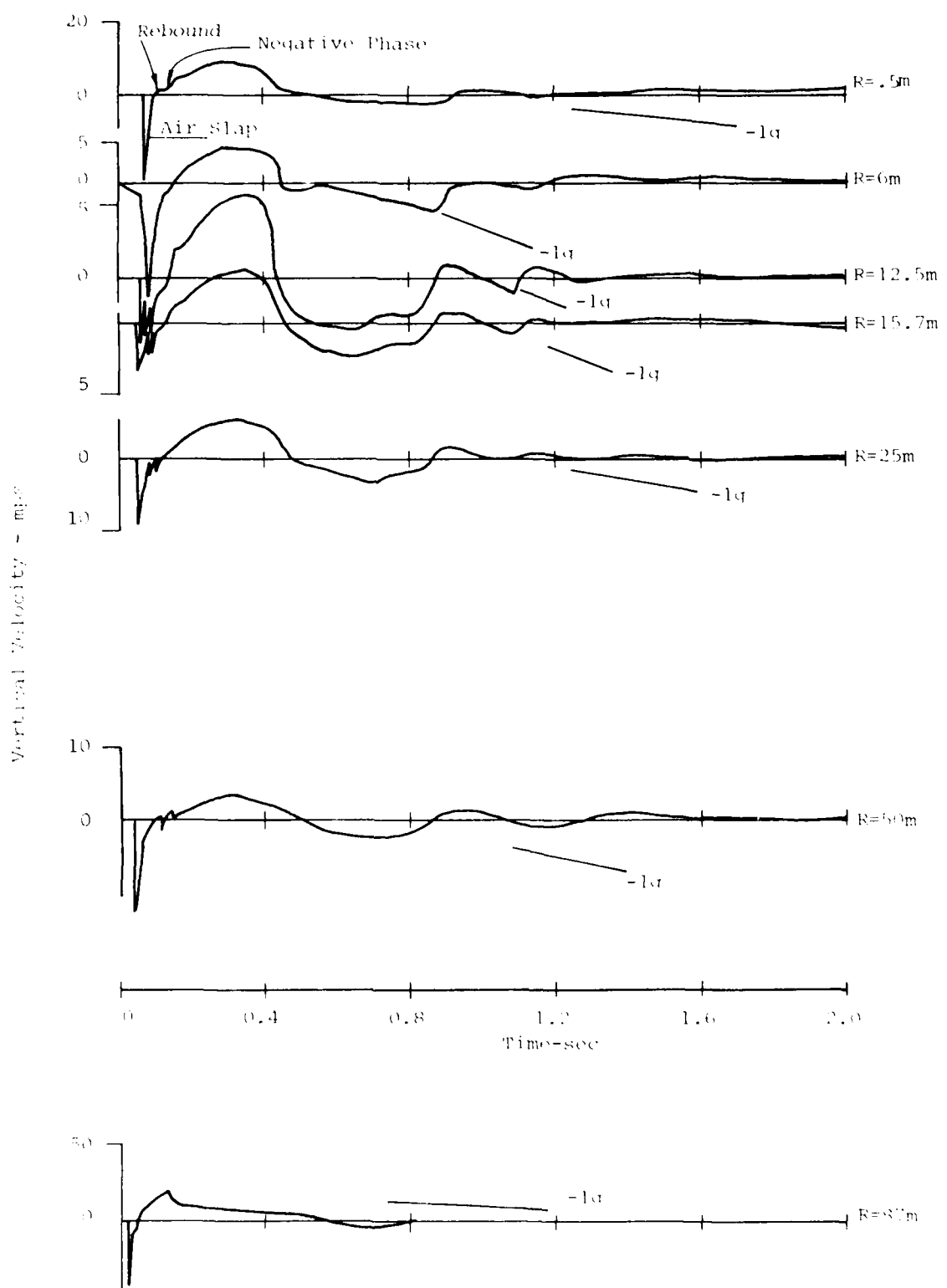


Figure 62. Vertical Velocity Waveforms on a Bisector at $z=0.5\text{m}$

motion is terminated by a small tertiary compressive phase in the airblast waveform, which initiates a downward motion. This downward motion continues until the upper material rejoins the lower material which abruptly reverses the motion at approximately 800 msec. This closure is brought about by a wave propagating upward from the deeper materials. This upward propagating wave is of sufficient magnitude to force the near-surface material into another separation (this wave in the deeper materials will be discussed later in this section). This material then free falls until a second rejoin occurs.

The motion of the waveforms beyond 12.5 m is similar to that seen in the first group. The main difference is the well defined multiple arrivals of the air-slap components from the different charges in the array. Again negative phase effects appear to dominate the low frequency motion.

The matching horizontal velocities are shown in Figures 69 and 70.

Motion is initialized by the air slap. Following the air slap there is a small crater-related pulse and motion returns to essentially zero. This time frame corresponds to the time of the airblast negative phase observed in the vertical motions. At ranges less than 6 m from the array center, a relative large outward signal is then seen. Motion is then completed with small magnitude oscillatory motions.

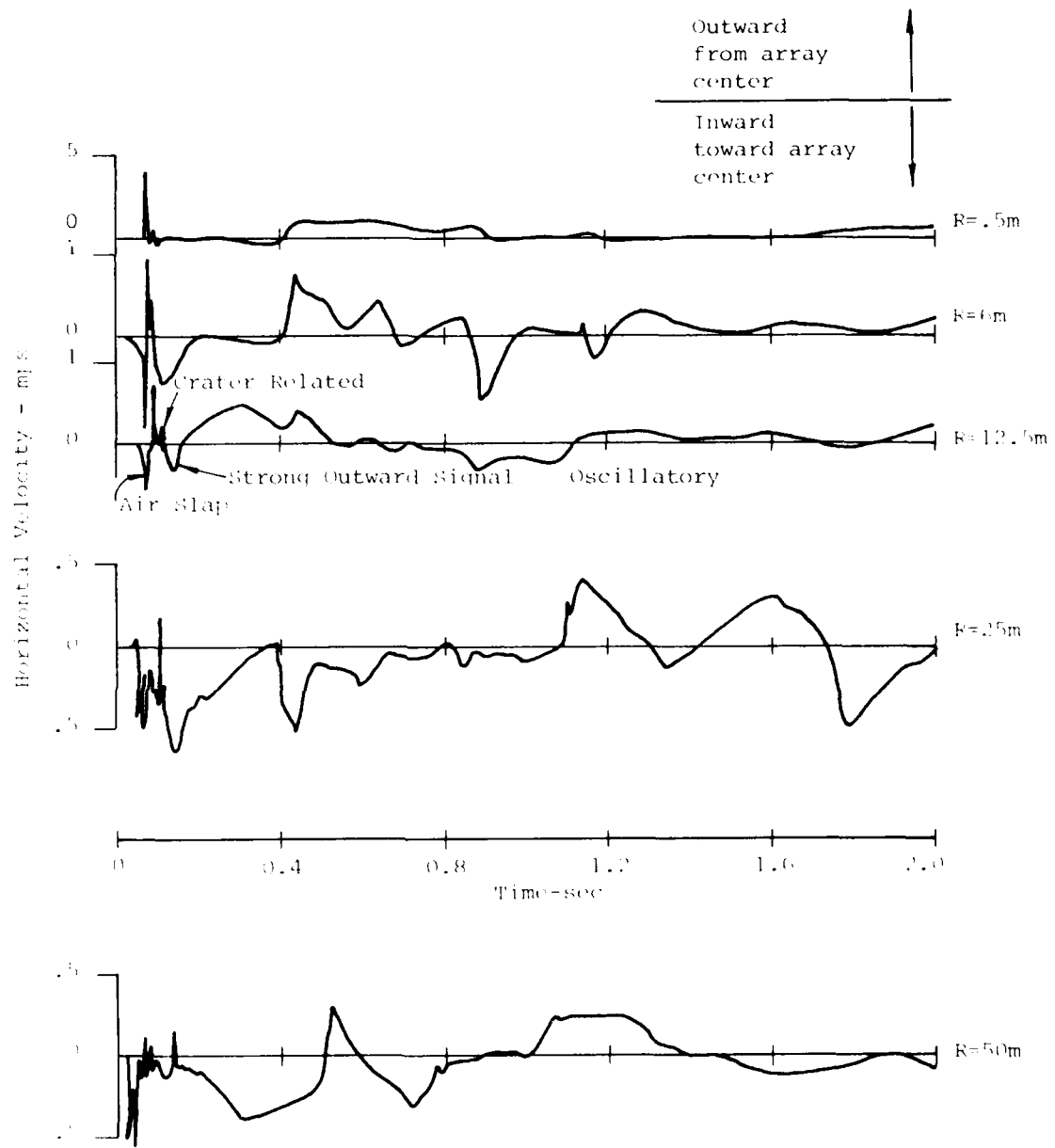


Figure 69. Horizontal Velocity Waveforms on a Charge Radial at $Z=0.5\text{m}$

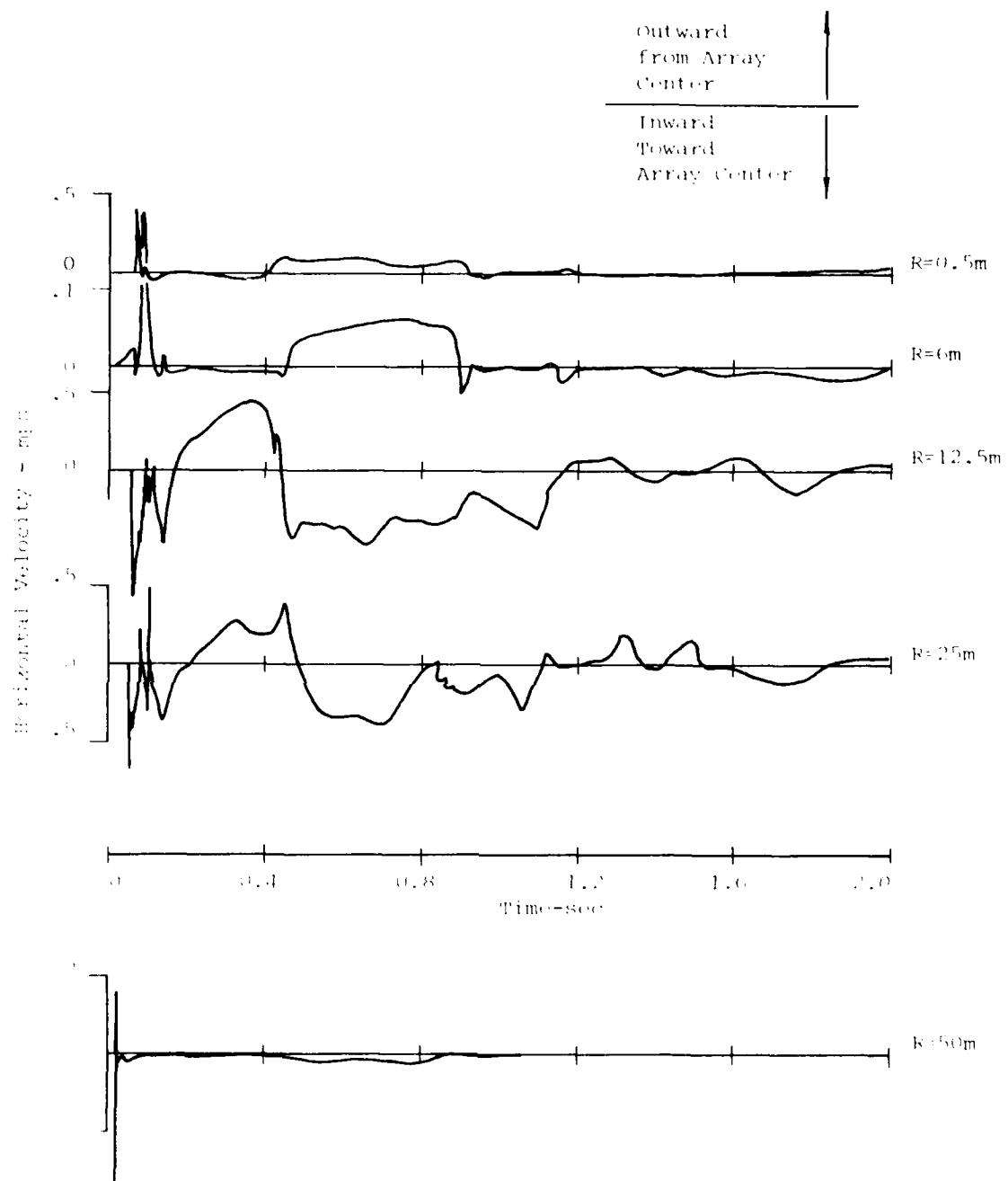


Figure 11. Horizontal Velocity Waveforms on a Bisector
 $\theta = 0.5^\circ$

Beyond 6 m a similar air slap portion is observed, but in the time frame of the negative phase effect in the verticals (at approximately 150 msec) there is a strong outward (from the center) motion. The strong outward motion may be the result of the direct induced signal reflecting from the array center. This type of phenomenology would result in motion away from the center in the proper time frame. The outward signal is seen in both bisector and charge line at the 12.5 m and 25 m ranges. At the 50 m range the signal (at approximately 200 msec) is opposite in direction to the signal at the 12.5 m and 25 m ranges. This may be due to the attenuation of the reflected wave coupled with the fact that the closest charge is starting to dominate the waveform in the crater-related time domain. In other words at this range the effects from other charges are "riding along" on the crater-related signal of the closest charge. This would account for the direction reversal. Following this outward motion is the inward motion from small secondary compressive phases occurring in the airblast at approximately 400 msec. Finally an oscillatory motion completes the waveform.

Figures 71 and 72 show the variation in the waveforms with depth at a range of 25 m on a charge line. The phenomenology observed in these waveforms is reasonably straightforward. Motions near surface have already been discussed.

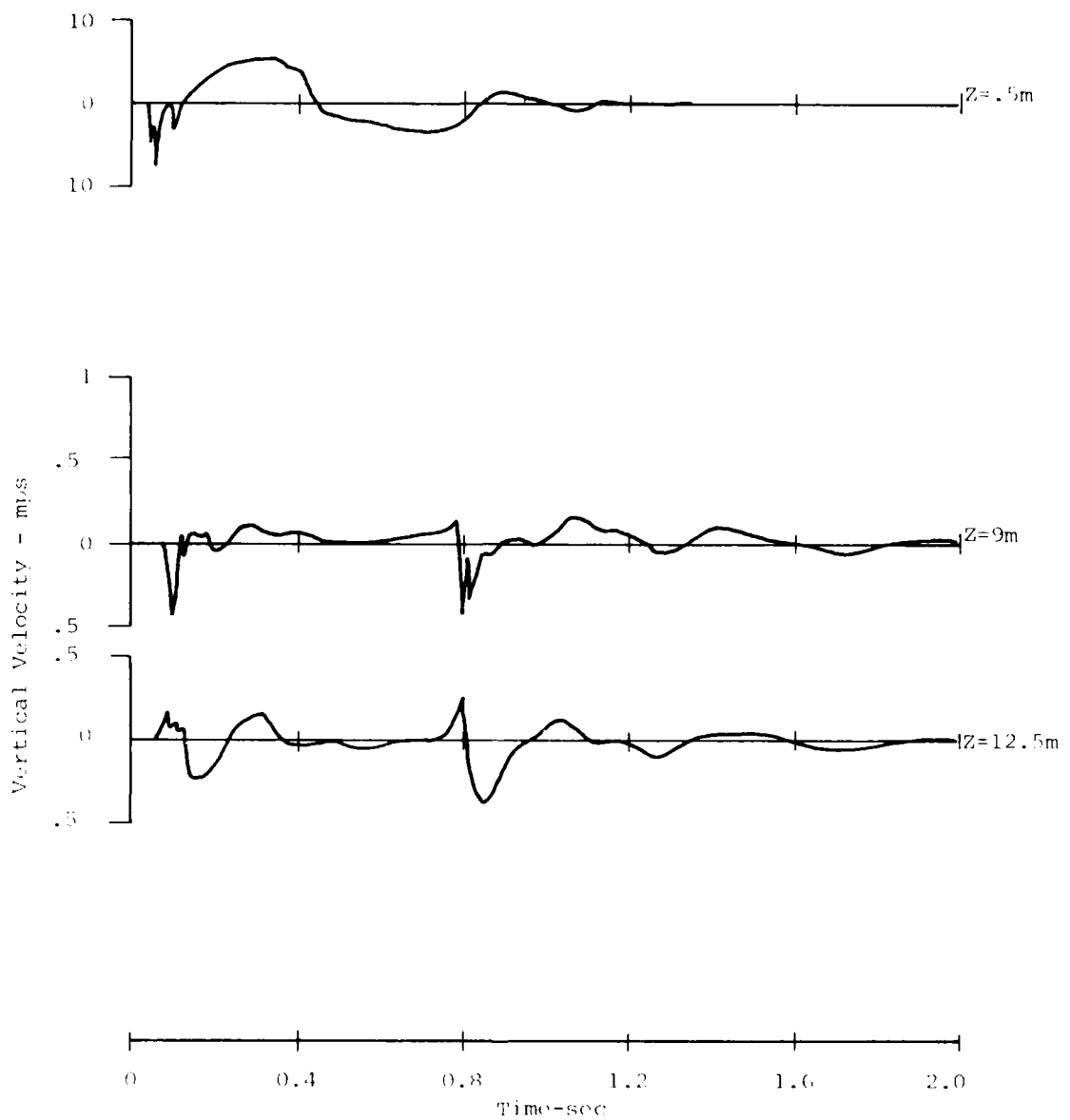


Figure 71. Vertical Velocity Waveforms at 25m Range on a Charge Line

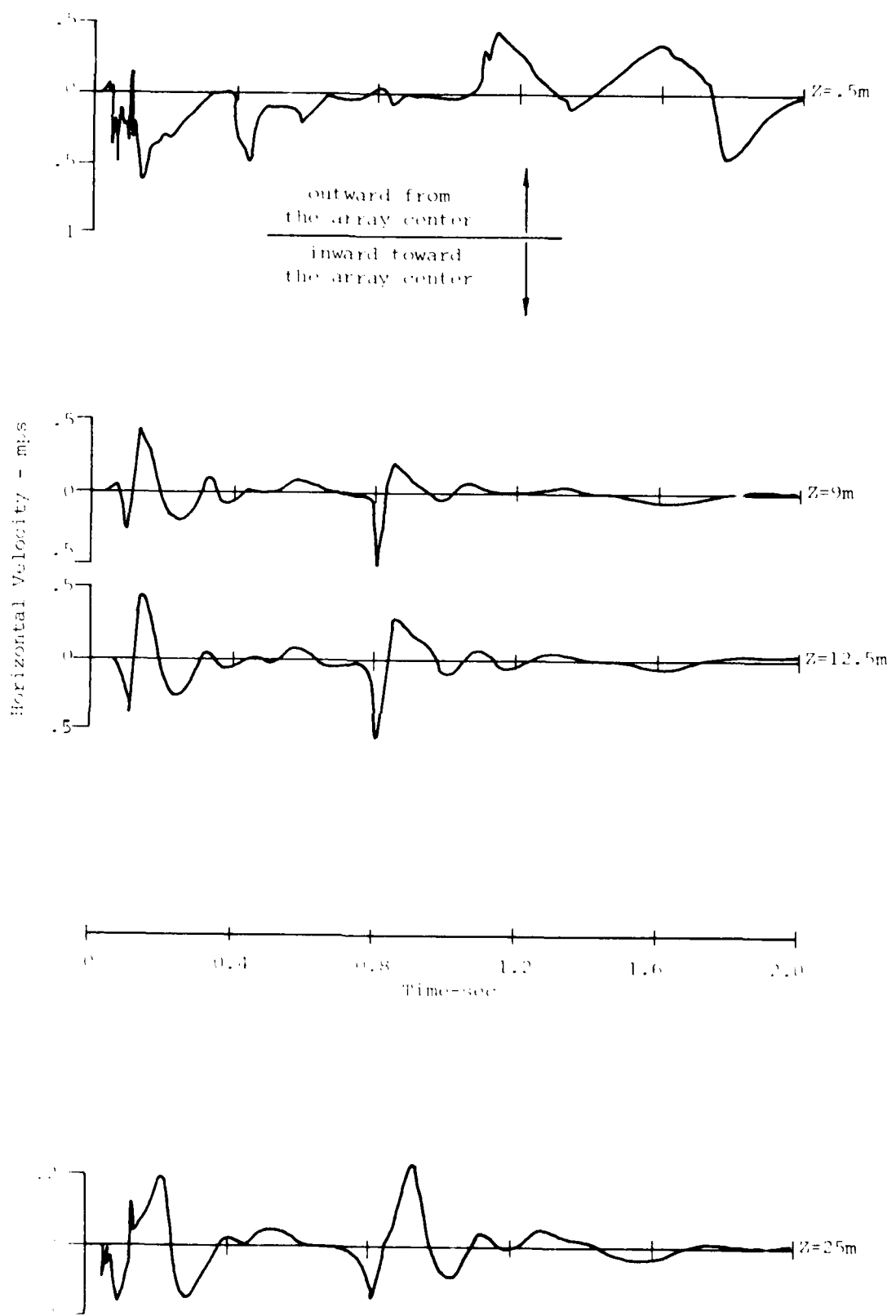


Figure 72. Horizontal Velocity Waveforms at the 25m Range on the Charge Line

Motions at the greater depths are initialized by airblast induced motions from above as well as upstream effects traveling in the soil. Following these initial motions, the oscillatory component begins. This oscillatory motion is interrupted by an uncharacteristically sharp and large magnitude upward and inward (toward the array center) signal at approximately 800 msec. Following this signal the oscillatory motion continues and complete the waveform

The signal at 800 msec can be traced from the greater depths up to the surface at most locations inside the charge array. Due to the widespread presence of this signal and its large magnitude, a study of its behavior was performed to determine if it was peculiar to this particular site geology and experiment geometry or if it was a more general multiburst effect which might be expected for a full-scale site. For purposes of study, two readily identifiable quantities were identified. These quantities were peak-to-peak particle velocity and the time-of-peak. Graphical definition of these quantities are shown on Figure 73. Since the presence of the signal is most dramatic on the waveforms measured at the 9 m, 12.5 m, and 25 m depths the following discussion will be limited to these depths.

Figure 74 presents the time-of-peak versus azimuth and range at the 12.5 m depth (this depth was chosen because it was the best instrumented of the three depths of interest). This figure shows that there is no apparent timing

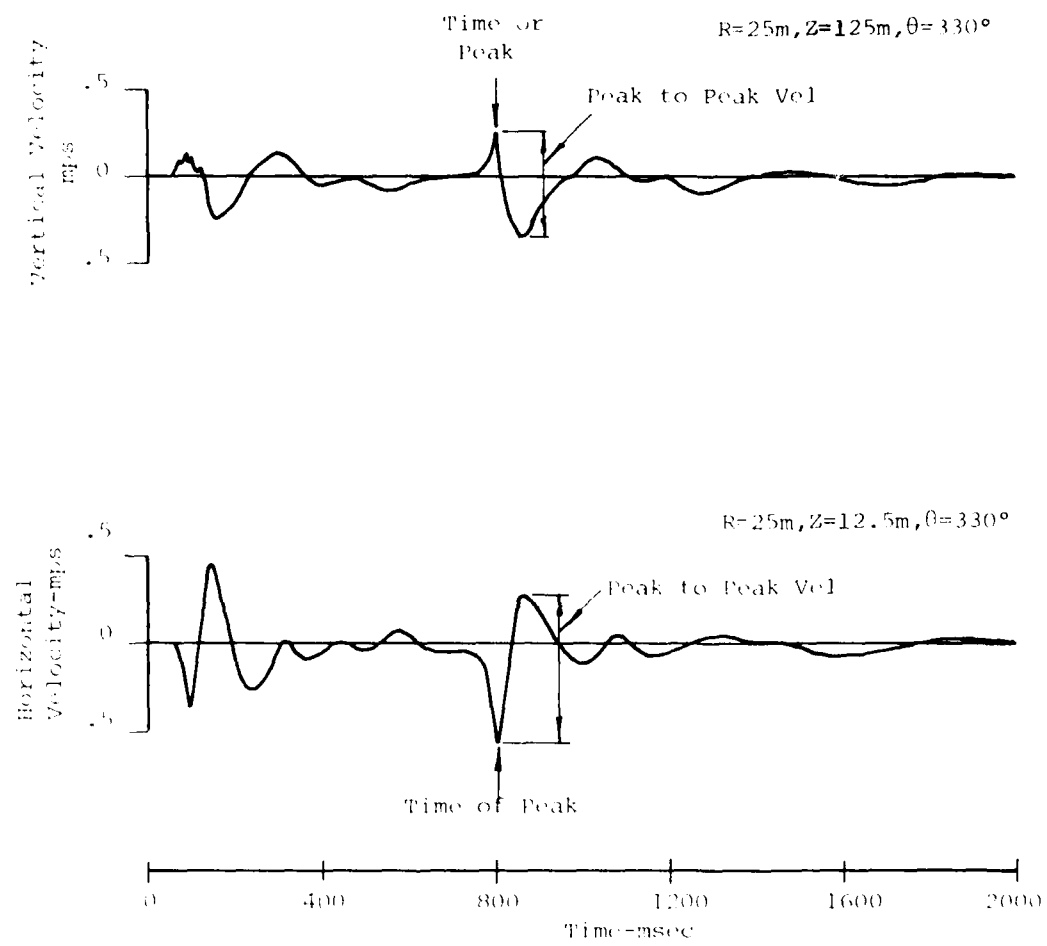


Figure 73. Definition of Time and Peak Values of "800 msec Signal" MBI-2

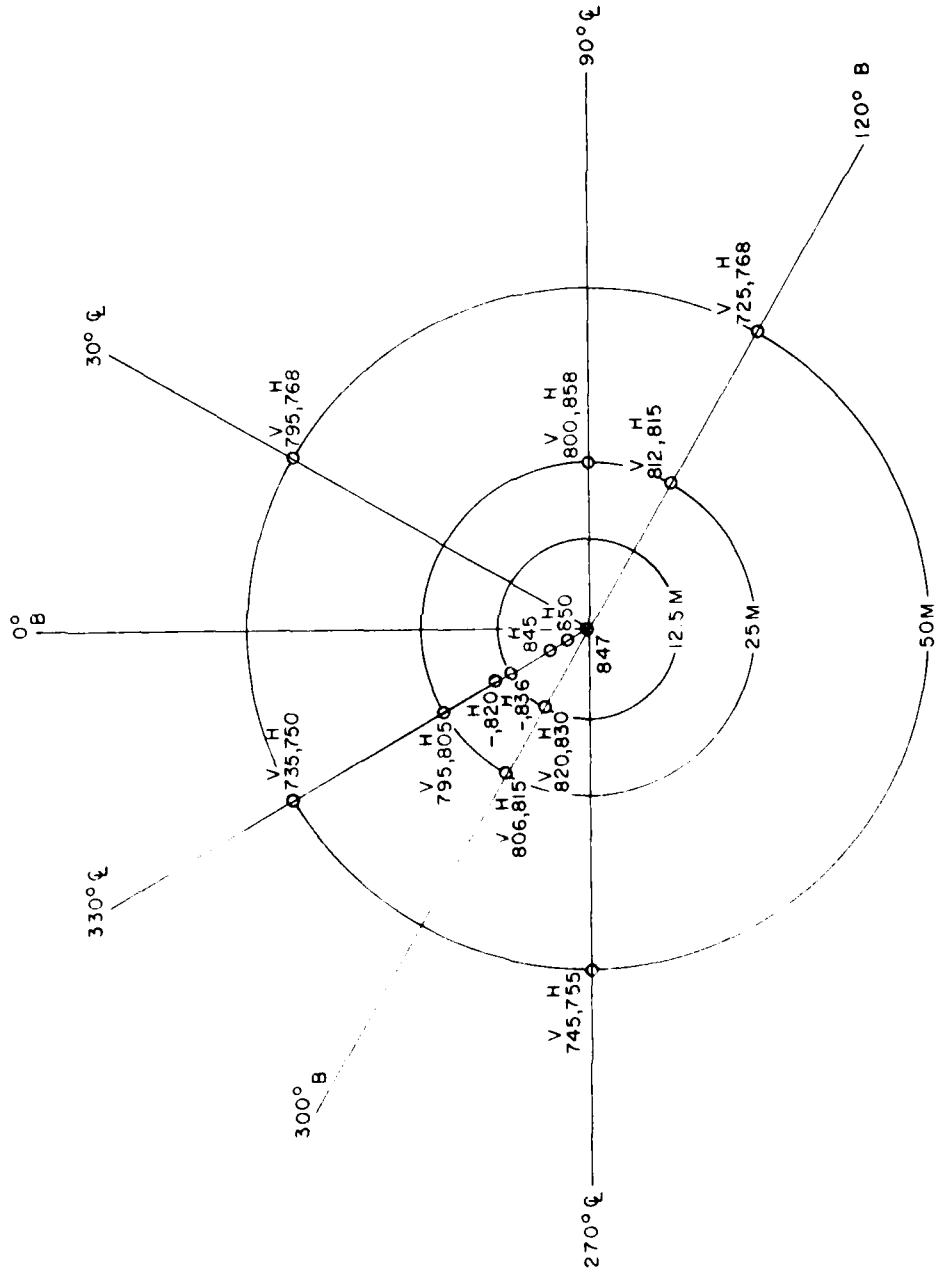


Figure 74. Azimuthal variation of peak (msec) for "800 msec Signal"
MBII-2 - Z=12.5m

dependence on azimuth and that the signal is traveling toward the array center.

Time-of-peak versus depth for various ranges are shown in Figure 75. This figure illustrates that the signal is propagating upward and that the apparent upward propagation velocity is decreasing as the array center is approached. This appears to be due to the signal in the lower more competent material "outrunning" the signal in the less competent shallower material.

Figures 76 and 77 illustrate the behavior of the time-of-peak versus range for vertical and horizontal motions. At the 25 m depth the apparent inward propagation velocity is approximately 1250 mps toward the array center. At the 9 and 12.5 m depth the apparent inward propagation velocities are 400 mps to 600 mps. The horizontal velocity data shown in Figure 77 generally exhibit the behavior shown by the second group described above.

A summary of the timing behavior of this signal is:

- there is no azimuthal variation;
- the signal is propagating upward toward the surface; and
- the signal is propagating inward toward the array center.

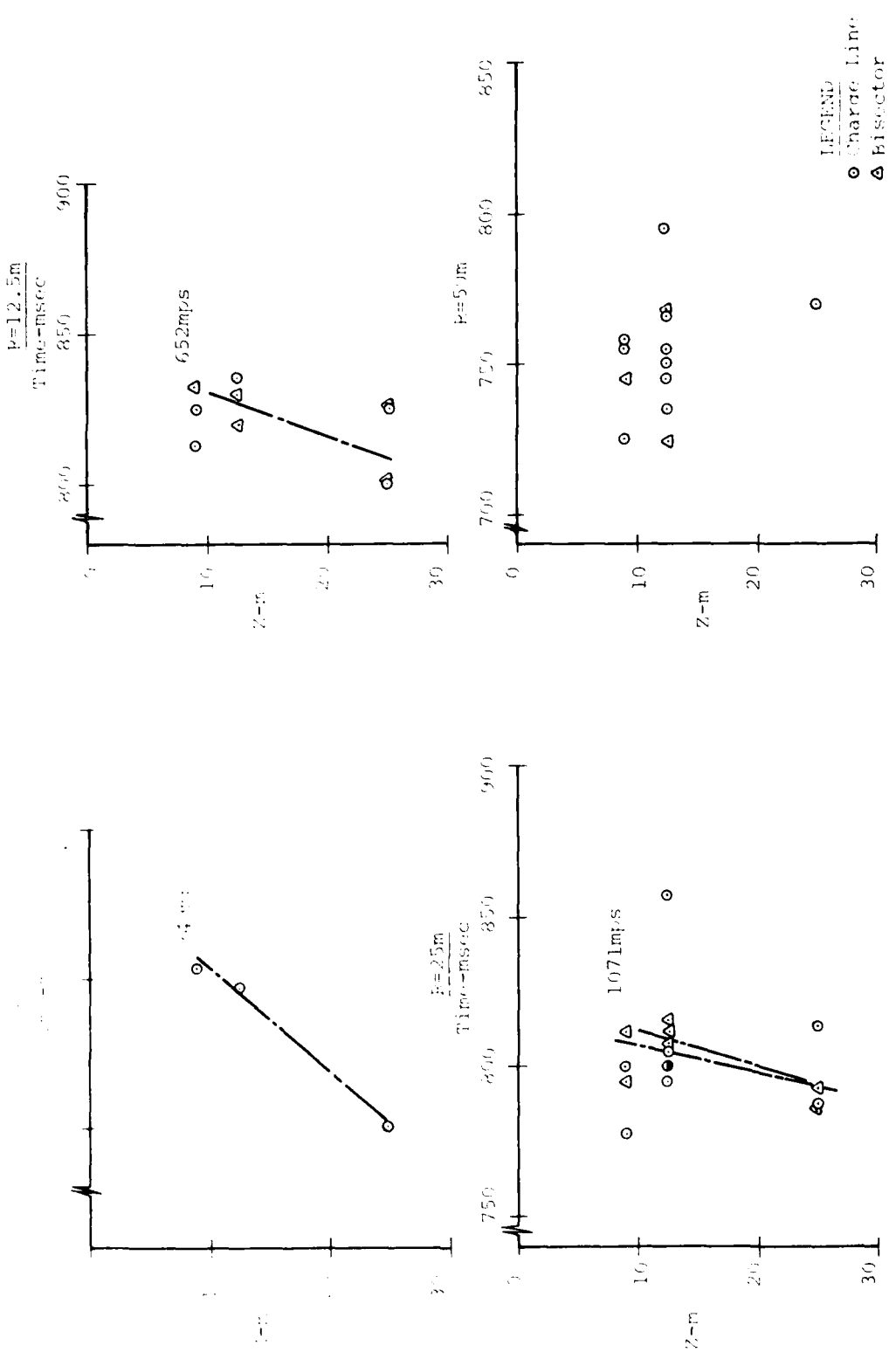


Figure 75. Time-of-Peak vs Depth - "800 msec Signal" MBII-2

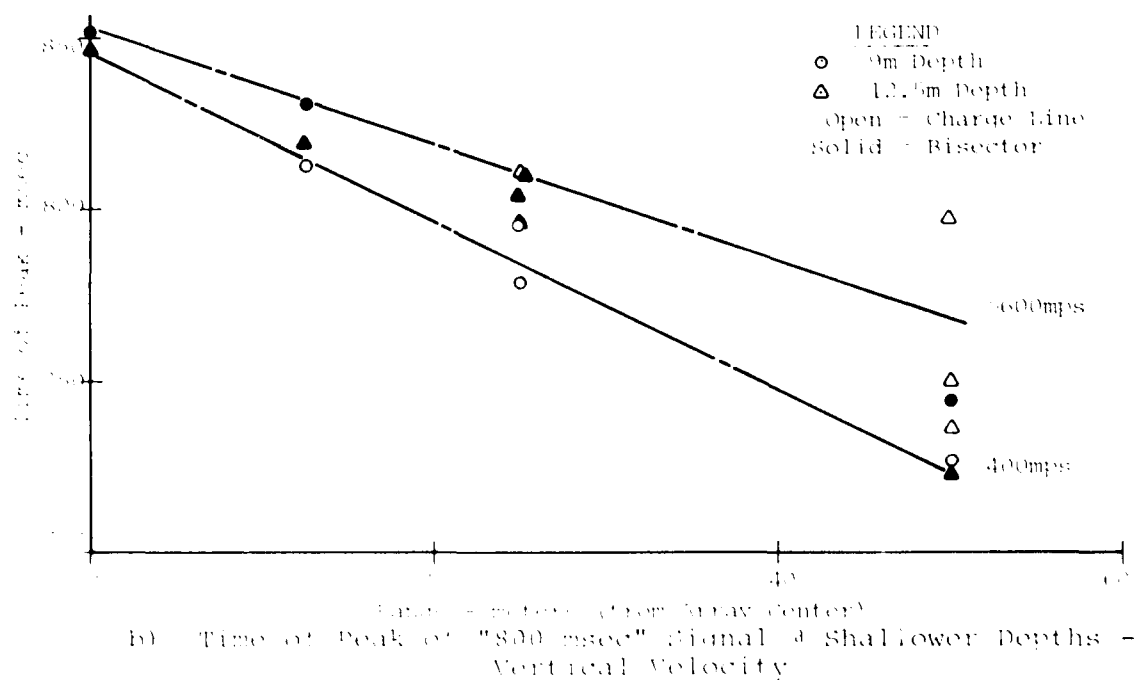
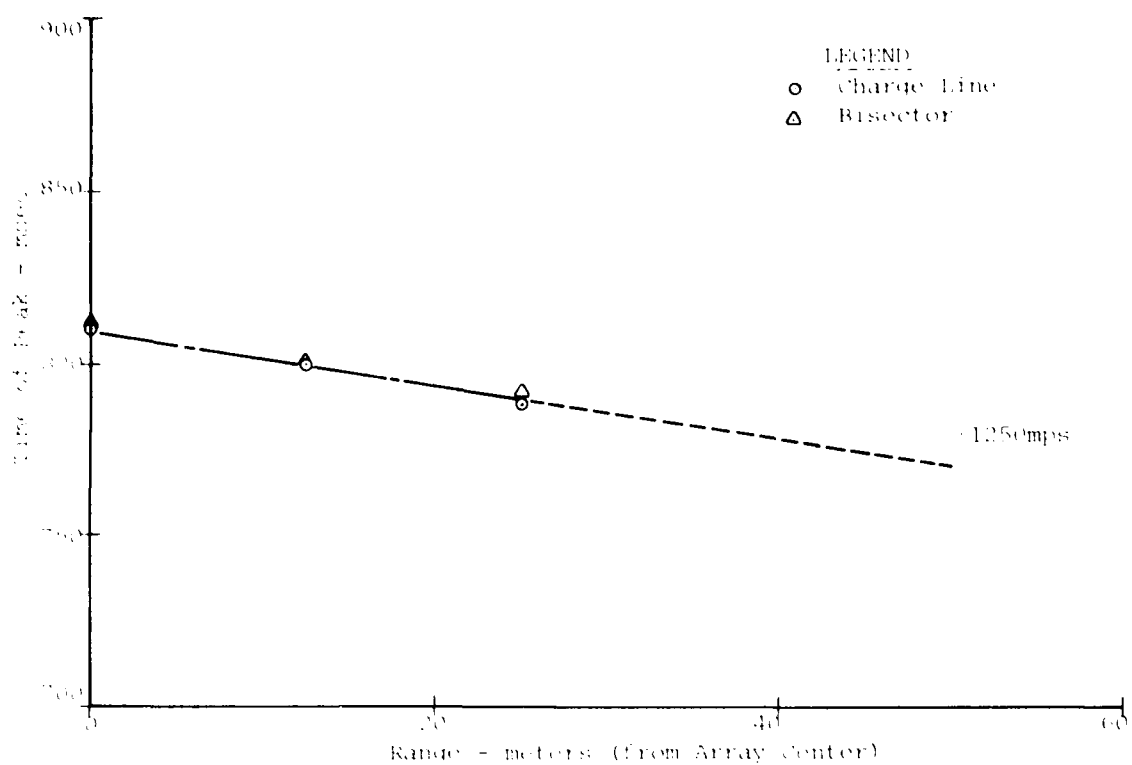


Figure Ten. Timing of "800 msec Signal" - Vertical Velocity

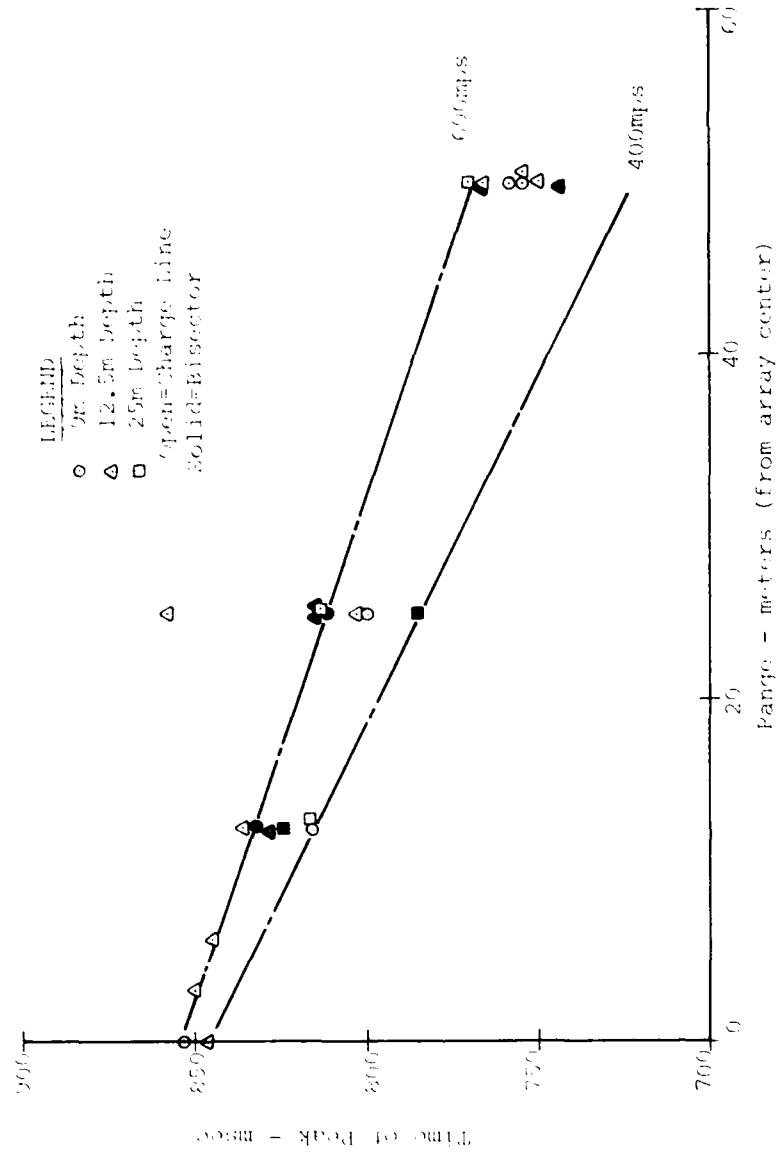


Figure 77. Time of peak of "800 msec Signal" - Horizontal Velocity

The behavior of the peak-to-peak magnitudes of this signal for vertical and horizontal velocities are shown in Figures 78 and 79, respectively. The vertical motion increases in magnitude as the array center and the ground surface is approached. This increase is more dramatic at the shallower depths. The horizontal data show more scatter but also increase as the array center and ground surface is approached. This increase in magnitude toward the array center may indicate a convergent effect due to the test geometry.

Another observation concerning the behavior of this signal is illustrated by Figures 80 and 81. These waveforms show a relatively strong -lg slope through the signal. This -lg slope and the waveform are indicative of a material which has spalled. This -lg slope is felt to imply a layer separation somewhere below this depth.

There are two major pieces of evidence which support the theory of layer separation. The first, comes from the site profile (Fig. 5) for this experiment. At a depth of approximately 26 m is a p-wave velocity interface. This is indicative of a change in material and a potential plane of weakness. The second piece of evidence is shown on Figure 82. This figure shows that the motion below the interface (48.5m) is similar in magnitude and character, but opposite in direction to the motion above the interface.

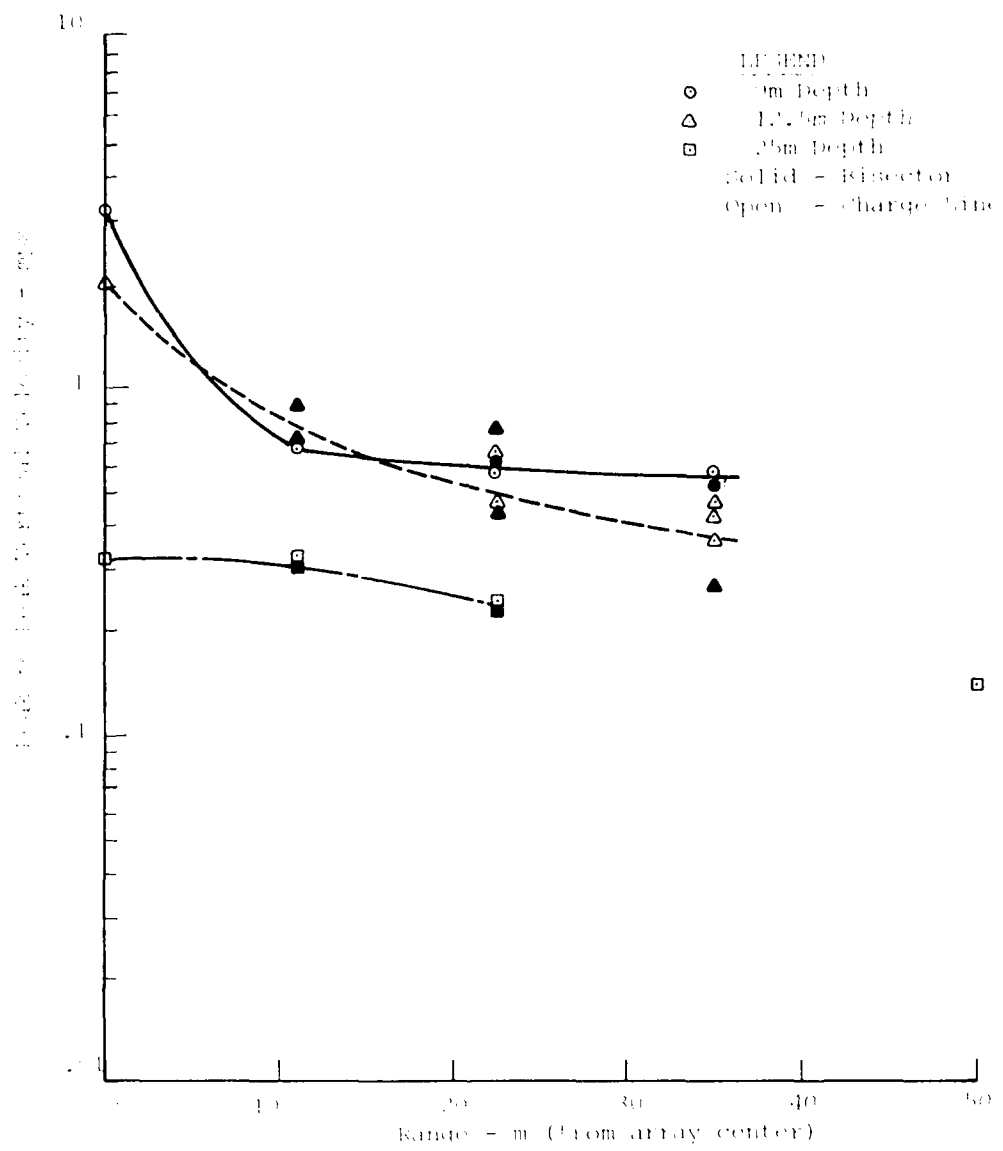


Figure 78. Peak-to-Peak Magnitude of "800 msec signal" - Vertical Velocities

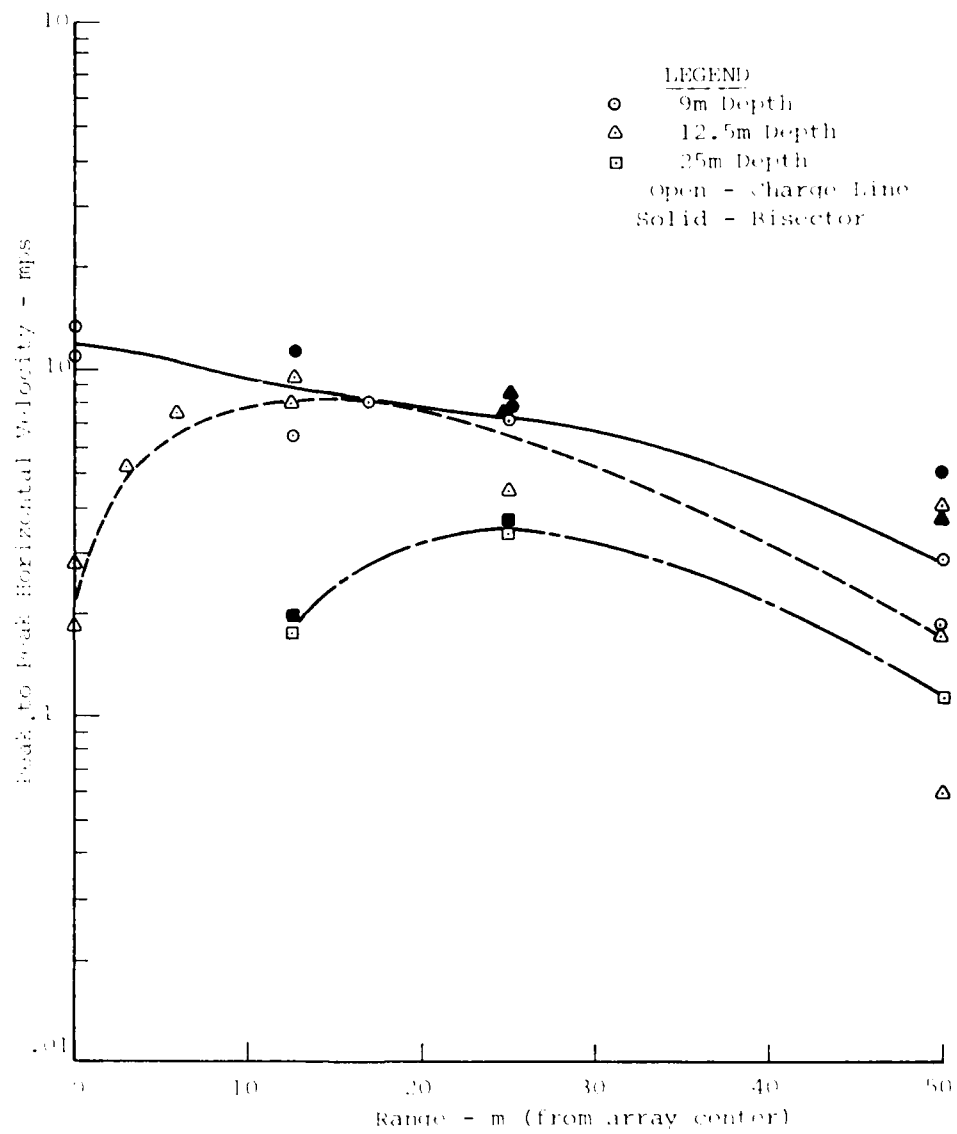


Figure 79. Peak-to-Peak Magnitude of "800 msec Signal" - Horizontal Velocities

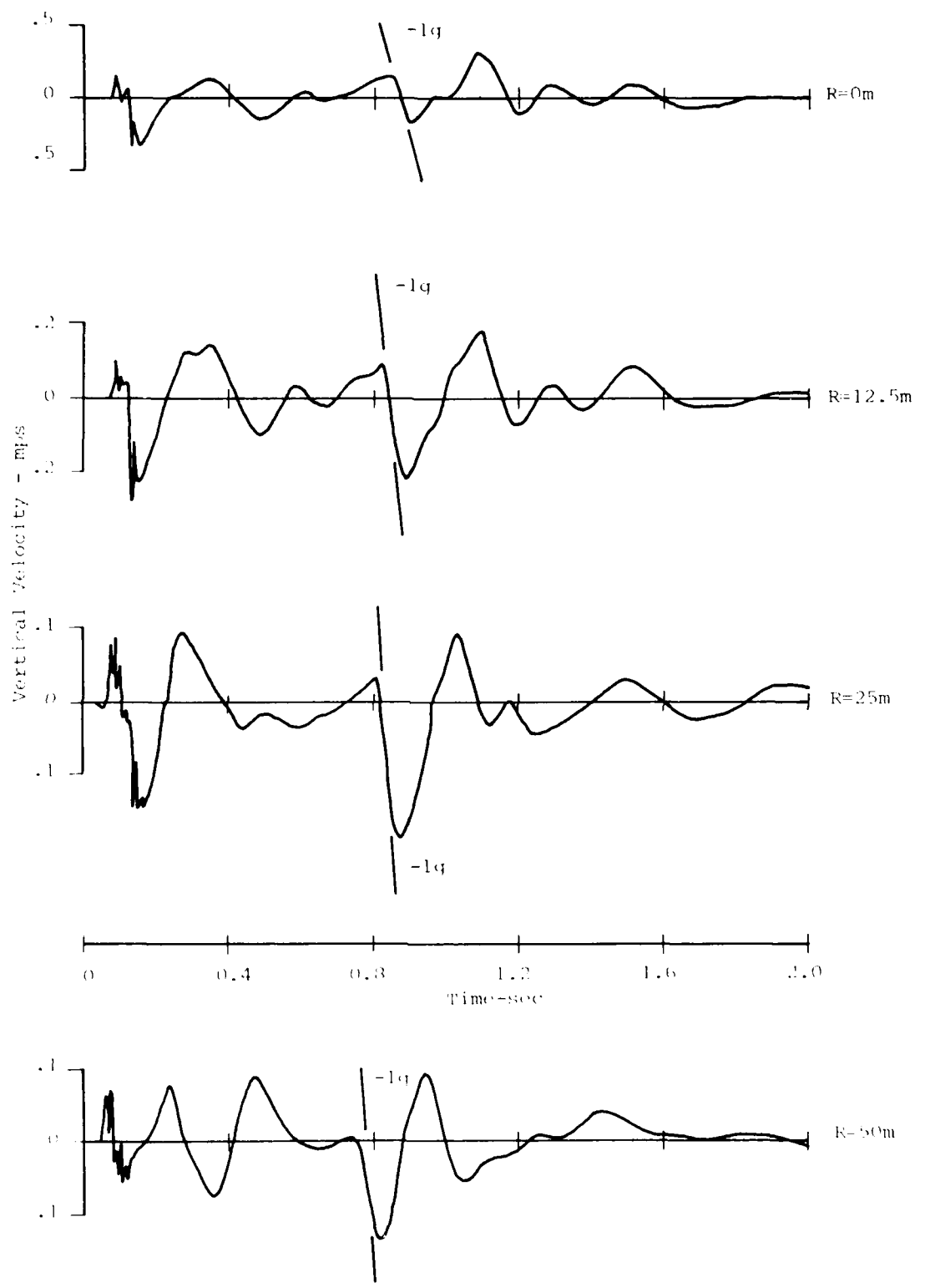


Figure 80. Vertical Velocity at the 25 m Depth - Charge
Radial MBII-2

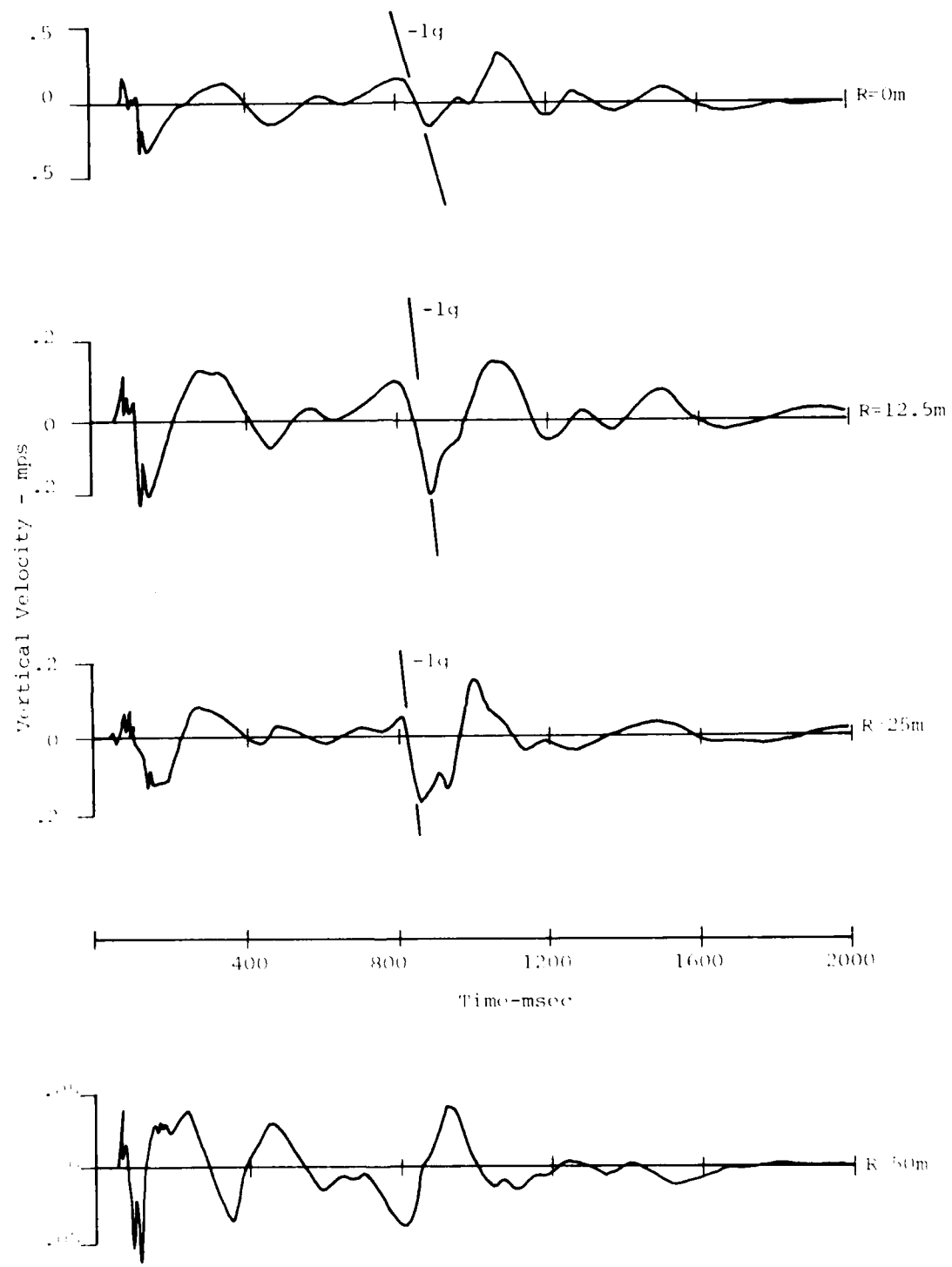


Figure 81. Vertical Velocity at the 25 m Depth - Bisector MBII-2

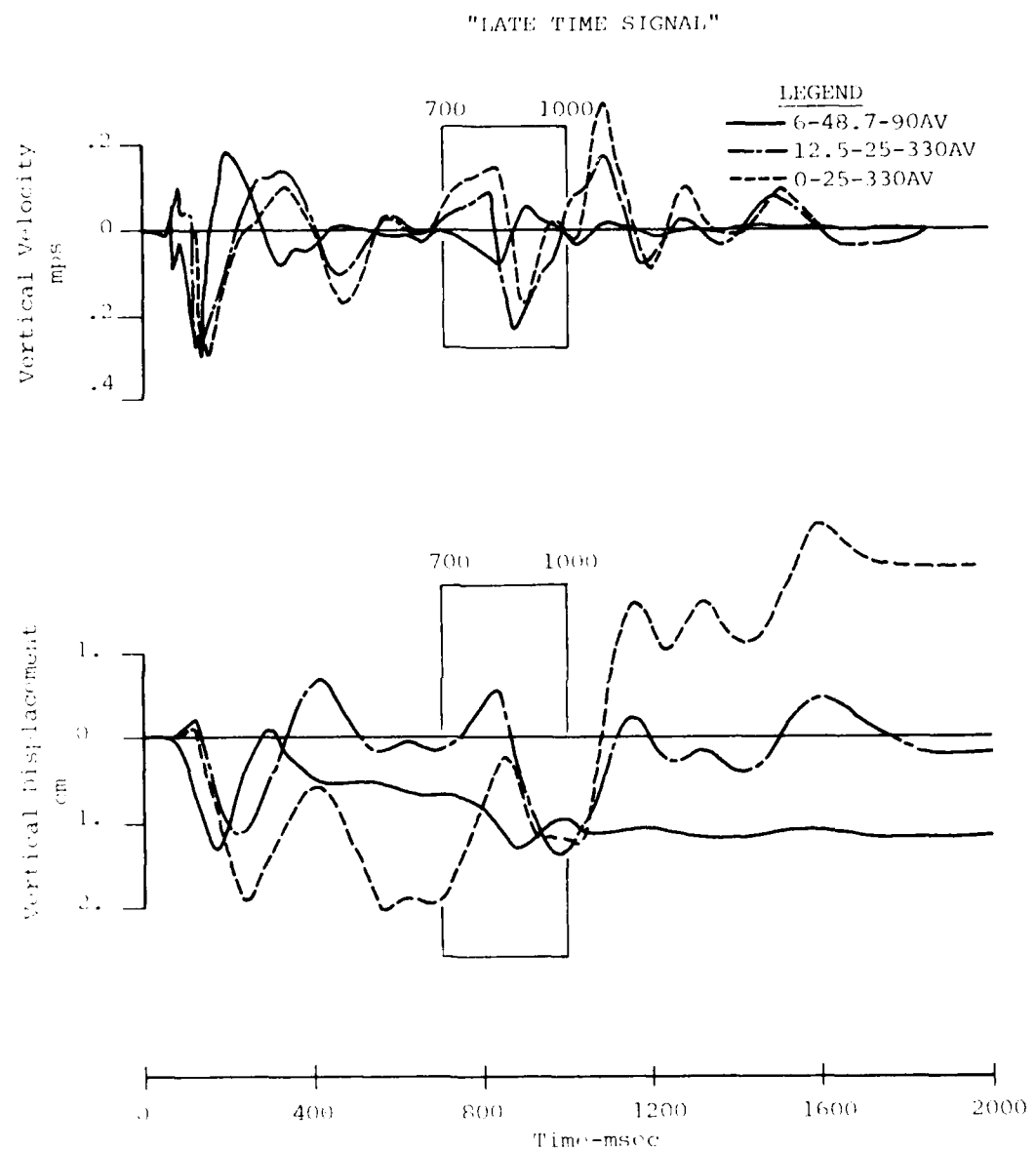


Figure 82. Motions at and Below 25 m Depth

The mechanism responsible for this signal is believed to be the addition of Rayleigh waves from the individual charges. The supportive evidence for this theory is the fact that in the preparation of the superposition waveforms for these depths, the Rayleigh wave motions from the individual charges were near exact in phasing. This was producing relatively large late time motions at approximately 600 msec. When the timing of the superposition waveform were corrected for the differing rock elevations between MBII-1 and MBII-2 (See Sec. 3. .3.3 for discussion of this correction), this relatively large magnitude Rayleigh motion was moved to the 800 msec time frame. The character of the superimposed motions are not as sharp as the MBII-2, but there is no way to predict the effect of separation on the waveforms. The magnitude of the superimposed signal was somewhat lower than that seen in the data which may indicate a nonlinearity in the addition of these low frequency motions, or the effect of the material separation upon the magnitudes. (Theoretical discussion of convergent Rayleigh Waves may be found in Ref. 22).

3.3.3 Airblast Results

The airblast environment for the multiple burst experiment was predicted with the Low Altitude Multiple Burst Model (LAMM, Ref. 22) developed at the Air Force Weapons Laboratory. LAMM models the nonlinear characteristics of the atmosphere combining overpressures of multiple nuclear

bursts. Although LAMB was developed for predicting nuclear events, it was felt to provide a reasonable prediction for the HE Misers Bluff event, if the rule-of-thumb assumption is made that HE is twice as effective as NE in producing air-blast. (This is generally accepted practice below the 2.0 MPa overpressure level.)

Peak pressures from MBII-1, MBII-2, and LAMB are shown in Figure 83. The peak pressure in the multiple burst experiment is a maximum at the array center and decreases to a minimum at the 25 m range. At ranges greater than 25 m the peak pressure begins to increase in magnitude again as the nearest single charge begins to dominate. Outside the charge array, peak pressures attenuate similar to the single burst experiment. The LAMB predictions are low near the array center, ranging from about a factor of 6 at the center to a factor of 2 at a range of 12.5 m. Beyond this range the LAMB prediction is reasonably good both inside and outside the charge array. Although LAMB is low near the center, the character of the prediction is similar to the data and in both the data and LAMB there seems to be little difference in peak pressure between the bisector and the charge line. Reasons for the failure of LAMB and empirical fixes to LAMB have been discussed extensively by others (e.g., Refs. 24 and 25).

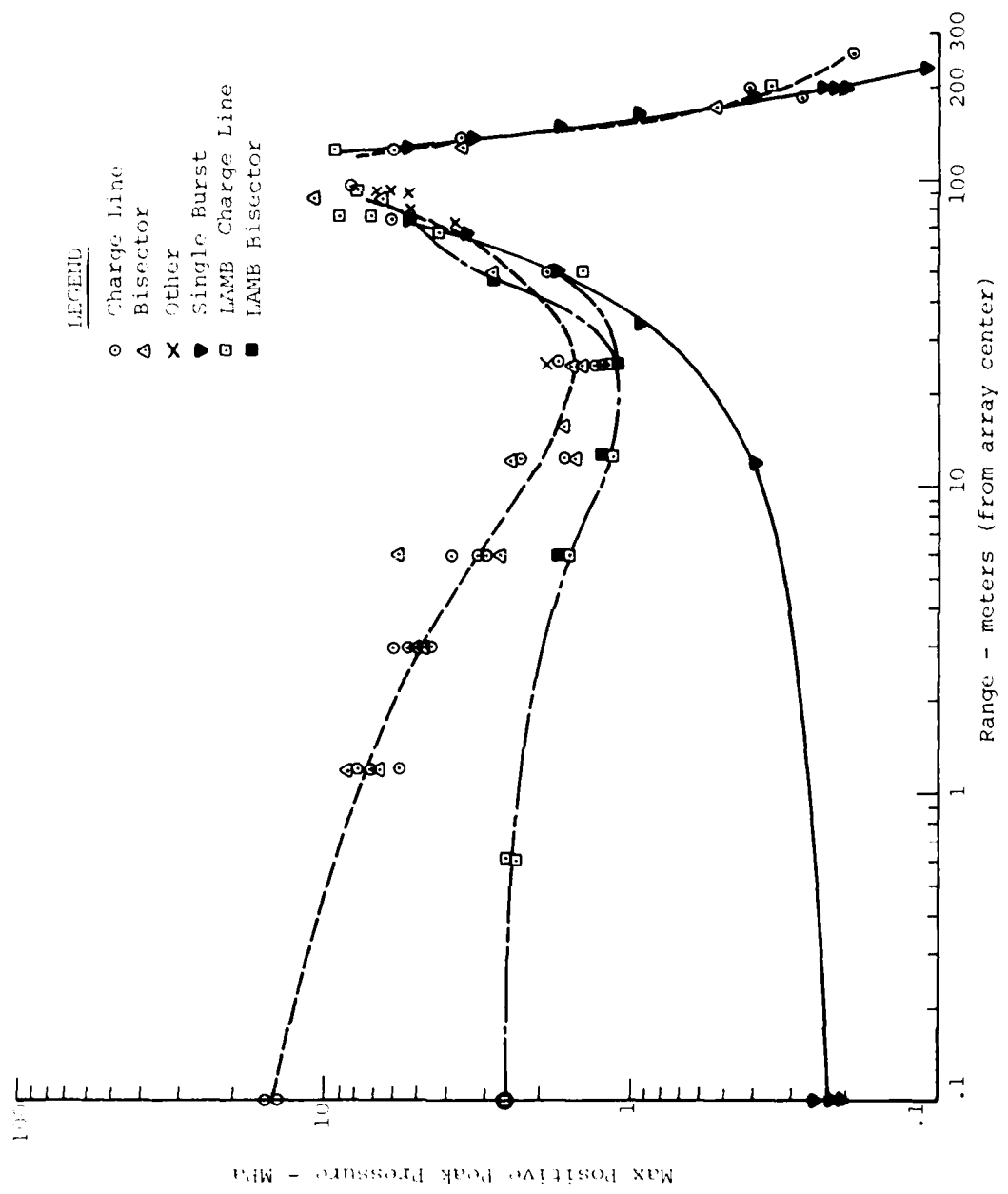


Figure 83. Peak Pressure vs Range for MBII-2

Peak overpressure impulse vs range is shown in Figure 84. The behavior here is somewhat different than the peak pressures in that there are more distinct differences in the charge line and bisector, especially as the charge is approached. The bisector, however, is similar to the peak pressure. It is maximum at the center, decays to a minimum at about a range of 25 m and increases again as the charge is approached. Generally there is very little difference in the charge line and the bisector from the array center to the 25 m range. Outside the charge array the bisector and charge line values tend to converge at about the 160 m range. The prediction of impulse from LAMB was considerably better than the peak pressure predictions, consistent with the observation that the pressure wave shape predictions were good, except that only the high frequency peak pressures were not accurately reproduced. Again there was slight underprediction near the center, but the factor was only about 1.4 (as compared with 6 for the pressure). At greater distances from the center, the prediction fell within the data scatter. The difference between the peaks measured on the charge line and the bisector within about 70 m of the charge is not mirrored in the prediction.

3.3.4 Ground Motion

The superposition assumption will be evaluated in the following sections on a component-by-component basis.

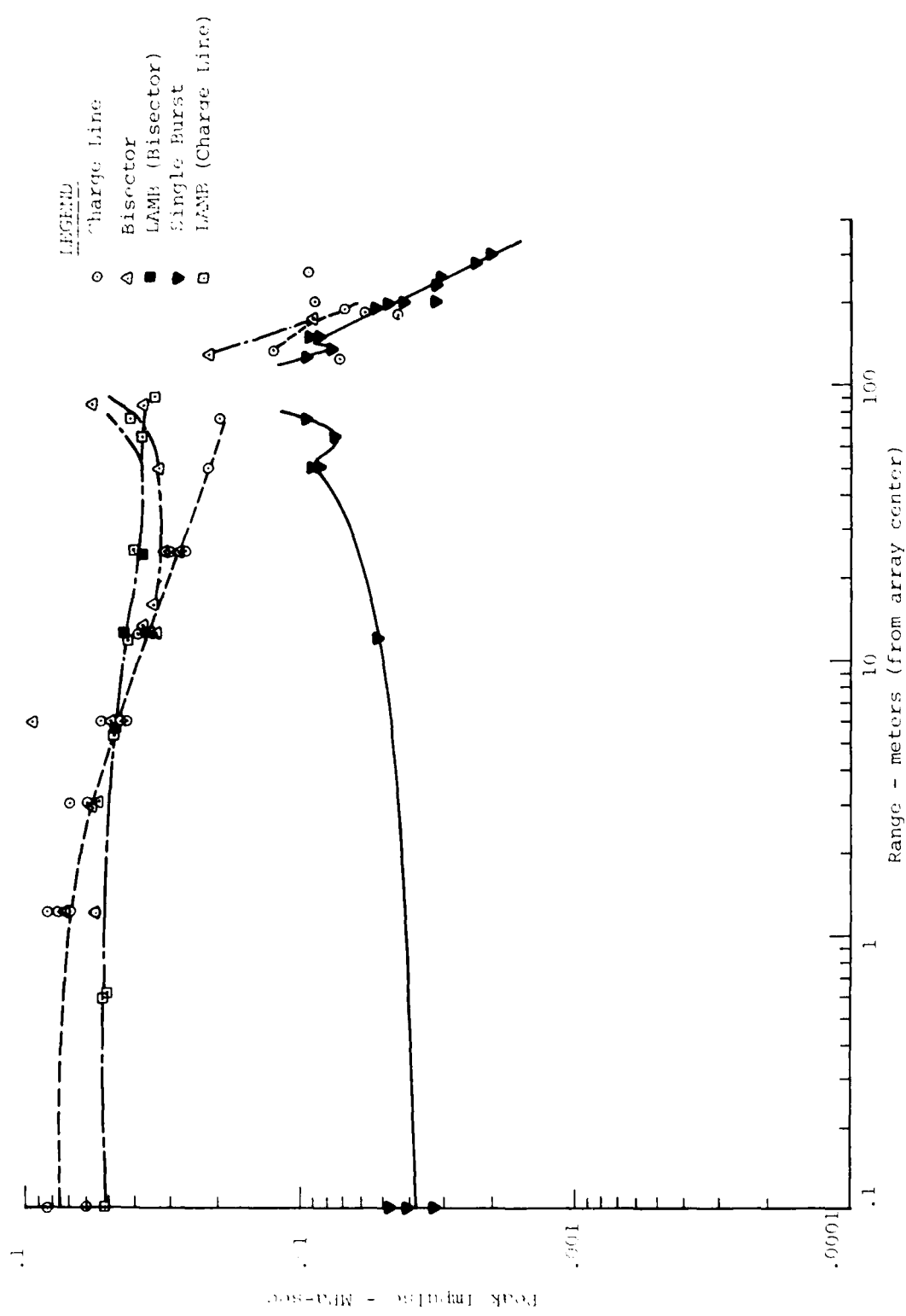


Figure 84. Peak Impulse vs Range for MBII-2

The superposition waveforms from which the following conclusions are based are included in Appendix A. The frequency domain data comparisons are included in Appendix B. The superposition waveforms were determined by the addition of the properly time phased measured single burst effects. The details involved in the production of these waveforms are described in Reference 4.

3.3.4.1 Air-Slap Component of Ground Motion

a) Peaks

Naturally, the airblast waveform measured in the multiple burst environment is somewhat more complicated than the single burst airblast. The multiple shock passages create multiple peaks as well as complex, late-time negative phases. The airblast-induced particle velocities necessarily mirror these complications. To effectively discuss these complexities, the compressive air slap portion of the motion will be divided into the particle velocity changes associated with the first three major compressive phases in the airblast.

Figure 85 shows the change in vertical velocity associated with the passage of the first major compressive phase. Close to the center of the charge

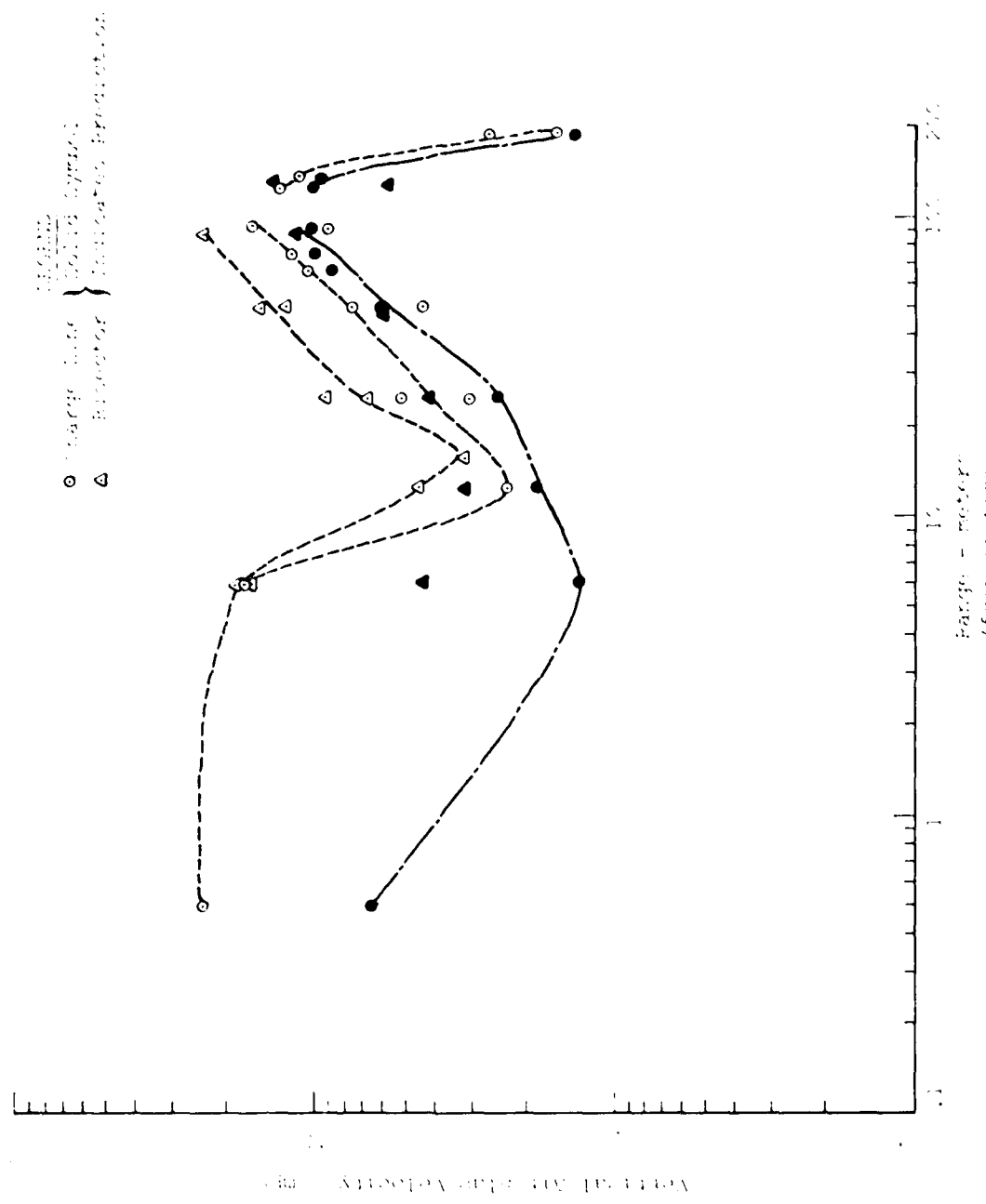


Figure 8i. Vertical Velocity Associated with Passage of the First Compressive Phase of the Airblast - Superposition of Data

array, superposition underpredicts by about a factor of 4. This underprediction is due to the nonlinear interaction of the overhead airblast. The superposition prediction improves as distance from the center is increased. The underprediction varies from about 2.5 at the 12.5 m range to about 1.2 near the charge. Outside the charge array, the prediction is fairly accurate. The underprediction is a maximum of about 1.3. This improvement of the prediction as distance from the center increases should be expected as the phenomenology is becoming dominated more and more by the nearest single charge. In general the charge line target points were better predicted than those on the bisector. This is due to the fact that the bisector is a plane of symmetric interaction of the airblast from two charges. These interactions are nonlinear in nature and therefore, linear superposition of the ground motion effects caused by the single burst airblast should not be expected to be accurate. The charge line, however, is generally dominated (at ranges >25m) by the effects of the nearest single charge and, therefore, superposition is a fairly accurate representation. Outside the array the motion again is much like single burst phenomenology as the shocks are divergent and, therefore, airblast interactions are not as significant.

Figure 86 shows the second and third changes in velocity associated with the second and third major compression phases in the airblast. Generally superposition underpredicts these peaks to a greater degree than the

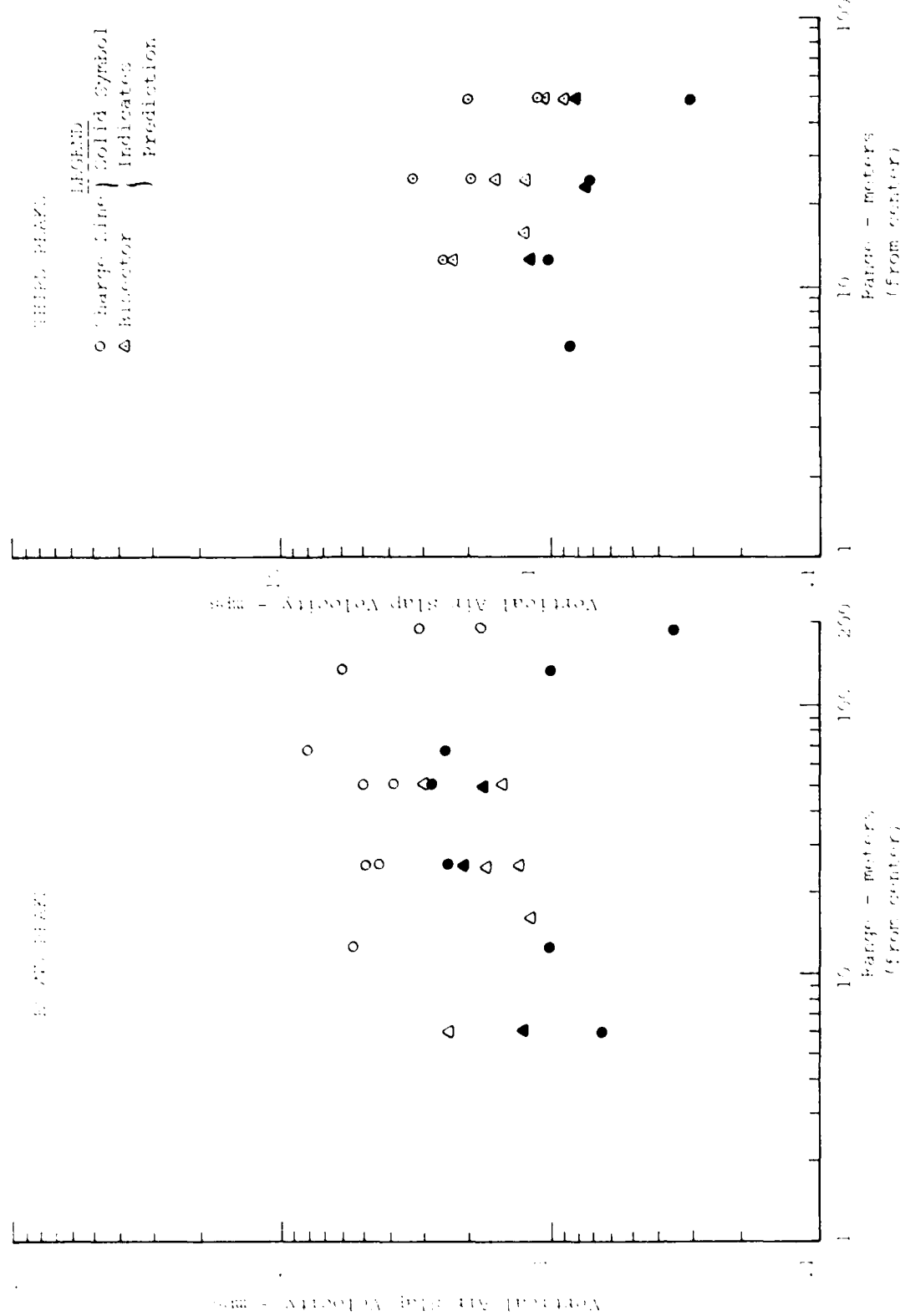


Figure 86. Vertical Velocities Associated with Passage of Second and Third Compressive Phases of the Airblast

first peak. The first possible explanation for the relatively large secondary and tertiary peaks that was explored was, that since they occur when the material was in a dilated state (due to the negative phase of the airblast from the closest charge), small changes in pressure would result in relatively large changes in velocities. A study of the data showed that the scatter and attenuation of the first, second and third charges in pressure vs the respective changes in velocity were essentially the same. The behavior is now thought to be related to the changing material properties at the two sites. MBII-1 was conducted where the near-surface highly compressible silt was of maximum depth at the charge and tapered up to a depth of less than 0.5 m at the 100 m range. Interior to the charge array on MBII-2 the silt layer was greater than 0.5 m in depth. Therefore, superposition predictions which required data from ranges greater than 100 m reflect the behavior of the sand rather than the silt. Since the silt is more compressible than the sand, it should show higher velocities as in the MBII-2 waveforms.

Figure 87 shows the first and second air slap peaks for the horizontal velocities. Scatter for the first peaks are fairly large and superposition is generally within the scatter both inside and outside the array. Secondary peaks were also generally within the data scatter

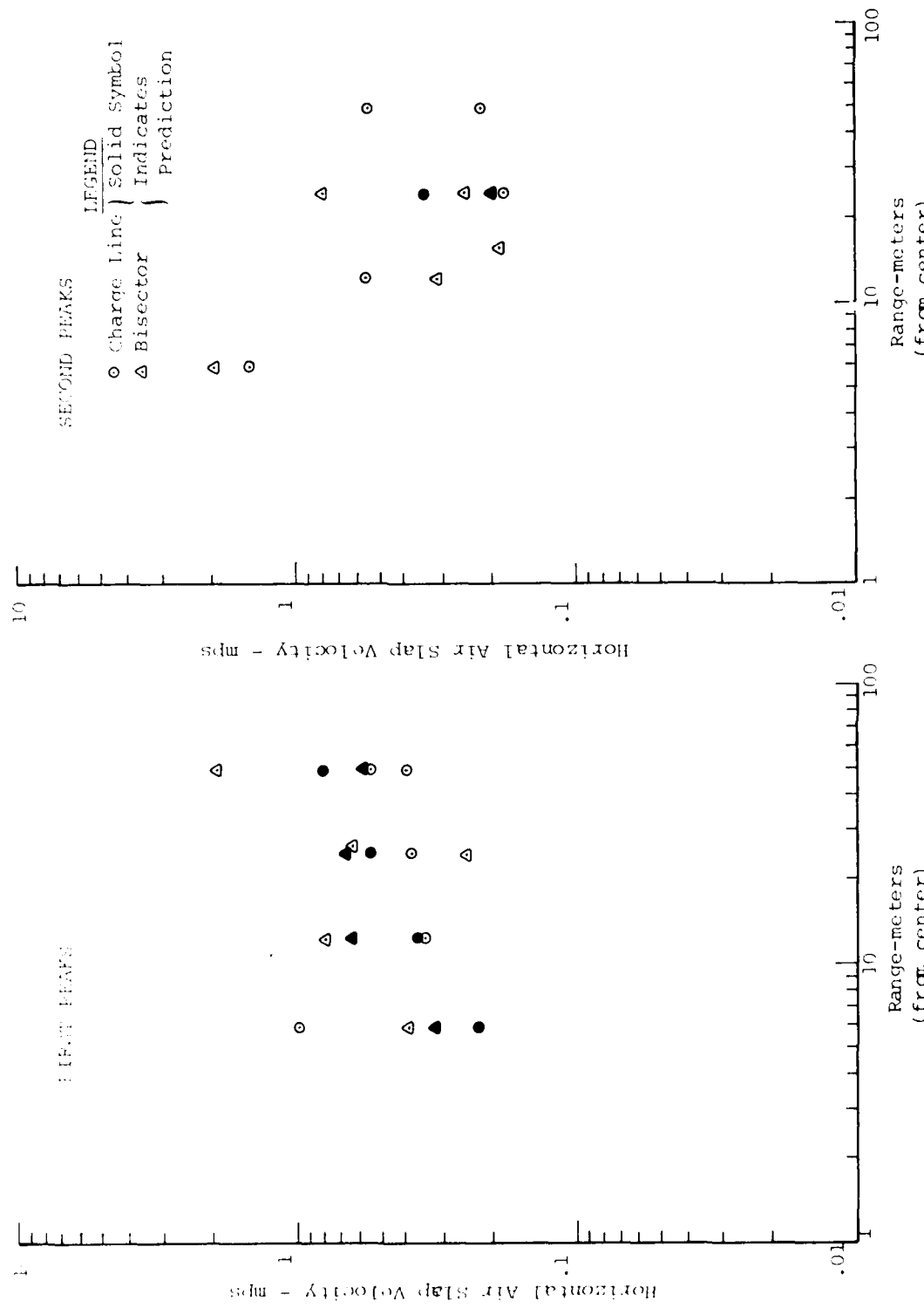


Figure 87. Horizontal Velocities Associated with Passage of the First and Second Compressive Phases of the Airblast

although secondary peaks in superposition were difficult to isolate, possibly for reasons postulated above for the verticals (i.e., secondary air slap peaks in superposition waveforms were measured in the sand rather than the silt).

Upward velocity peaks are compared in Figure 88. These peaks are due to the negative phase (airblast) effect plus upstream and convergent effects. The peak value of this portion of the air slap component was generally predicted within a factor of 2. The tendency of superposition appears to be one of underprediction. In terms of peak velocities, superposition appears to be reasonably accurate.

Upward displacement peaks associated with the upward velocity discussed above are also shown in Figure 88. The tendency is for underprediction. Generally this underprediction is a factor of 3 or less. The fact that displacements are more poorly predicted than the velocities is an indication that the duration of the upward velocity is somewhat longer in the data than in superposition. The duration may in fact be the only factor in which the multiple burst negative phase airblast is enhanced.

b) Waveforms

Waveform comparisons of the air-slap component for selected locations are shown in Figures 89 and 90. The vertical waveforms shown in Figure 89 illustrate what was discussed about the peaks earlier, i.e., underprediction close to the array center and underprediction of the

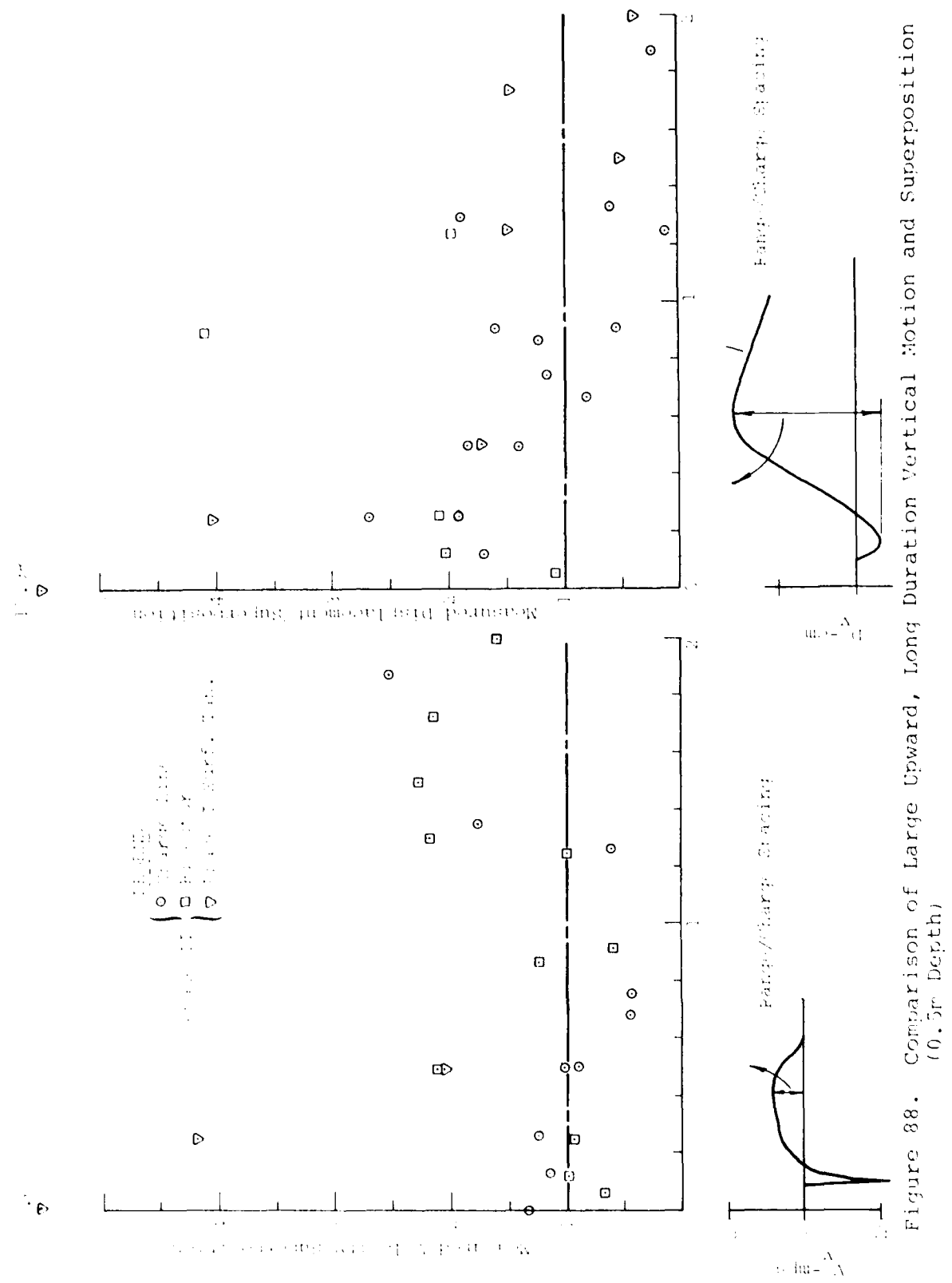


Figure 88. Comparison of Large Upward, Long Duration Vertical Motion and Superposition
(0.5m Depth)

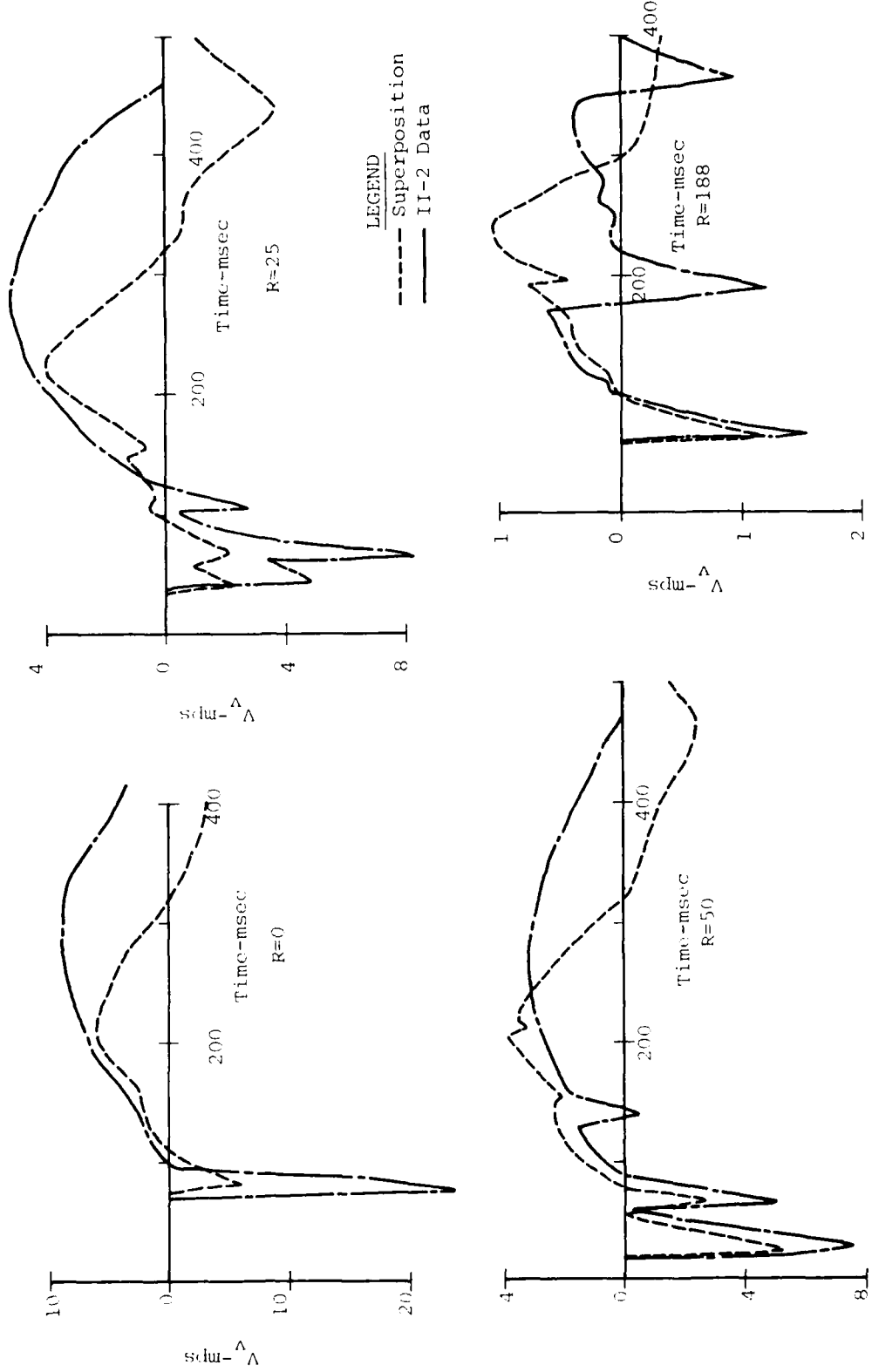


Figure 89. Comparison of Superposition and MBII-2 for Vertical Velocity Air-Slap Component

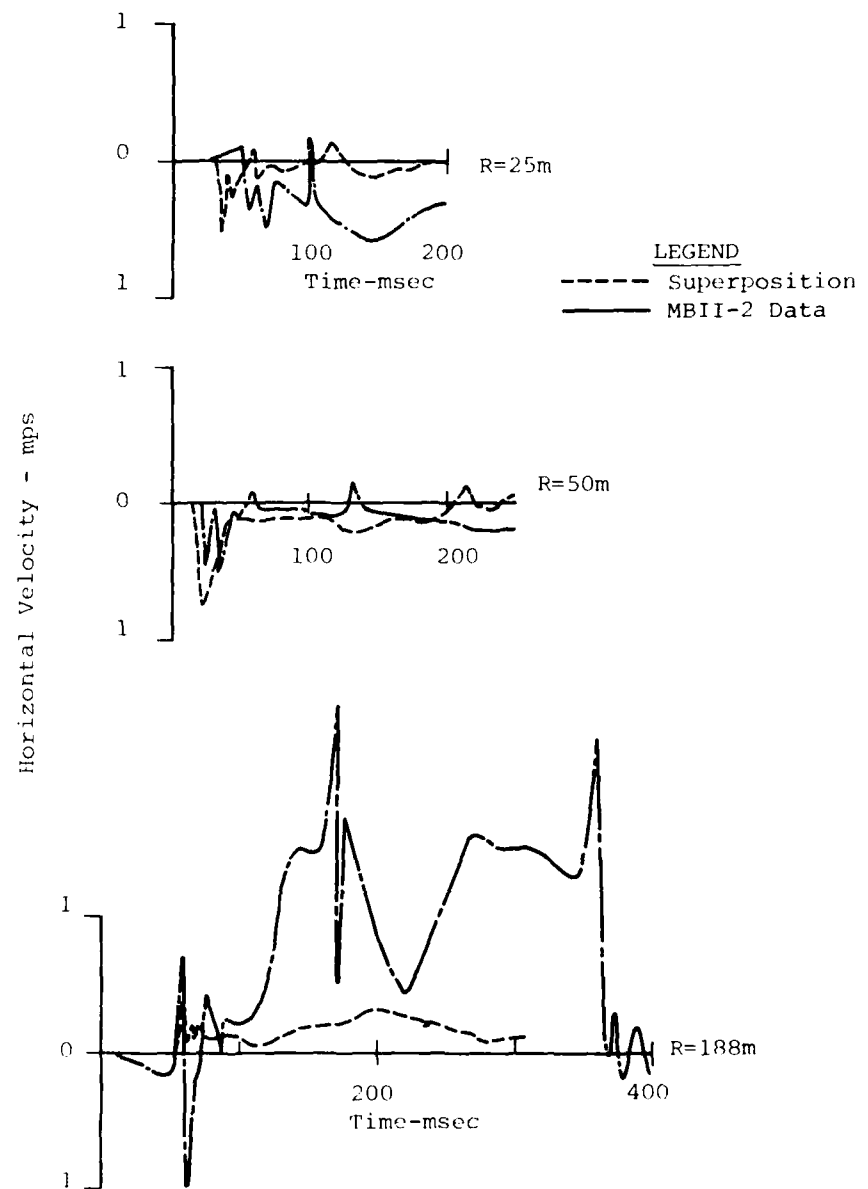


Figure 90. Comparison of Superposition and MBII-2 for Horizontal Velocity Air-Slap Component

secondary compressive phases at all ranges. The duration of the upward velocity pulses are somewhat longer in the data while peak values are roughly the same. Comparisons of the horizontal waveforms (Fig. 90) bear out what was said concerning peak values. From the waveform at 188 m it can be seen that secondary arrivals of the compressive phases also have a larger effect than is predicted by superposition. It is also seen that in the time frame of negative phase effects in the vertical motions, the horizontal motions are not significantly affected (this can be seen by comparing Figs. 89 and 90). The horizontal motions appears to be more controlled by upstream effects than by the negative phase of the airblast.

c) Evaluation

The vertical downward air-slap velocities were most poorly predicted near the center and superposition as a predictive model improved substantially as range from the center increased. The tendency of superposition was to underpredict by a factor of 2.5 to 4 near the center. This is the result of nonlinear interaction of the overhead airblast. The upward portion of this signal was predicted more accurately than the downward because the single burst waveforms experienced dilation or spall beyond 100 m. As distance from the center increased, superposition underpredicted by a factor of 2. Although magnitudes of

velocities were predicted accurately, displacements of this upward motion were substantially underpredicted by superposition (as much as a factor of 5 but generally 3 or less).

The magnitude of this under-prediction could be reduced if the free fall seen in the single burst data is maintained after the amplitude modification. An example of this is the superposition prediction at the array center. The magnitude of the waveform was multiplied by 6. This produced a -6g downward acceleration where the material should be in free fall. If this -6g acceleration is corrected to a -1g acceleration, the duration is increased, and thus the upward displacement. The major problem associated with this correction is that the criteria for rejoin of the material (termination of the -1g acceleration) is not straight forward. Therefore, no general rules can be given for this correction procedure. Each case must be handled on an individual basis and the judgement of the predictor plays a major role in the procedure.

Horizontal velocities were generally predicted within the data scatter as far as the compressive phase of the airblast. Horizontal velocities do not seem to exhibit a large effect of the negative phase airblast.

Superposition did not predict the effects of the secondary airblast peaks as well as the initial arrival. The reason for this is believed to be the result of the variable thickness silt and, therefore, should not be factored into the prediction procedure.

3.3.4.2 Crater Related Component

As discussed previously, airblast negative phase effects (pore air expansion) appear to dominate the vertical velocity waveform in the time frame of crater related effects. This makes it virtually impossible to study the crater-related component in the vertical waveforms. However, pore-air expansion does not appear to have a large effect on horizontal waveforms. Consequently, only horizontal motions will be included in the study of crater-related effects.

a) Peaks

Magnitudes of the horizontal crater-related velocity component are shown in Figure 91. Ratios of data to superposition are plotted vs range from the center. As can be seen the tendency was for superposition to underpredict, although this underprediction was never more than a factor of 3.

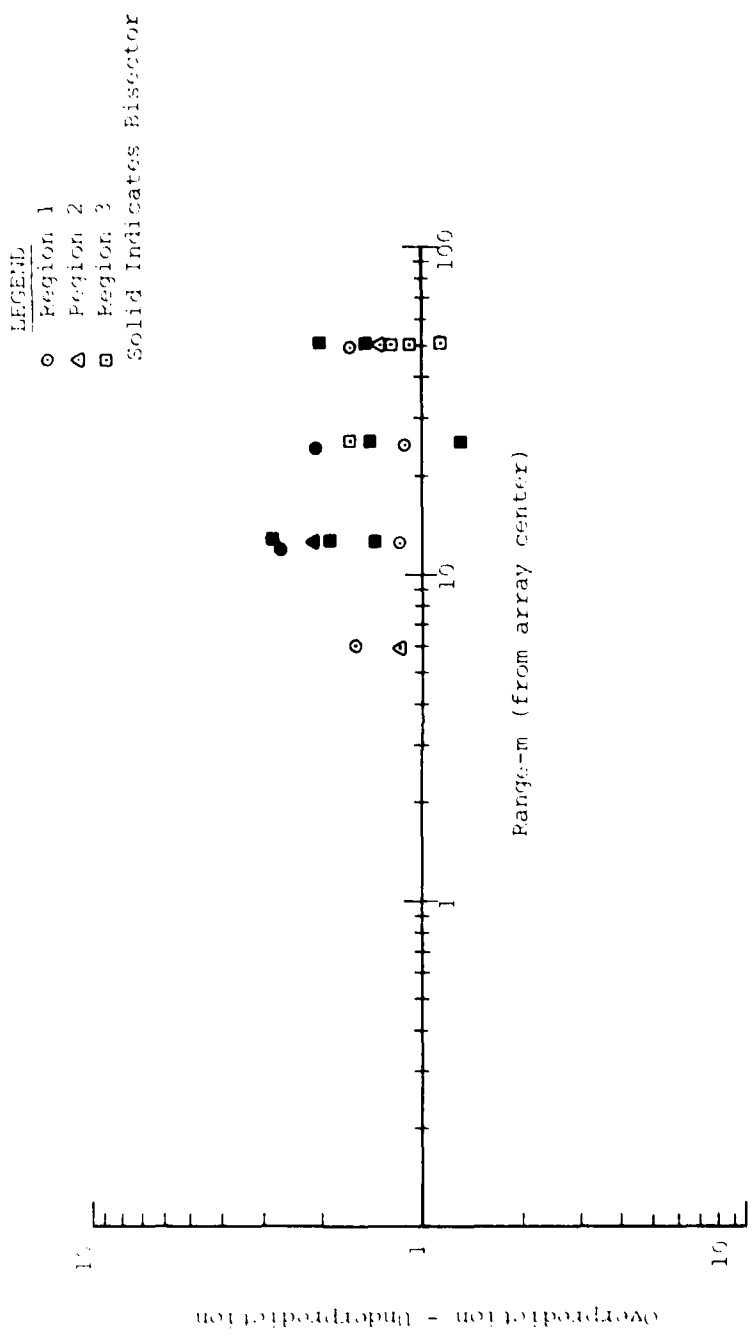


Figure 91. Evaluation Plot of Superposition for Horizontal Crater Related Velocities

b) Waveforms

Crater related, timing and character were also predicted within reasonable limits as illustrated in Figure 92 for the 50 m range and 3 m depth. Circled is the crater related component. Other waveform comparisons are contained in Appendix A.

c) Evaluation

The crater-related signal, as was mentioned for MBII-1, is a difficult signal to isolate. What is called crater-related is most likely a combination of upstream effects including upstream airblast, crater-induced, direct-induced, and airblast negative phase effects. The crater-related component appears to be predicted within a factor of 3 in magnitude by superposition and the character of the waveform is similar. Although this error is not considered to be unsatisfactory with regard to the inherent single burst crater-related data scatter it is felt that the uncertainty involved in the understanding of this component is more critical. This uncertainty stems from the fact that this component is a combination of effects, as mentioned above, which are the result of different types of phenomenology. Until the relative effects of these different inputs are understood there will be large uncertainty. This signal is discussed further in Section 3.3.3.5.

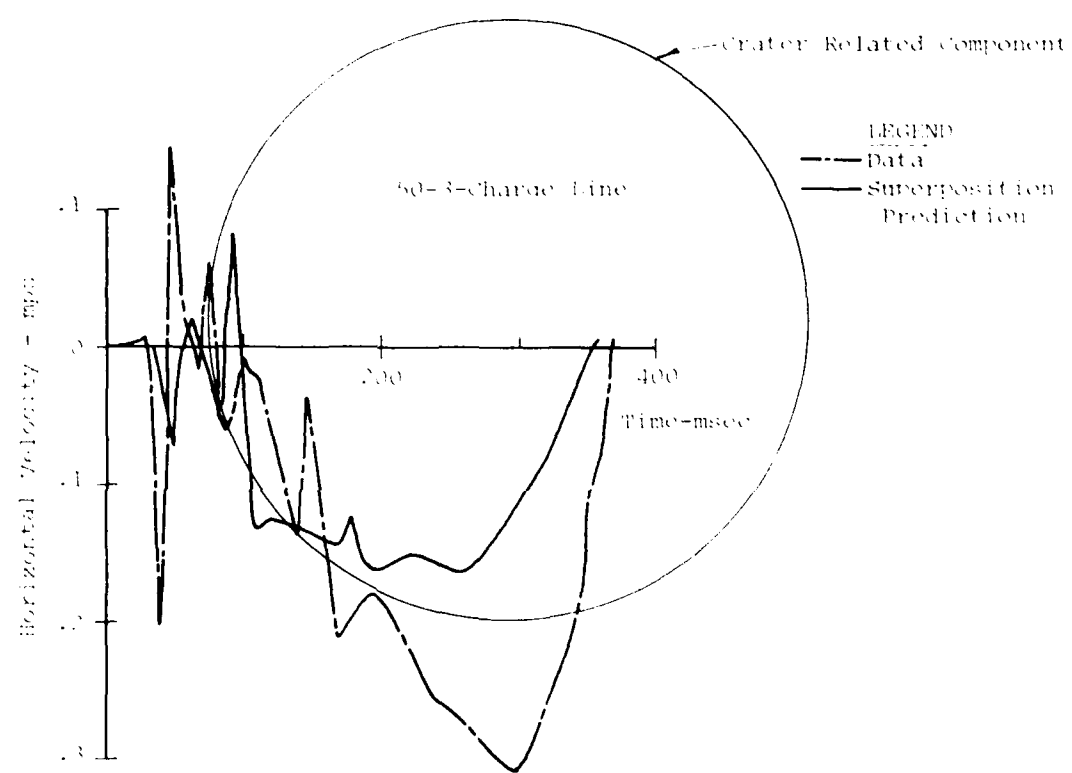


Figure 92. Comparison of Superposition and MBII-2 for Horizontal Velocity - Crater-Related Component

3.3.4.3 Oscillatory Component

The isolation of the oscillatory component was somewhat difficult for the MBII-2 experiment. The near surface waveforms (0.5-3m) were all dominated by the airblast effects. This left the waveforms at the greater depths for a comparison of superposition and data. Unfortunately, these waveforms are somewhat complex and not easy to dissect. The oscillatory component is made up of a headwave component traveling at the compressional wave speed of the layer of interest and a Rayleigh wave component traveling at approximately the shear wave speed of the layer. Since the peak oscillatory component motion is caused by the Rayleigh wave this is the motion compared in this section. The time frame of this motion was identified by calculating the time of arrival of a wave traveling at the shear wave speed of the material. Shown on Figure 93 is a typical waveform showing the parameters discussed in this section.

a) Peaks

Figure 94 shows the comparison of the ratios of peak-to-peak velocities. This figure includes both horizontal and vertical motions. It appears that the horizontal motions were better predicted by superposition, than the verticals were. The horizontals were predicted within a factor of ± 2.5 (+ is overprediction, - is underprediction)

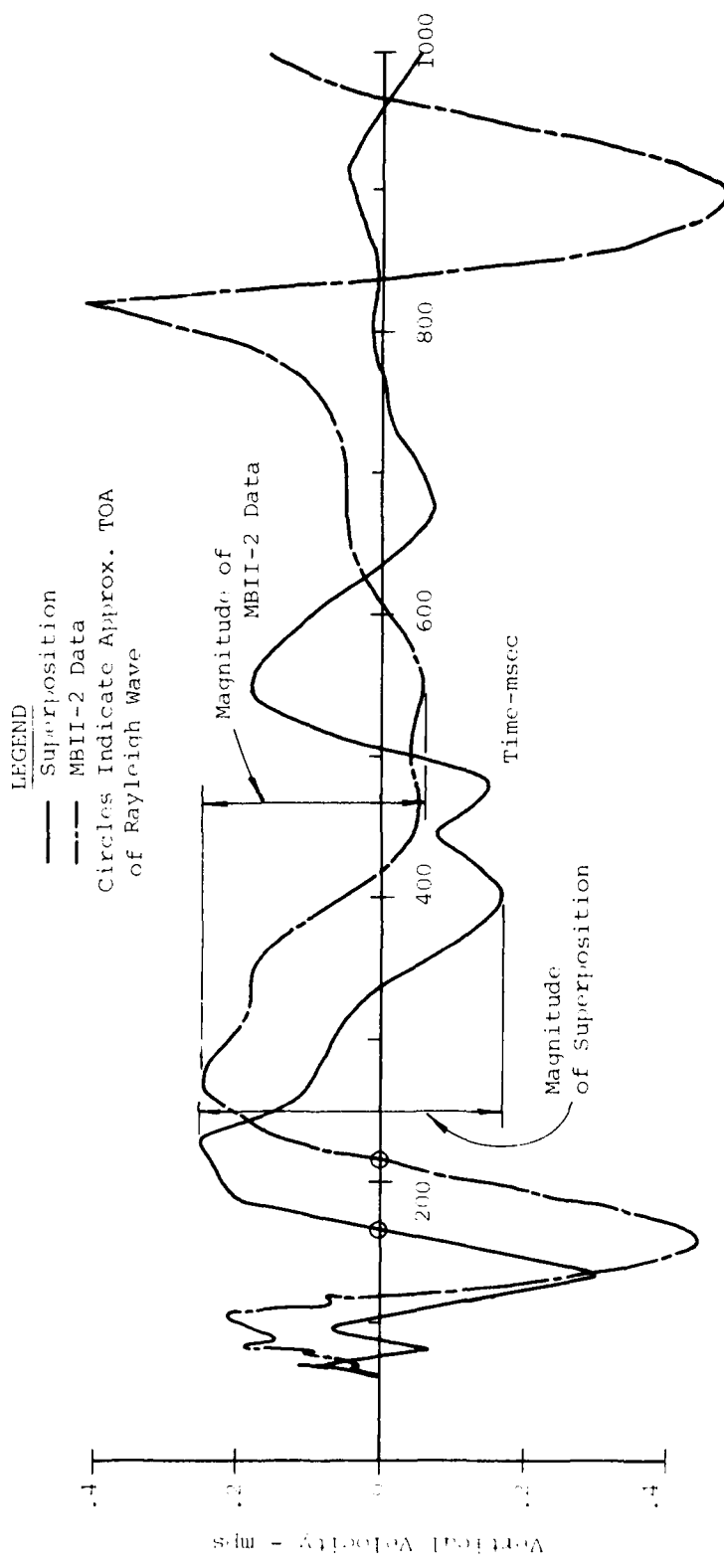


Figure 93. Identification of Peak Oscillatory Motion for Comparison Purposes R=12.5 m; z=12.5 m, Bisector

AD-A092 874

CIVIL SYSTEMS INC ALBUQUERQUE NM
MISERS BLUFF PHASE II, GROUND SHOCK DATA ANALYSIS. (U)

F/G 18/3

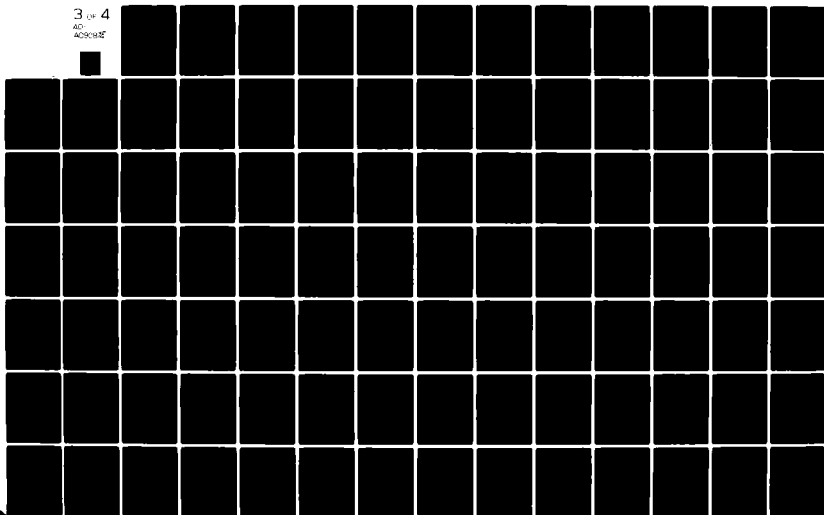
OCT 79 J S PHILLIPS, L S MELZER, J L BRATTON DNA001-79-C-0168

DNA-51352

NL

UNCLASSIFIED

3 of 4
AD-
4090ME



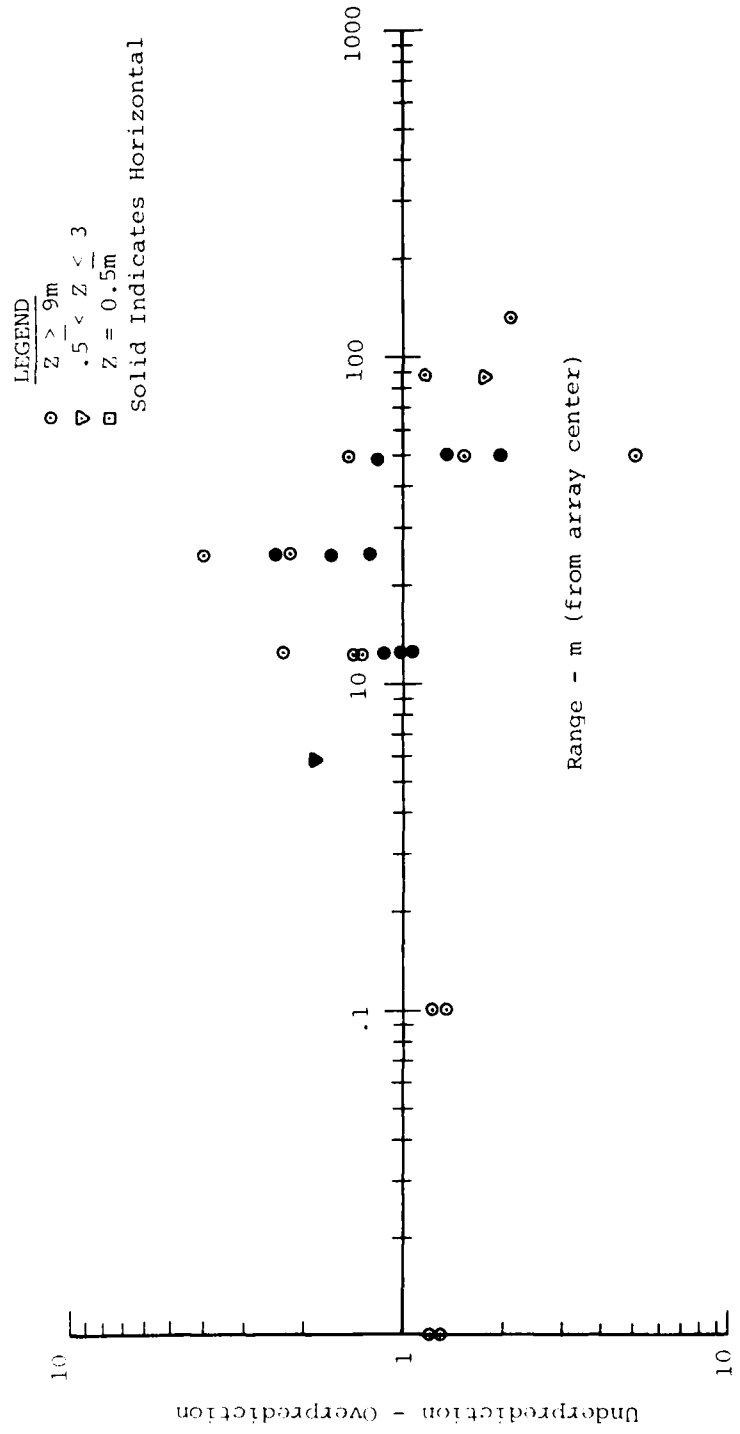


Figure 94. Evaluation Plot of Superposition for Oscillatory Component Peak-to-Peak Velocities

with the majority being within a factor of ± 1.5 . In general, the horizontal motions were overpredicted rather than underpredicted. Vertical motions experienced a somewhat larger variation of approximately ± 3 , but the majority of points are within factors of ± 2 . There appears to be no systematic trend of either under or overprediction in the vertical motions.

b) Waveforms

The reader is directed to the waveforms presented in Appendix A. Figure A.1 is typical of all the near surface waveforms in that there are negligible oscillatory motions. At greater depths (9m-25m) the waveforms become more oscillatory in nature. Two observations are made concerning the waveforms at these depths. The first and most obvious is the signal at approximately 800 msec. The second is a phasing problem between the superposition and the data.

The cause of the 800 msec signal was postulated in an earlier section. The phasing problem is believed to be (to a large extent) due to the nonuniform elevation of the top of bedrock between the two experiments of Phase II. (The reader is referred to the plot of the bedrock elevation - Fig. 3.) Work done by Auld and Murphy (Ref. 26 & 27) suggests that fundamental mode frequency (and periods) of the late time oscillatory motion is governed by the weighted average shear wave velocity of the soil above the rock (β) and the depth to bedrock (H) as follows:

$f = \beta / 2H$. From this equation it is observed that deeper rock yields lower frequencies. The waveforms in Appendix A show that the superposition predictions are of higher frequency than in the data. The average rock elevation in the single burst experiment (data from which the superposition predictions were produced) was 43 m below the surface while at the Event 2 site had bedrock at an average elevation of 63 m. If shear velocities are assumed to be equal at the two sites; then the equation above may be solved for a time scaling factor due to the differing rock elevations. The result of scaling the superposition waveform by this factor is shown in Figure 95. The timing of the low frequency oscillatory motions are substantially improved. This time scaling placed a relatively large amplitude signal in the same time frame as the 800 msec signal in the data. This signal was produced in the superposition process because of near exact phasing of the low frequency motions in the single burst waveforms. This suggests that the large 800 msec signal is due to the additive effect of Rayleigh waves. The tensile weakness, and impedance mismatch at ~26 m results in layer separation as a result of the passage of this large signal. This failure would result in the rather dramatic velocity signals seen in the data above this depth.

c) Evaluation

The oscillatory component of ground motion is fairly well predicted by superposition. The

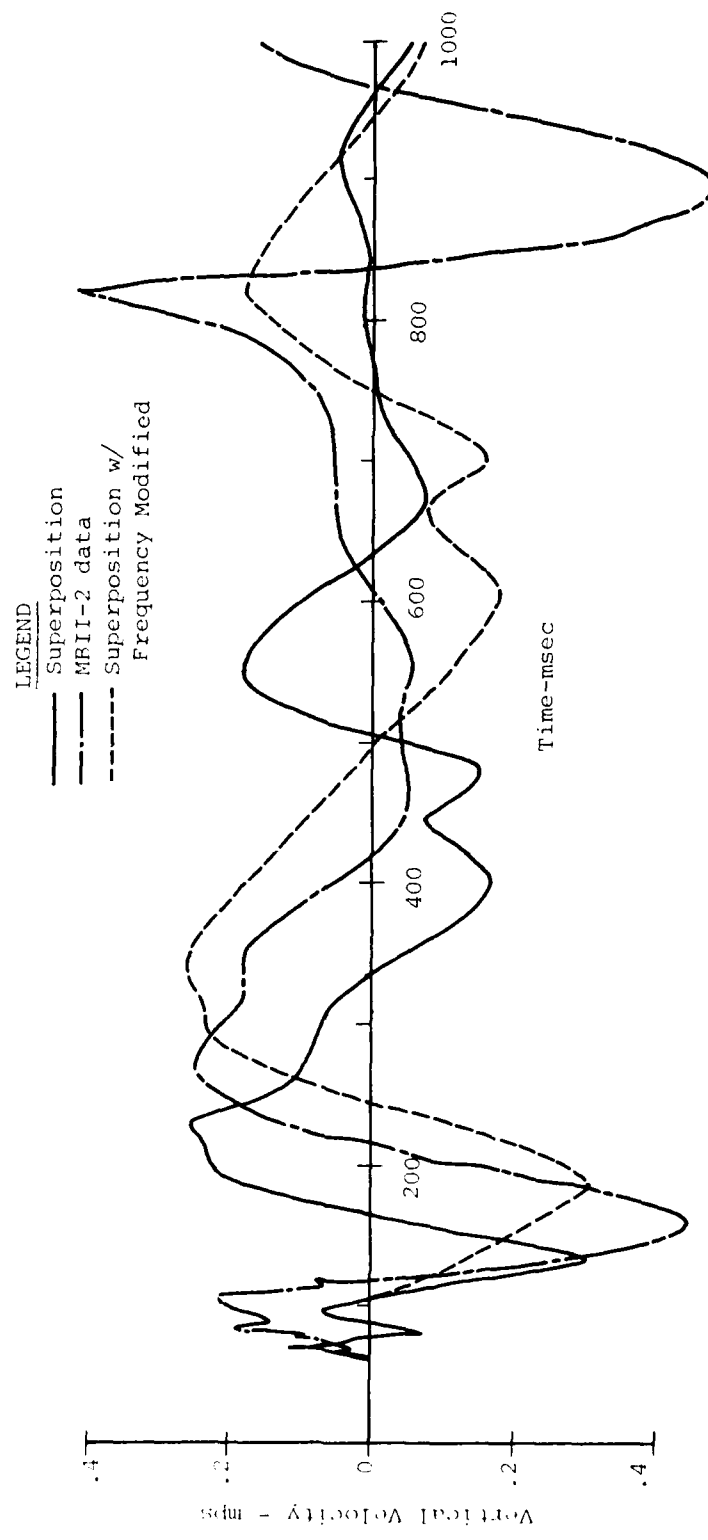


Figure 95. Correction of Superposition for Differing Rock Elevations of MBII-1 and MBII-2

vertical and horizontal motions were generally within factors of ± 3 . The phasing problems seen between the data and superposition are primarily governed by the differing rock elevations. It is felt that superposition is a good estimate of the multiple burst environment for the oscillatory component magnitudes. The frequencies of the oscillatory component will be governed by the depth to rock and shear velocities of the material above the rock.

3.3.4.4 Multiple Burst Nonlinear Effects

As has been discussed, the largest area of nonlinear behavior was near the center of the charge array. The component most affected was the vertical air-slap component (both compressive and negative phases).

The reasons for this nonlinear behavior in the compressive phase portion of the air slap is the shock-on-shock interactions which are the result of the nonlinear nature of the equation-of-state of the air. As pointed out before this problem is being worked on by others and given the correct compressive portion of the airblast the air-slap ground motion component can be fairly accurately predicted.

The nonlinear behavior of the air-slap component in the time domain of the negative phase is shown in Figure 96. The nonlinearity (data vs superposition) begins at approximately 40 m from the array center and increases

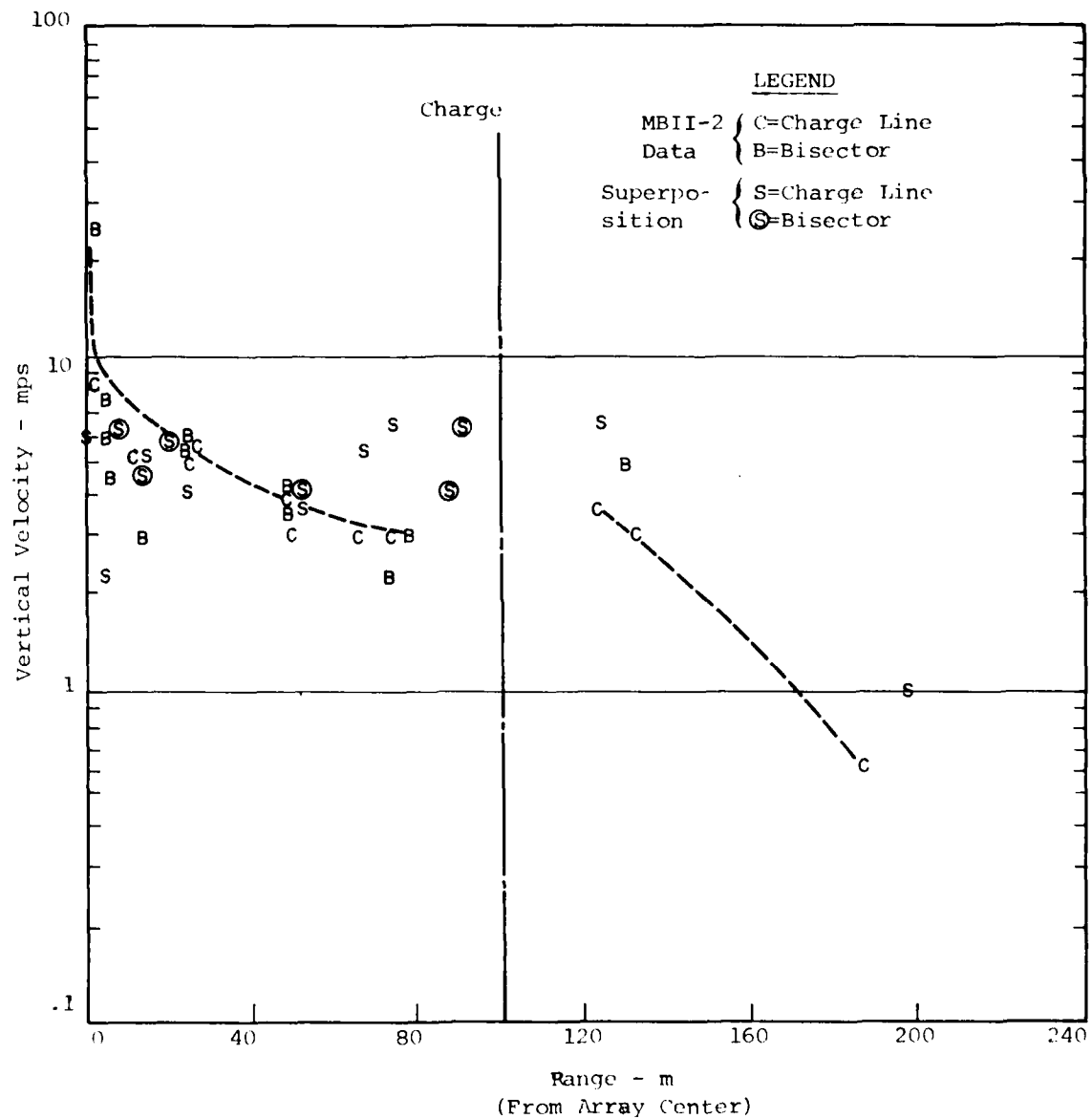


Figure 96. Large Upward Signal - MBII-2 VS Superposition

toward center. This behavior is due to the pore air expansion related to the airblast negative phase as well as the convergent nature of the geometry.

The pore-air expansion concept was discussed in preceding sections as it applied to the single burst experiment. The enhancement of negative pressure in the multiple burst experiment as compared to the negative pressures measured in the single burst experiment is shown in Figure 97. The multiple burst negative pressures are "greater" than in the single burst, but in most cases superposition of negative pressures from single burst experiment would yield approximately the same results as seen in the multiburst experiment. This is mainly due to the fact that there is a limitation of 1 atmosphere on the negative pressure and therefore, nonlinear interaction of the air can produce no more than this amount of underpressure. Figure 98 shows the timing correlation between the positive and negative phases of the airblast along with the arrival time of the large upward signal in the velocity. This shows that the velocity and the negative phase arrival times parallel one another and indicates the direct involvement of the negative phase of the airblast in this upward peak.

PLID calculations with the measured overpressures and the pore-air model were performed to determine

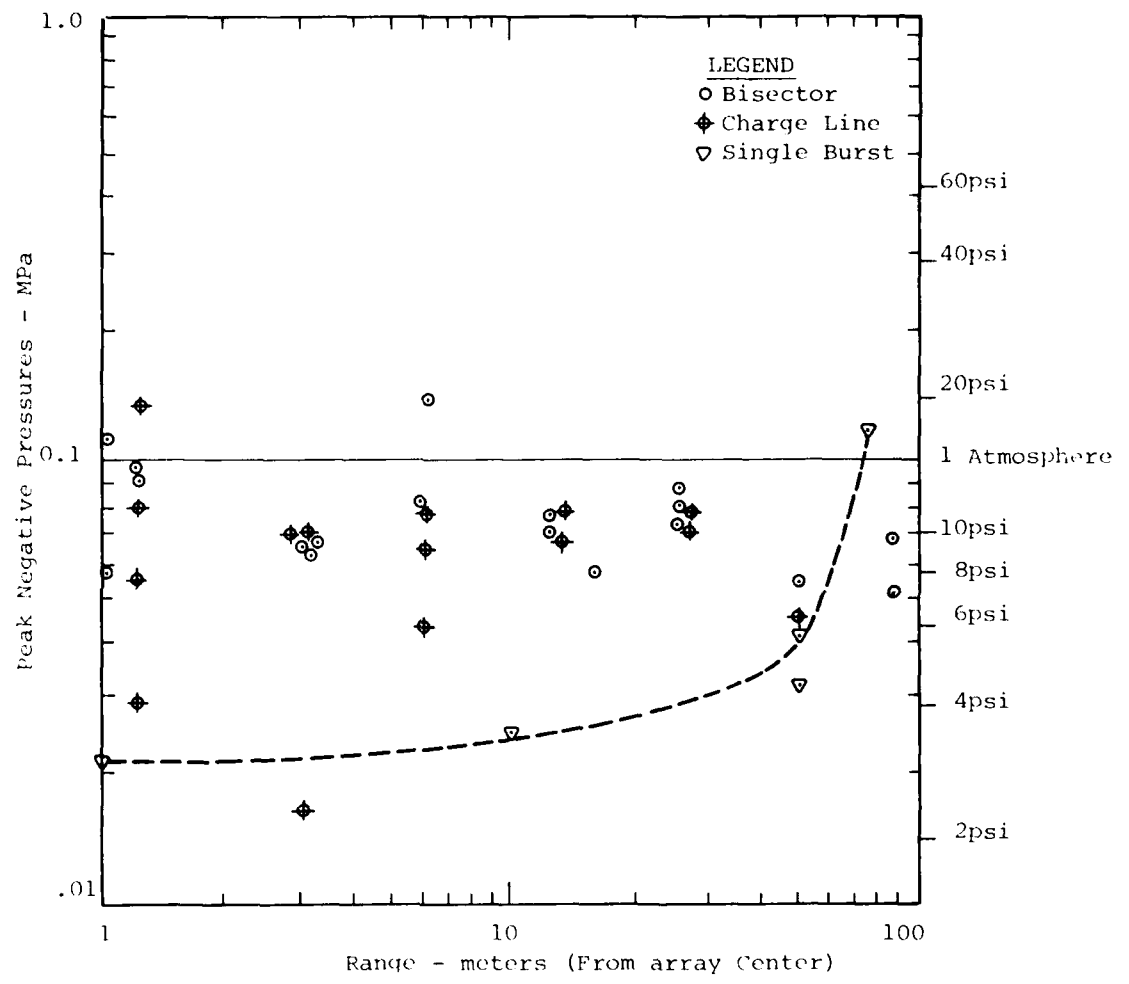


Figure 97. Magnitude of Negative Phase - MBII-2

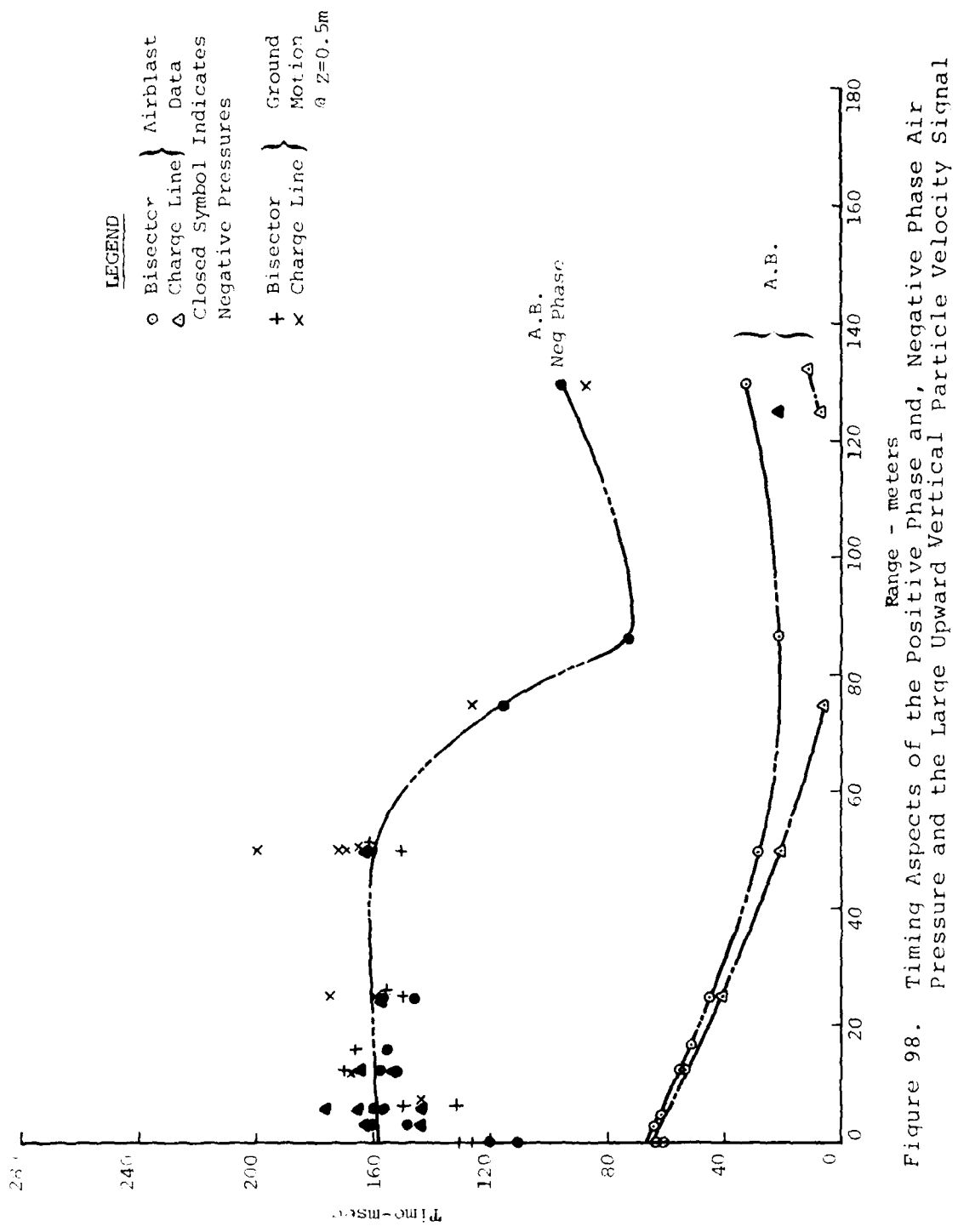


Figure 98. Timing Aspects of the Positive Phase Air Pressure and the Large Upward Vertical Particle Velocity Signal

if this effect alone produced results comparable with the data. The comparison of the data and calculations are shown in Figures 99 through 110.

Figure 99 shows the comparison of the pore-air model calculations and the MBII-2 data near the array center at the 0.5 m depth. The character of the calculated waveform is very similar to that seen in the data and magnitudes are within a factor of 1.5. The timing and magnitude differences seen are felt to be due to the fact that the calculation was made at the exact center point, while the data was 0.5 m off the center.

Figures 100 and 101 are the comparisons of the calculations and data at the 25 m range, 0.5 m depth on the bisector and charge lines respectively. On the bisector the initial compressive downward air slap is within the scatter of the data. Secondary and tertiary compressive air slap peaks are somewhat undercalculated. The upward motion is slightly overcalculated while the durations of the calculation and the data are almost the same. On the charge line the compressive portion of the air slap is undercalculated while the upward motion is again slightly overcalculated. Duration of the pore-air signal is calculated to be somewhat shorter than the data indicates.

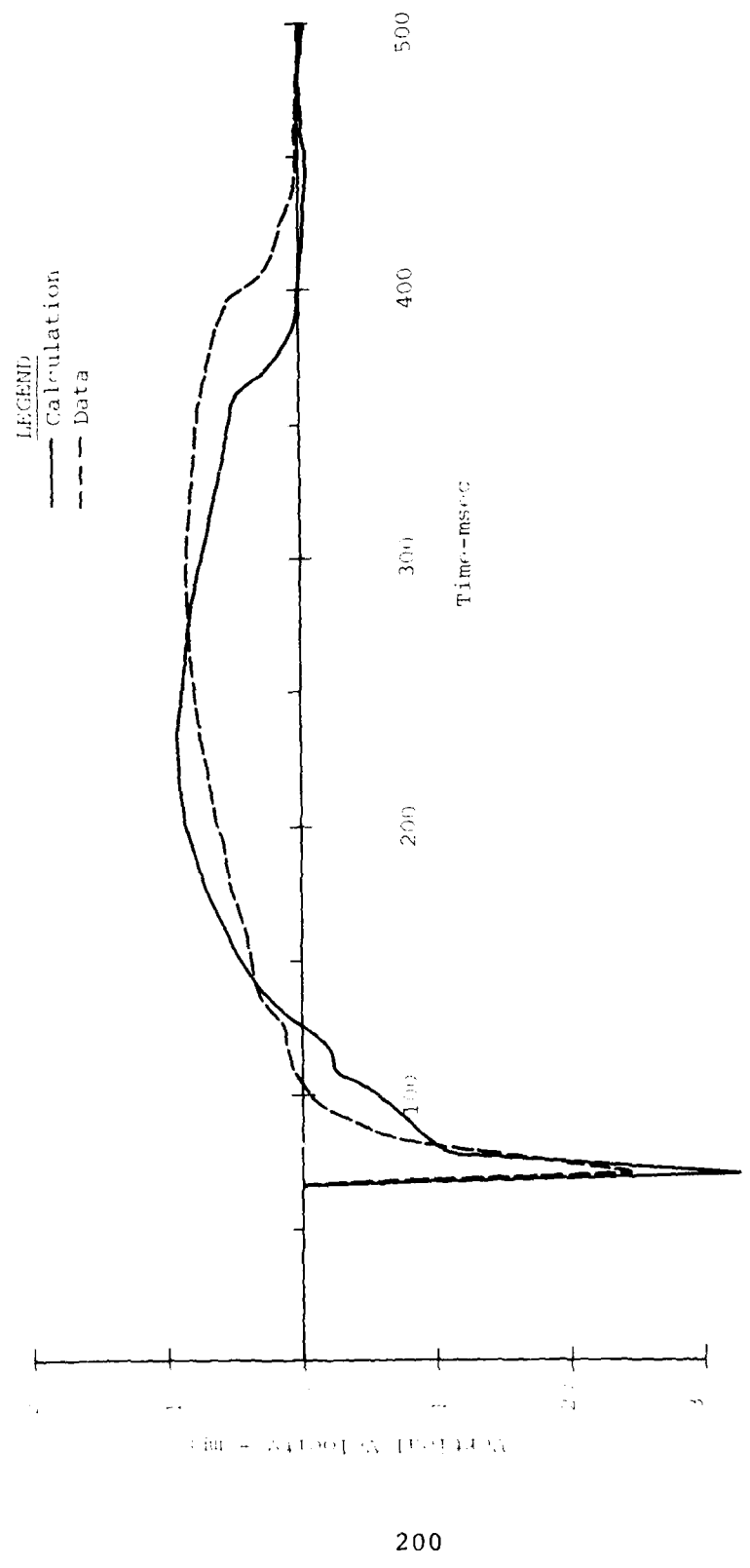


Figure 99. Comparison of Pore-Air Calculation and MBII-2 Data @ the Array Center

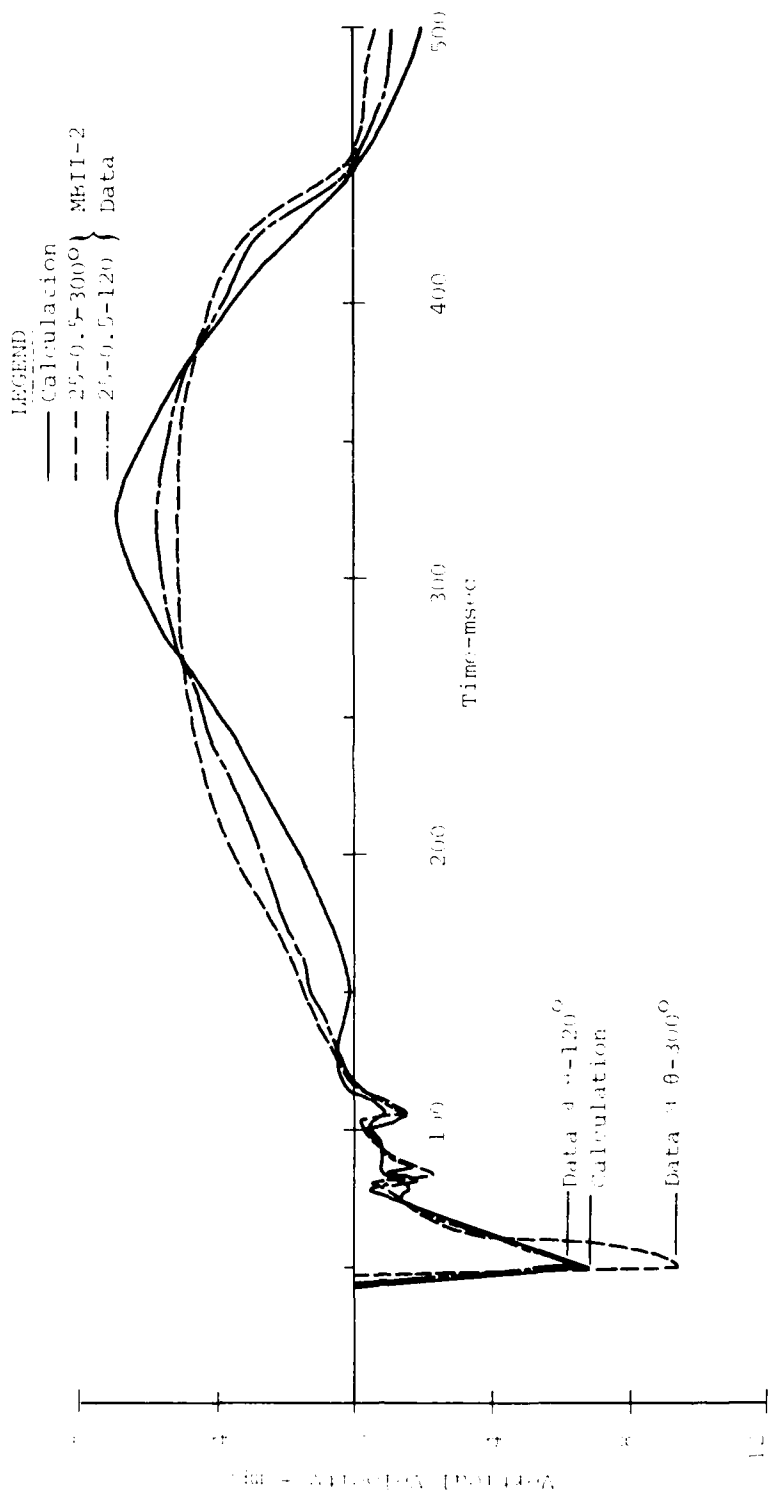


Figure 100. Comparison of the Fore-Air Calculation and MBII-2 Data at $R=25$ m, $z=0.5$ m, on a Bisector

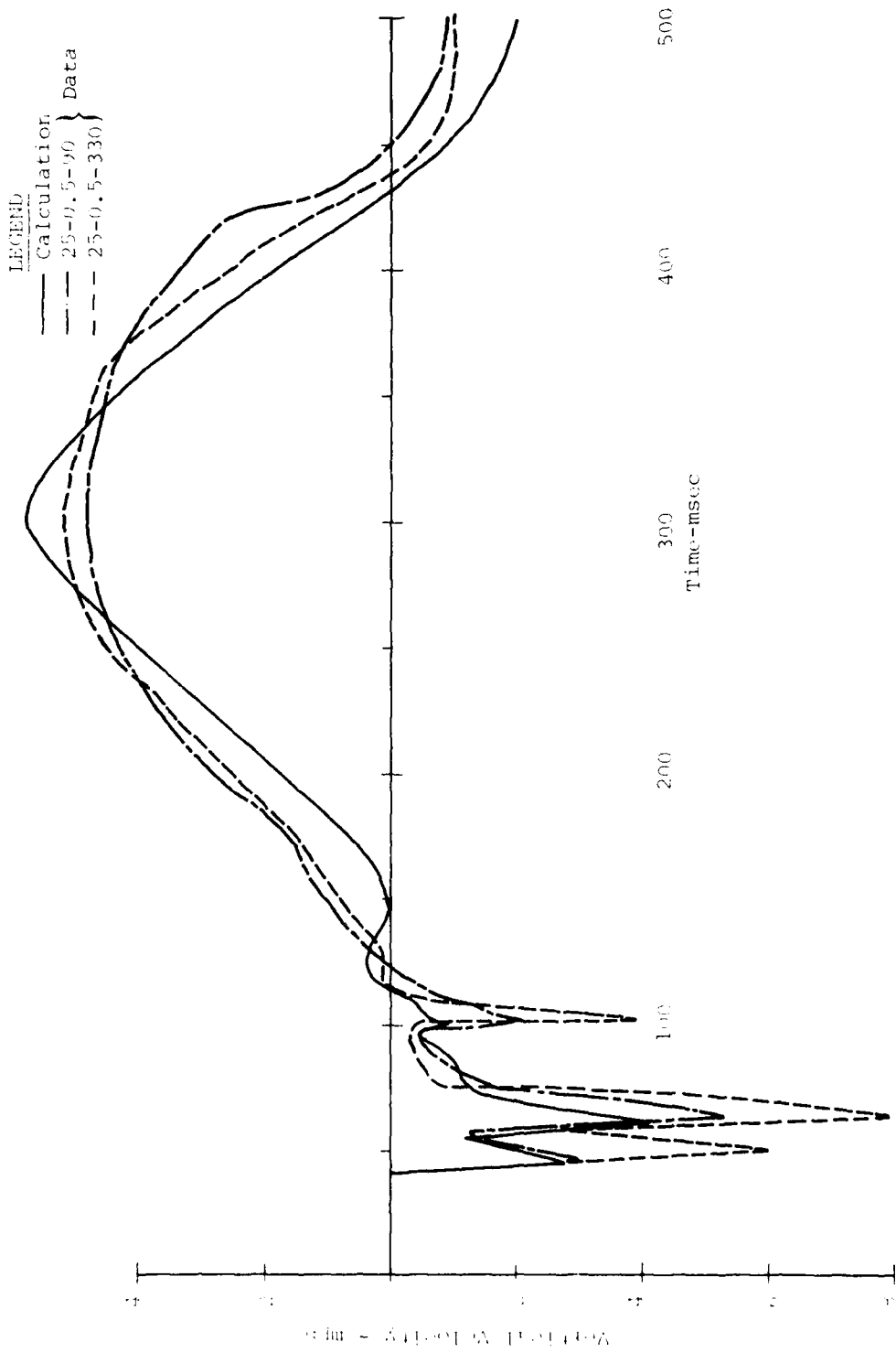


Figure 101. Comparison of Pore-Air Calculation and MBII-2 Data @
 $R=25 \text{ m}$, $Z=0.5 \text{ m}$, on a Charge Line

Figures 102 through 104 show comparisons for the 50 m range on a bisector to a depth of 3 m. This is the first range at which there was useable data with which to evaluate the calculations to these depths. Figure 102 shows the 0.5 m depth comparisons. The comments made for previous comparisons appear to apply for this comparison. Figure 103 shows the comparison made at the 1.5 m depth. Generally, the character of the calculated waveform is very similar to the data. The compressive downward air slap is undercalculated by a factor of approximately 1.6. Upward motions were undercalculated by a factor of approximately 1.4. Figure 104 is the comparison at the 3 m depth. For this depth the calculation is overpredicting the downward air slap by a factor of 1.4. The data then shows a cycle of motion not seen in the calculation. This motion is the direct waves from the two closest charges and obviously not included in the 1-D calculation. The pore air expansion begins at approximately 400 msec in the calculation. The data at this point also starts a turn upward. At the end of the calculation (500 msec) both the data and the calculation were approximately equal in magnitude.

Comparisons for the 50 m range on the charge line are shown in Figures 105 through 107. At the 0.5 m depth the initial air slap is fairly well calculated, but the succeeding air slap peaks are undercalculated by as much

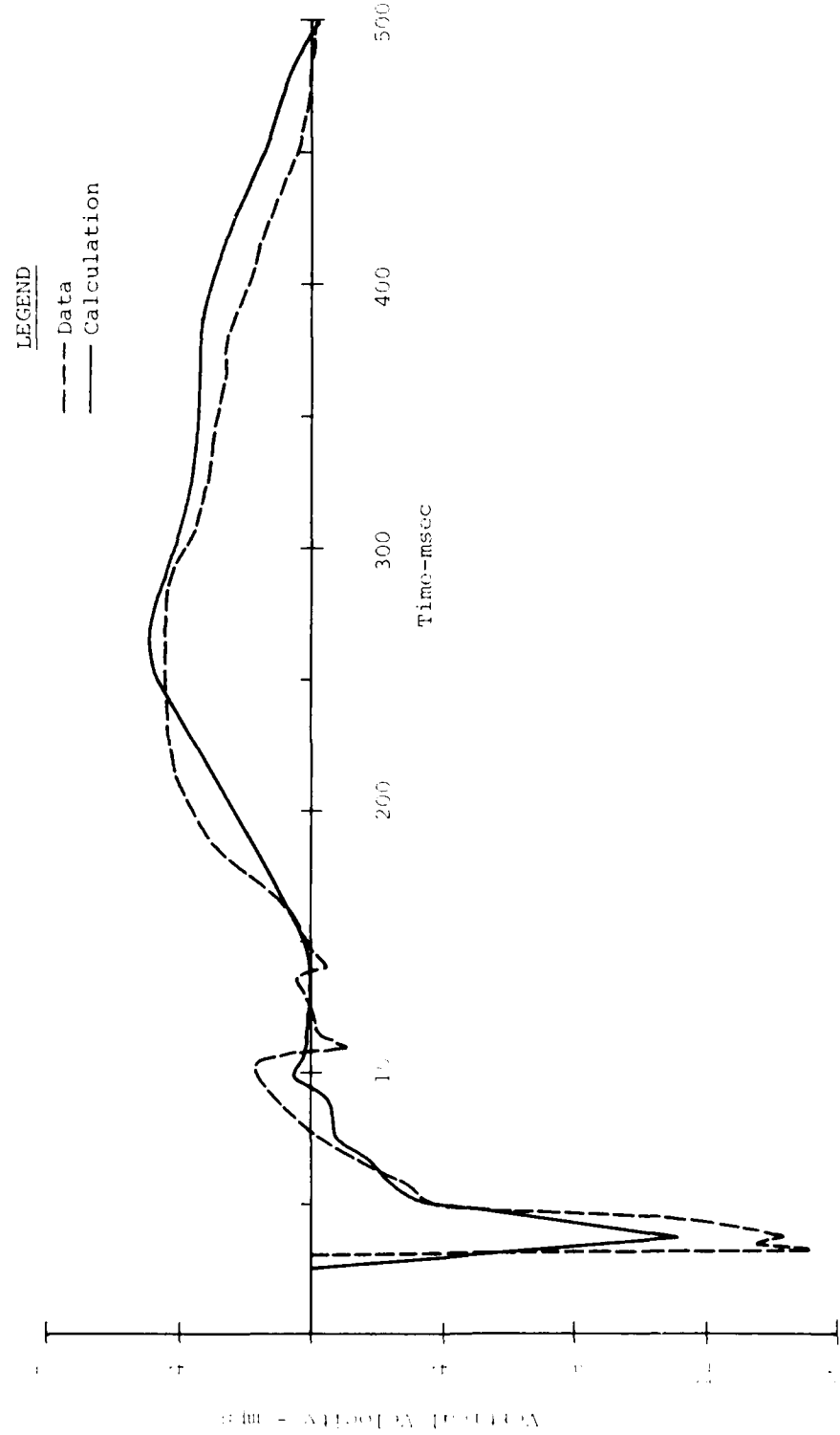


Figure 102. Comparison of Pore-Air Calculation and MBII-2 Data
a R=50 m, z=9.5 m on a Bisector

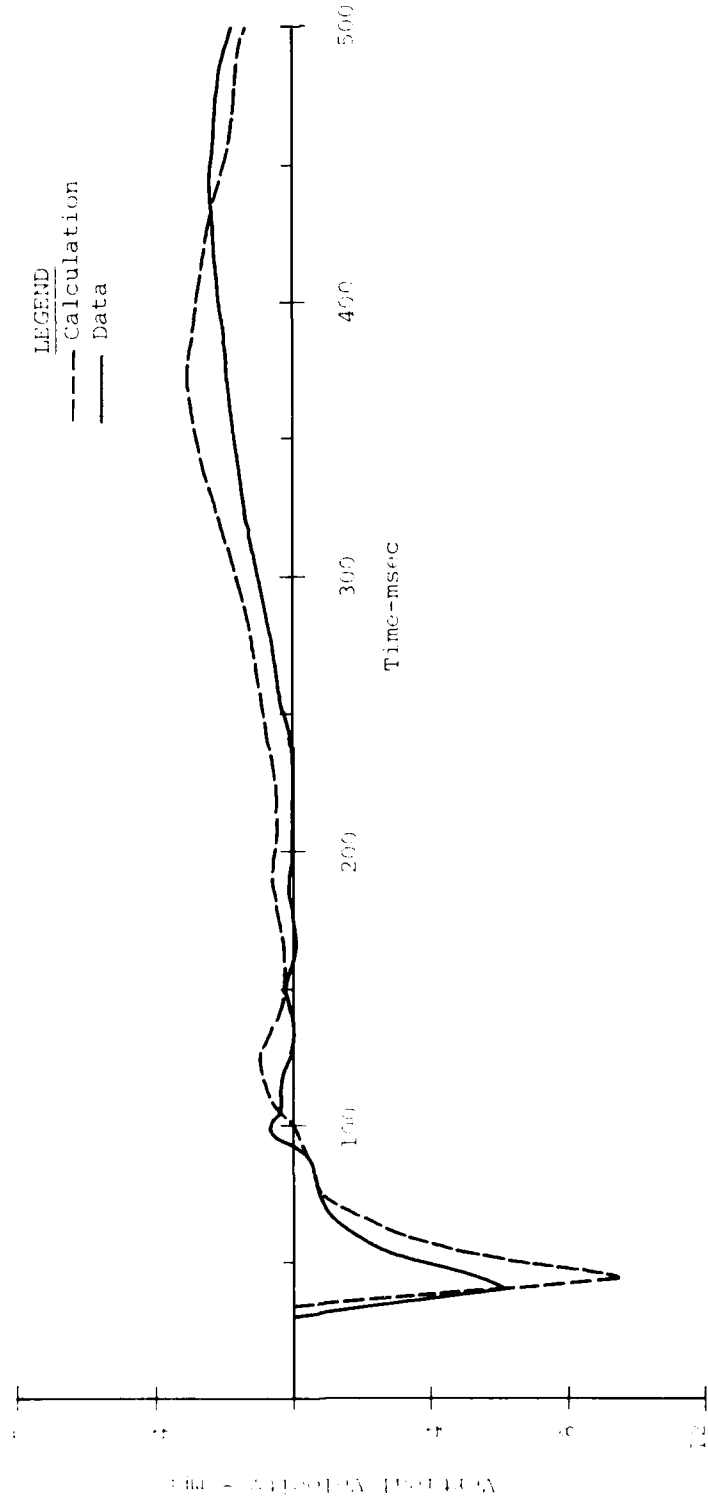


Figure 103. Comparison of the Pore-Air Calculation and MBII-2
at $R=50$ m, $Z=1.5$ m on a Bisector

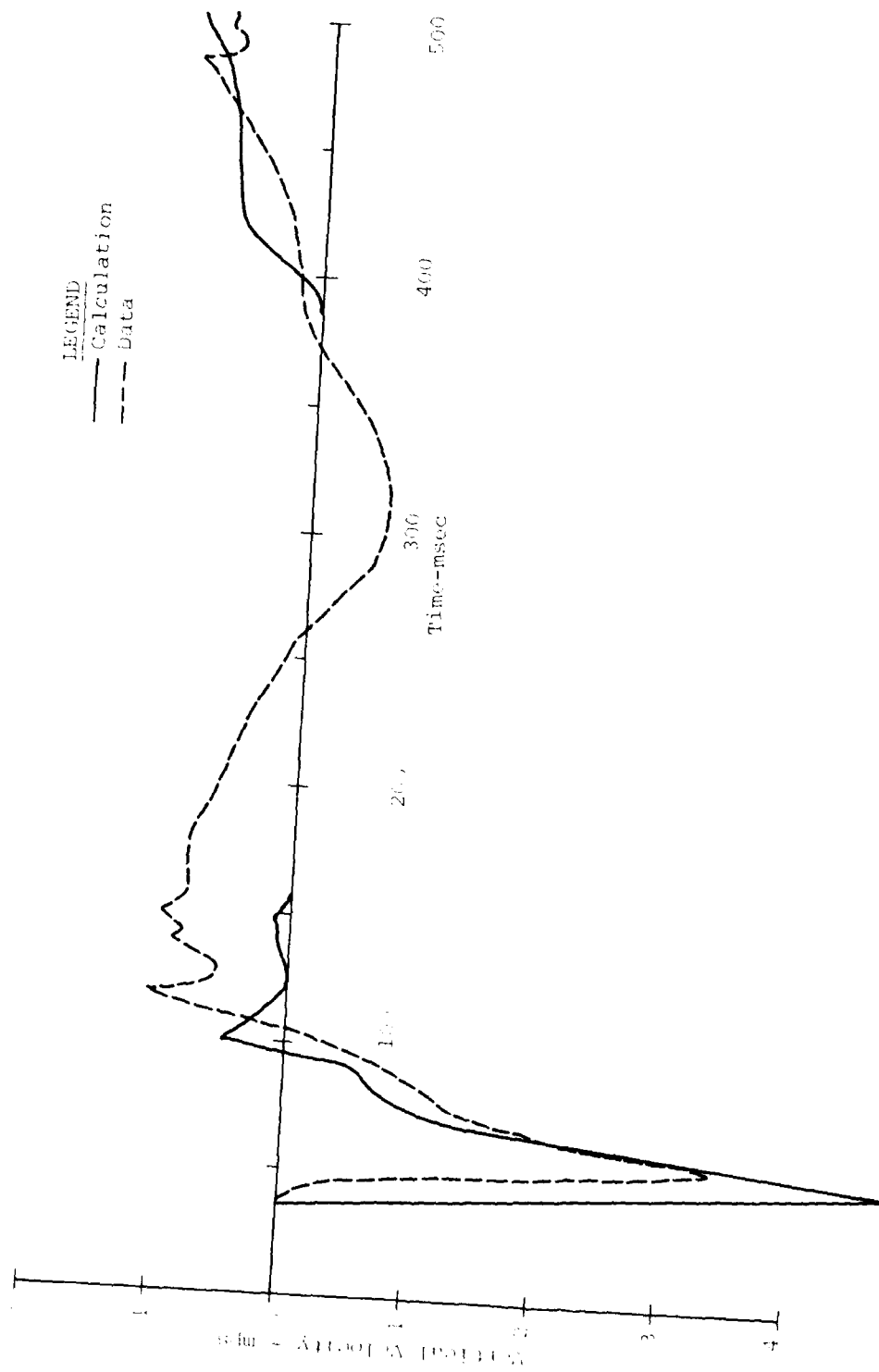


Figure 104. Comparison of Pore-Air Calculation and MBII-2 Data on a Bisector
 $R=50$ m, $z=3$ m, a

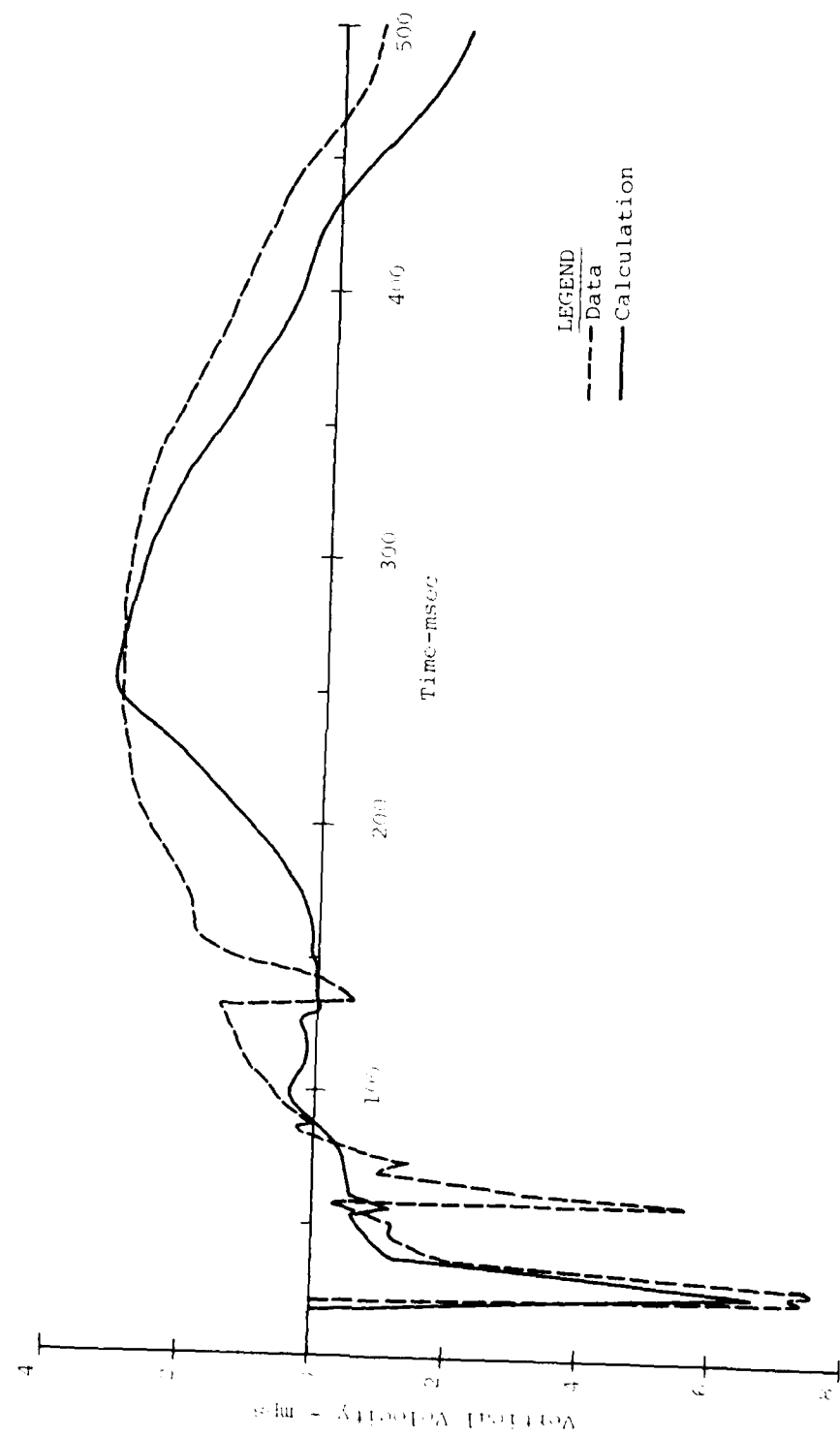


Figure 105. Comparison of Pore-Air Calculation and MBII-2 Data
at $R=50$ m, $z=0.5$ m, on a Charge Line

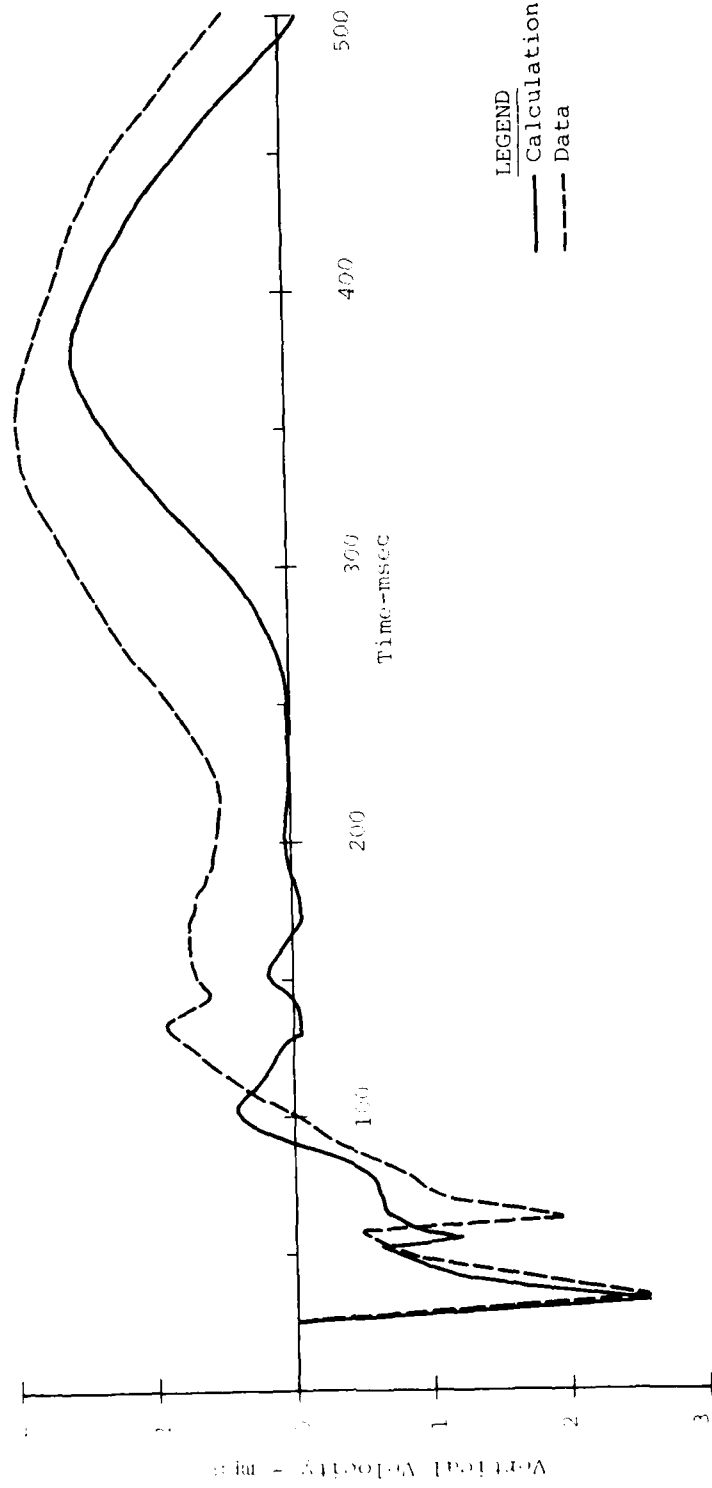


Figure 106. Comparison of Pore-Air Calculation and MBII-2 Data
at R=50 m, z=1.5 m, on a Charge Line

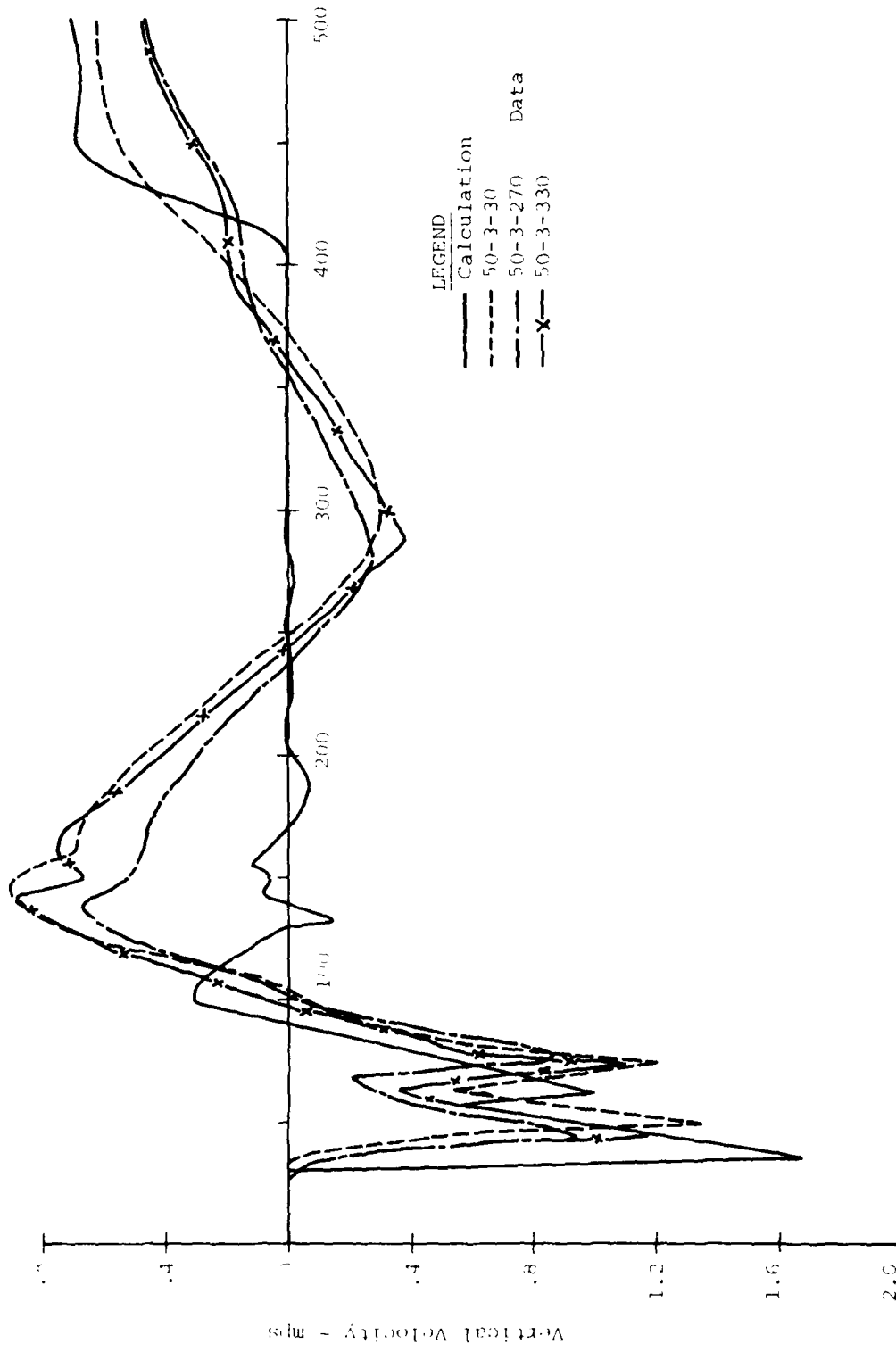


Figure 107. Comparison of Pore-Air Calculation and MBII-2 Data
 $R=50$ m, $Z=3$ m on a Charge Line

as a factor of 7.5. The upward portion of the signal has somewhat the same character as the data but the duration is undercalculated. The 1.5 m depth comparisons (Fig. 106) are better but the secondary air slap is still undercalculated. In the upward portion of the signal the data is greater in magnitude than the calculation, but the calculation is very similar in character. The 3 m depth comparisons are shown in Figure 107. The calculation at this depth overestimates the first compressive air slap and is within the data scatter on the second peak. The initial upward motion is undercalculated and not the same character as the data. Between 200 msec and 400 msec the calculated motion is essentially zero. During this time, the data has one cycle of fairly large magnitude motion. This is the crater-related motion from the closest charge. Finally at about 400 msec, the pore-air expansion effect begins in the calculation. At approximately the same time the data also begins an upward motion. At the end of the calculation (500 msec) the data is somewhat lower than the calculated value.

Figures 108 through 110 show the comparisons made for the location directly between two charges. At the 0.5 m and 1.5 m depths the air slap portion (due to the compressive phase of the airblast) of the waveform is well

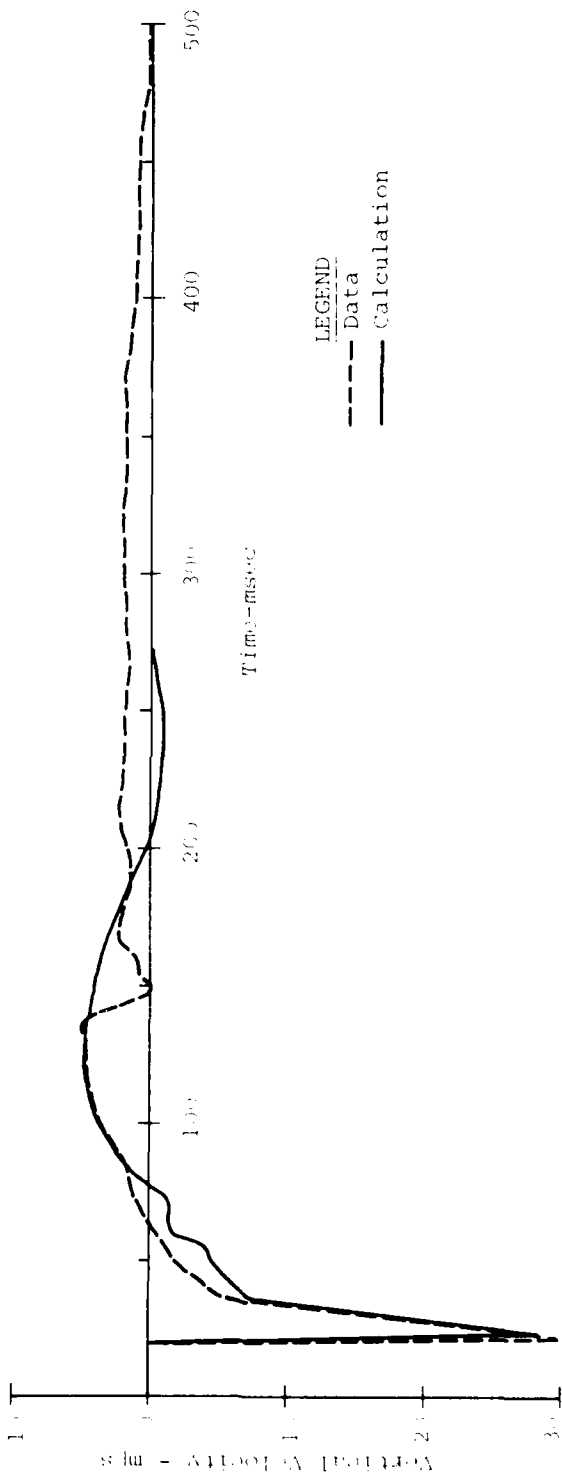


Figure 108. Comparison of Pore-Air Calculation and MBII-2 Data
at R=86.6 m; z=0.5 m, on a Bisector

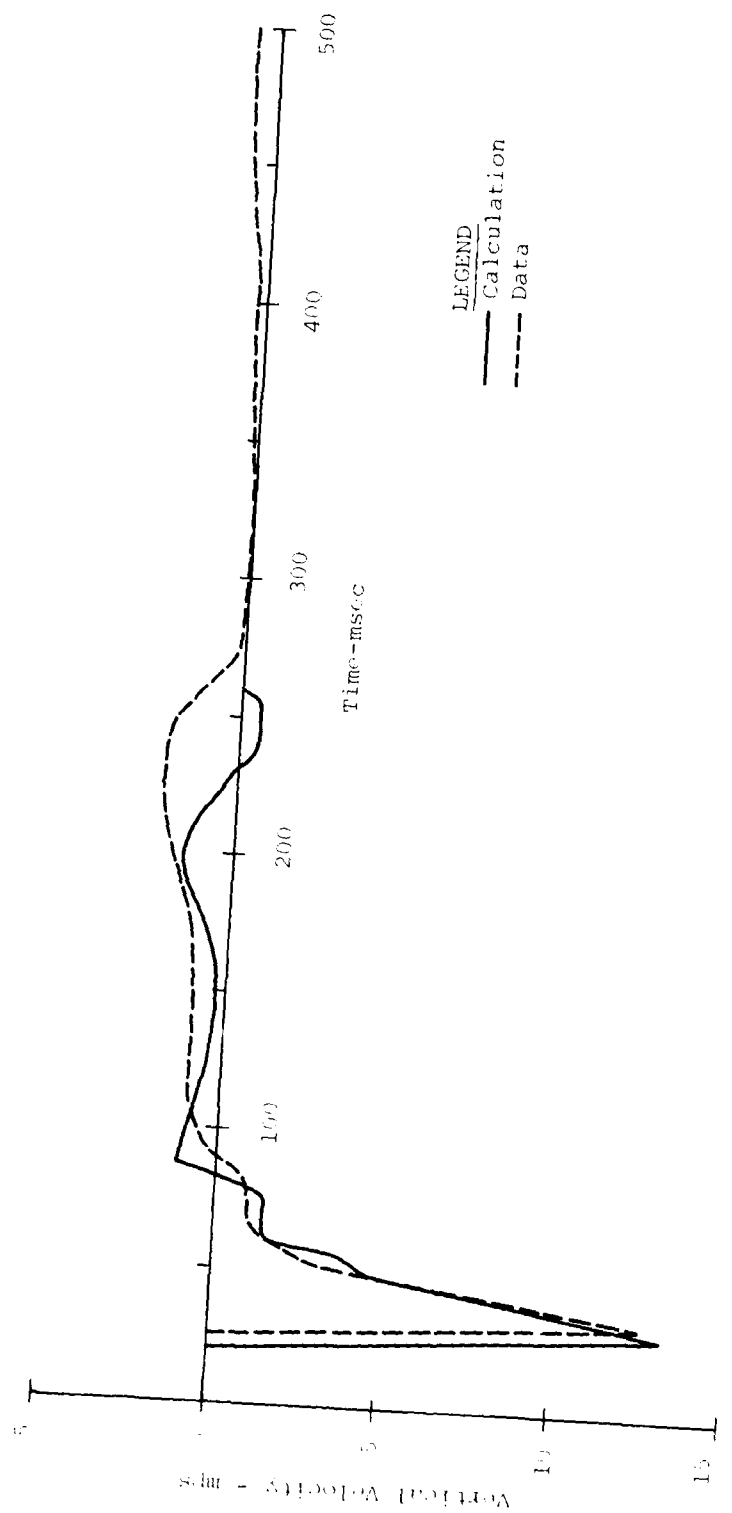


Figure 109. Comparison of Pore-Air Calculation and MBI I-2 Data
at $R=86.6$ m; $Z=1.5$ m on a Bisector

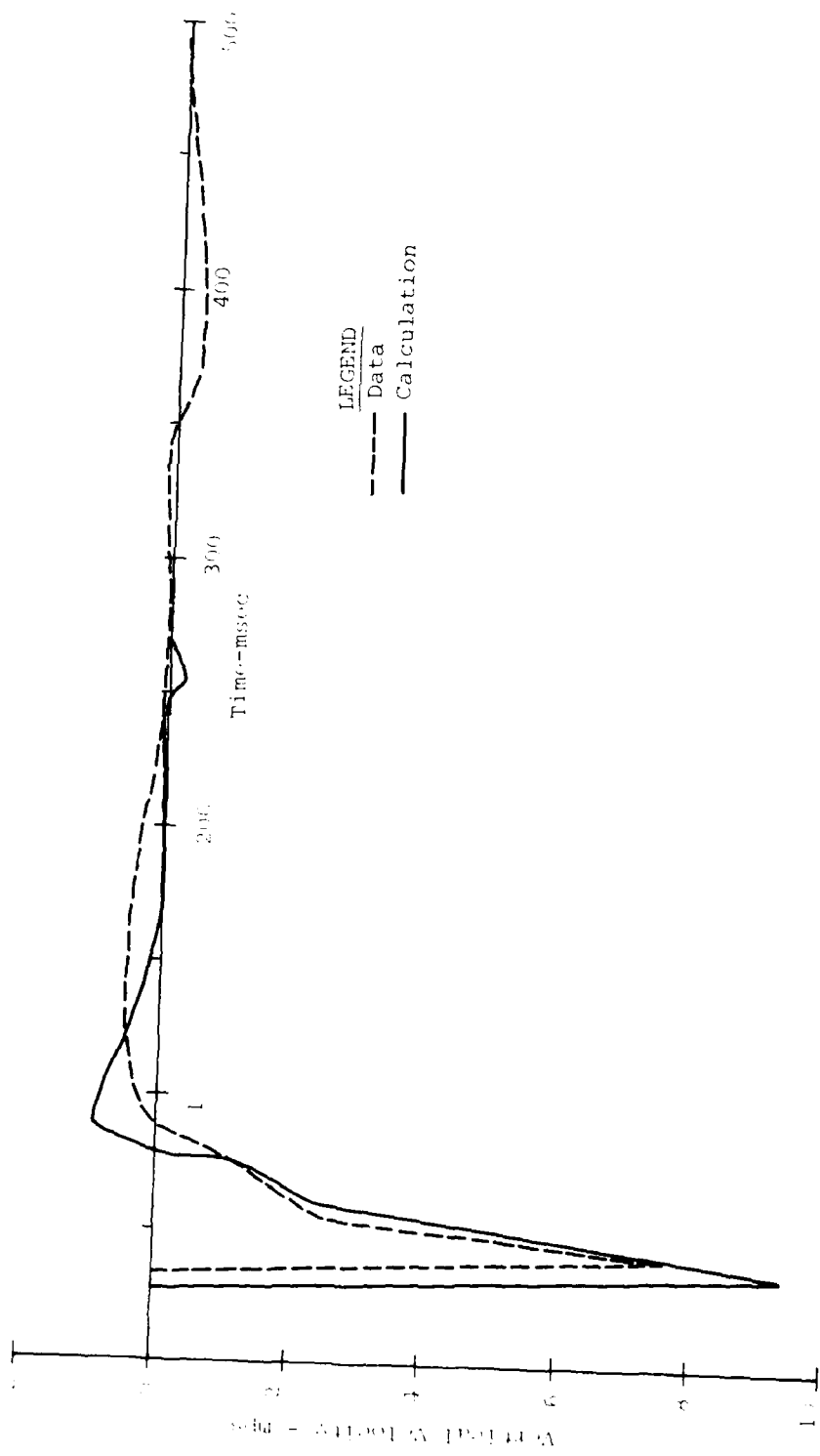


Figure 110. Comparison of Pore-Air Calculation and MBII-2 Data
@ R=86.6 m; Z=3 m on a Bisector

calculated. The upward portion (due to the negative phase of the airblast) is well calculated in magnitude, but the character of the data is somewhat different than the calculation. The 3 m depth comparison (Fig. 110) shows that the air slap is overcalculated in magnitude. The upward motion seen in the calculation is different than that seen in the data. The calculated waveform is generally too large in magnitude and too short in duration.

From these comparisons it would appear, that at least in the near surface silt, the ground motion is well calculated by PLID with the pore-air model. However, at the greater depths (Fig. 104 and 107) the calculation began to miss a rather significant signal, not attributable to one-dimensional effects. It is also interesting to note that at the location between two charges (Fig. 110) this signal was not seen. The fact that this signal is a result from two-dimensional effects is illustrated on Figure 111. As can be seen; the horizontal motion is experiencing a relatively large magnitude inward (toward the center) signal in the same time frame as the upward signal appears in the data. This signal is the direct wave from the nearest charge and is travelling at the p-wave speed of the sand between the silt and the saturation zone (see the site profile, Fig. 6). It is also pointed out that there is a relatively strong -lg slope on the vertical waveform. This spall is not the direct result of the pore air

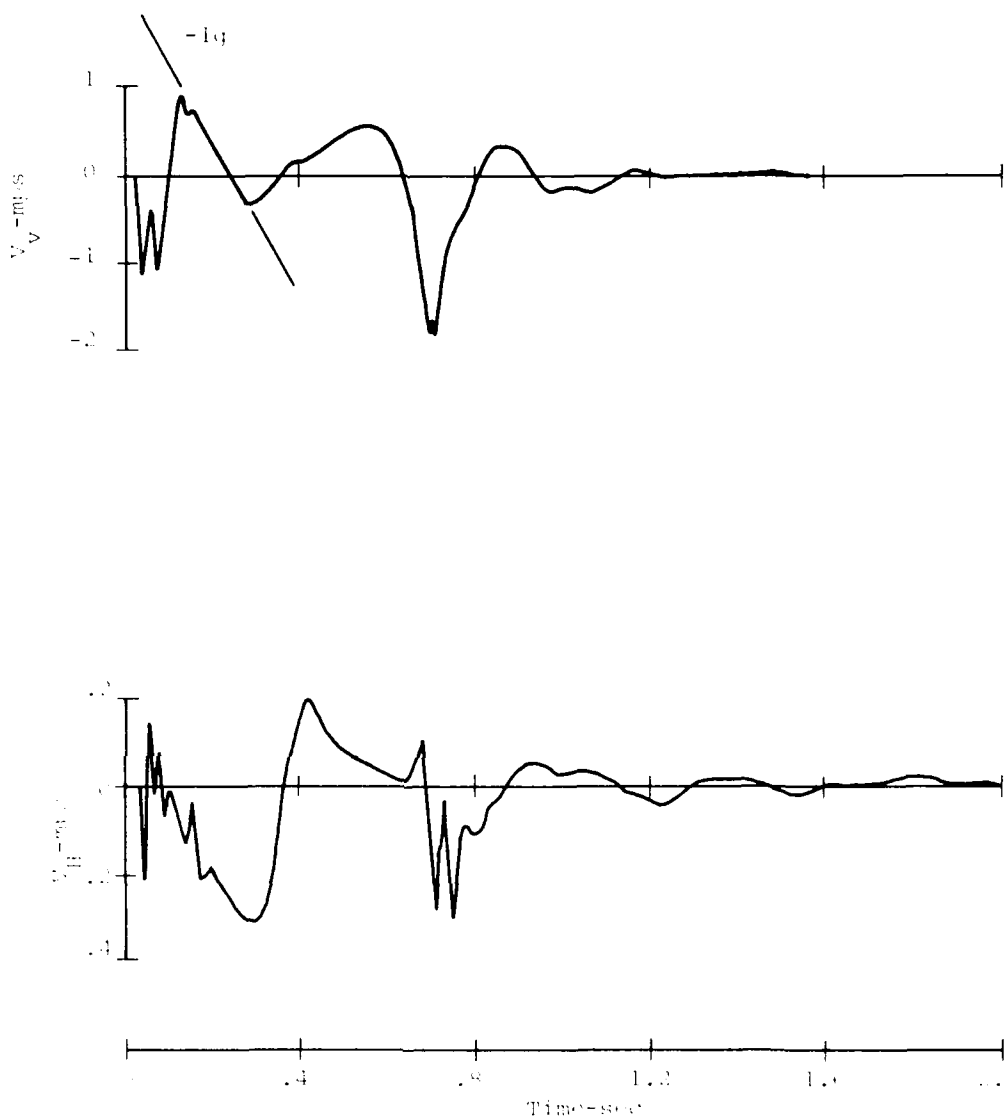


Figure 111. Horizontal and Vertical Waveforms Measured
at $R=50$; $Z=3m$ on a Charge Line

effect at this depth. This spall results from the tensile failure of the material due to compressive waves striking a free surface and reflecting as tensile waves combined with the reduction of the overburden stresses due to the lofting of the upper material by the pore-air expansion mechanism.

Figure 112 compares the peak values of this direct wave at the 3 m depth and shows that there is very little attenuation of this peak as the array center is approached. Also shown on this figure is the superposition predictions of this same peak. Although the data is limited the superposition is low at all locations. Superposition is generally most accurate for both the horizontal and vertical velocities at the 50 m range and progressively deteriorates as the array center is approached.

This figure shows that there is essentially no attenuation of this direct-induced motion and is underpredicted by superposition. It is felt that this effect is the result of the convergent nature of the geometry.

Figure 113 shows the airblast and stress waveforms measured near the array center of MBII-2. Included on these figures are the linearly superimposed waveforms from MBII-1 experiment. The air pressure in MBII-2 was higher (as would be expected) than MBII-1. Linear superposition results in a factor of 5 difference. Including the

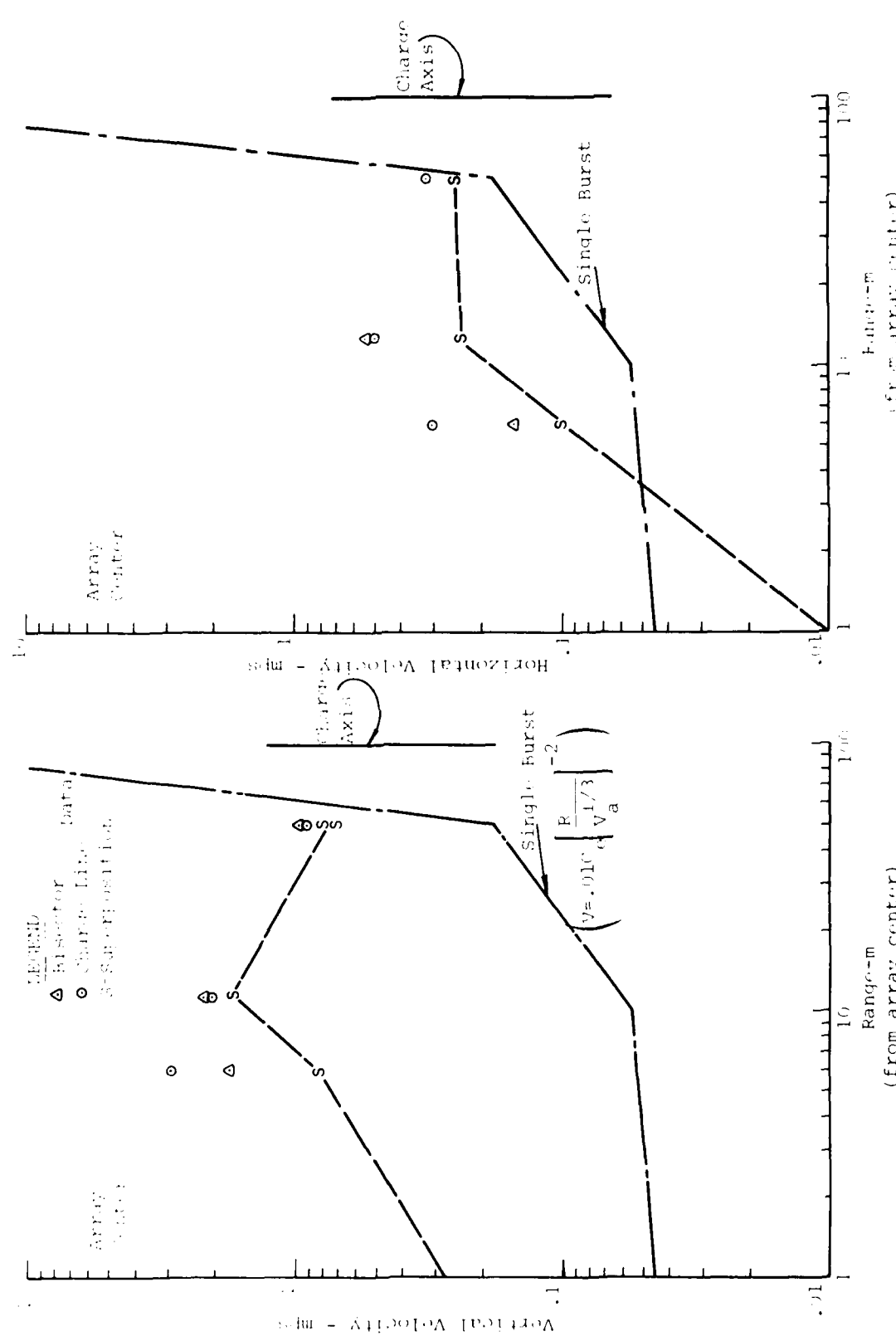


Figure 112. Behavior of Direct Wave Interior to the Charge Array at the 3 m Depth

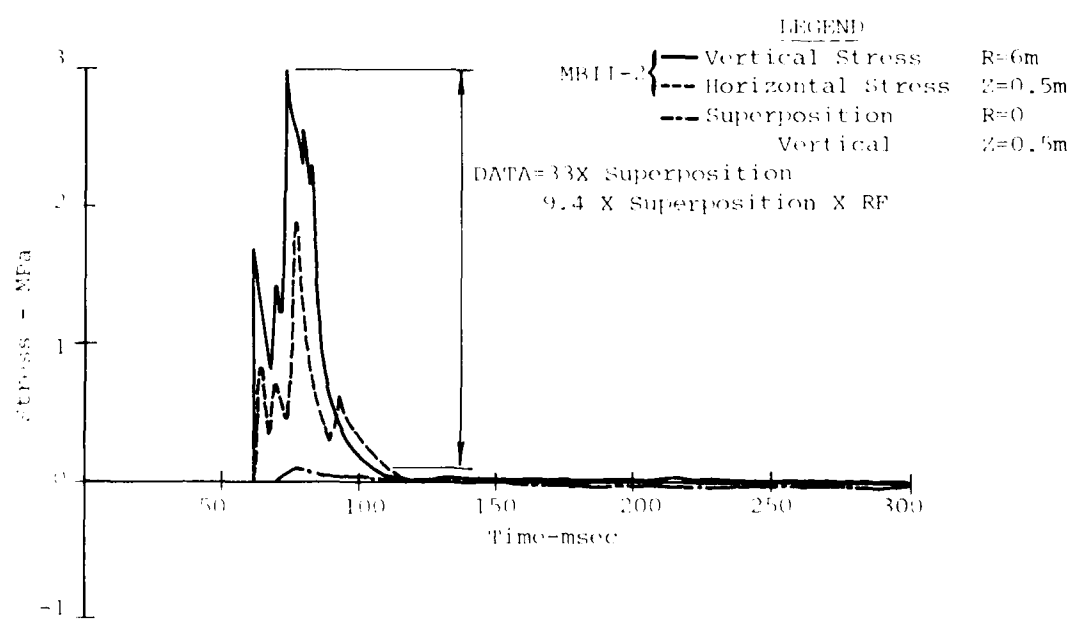
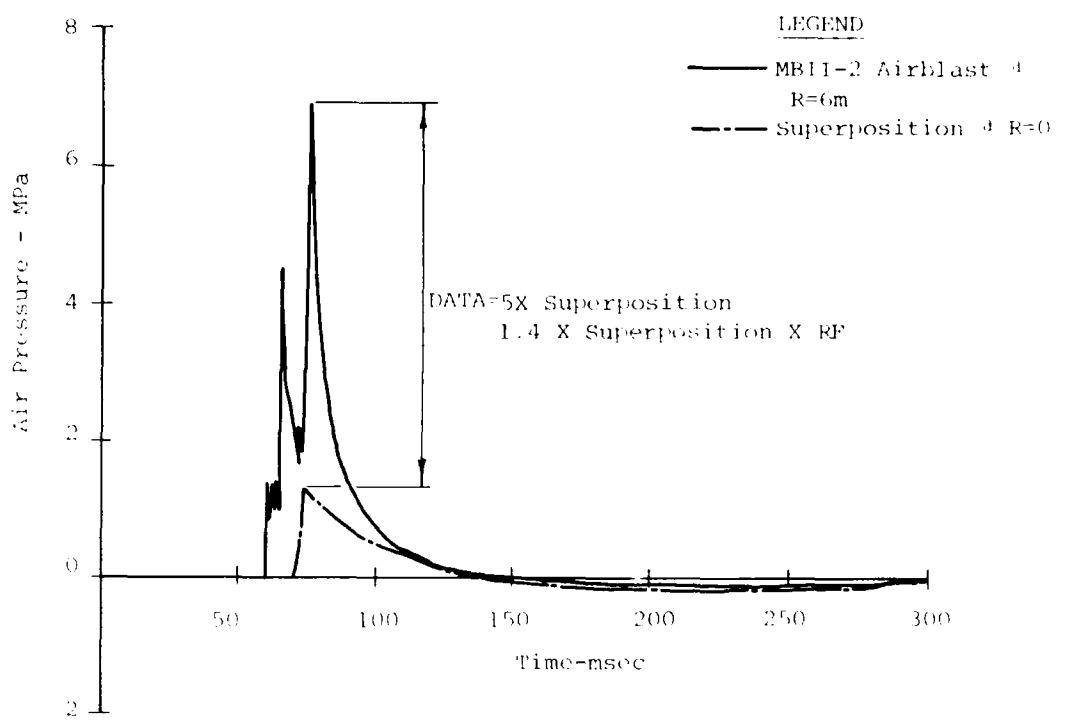


Figure 113. Differences in the Air Pressure and Stress Waveforms Near the Array Center - MBII-2 vs Superposition

reflection factors reduces the difference in the peak airblast values to a factor of 1.4. The stress waveform at the same location for linear superposition shows a peak stress that is a factor of 33 less than the MBII-2 data. If reflection factors are considered, the factor reduces to 9.4. The conclusion drawn from this figure is that the differences in stress cannot be explained only by the differences in the overhead airblast. This increase in stress over superposition and the nonlinear interaction of the air is believed to be attributable to wave convergence. The stress data available to fully evaluate this idea (i.e., to observe airblast and stress behavior at several locations as the center is approached) is nonexistent for these tests.

These observations are felt to provide evidence that wave convergence does exist and can be an important effect. This effect coupled with the pore-air effect acting on the material above can significantly increase the depth extent of spall.

3.3.5 Results of MBII-2 Analysis

The results of the MBII-2 data analysis may be summarized as follows:

- Superposition fails in the airblast related portion of the signal in the near-surface region. This

is not considered a problem because, as was shown, this component can be fairly accurately calculated;

- The pore-air model used in the calculation of MBII-2 compares favorably with data in the near surface region;

- Superposition appears to be accurate for the "late time" low frequency (Rayleigh) motions in the near surface as well as the deeper materials. The early time low frequency (direct wave) motion at locations interior to the array at the 3 m depth, do not appear to attenuate as the array center is approached. This reduces the accuracy of the superposition prediction near the array center, and supports the theory of wave convergence;

- The relationship derived by others concerning the effect of bedrock upon low frequency motions is verified by the results of Misers Bluff;

- The 800 msec signal is thought to be the result of near exact phasing of Rayleigh waves at late times and a weakness plane at the ~26 m depth. The amplitudes of this signal show little attenuation (and in some instances increase) as the array center is approached which provide additional support for the theory of wave convergence;

● The convergence effect appears to exhibit itself in the direct induced motion at the 3 m depth and in the 800 msec signal at the 9m-12.5m depths. The behavior is not shown as a dramatic increase in measured particle velocities as the array center is approached as would be expected, but rather, there is no attenuation in peak motions;

The effect of these observations on the Waveform Synthesis Model will be discussed in the next chapter.

4. Recommended Prediction Procedures

The preceding sections of this report have been concerned with the analysis of the data recorded in Misers Bluff Phase II. This included evaluation of various prediction procedures used pretest and posttest. The culmination of the study and evaluation of these procedures is a Waveforms Synthesis Model (WSM) for predicting multiple burst ground motions.

4.1 Air-Slap Component

4.1.1 Single Burst

Near surface vertical single burst air slap motions were well calculated by the PLID 1-D finite difference model. This is especially true of the compressive phase. In the airblast negative phase the pore-air expansion model provides a substantial improvement over the past procedures. The main problem is in determining the correct (realistic) material properties that reflect the in-situ properties of the site.

For the horizontal air-slap signal the AFDM procedure is the best available at this time. This procedure should be used only for the compressive portion of the airblast as the negative phase appears to be primarily a vertical effect. This procedure does not account for the airblast induced shear

wave seen in data. This shear wave clips the horizontal air slap and shortens the duration of the outward pulse. Thus the prediction should produce somewhat higher magnitudes and longer pulse durations than what will actually occur. This will result in design conservative estimates of the horizontal air slap induced ground motion in the single burst environment.

4.1.2 Multiple Burst

The vertical near surface multiple burst air slap motion can be calculated in the same manner using the multiple burst airblast as the driver.

The horizontal air slap is handled in a slightly different way. The approach used is basically the same as in the single burst, but due to the directionality of the horizontal motions in the multiple burst environment, each burst must be handled individually and then superimposed to form the complete waveform. To account for the airblast nonlinearities a reflection factor is calculated. This factor is the ratio of the peak overpressure calculated for the vertical motions (from LAMB) to the peak overpressure calculated by superposition (as described above). This is only a "first cut" approach at this point and a more refined technique will be developed in the near future.

4.2 Crater-Related and Oscillatory Components

4.2.1 Single Burst

The recommended procedure for the prediction of these components is the WES procedure discussed in previous sections. This procedure appears to provide adequate prediction of frequencies but shows a tendency to overpredict magnitudes. Another observation about this procedure is that the first cycle of motion (which close to a charge is the crater-related portion of the signal) is down and out. This is contrary not only to Misers Bluff but to the rest of the data base. This indicates that a modification to the procedure may be in order. The remainder of the signal is adequate.

4.2.2 Multiple Burst

The recommended procedure is to determine the low frequency motion due to a single burst and use linear superposition to obtain the multiple burst ground motion. Superposition is an adequate technique for the low frequency motion outside the charge array and for the oscillatory component inside the array. Study of the limited amount of data available (Section 3.3.4.5) suggests that the crater-related component may not attenuate inside the inner half of the charge array. This nonlinear behavior is treated by the Waveform Synthesis Model with an empirical developed algorithm.

4.3 Waveforms Synthesis Model (WSM)

The WSM is a compilation of computer codes for applying the procedures discussed above to the prediction of waveforms from multiple explosions. The WSM contains six basic elements. They are:

- A statistical package which allows Monte Carlo treatment of the uncertainties in CEP, height of burst, and time on target,
- An air slap induced prediction procedure which uses the LAMB (Ref. 22) to predict the multiburst air pressure waveforms at points of interest and a one-dimensional finite difference code (PLID) which includes the pore air expansion model, to calculate the air slap induced vertical ground motions.
- The Waterways Experiment Station low frequency prediction procedure which yields empirical predictions of the crater-related and surface wave effects based on a compilation of high explosive and nuclear data.
- A routine for calculating the proper time phasing and geometrical relationships of the contribution of each single burst to the horizontal air slap motions at designated target points, modifying the magnitudes by reflection factors, and combining these effects,

- Algorithms for adjusting the linear combinations of low frequency motions to account for the nonlinearities.
- An input/output routine to provide plots and listings of pertinent data.

A generalized flow diagram for the WSM is shown in Figure 114.

This program has evolved over the last two years. Previous versions contained different methods of predicting both the air slap and low frequency effects. The current version represents the state-of-the-art procedures discussed above. The algorithms for treating the nonlinearities represent the greatest uncertainty in the procedure although it should be emphasized that uncertainties in single burst predictions are inherent in this procedure.

Figures 115 through 123 show comparisons of the WSM with some Misers Bluff single burst and multiple burst data. The measured overpressures from MBII-1 and MBII-2 were used to generate the WSM waveforms. This was done because our concern was to determine the accuracy of the WSM in calculation of ground motion. These figures show that in the vertical motions the WSM is reasonably accurate. This is true of both the single and multiple burst environment. The horizontal motions in the single burst environment were adequate but were not as accurate as the corresponding vertical motions.

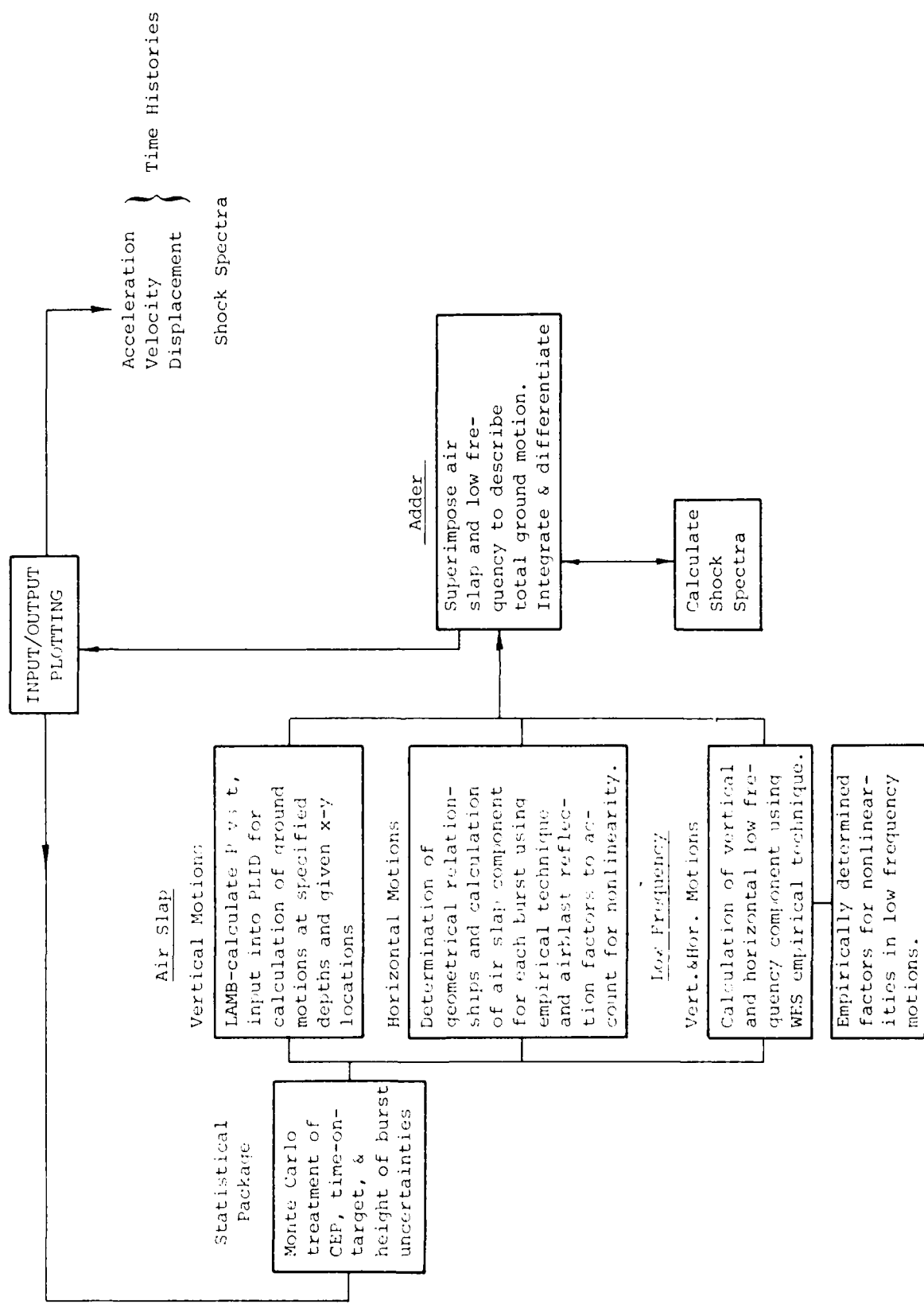


Figure 114. Generalized Flow Diagram of WSM

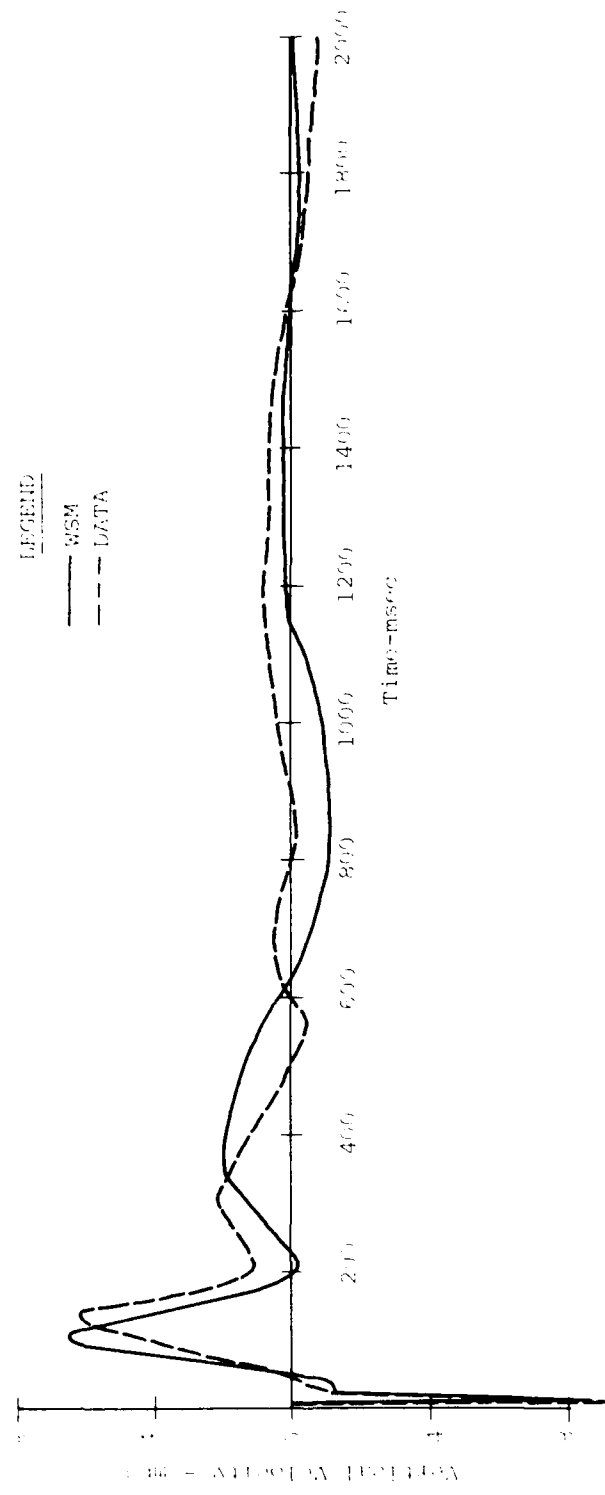


Figure 115. Comparison of MBII-1 Data and the Waveforms Synthesis Model
at R=25 m; z=0.5 m

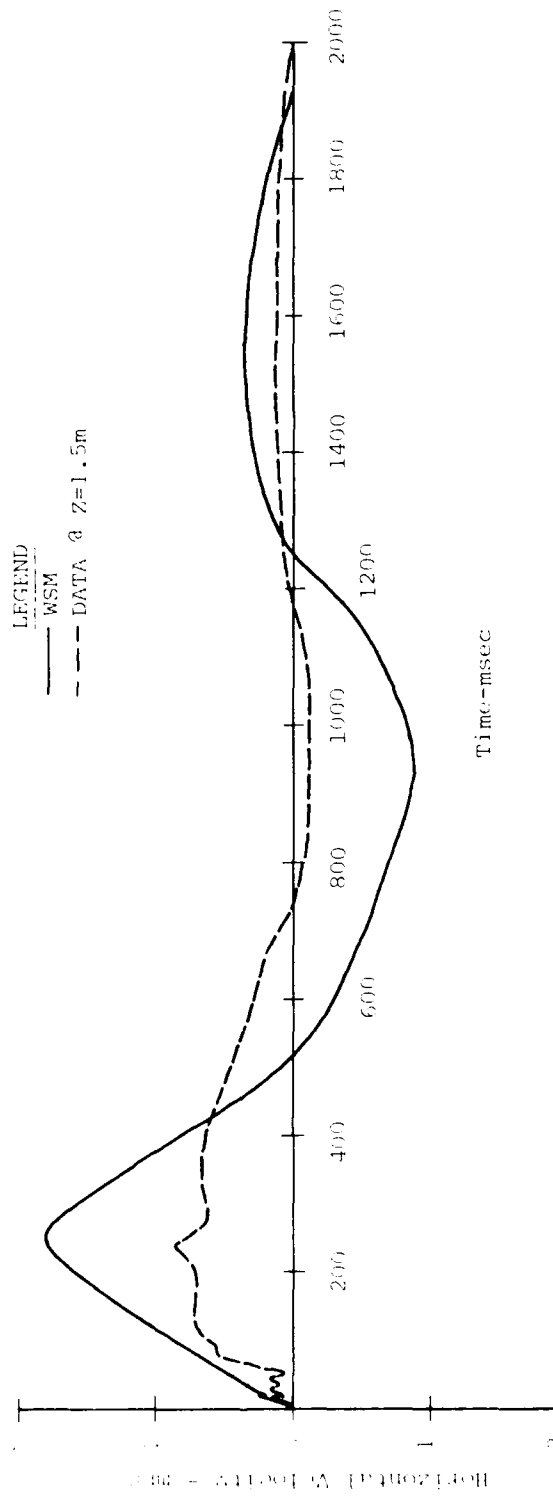


Figure 116. Comparison of MBII-1 Data and the Waveforms Synthesis Model @ $R=25\text{ m}$; $Z=0.5\text{ m}$

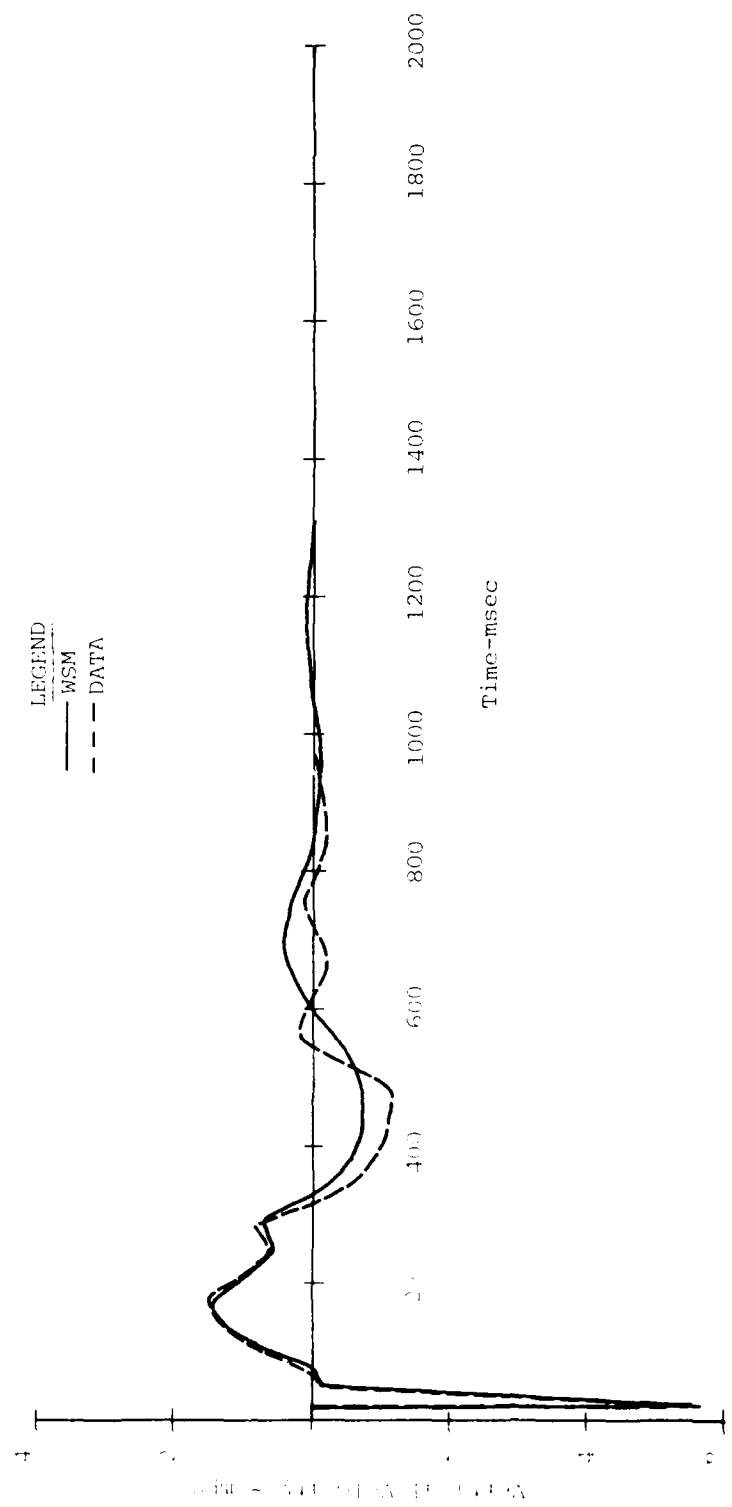


Figure 117. Comparison of MBII-1 Data and Waveforms Synthesis Model at R=50 m; Z=0.5m

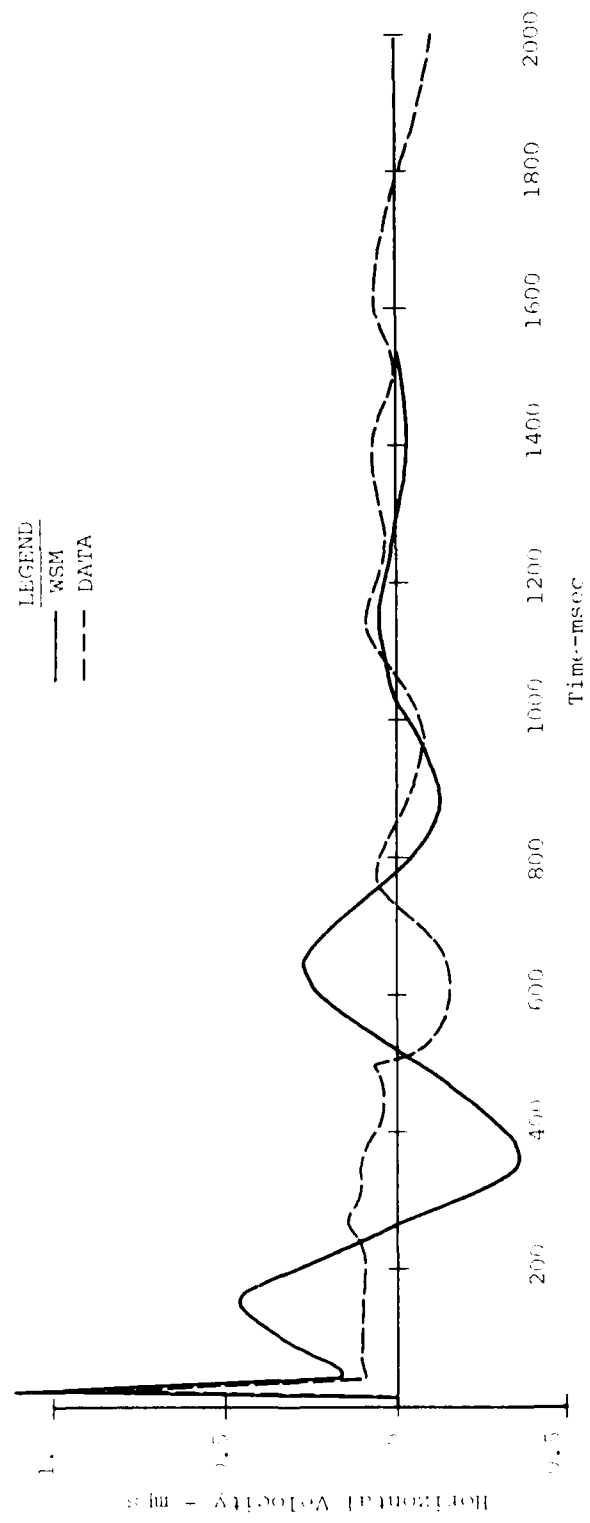


Figure 118. Comparison of MBII-1 Data and the Waveforms Synthesis Model at R=50m; Z=0.5 m

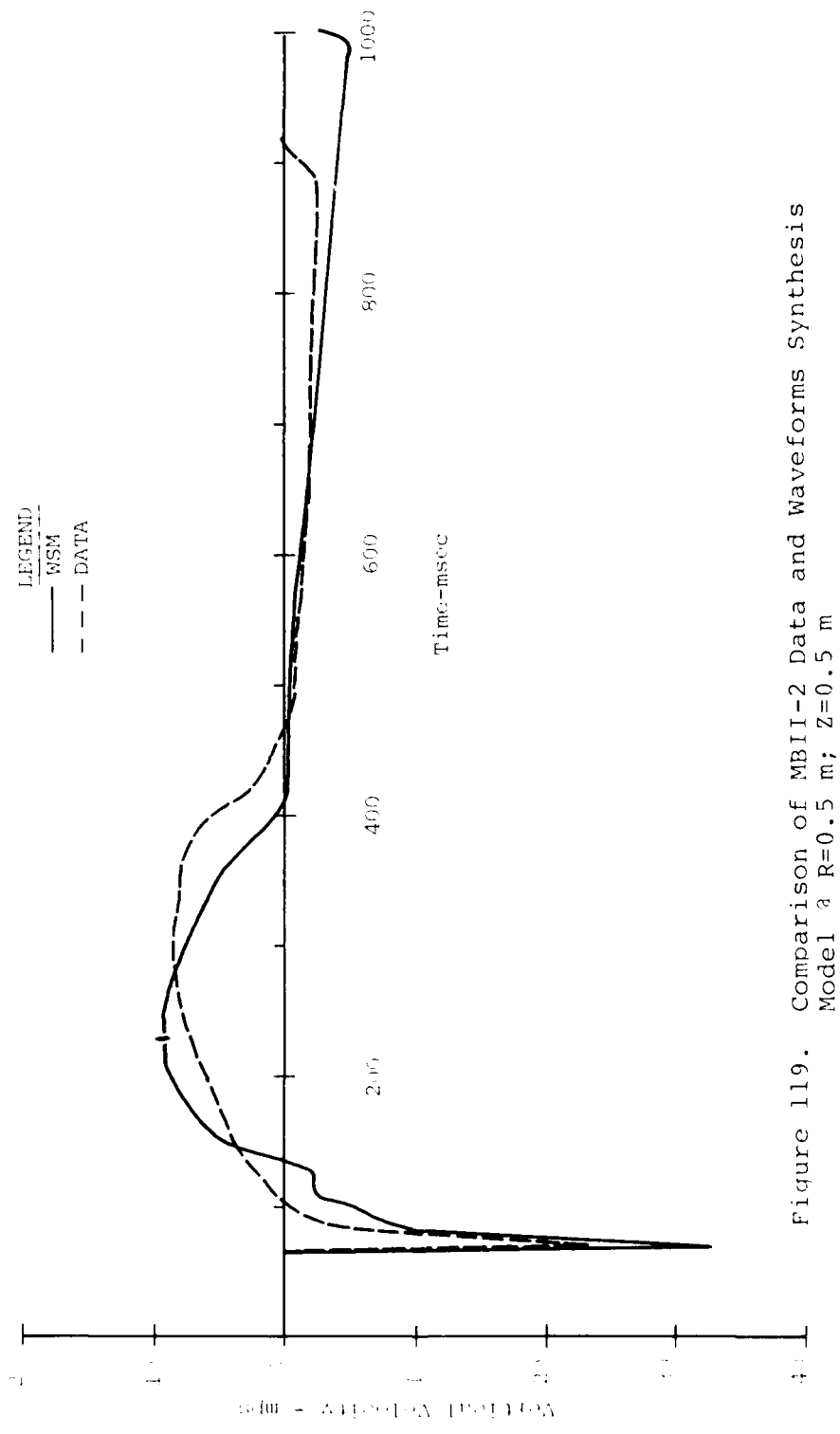


Figure 119. Comparison of MBII-2 Data and Waveforms Synthesis
Model a R=0.5 m; Z=0.5 m

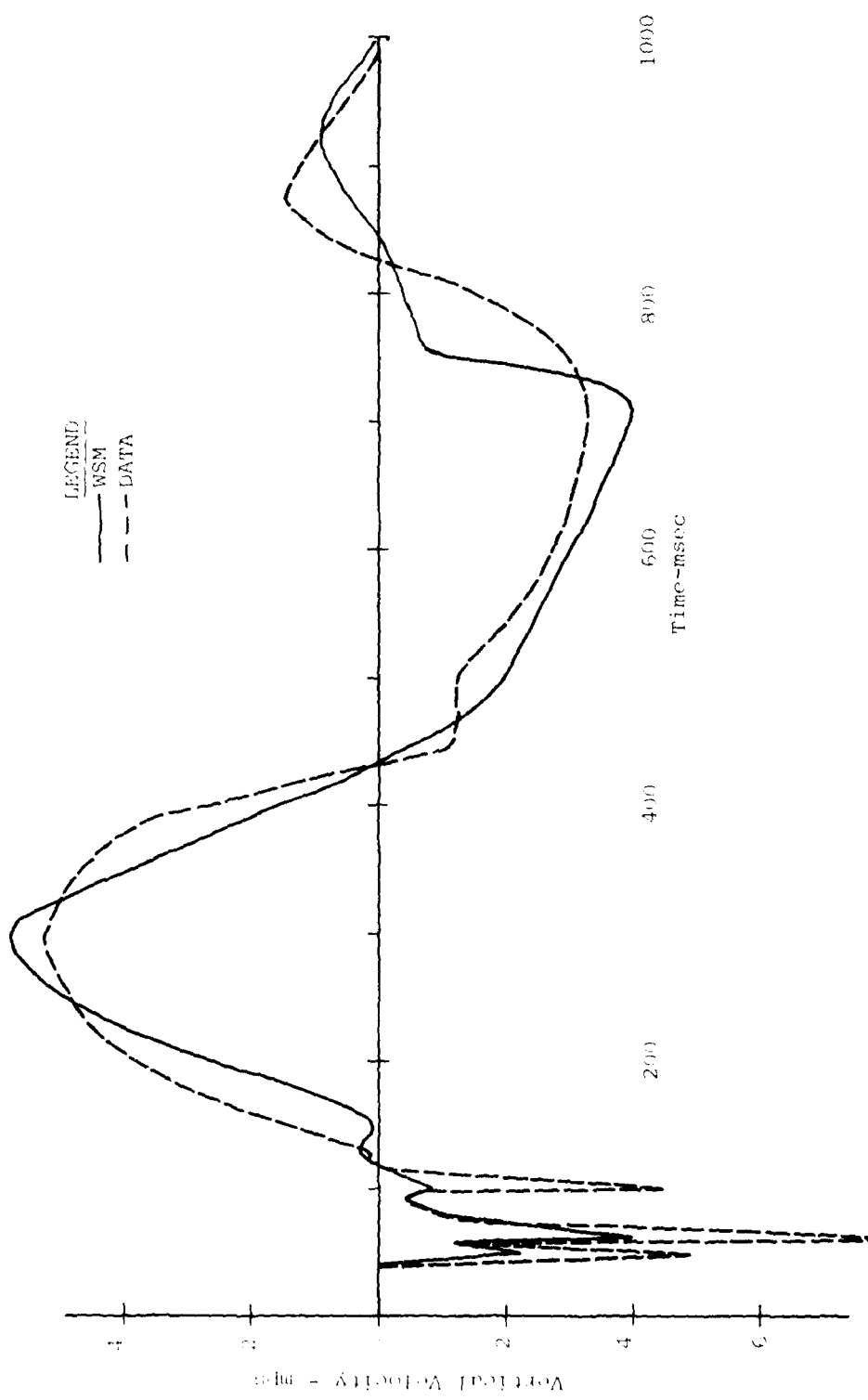


Figure 120. Comparison of MBII-2 Data and Waveforms Synthesis Model a R=25 m; z=0.5 m; Charge Line

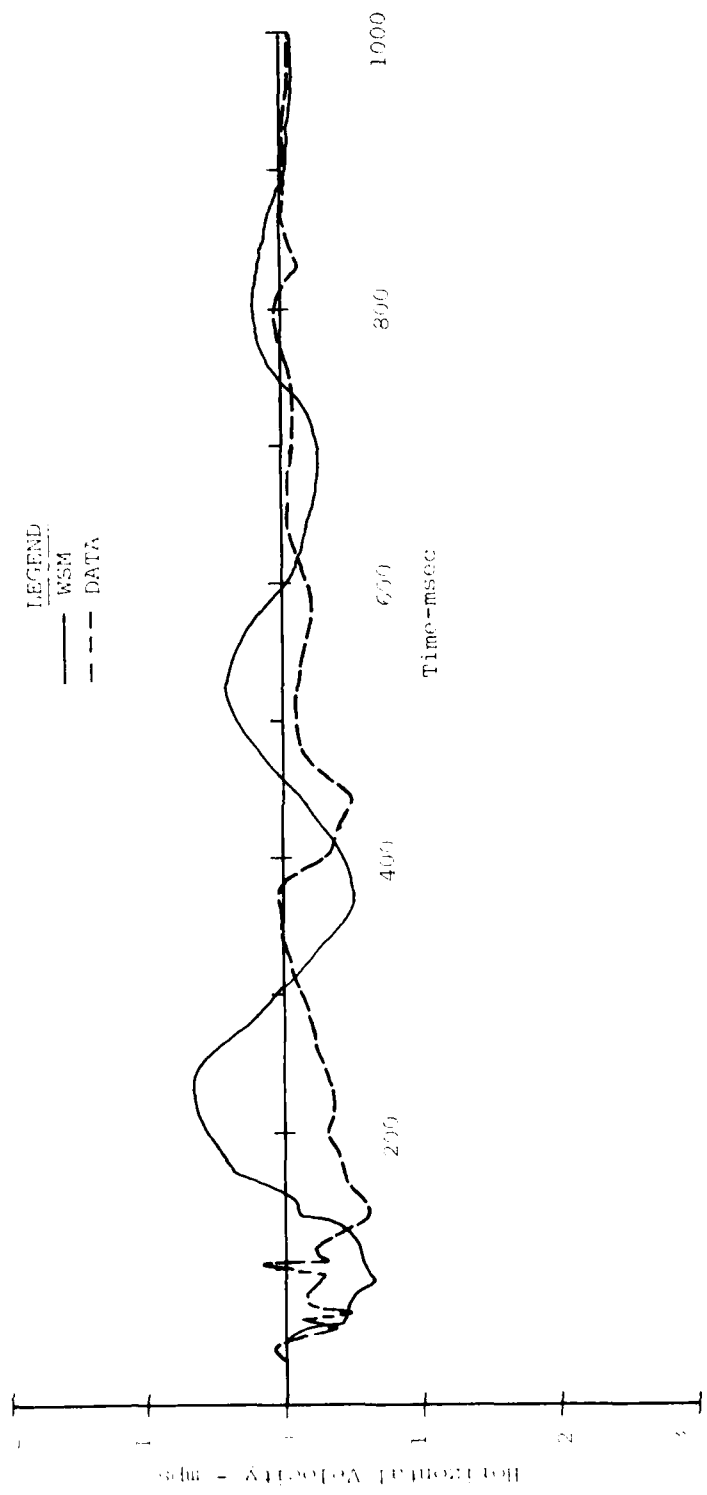


Figure 121. Comparison of MBII-2 Data and Waveforms Synthesis Model 3 R=25 m; Z=0.5 m; Charge Line

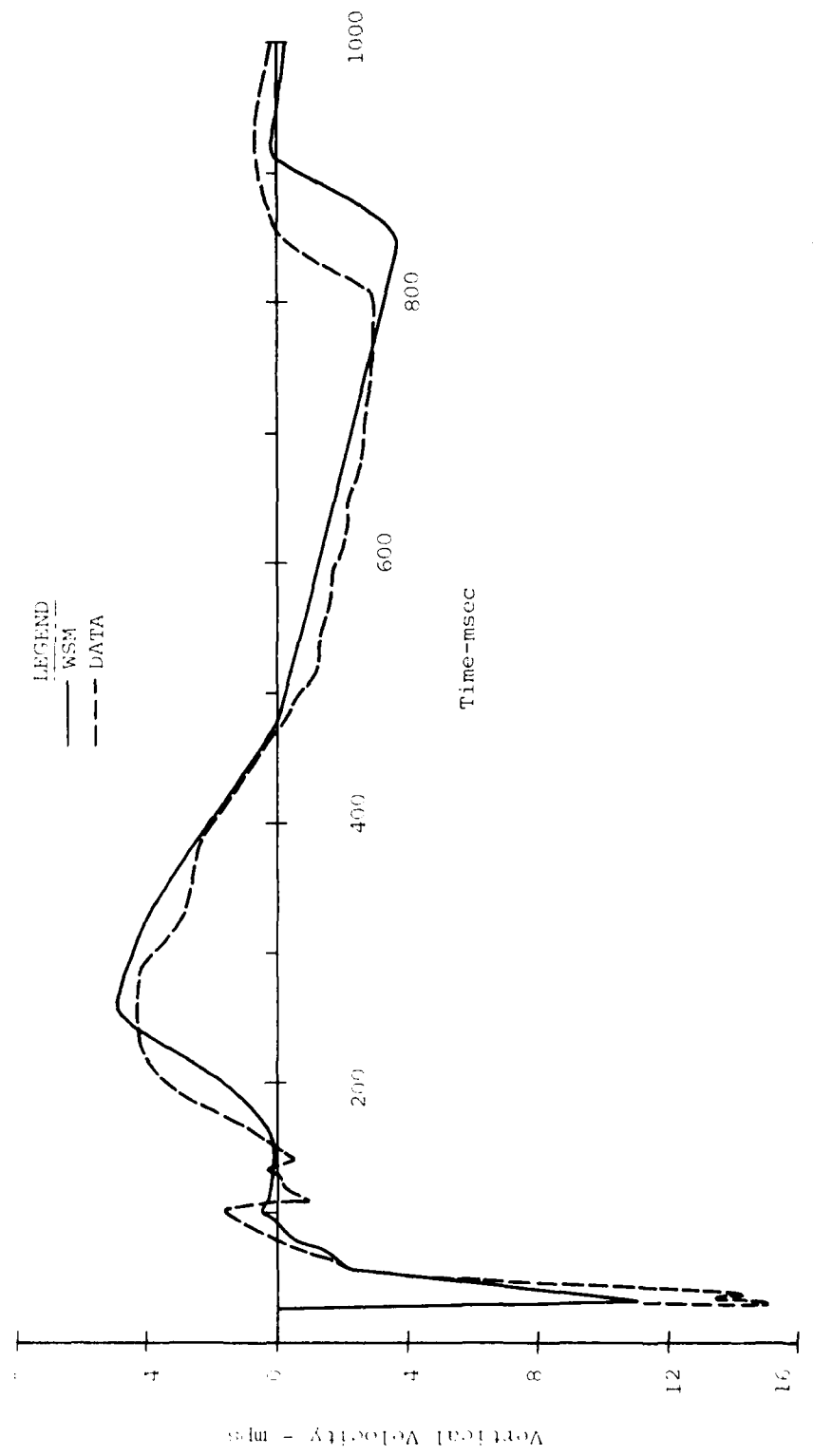


Figure 122. Comparison of MBII-2 Data and Waveforms Synthesis
Model 1 @ R=50 m; z=0.5 m; Bisector

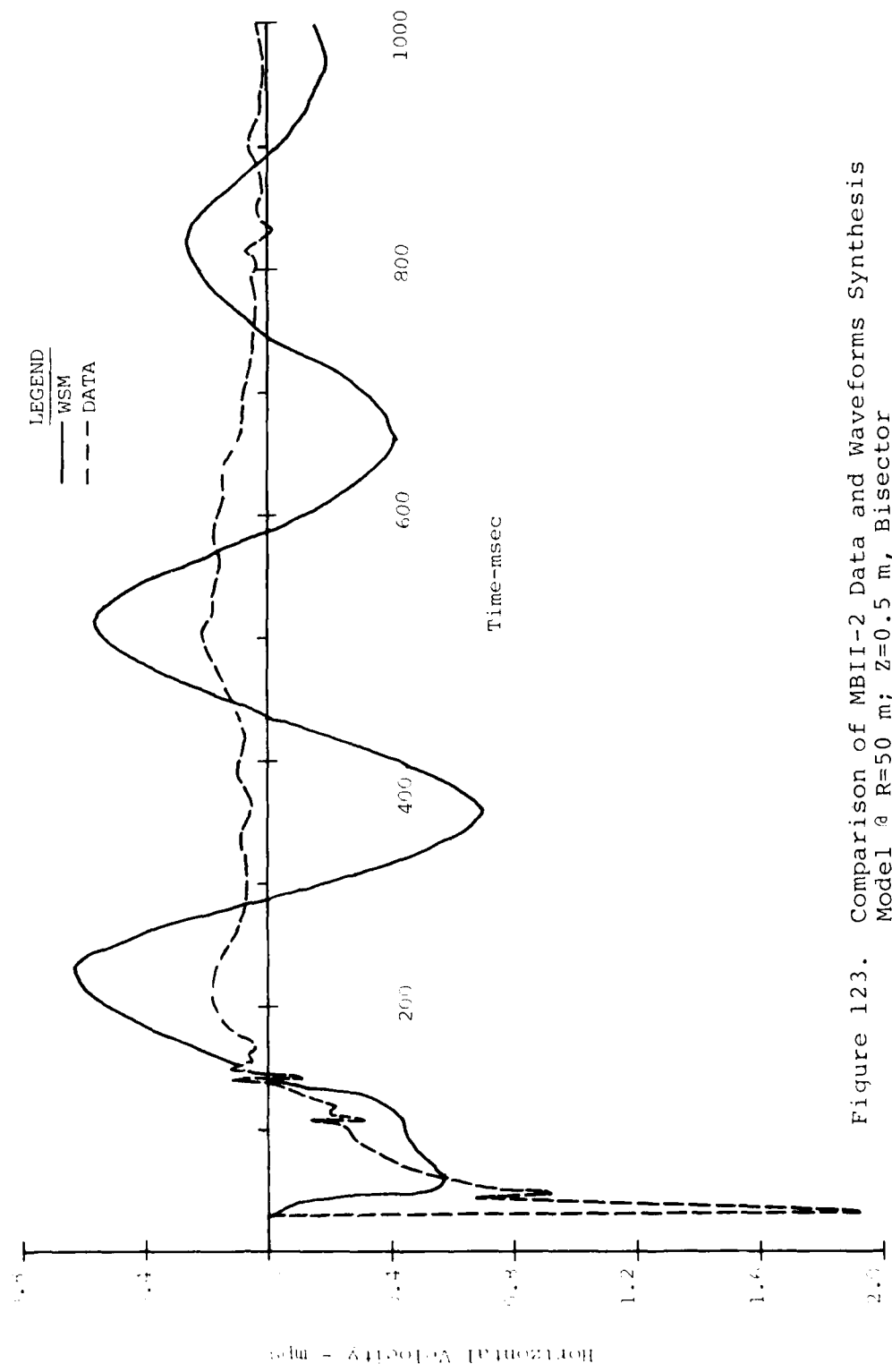


Figure 123. Comparison of MBII-2 Data and Waveforms Synthesis
Model at R=50 m; z=0.5 m, Bisector

The accuracy level of the horizontal motions degenerated further in the multiple burst environment. It appears that the prediction of horizontal motions in both single and multiple burst environments require further study and refinement.

5. Conclusions and Recommendations

5.1 Conclusions

This analysis of the Misers Bluff Phase II data focused on an evaluation of ground shock prediction procedures for both single and multiple burst conditions. The conclusions listed below, therefore, reflect the validity of those procedures and for the multiple burst event compare the results with the Phase I findings.

5.1.1 Event II-1 (Single Burst)

- The near surface vertical air-slap motions were well predicted by the 1-D finite difference calculational procedure. Addition of the first order pore-air model significantly improved the comparison of the later time upward motions.
- The pore-air expansion model is quite sensitive to small changes in the tensile strength, air void content and layer reflections which are very difficult to establish in-situ. The 1-D calculational procedure must correctly model gravity to yield creditable late time calculations.
- Horizontal air-slap motions semi-empirical predictions are acceptable but omit the airblast induced shear wave which often results in the peak amplitude and shortens the horizontal outward pulse.

- The low frequency components of motions were predicted within the scatter of data upon which the empirical predictions were based. However, the WES procedure does not allow the crater-related pulse to propagate at a different velocity from the surface wave component. They both currently propagate at p-wave velocities. This leads to peaks in the oscillatory component occurring too early at larger ranges.

- Prediction of the frequency of the surface wave component based on the depth-weighted shear wave speeds and the depth to rock resulted in good agreement with the data.

5.1.2 Event II-2 (Multiple Burst)

- Superposition of single burst data provided acceptable predictions of the multiple burst event at all measurement stations outside the explosive array and within half the charge spacing away from the charge. These locations were also well predicted by superposition in Misers Bluff Phase I.

- The superposition predictions were not satisfactory for all components near the surface and for the crater related component at depth in the center half of the array. However, near the surface, the peak downward vertical velocities were well predicted by the 1-D calculations when the airblast shock-on-shock interactions were properly treated. The

peak upward vertical velocities were predicted much better by superposition than in Phase I, but the displacements were significantly underpredicted. Utilization of pore air expansion model in the 1-D calculation improved the displacements and did not significantly alter the upward velocities. Superposition predicted the upward velocities because the single burst spall radius was greater than the charge spacing whereas in Phase I it was less than the charge spacing. Correction of the superposition prediction to preserve -lg during free fall also improved the displacement prediction significantly.

- The near surface horizontal motions were not predicted satisfactorily by superposition. These motions appear not to be significantly affected by the pore air expansion phenomenon, but indicate, as do the deeper horizontal motions, that the geometry of the experiment (wave convergence) is resulting in larger motions than predicted by superposition. In Phase I superposition did a better job of predicting these horizontal motions, indicating a possible geology or yield effect.

- The principle nonlinearities causing the failure of superposition were the nonlinear equation of state of air, the pore-air expansion phenomenon, the geometry leading

to the wave convergence effects (related to the constitutive equations of the soil) and the nonlinearities associated with free fall after spall. Theoretical analysis of the first two of these are reasonably well in hand, but pretest evaluation of the in-situ soil properties controlling the pore air expansion represent a problem in practice. The wave convergence phenomenon is a two-dimensional approximation of the three-dimensional case. Since no three-dimensional theoretical work has been done, this effect can only be treated in an approximate manner. Spall can be treated theoretically, however the empirical predictions used for some components of the single burst in the Waveform Synthesis Model do not treat spall, therefore, there is currently no way to explicitly predict spall and to make subsequent corrections.

- The "800 msec signal" observed MBII-2 is a multiple burst effect related to the convergence of Rayleigh waves and the specific geology at this site. It's occurrence is not predictable at this time, but it could occur for other sets of conditions as well.
- The Waveform Synthesis Model has been significantly improved as a result of the Misers Bluff II-2 experiment and it does a creditable job of predicting that event. It is currently useable for predicting nuclear events, however some uncertainty remains with respect to wave convergence and spall effects.

5.2 Recommendations

Although this study resulted in substantial increase in understanding of the ground motion phenomenology, there are still areas of ground motion that need additional study for both the single and multiple burst case. These are, in order of priority:

- Study of spall and/or tensile behavior of soil subjected to surface explosive loading. This phenomena has been studied as it applies to metals and rocks but very little work has been devoted to soils. Spall is playing an important role in observed ground motion data and research to understand and predict this phenomenology should be pursued.
- Experiments should be conducted to study multiple burst ground motion in the absence of local airblast. This would be instructive in evaluating wave convergence effects of low frequency motions. This study should be complimented by 2-D and 3-D calculations to evaluate the 2-D approximations and aid in extrapolating the test results.
- The effect of pore-air expansion on the current crater-volume scaling techniques needs to be evaluated. Identification of those test sites which are susceptible to pore-air expansion could lead to better understanding of this effect and could influence the crater volume scaling relationships.

- The WES empirical prediction procedures do not explicitly separate upstream-airblast, crater related and surface-wave effects. As discussed above, the latter of these should propagate at different wave speeds. Addition of a stronger theoretical basis to the WES procedure would lead to better waveform prediction and greater confidence in extrapolating to greater yield.
- Analytical studies to evaluate the relative contribution of upstream-airblast and crater-related (direct-induced) effects would improve significantly our understanding of the low frequency motion components and the origin of surface waves. After a qualitative understanding of the relative effects for a variety of geologic and loading conditions has been developed, experiments to quantify the results should be planned.
- A study of the design implications of the transverse component of horizontal ground motion should be conducted. This could provide guidance for analysis of the data and in planning future experiments.
- The horizontal air-slap component of ground motion can be better described by inclusion of the air slap induced shear wave in the prediction. Development of a simplified procedure to treat this effect in the semi-empirical predictions should be undertaken.

REFERENCES

1. The Data Analysis Working Group, A Review of High Explosive Testing to Investigate Ground Motions Pertinent to the MX Multiple Aimpoint Systems, DAWG-TR-1, May 13, 1977
2. Phillips, J.S. and Bratton, J.L.; Misers Bluff Phase I Single Burst Experiments: Ground Shock Analysis, DNA 5004Z, Defense Nuclear Agency, Washington, D.C.
3. Phillips, J.S. and Bratton, J.L.; Misers Bluff Phase I Ground Shock Analysis of the Multiple Burst Experiments; DNA 5089Z, Defense Nuclear Agency, Washington, D.C.
4. Melzer, L.S., "The Planet Ranch Test Site Selection," Proceedings of the Misers Bluff Results Symposium, POR 7013-3, March 1979; Defense Nuclear Agency, Washington, D.C.
5. Misers Bluff Test Plan Volume II, Defense Nuclear Agency, 3 April 1978.
6. Jackson, A.E., Jr., Ballard, R.F., Jr. and Phillips, B.R., Geotechnical Investigation for Misers Bluff II: Results from the Subsurface Exploration Programs, U.S. Army Waterways Experiment Station; April 1979.
7. Geotechnical Investigation Misers Bluff Test Program Planet Ranch Test Valley, Arizona, Fugro National, Inc., 15 March 1978.
8. Ballard, R.F., Jr., Geophysical Survey, Misers Bluff - Event II-1; U.S. Army Waterways Experiment Station; 13 October 1978.
9. Crosshole Velocity Survey Misers Bluff Ground Zero-2 Planet Ranch Test Valley, Arizona, Fugro National, Inc., 20 March 1978.
10. Lodde, Peter, "CIST 19 Analysis and Derivation of Dynamic Properties for Misers Bluff Site", AFWL-TR-Air Force Weapons Laboratory, Unpublished.
11. Jackson, A.E., Interim Results from Geotechnical Studies of Misers Bluff, Phase II, Event 1, Letter Report to FC DNA/FCT MOT (Cpt. R.A. DeRaad), 2 October 1978.

REFERENCES (continued)

12. Murrel, D.W. and Stout, J.H., Misers Bluff Series; Phase II, Ground Shock and Airblast Measurements Data Report, U.S. Army Waterways Experiment Station Miscellaneous Paper SL-79-6, March 1979.
13. Edwards, T., MIDDLE NORTH Series, Pre Dice Throw II - Preliminary Results Report, Defense Nuclear Agency POR 6904, September 1976.
14. Rischbicter, F., "Soil Liquefaction - A Survey of Research", 5th International Symposium of Military Blast Simulation, Volume III, Royal Swedish Fortifications Administration; Stockholm, Sweden, May 1977.
15. Melzer, L.S., "The Nature and Effects of Explosive (in soil)", Transcripts of the International Workshop on Blast-Induced Liquefaction 10926-002-86, Dames and Moore, London, January 1979.
16. Crawford, R.E., Higgins, C.J., and Bultmann, E.H., The Air Force Manual for Design and Analysis of Hardened Structures, AFWL-TR-74-102, Air Force Weapons Laboratory, October 1974.
17. Ullrich, G.W., "Airblast/Ground Motion Effects from Simultaneous Detonation of High Explosive Charges", Nuclear Technology Digest, Vol. 1, Air Force Weapons Laboratory, 1978.
- 18.
18. Hurdle, P.M. and Port, R.J., MX Multiburst Ground Motion Study, RDA-TR-104806-007, October 1977.
19. Higgins C.J. and Schreyer, H.L., An Analysis of Outrunning Ground Motions, AFWL-TR-74-220, Air Force Weapons Laboratory, May 1975
20. Review of "Parametric Nuclear Weapons Environment for MX Multiple Aimpoint Basing Systems Definition", Appendix B; Prepared by the Data Analysis Working Group, DAWG TR-3, 14 December 1978.
21. Murphy, John R., Analysis of the Low Frequency Ground Motion Environment for MX Surface Waves and Valley Reverberation; DNA 5210, Defense Nuclear Agency, Washington, D.C.

REFERENCES (continued)

22. C.E. Needham and L.A. Wittwer, The Air Force Weapon Laboratory Low Altitude Multiple Burst (LAMB) AFWL-DYT-TN-75-2, Air Force Weapons Laboratory, Kirtland AFB, New Mexico 1975, Unpublished.
23. Kuhl, A.L., Simplified Analysis of Multiburst Shock Interactions, RDA-TR-107006-010, June 1978.
24. Fillipelli, K., Presented to the 19th DAWG meeting, Minutes of the 19th DAWG meeting held May 1979.
25. Review of "Parametric Nuclear Weapons Environment for MX Multiple Aimpoint Basing Systems Definition", pages 28-31, Prepared by the Data Analysis Working Group, DAWG TR-3, 14 December 1978.
26. Murphy, John R., An Analysis of the Characteristics of Rayleigh Waves, DNA 4826, Defense Nuclear Agency, Washington, D.C., 1980.

APPENDIX A
Superposition vs Data
Waveform Comparisons

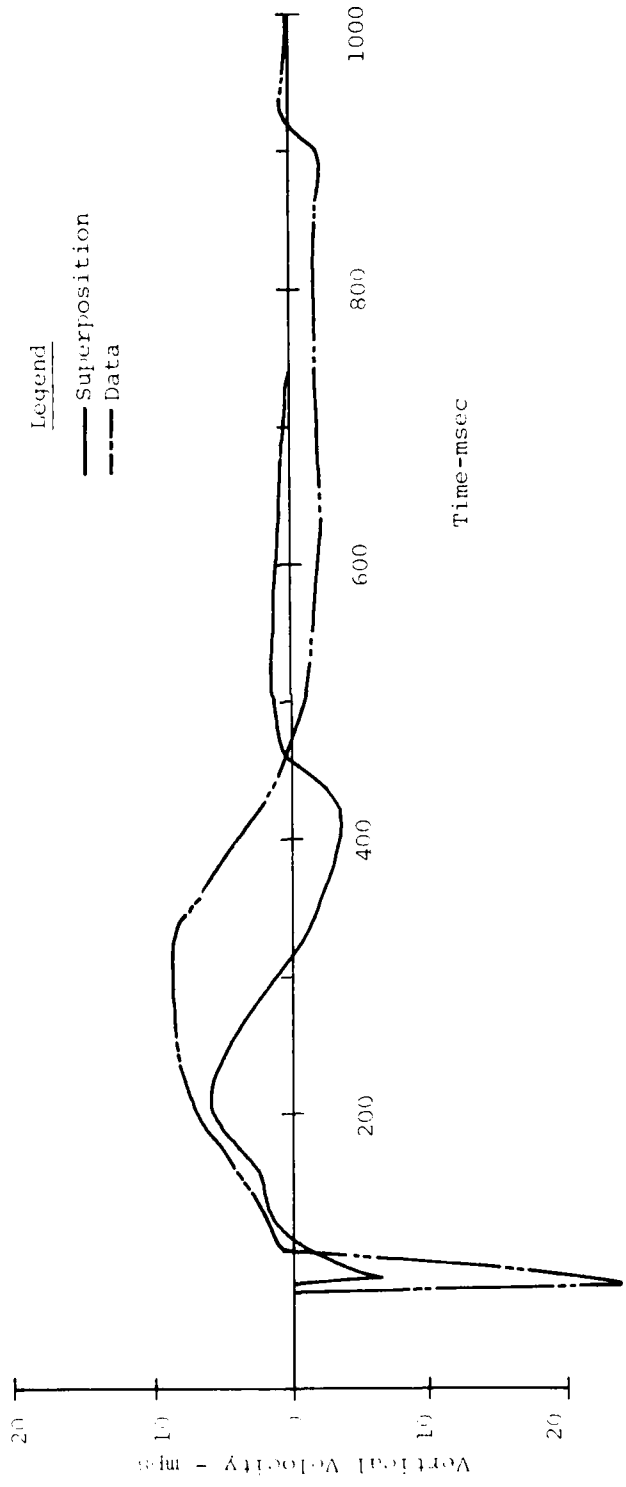


Figure A.1. Comparison of MBII-2 Data and Superimposed MBII-1 Data
at 0-0.5-Vertical Velocity

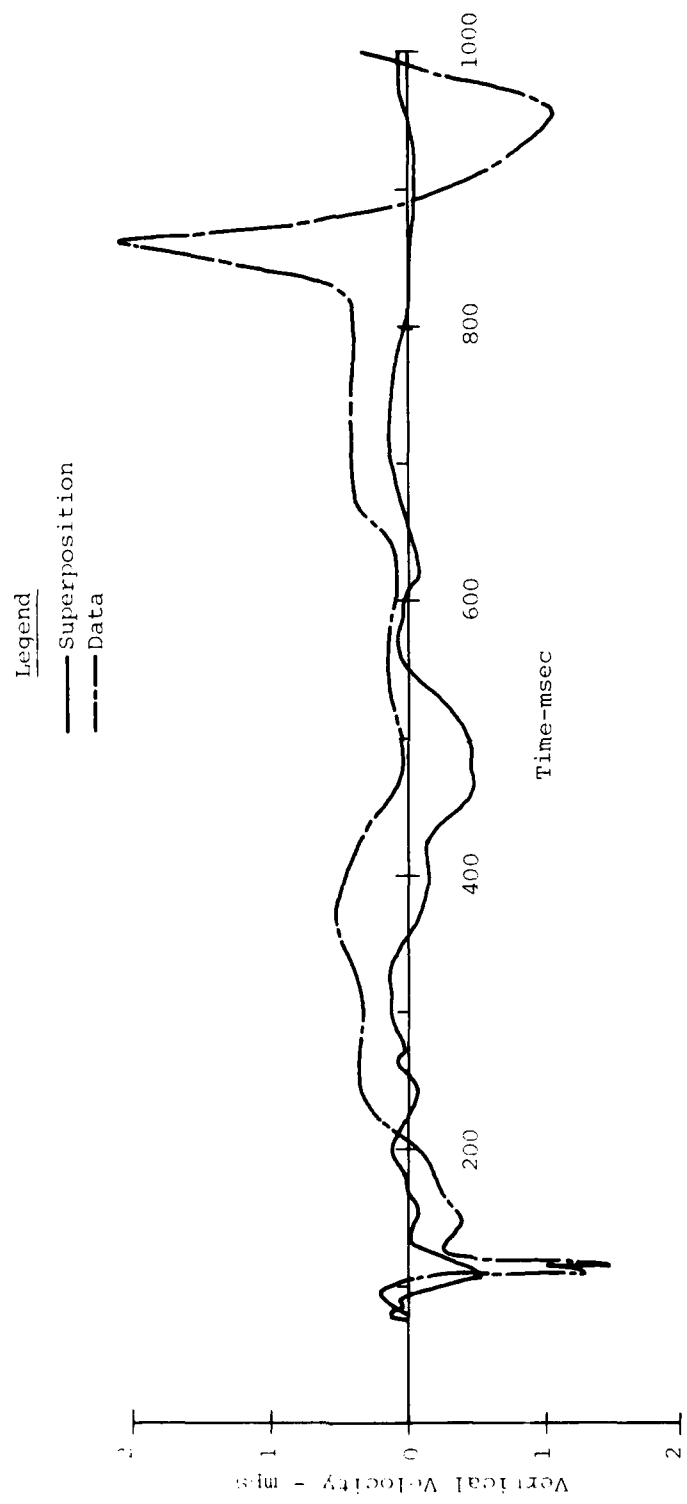


Figure A.2. Comparison of MBII-2 Data and Superimposed MBII-1 Data
a 0-9-Vertical Velocity

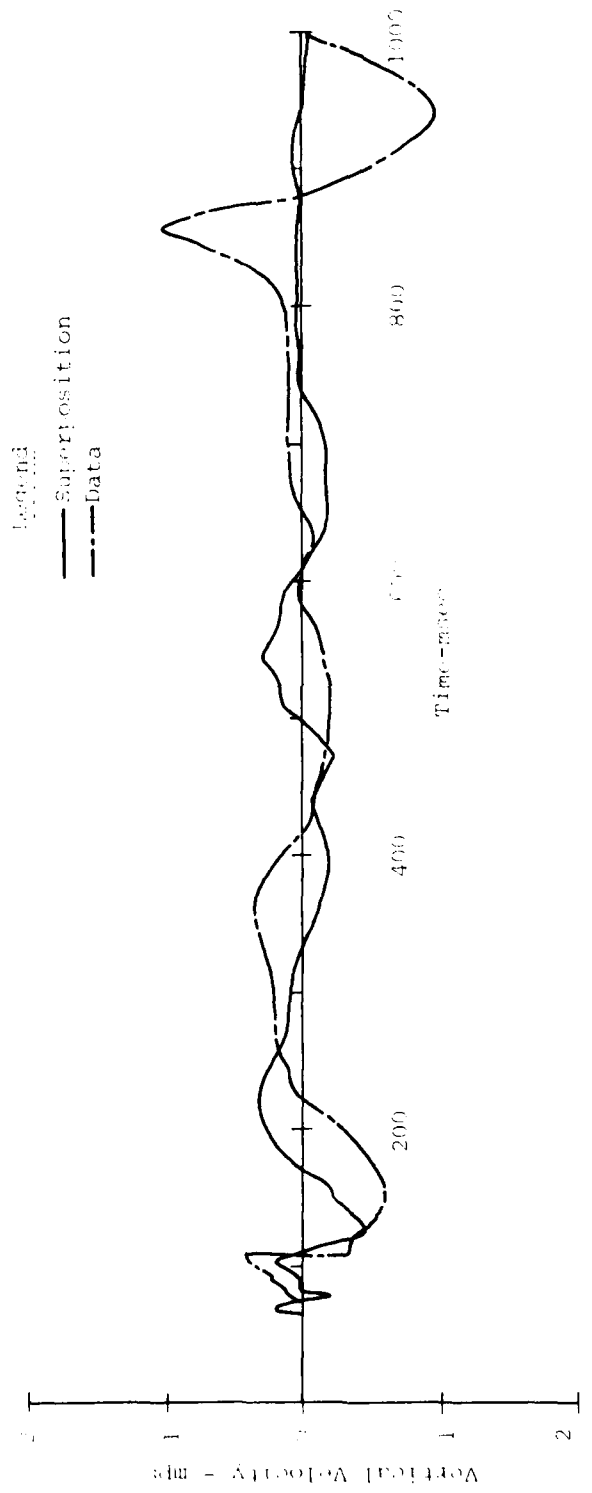


Figure A.3. Comparison of MBLI-2 Data and Superimposed MBLI-1 Data
at 0-12.5-Vertical Velocity

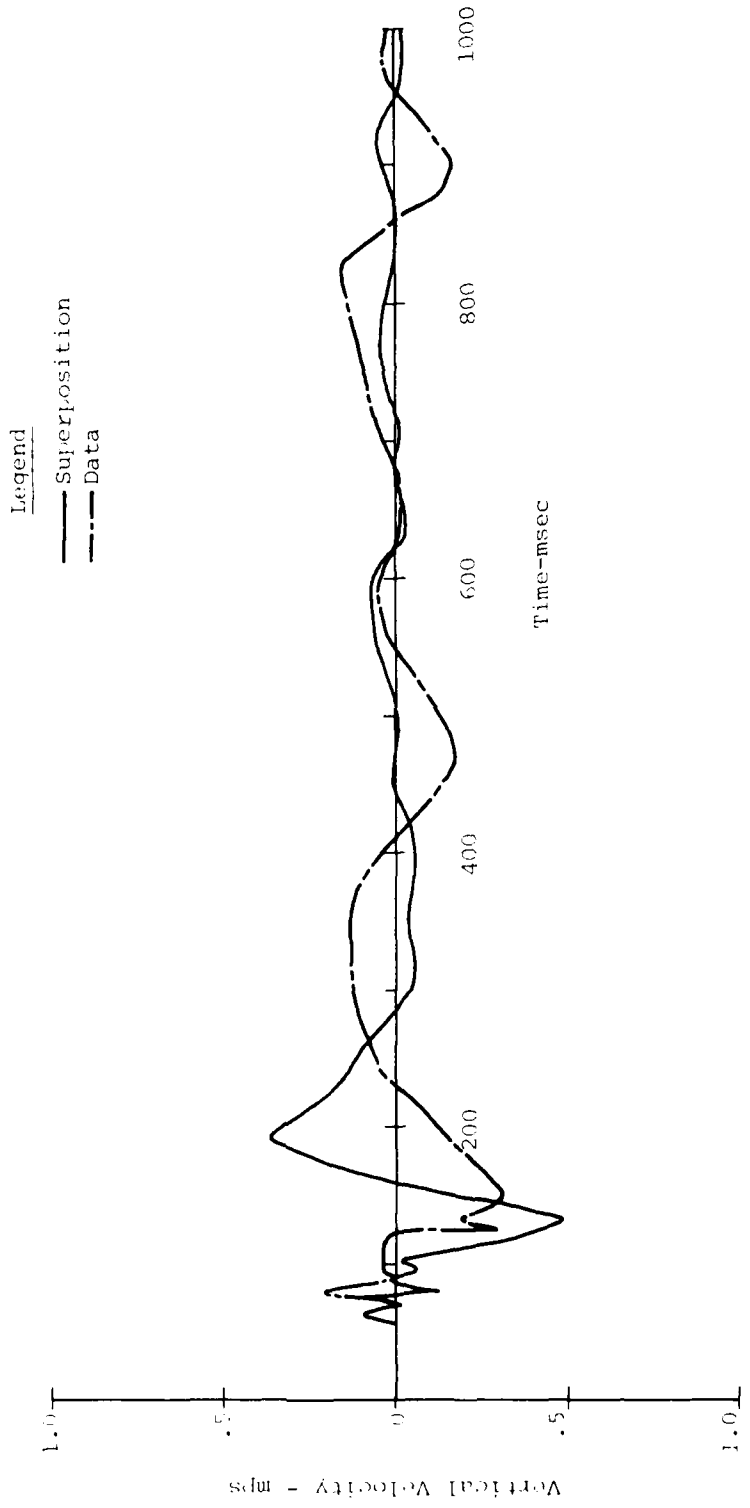


Figure A.4. Comparison of MBII-2 Data and Superimposed MBII-1 Data
@ 0-25-Vertical Velocity

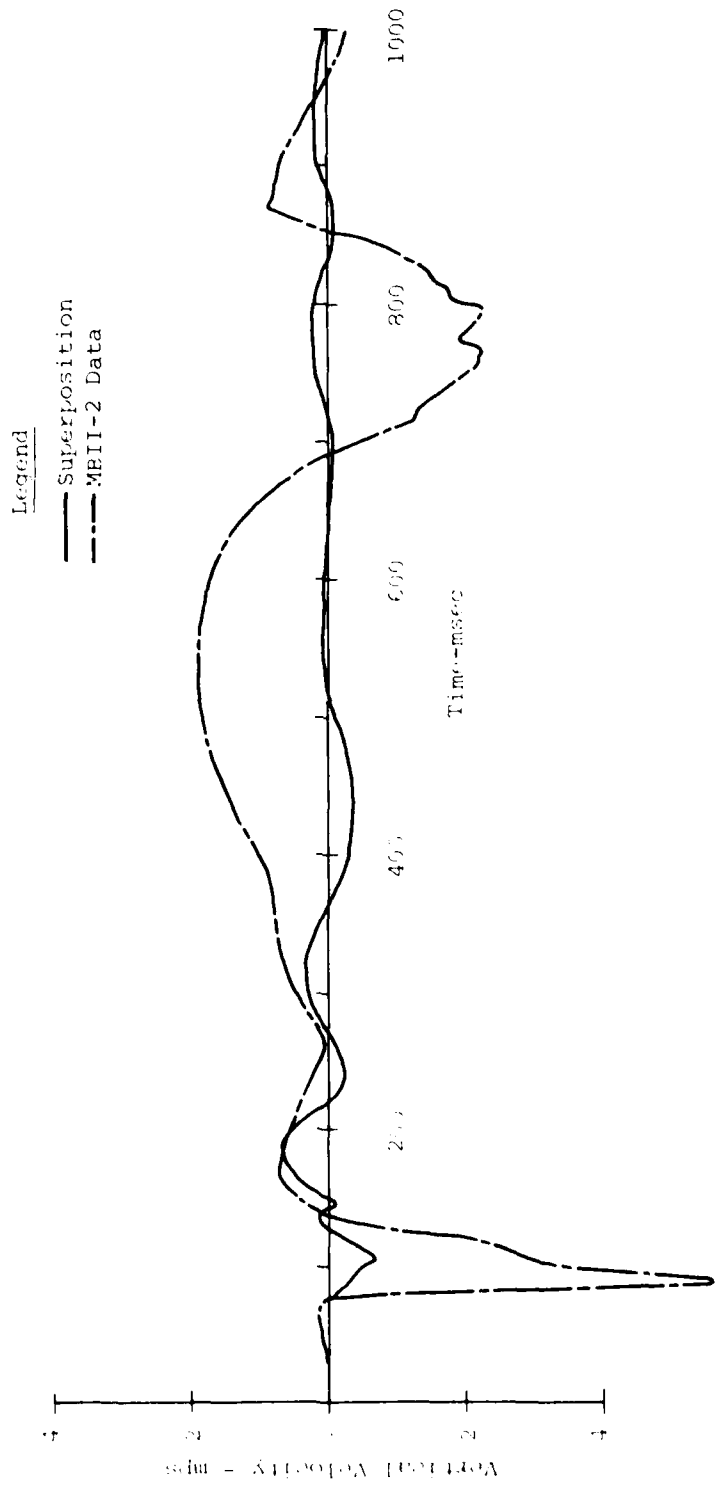


Figure A.5. Comparison of MBII-2 Data and Superimposed MBII-1 Data
of 6-3-Charge Line-Vertical Velocity

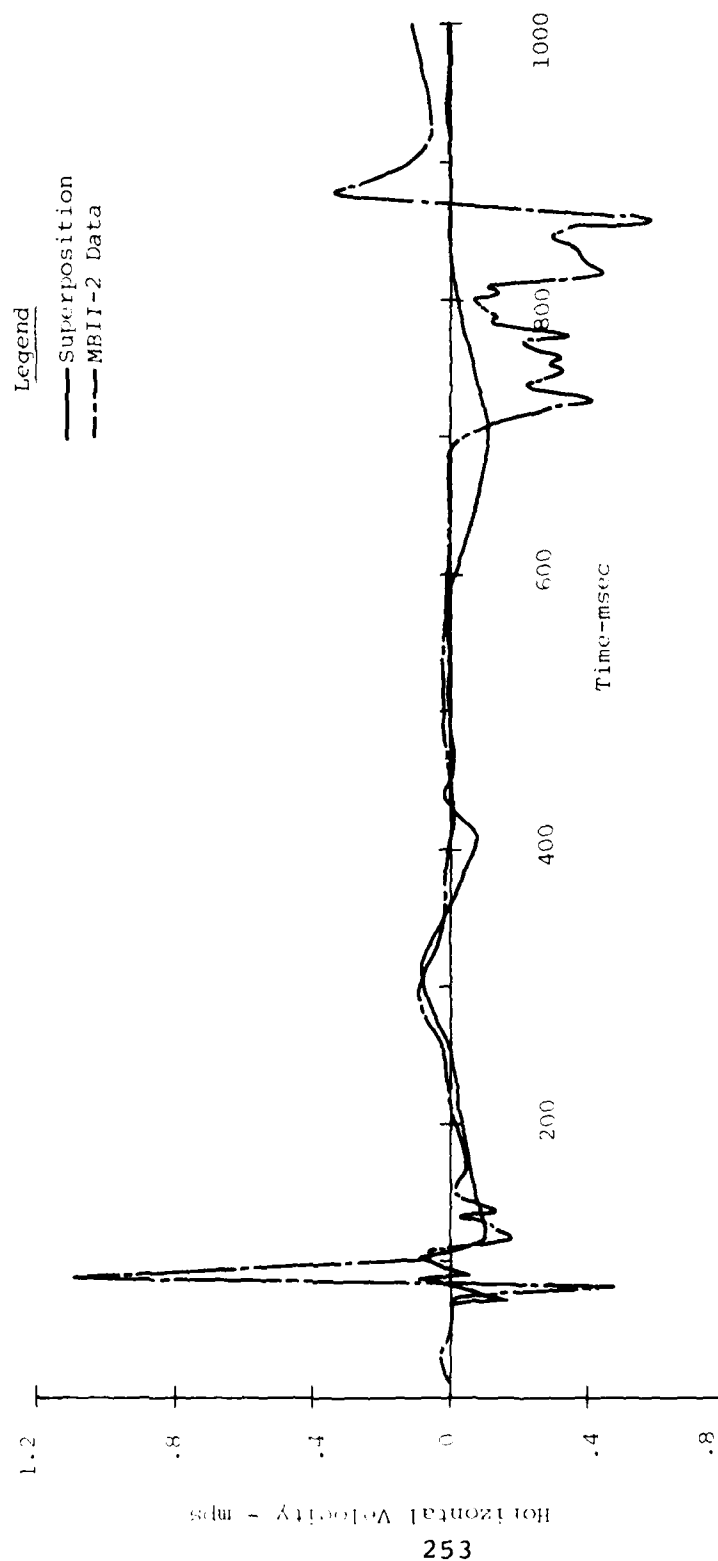


Figure A.6. Comparison of MBII-2 Data and Superimposed MBII-1 Data
at 6-3-Charge Line-Horizontal Velocity

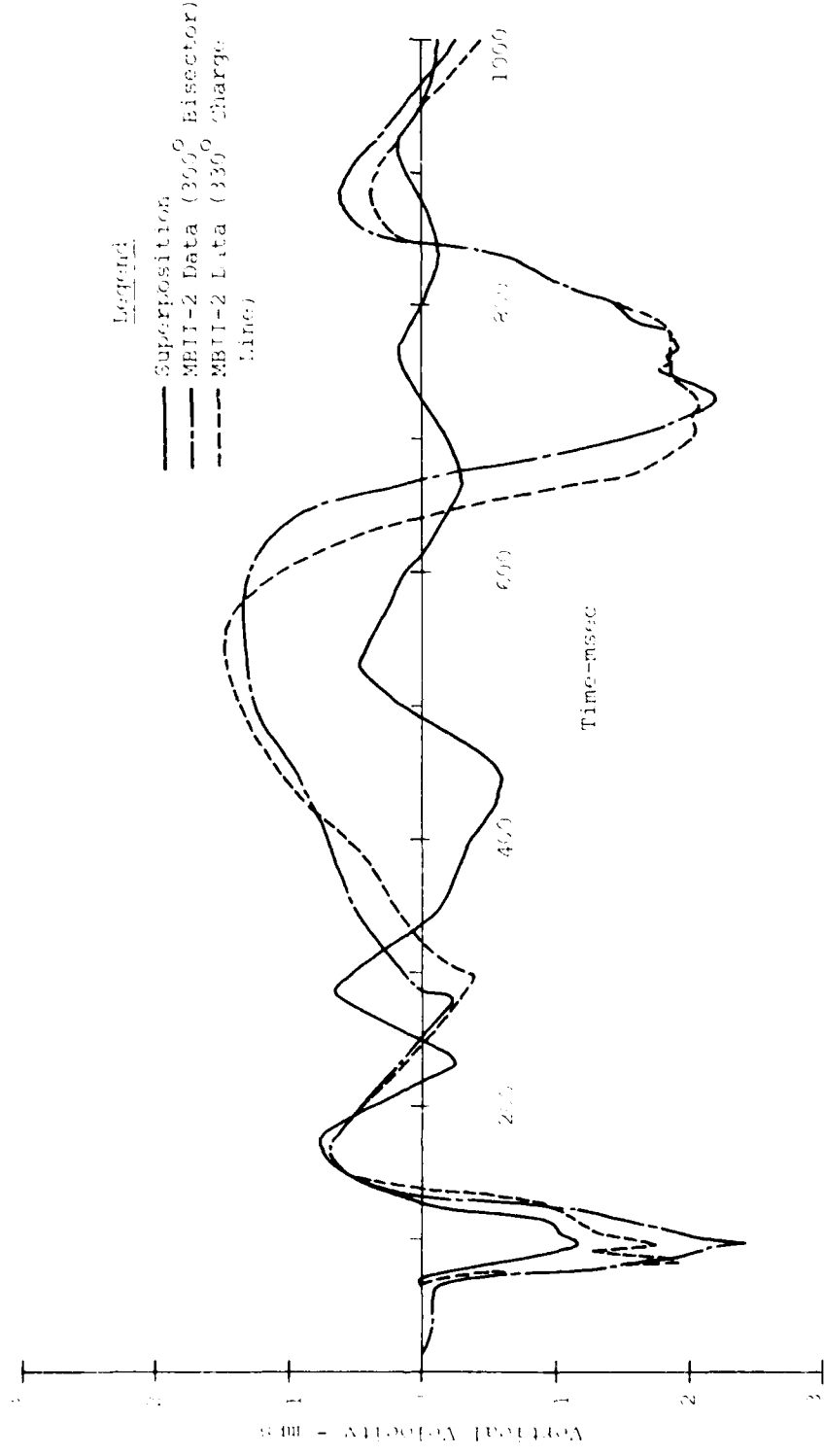


Figure A.7. Comparison of MBII-2 Data and Superimposed MBII-1 Data at 12.5-3-Bisector-Vertical Velocity

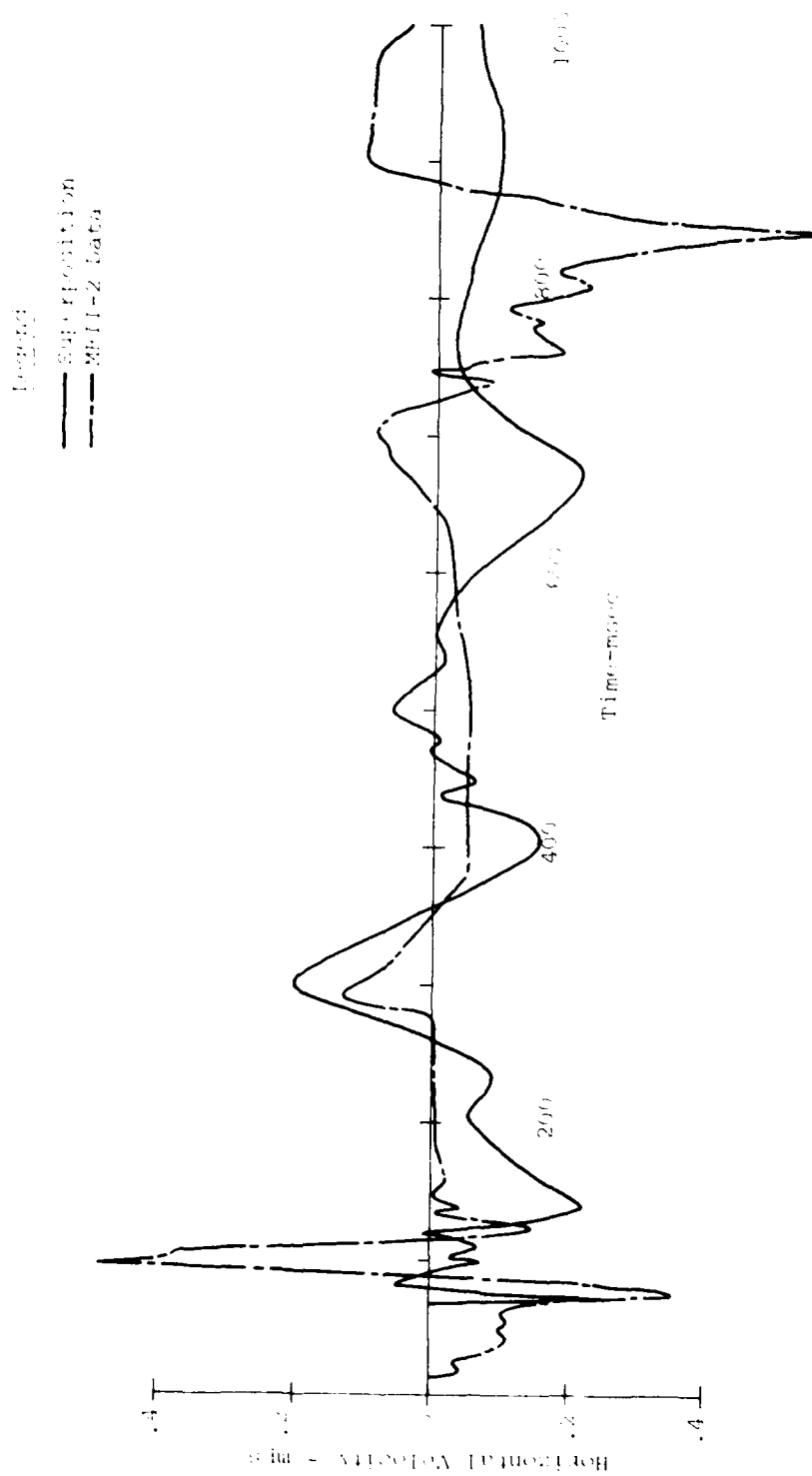


Figure A.8. Comparison of MBII-2 Data and Superimposed MBII-1 Data
a 12.5-3.0-Bisector-Horizontal Velocity

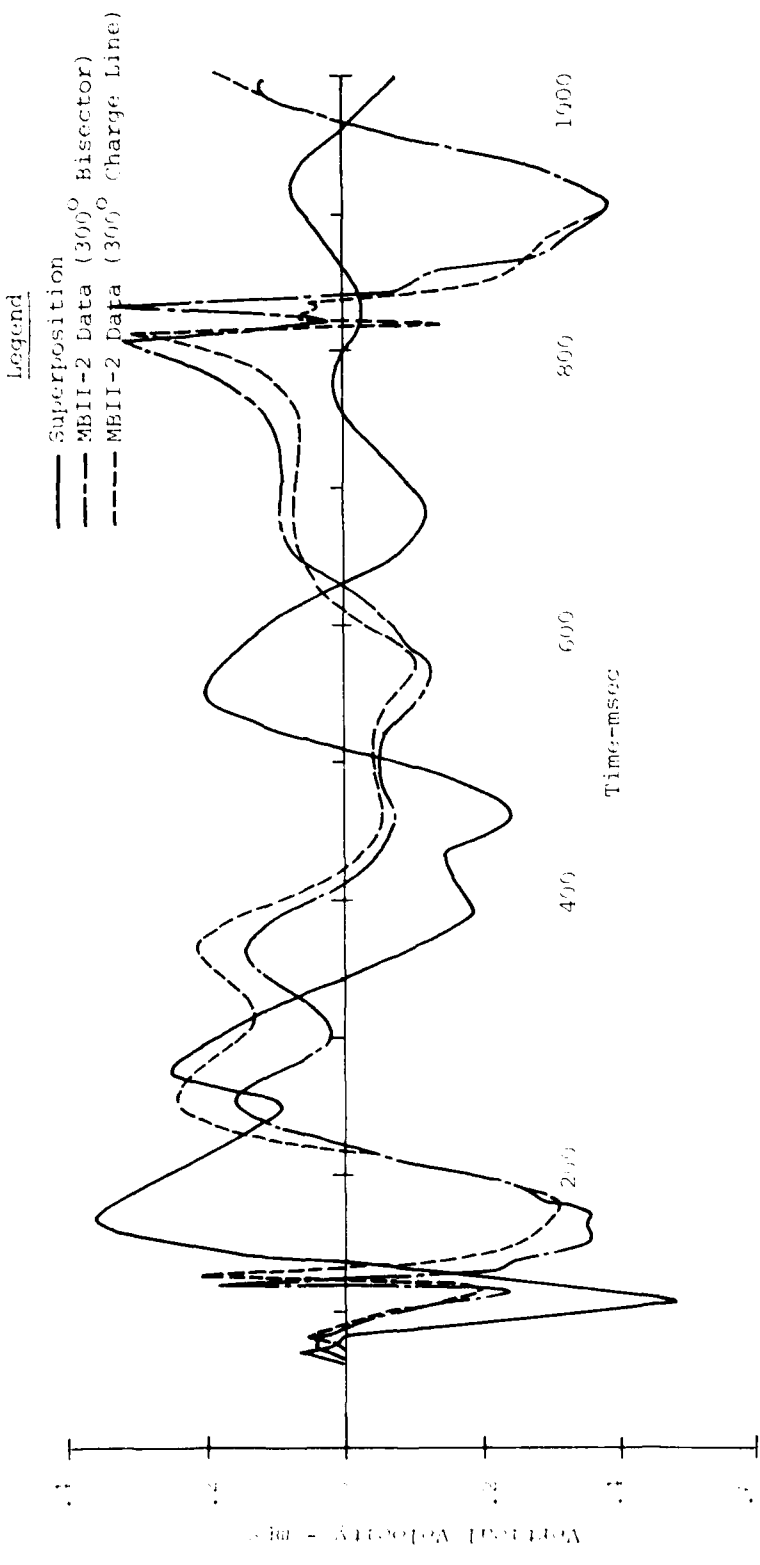


Figure A.9. Comparison of MBII-2 Data and Superimposed MBII-1 Data at 12.5-9-Bisector-Vertical Velocity

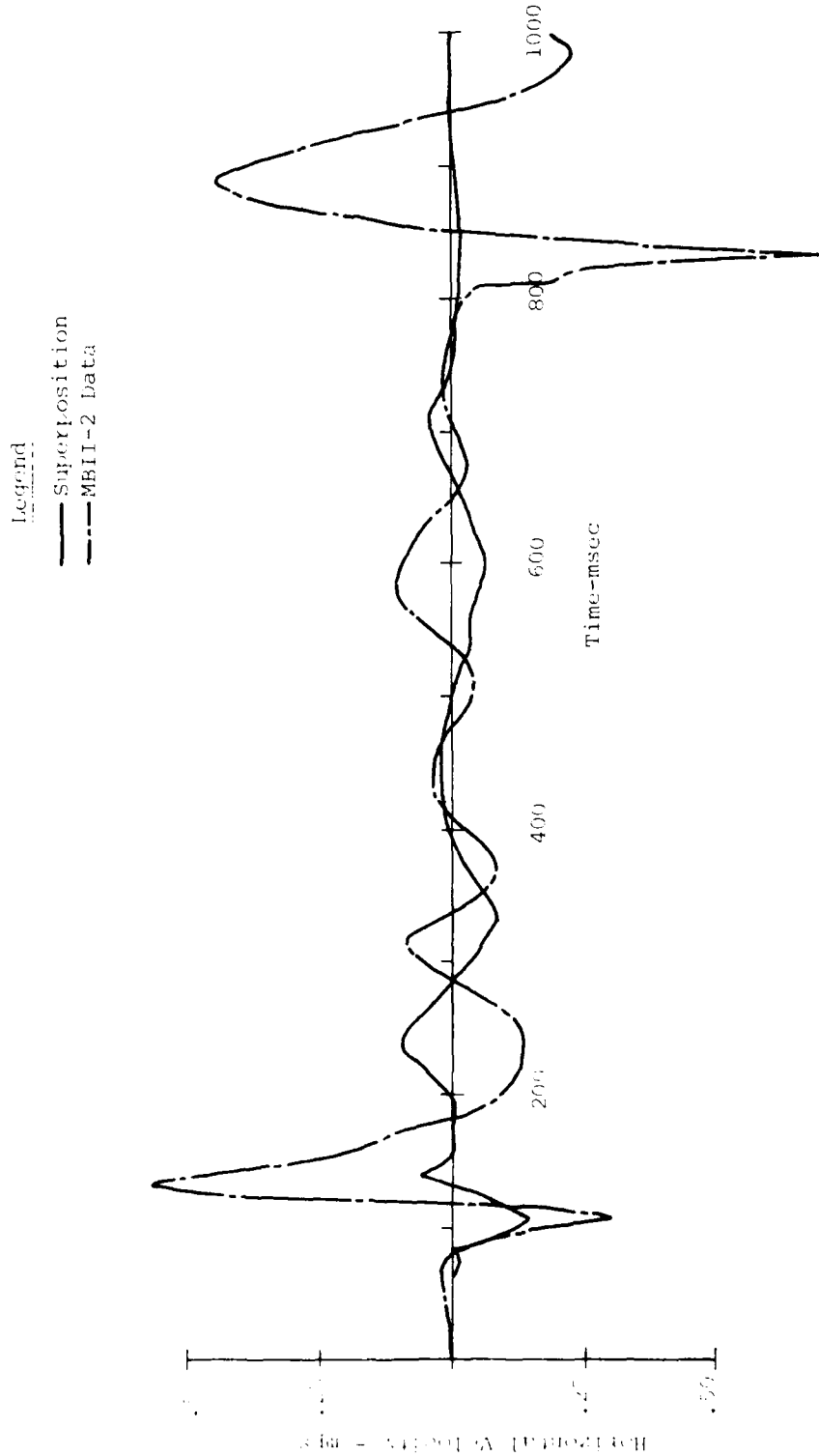


Figure A.10. Comparison of MBII-2 Data and Superimposed MBII-1 Data
at 12.5-9.0-Bisector-Horizonal Velocity

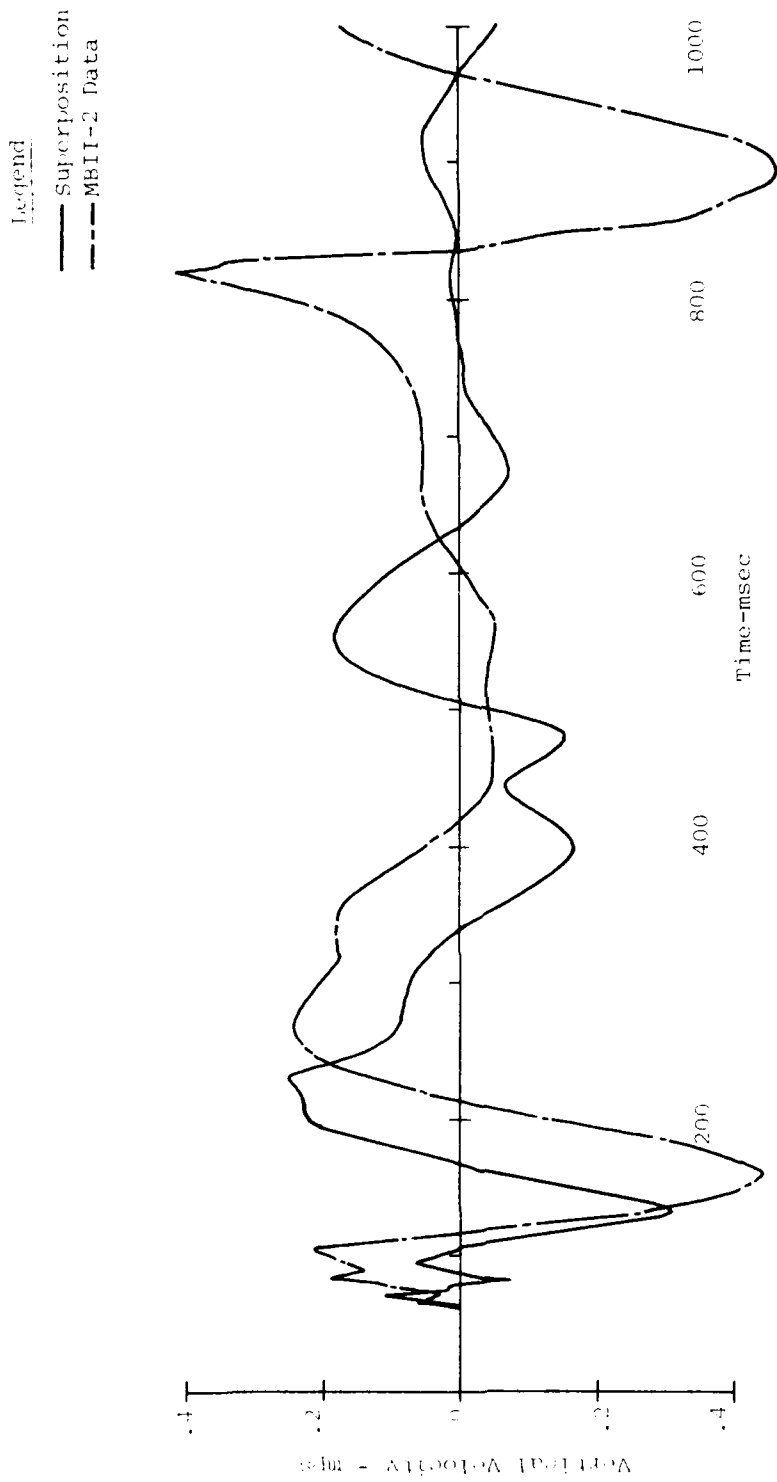


Figure A.11. Comparison of MBII-2 Data and Superimposed MBII-1 Data
 at 12.5-12.5-Bisector-Vertical Velocity

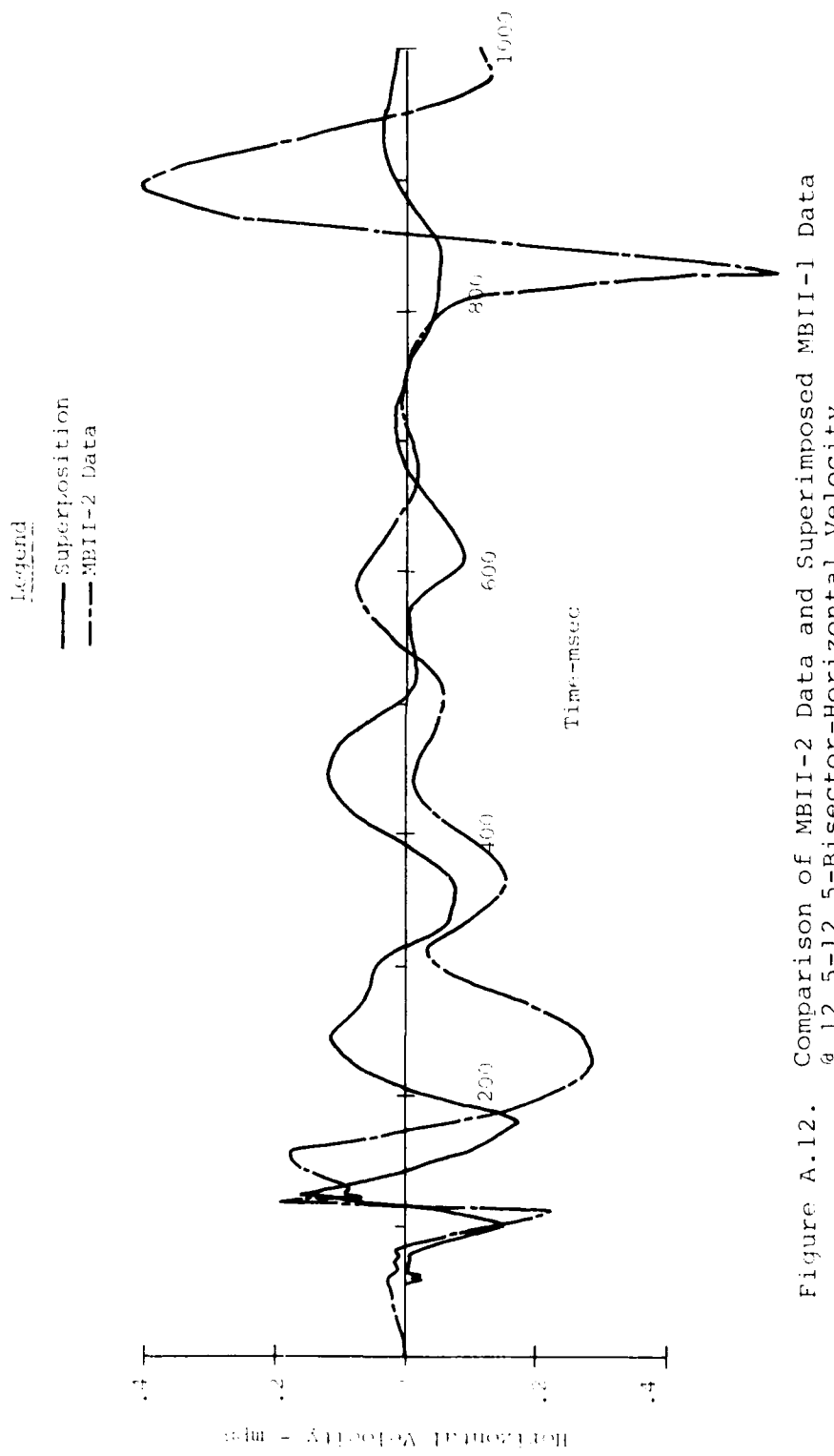


Figure A.12. Comparison of MBII-2 Data and Superimposed MBII-1 Data
at 12.5-Bisector-Horizonal Velocity

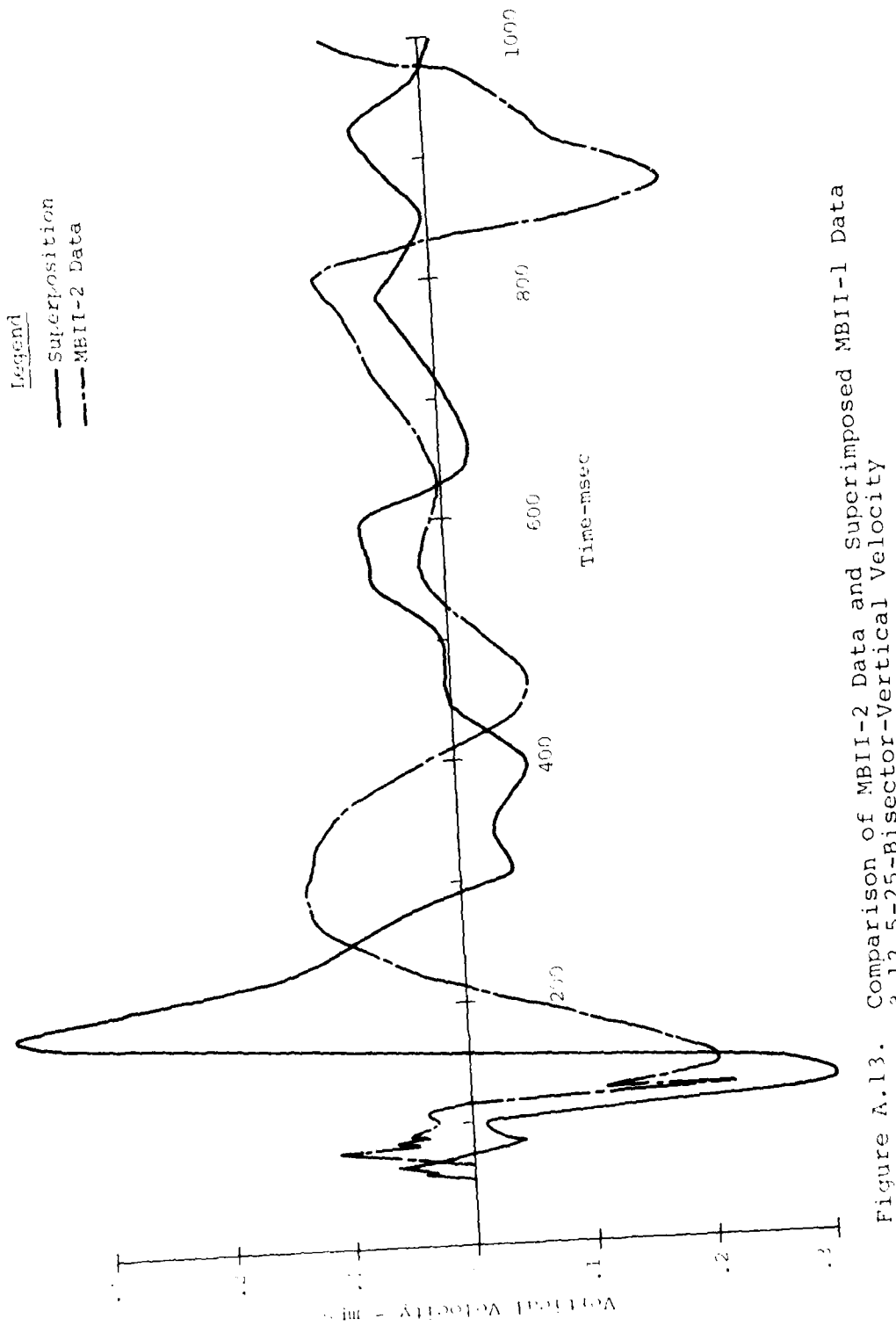


Figure A.13. Comparison of MBII-2 Data and Superimposed MBII-1 Data
at 12.5-25-Bisector-Vertical Velocity

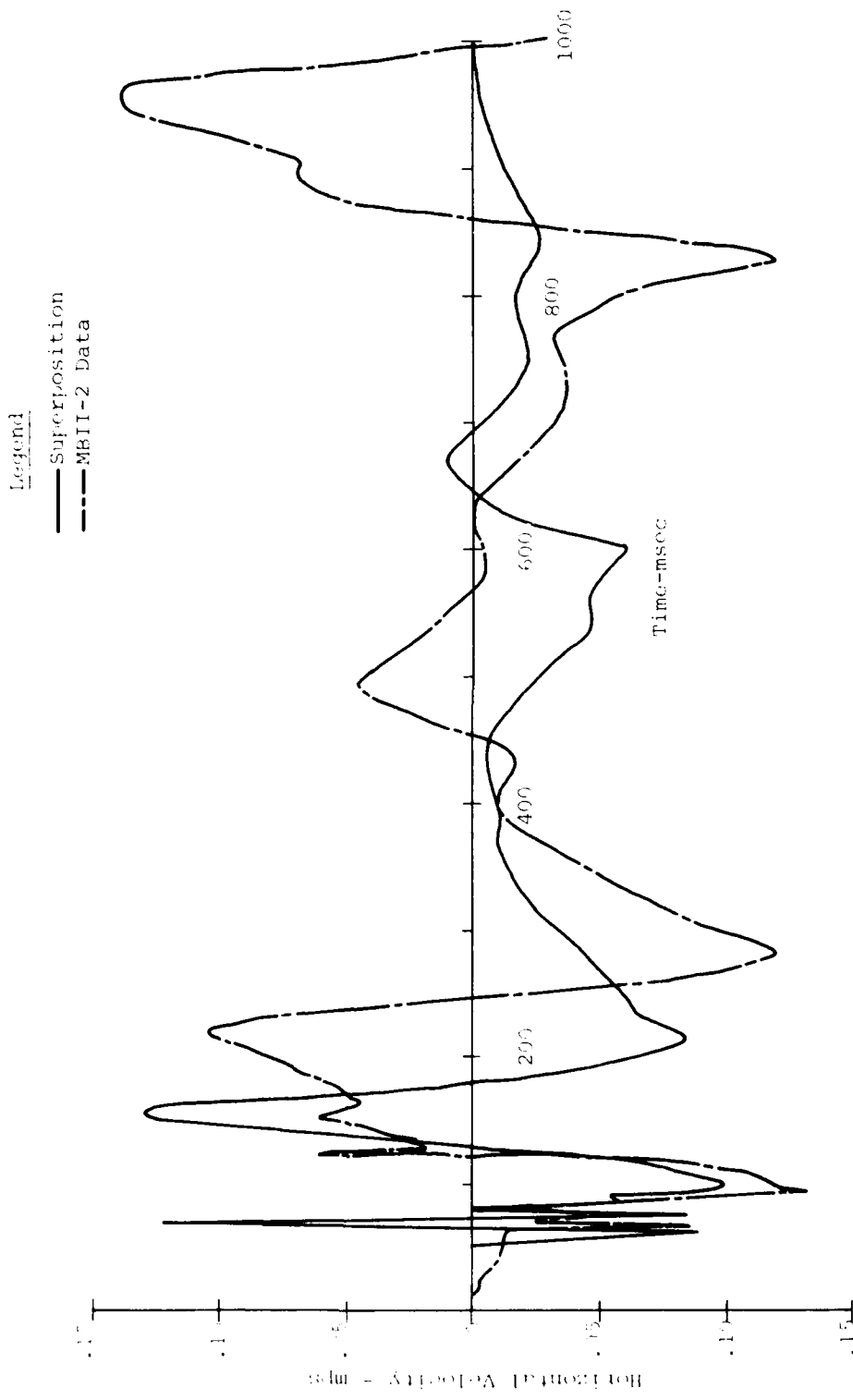


Figure A.14. Comparison of MBII-2 Data and Superimposed MBII-1 Data
a 12.5-25-Bisector-Horizontal Velocity

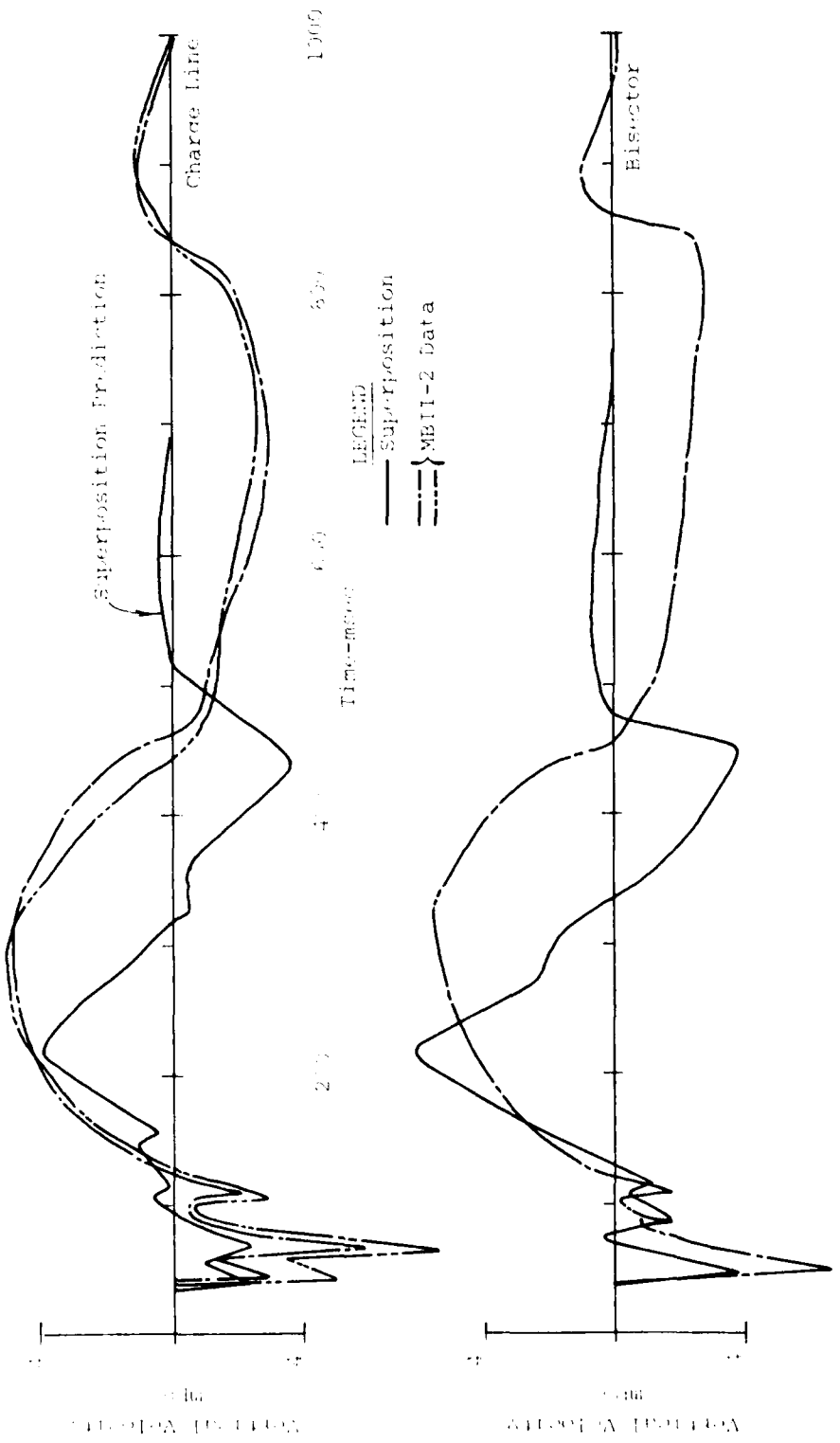


Figure A.15. Comparison of MBII-2 Data and Superimposed MBII-1 Data
at 25-.5 Charge Line and 25-.5 Bisector-Vertical Velocity

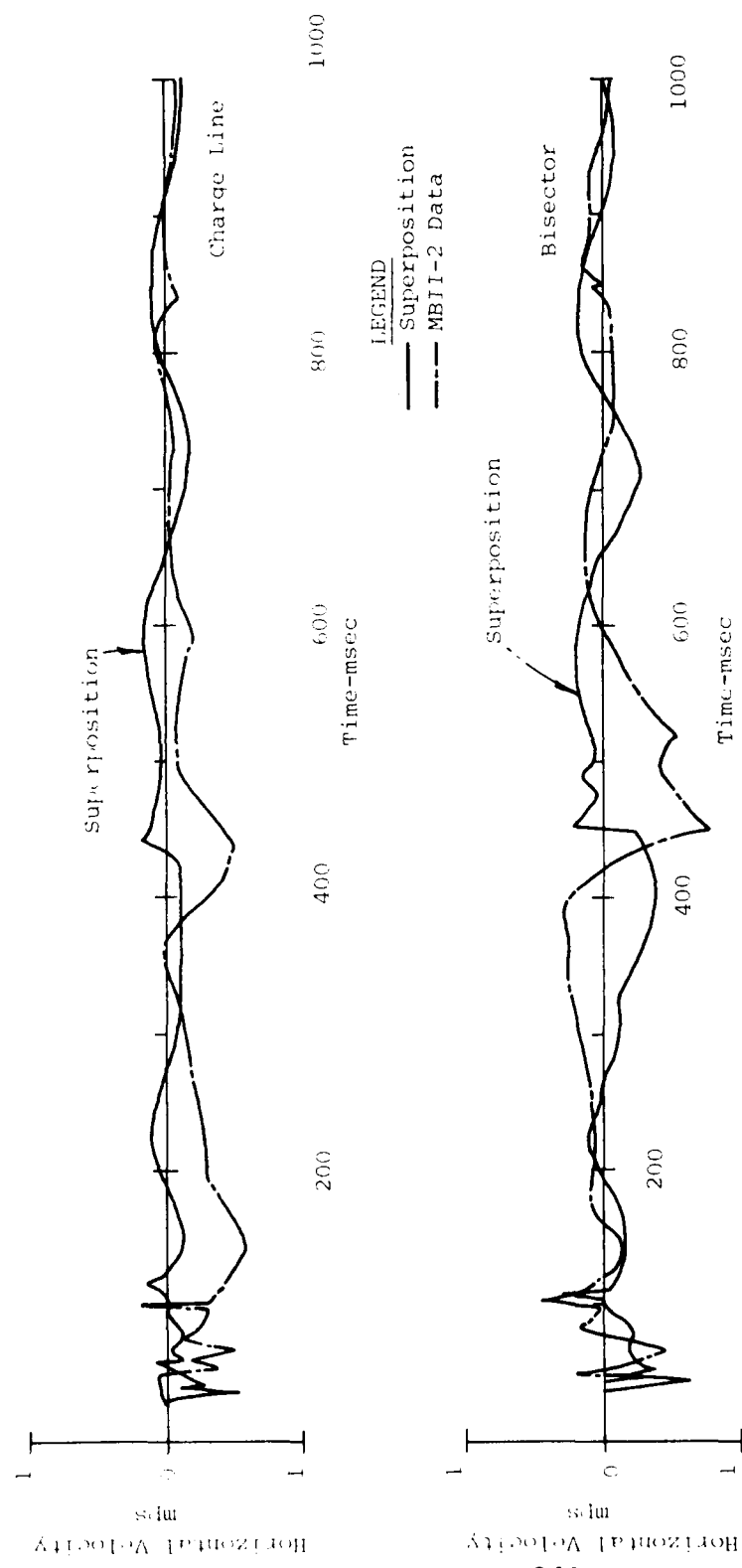


Figure A.16. Comparison of MBII-2 Data and Superimposed MBII-1 Data
 @ 25-.5 Charge Line and 25-.5 Bisector-Horizontal Velocity

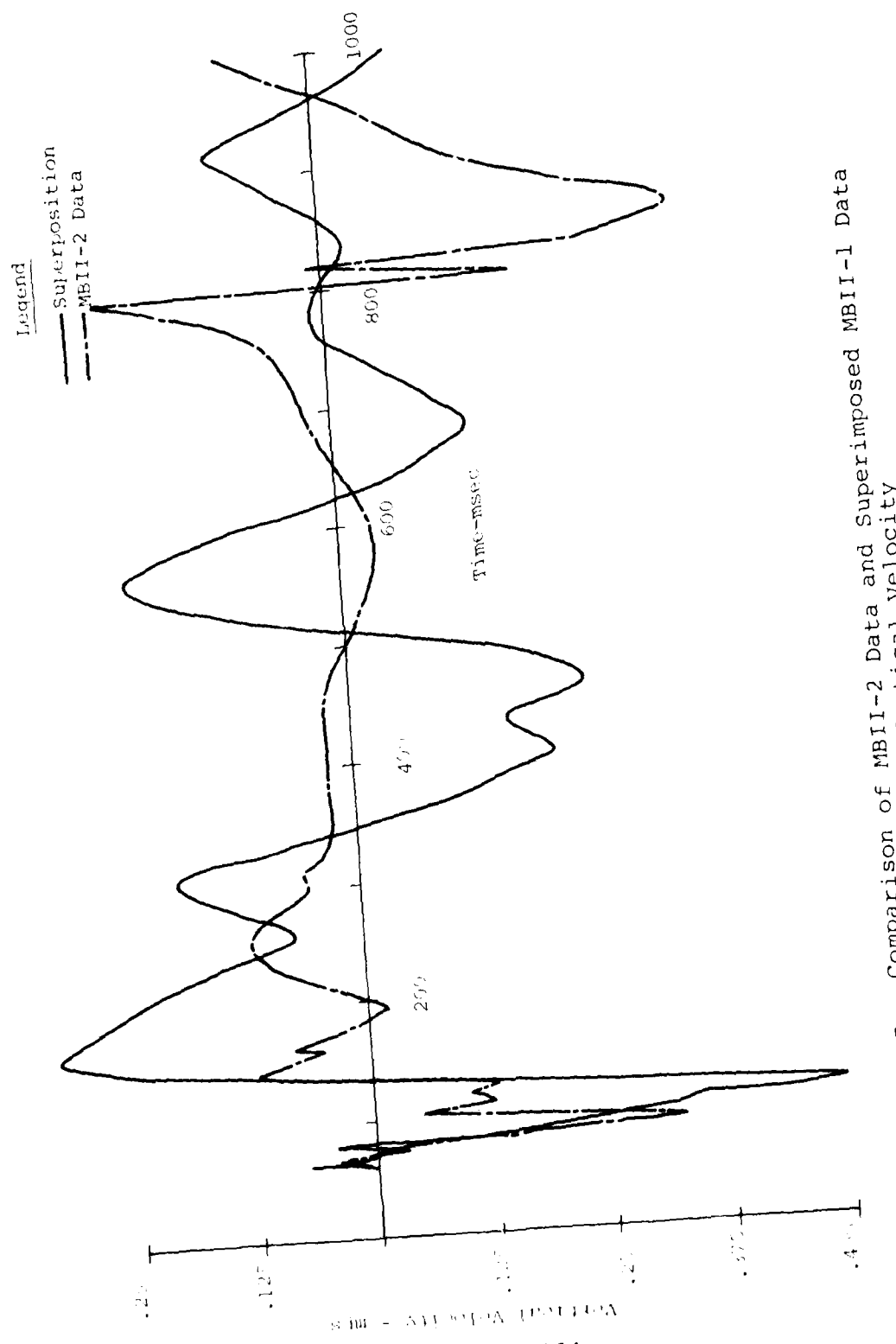


Figure A.17. Comparison of MBII-2 Data and Superimposed MBII-1 Data
a 25-9-Bisection-Vertical Velocity

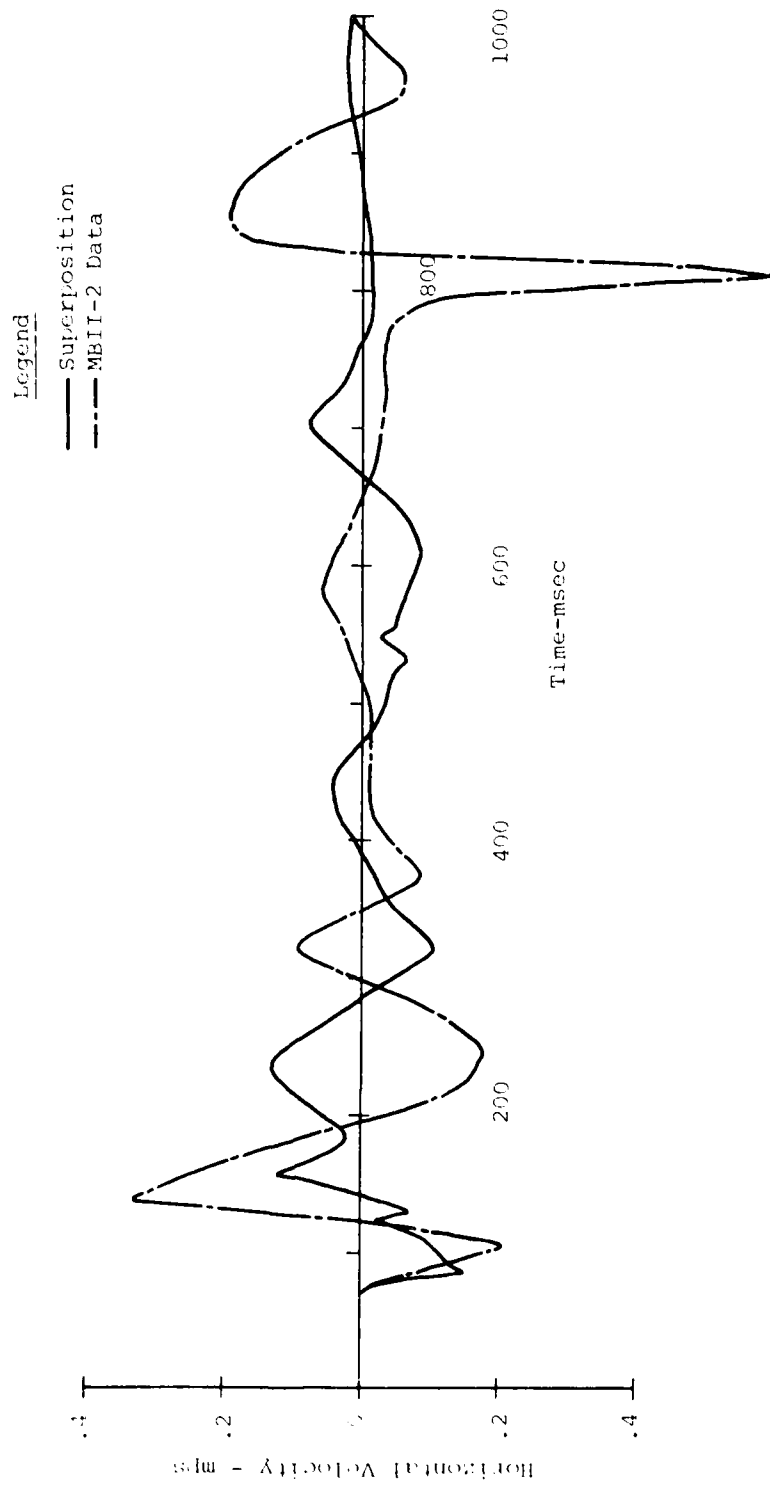


Figure A.18. Comparison of MBII-2 Data and Superimposed MBII-1 Data
at 25-9-Bisector-Horizontal Velocity

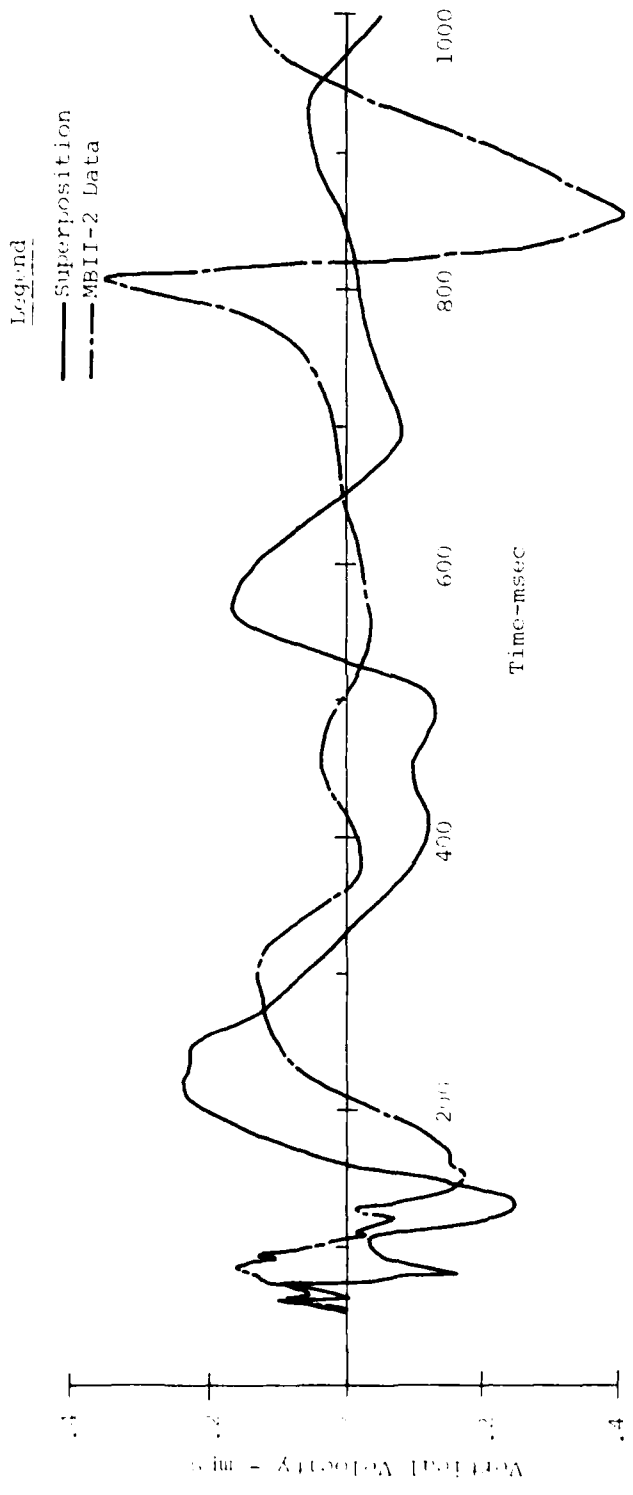


Figure A.19. Comparison of MBII-2 Data and Superimposed MBII-1 Data
a 25-12.5-Bisector-Vertical Velocity

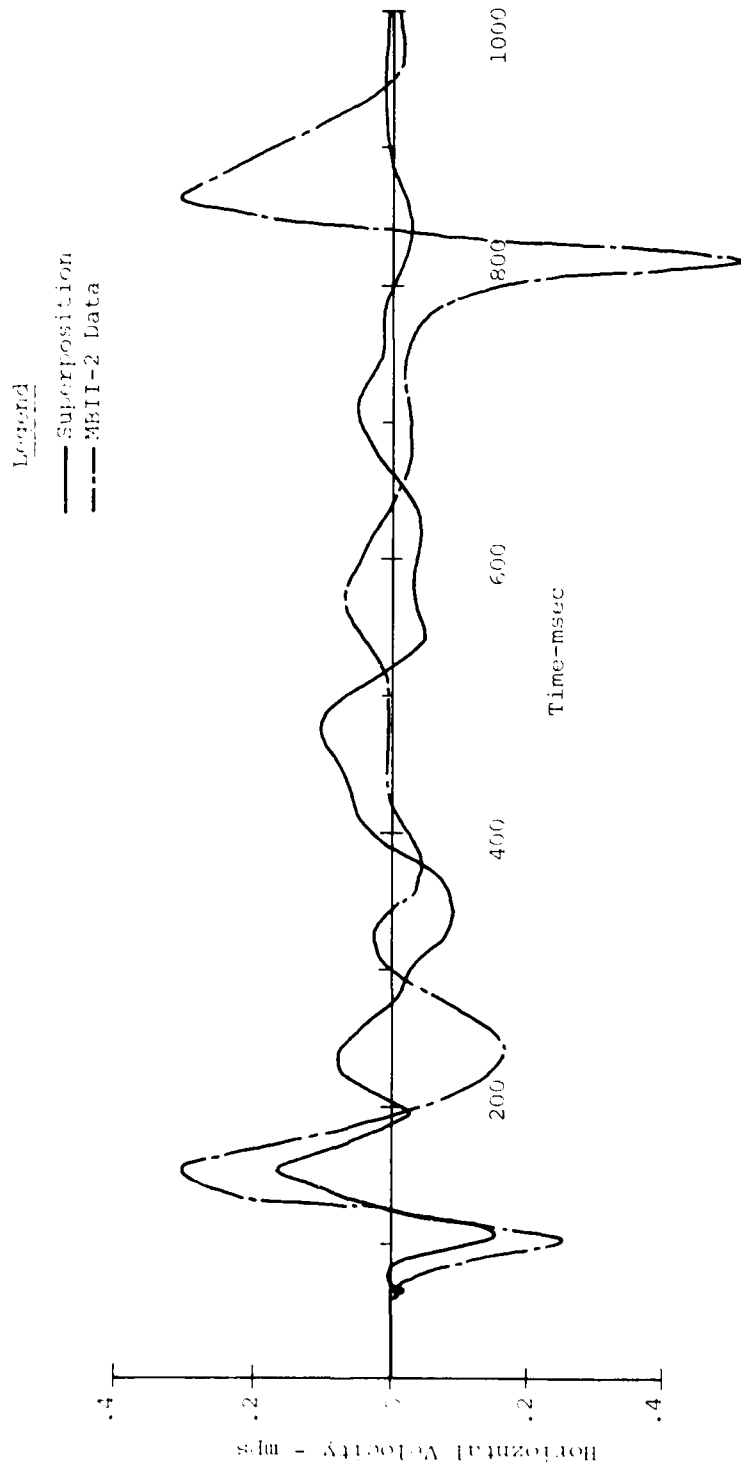


Figure A.20. Comparison of MBII-2 Data and Superimposed MBII-1 Data
at 25-12.5-Bisector-Horizontal Velocity

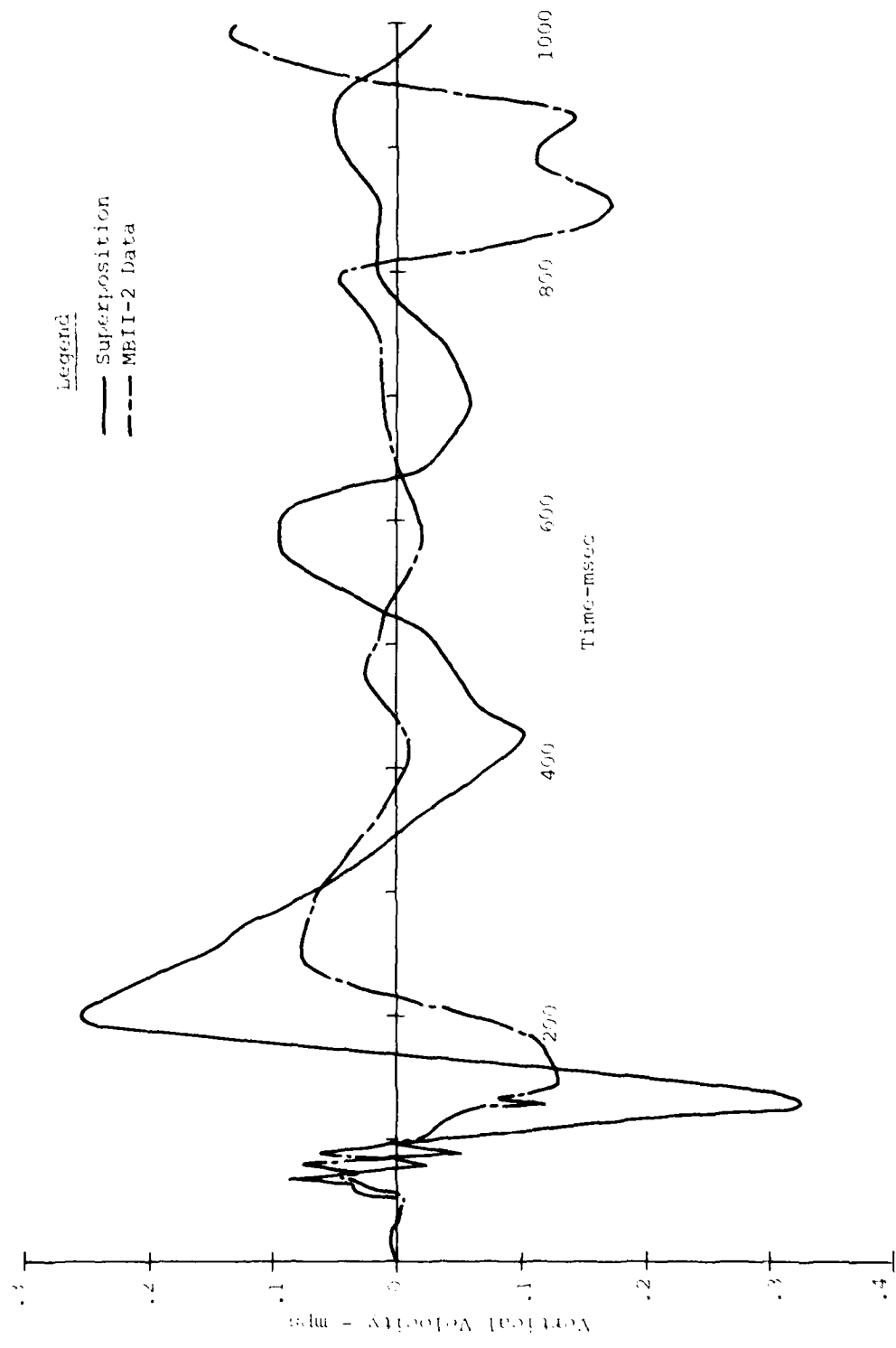


Figure A.21. Comparison of MBII-2 Data and Superimposed MBII-1 Data
a 25-25-Bisector-Vertical Velocity

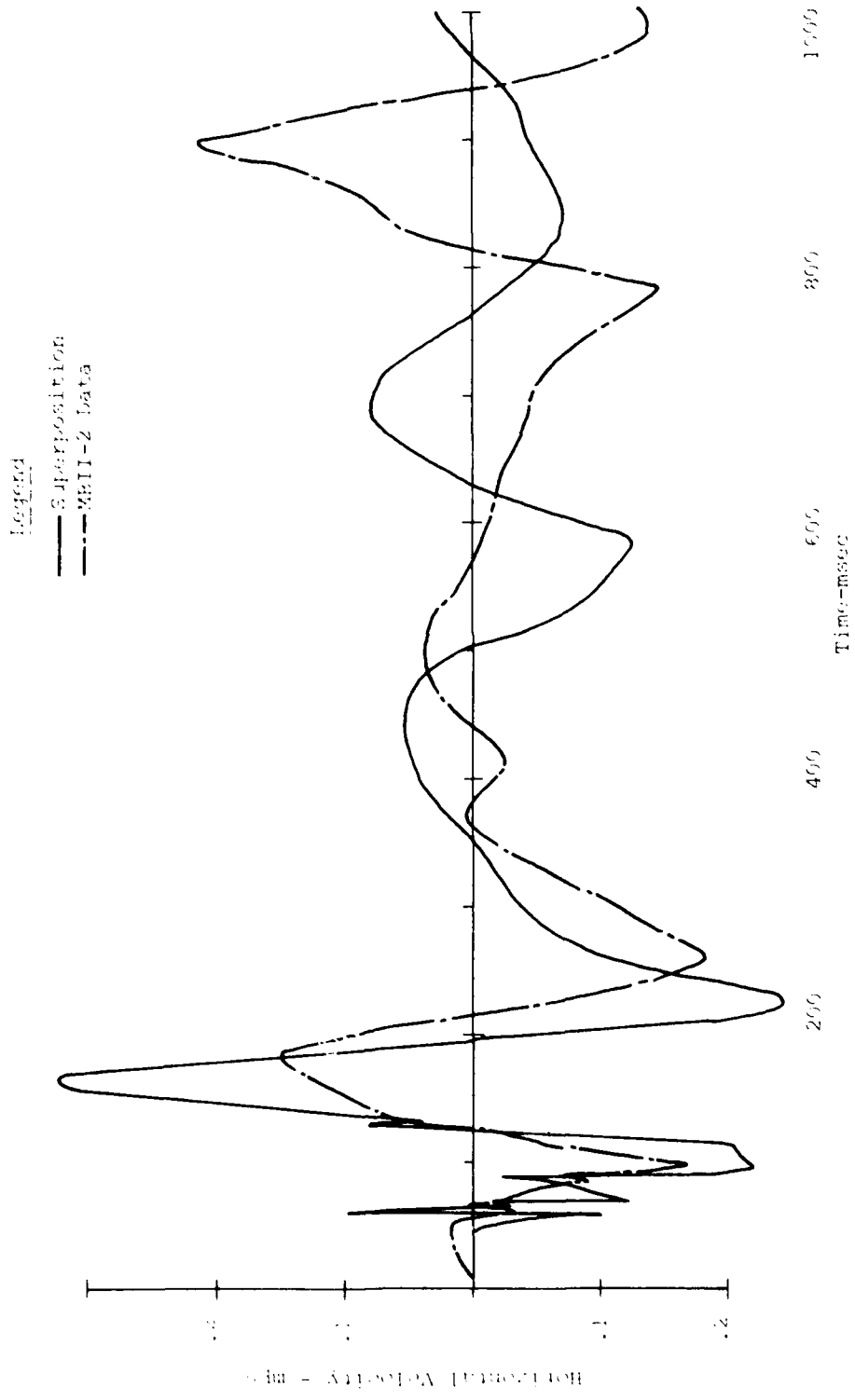


Figure A.22. Comparison of MBII-2 Data and Superimposed MBII-1 Data
at 25-25-Bisector-Horizontal Velocity

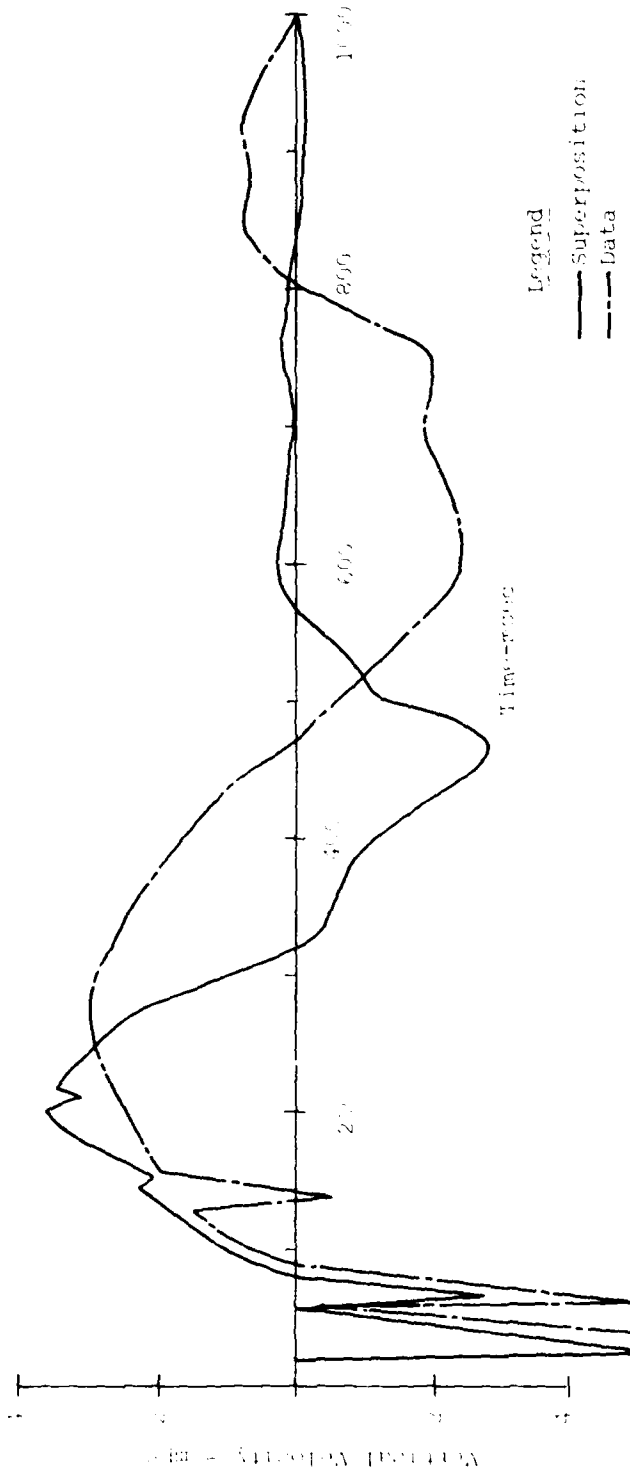


Figure K.23. Comparison of MBII-2 Data and Superimposed MBII-1 Data
at 50-0.5-Charge Line - Vertical Velocity

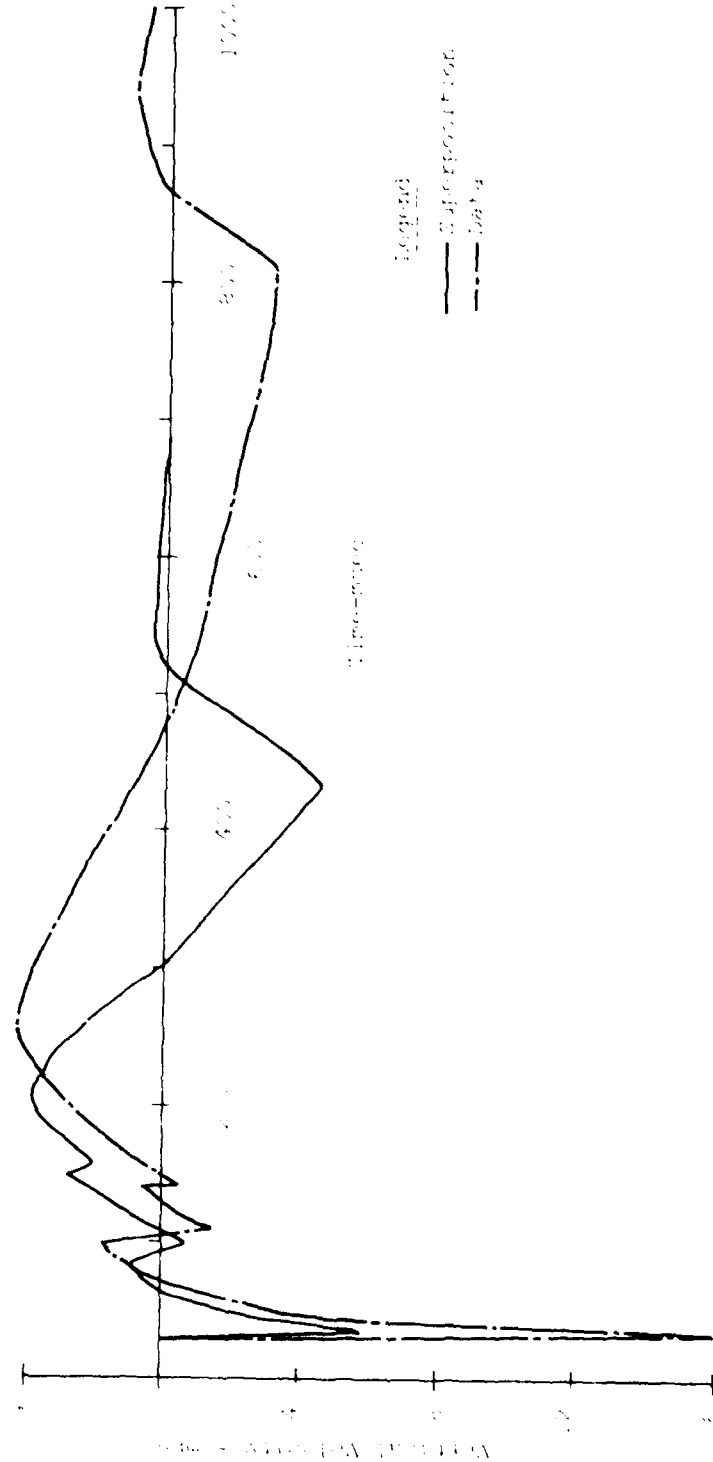


Figure 1.24. Comparison of MBII-2 Data and Superimposed MBII-1 Data
a 50-0.5-Bisector-Vertical Velocity

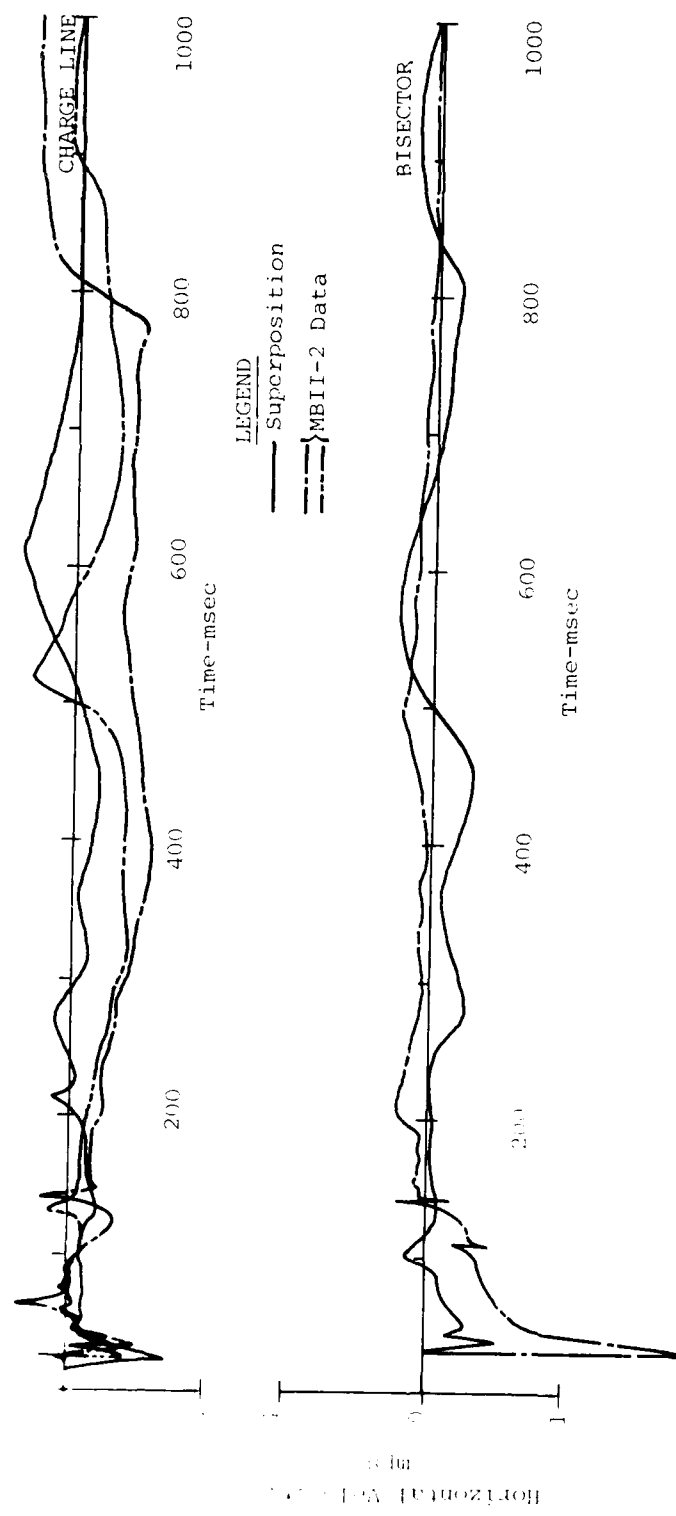


Figure A.25. Comparison of MBII-2 Data and Superimposed MBII-1 Data
a 50-0.5-Charge Line and 50-0.5-Bisection Horizontal Velocity

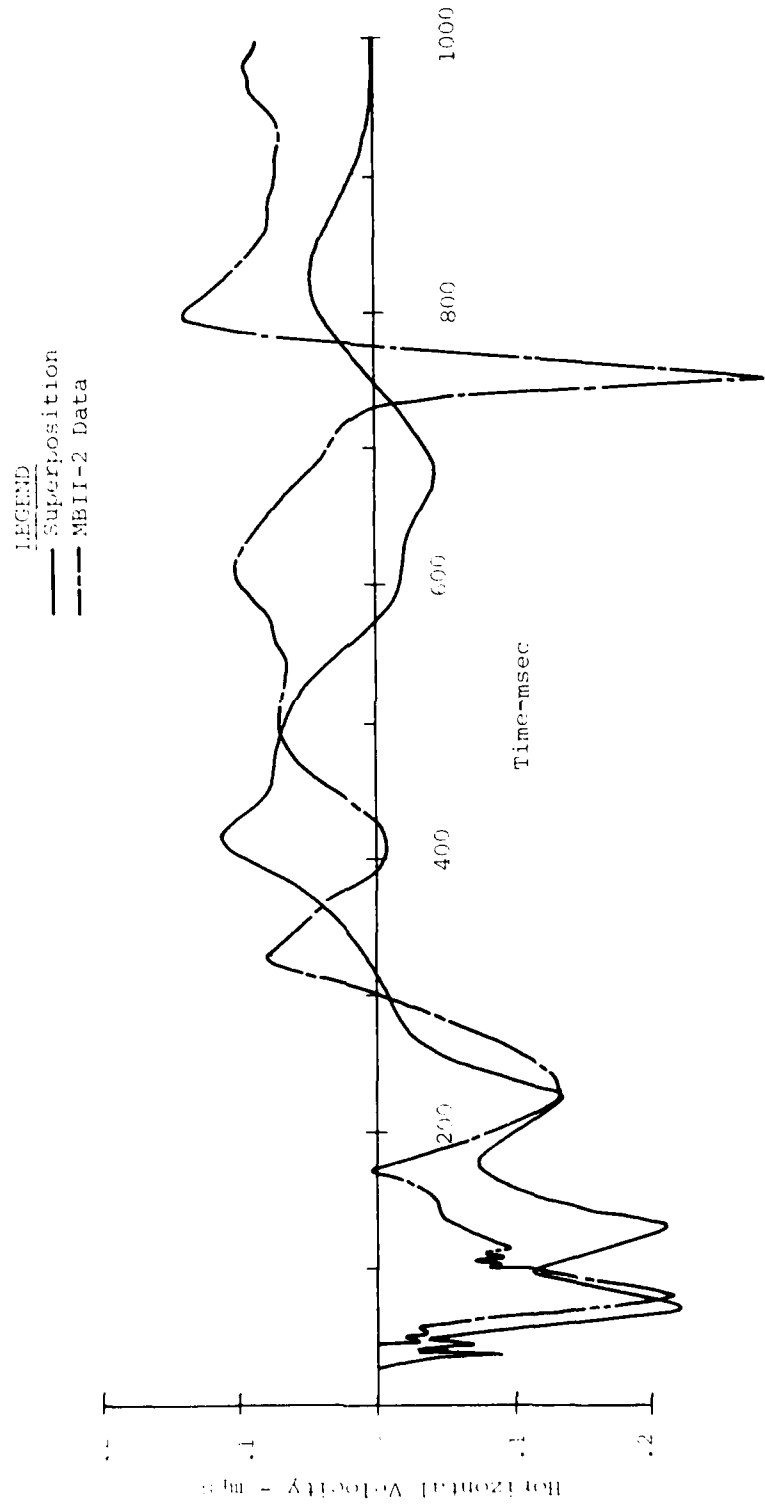


Figure A.26. Comparison of MBII-2 Data and Superimposed MBII-1 Data at 50-1.5-Charge Line-Horizontal Velocity

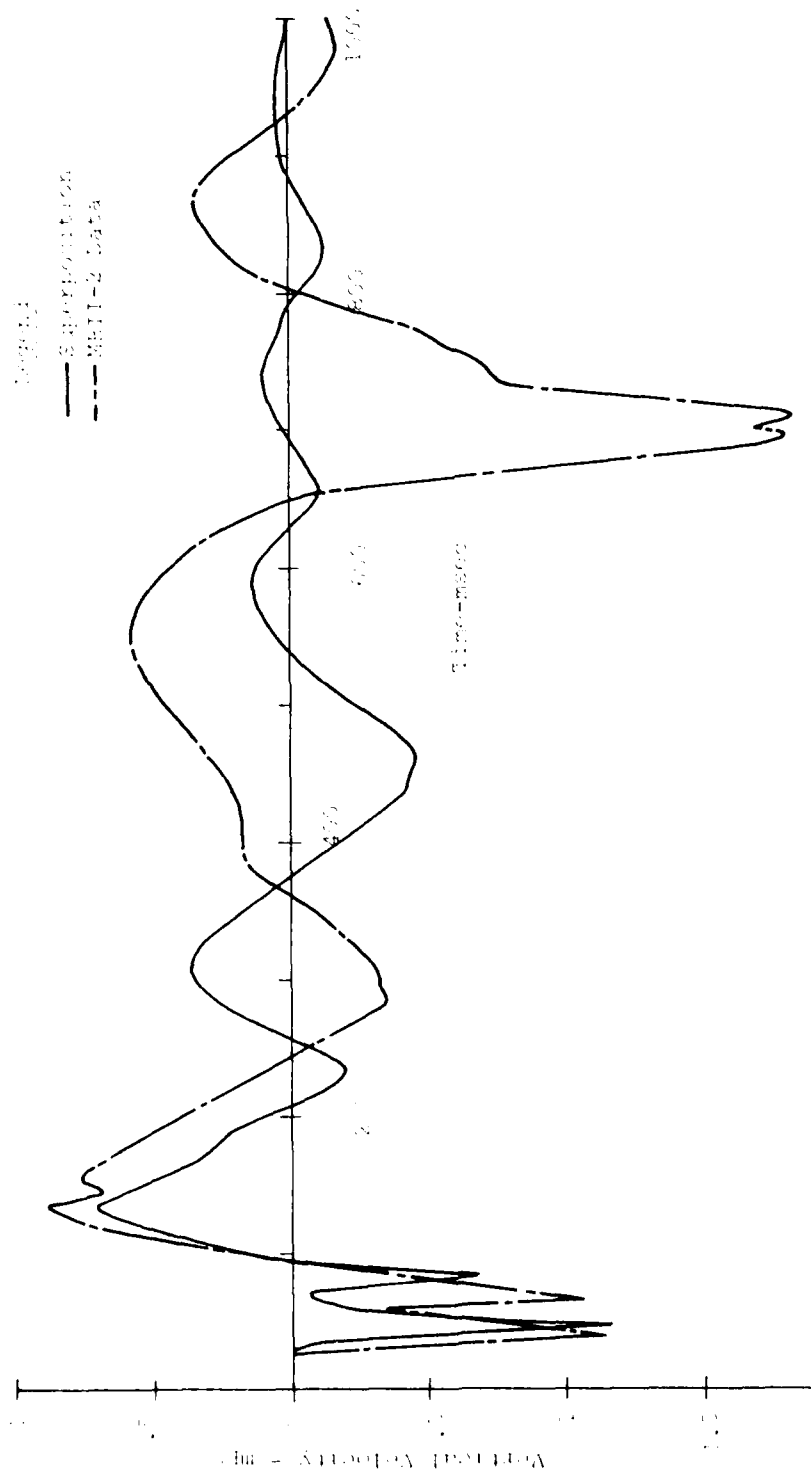


Figure R.27. Comparison of MBI-2 Data and Superimposed MBI-1 Data
at 50-3-Charge Line-Vertical Velocity

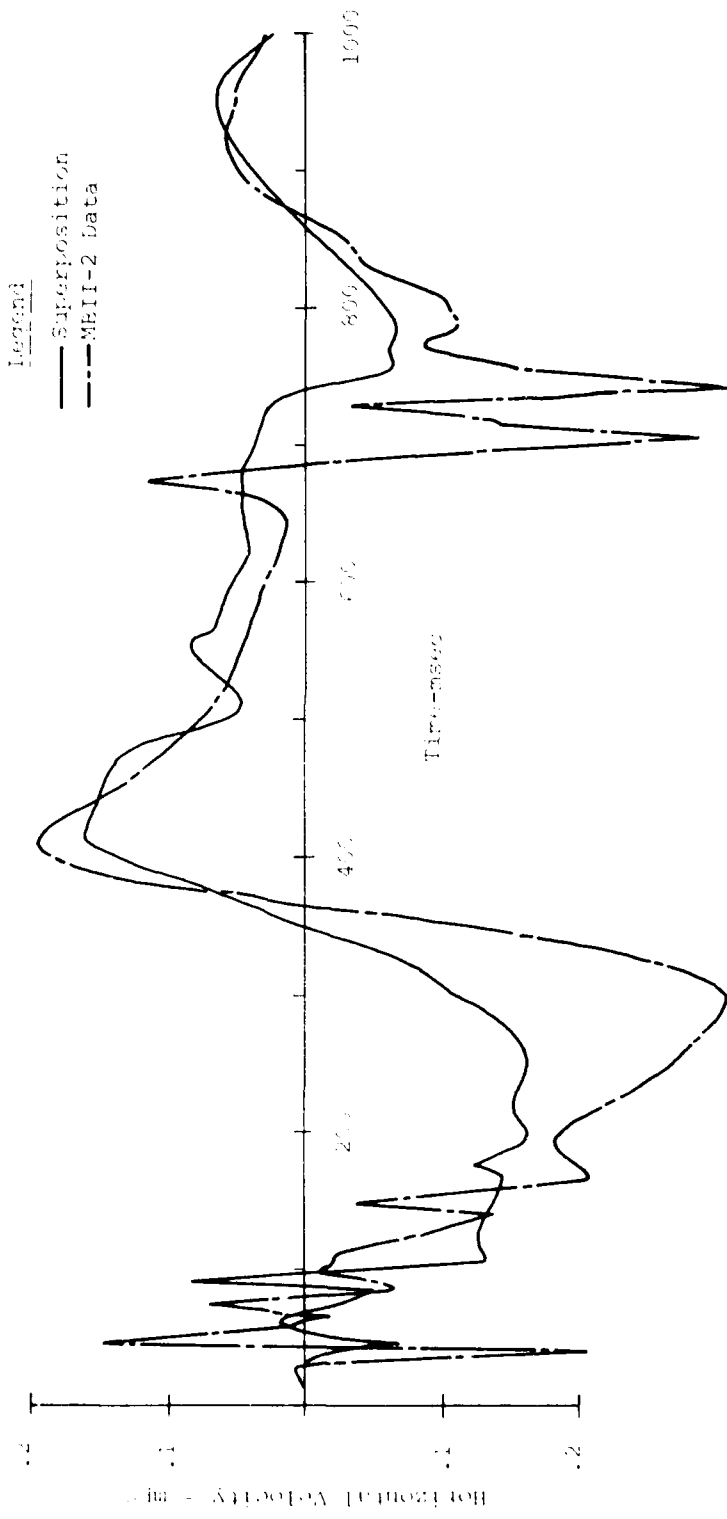


Figure A.28. Comparison of MBII-2 Data and Superimposed MBII-1 Data at 50-3-Charge Line-Horizontal Velocity

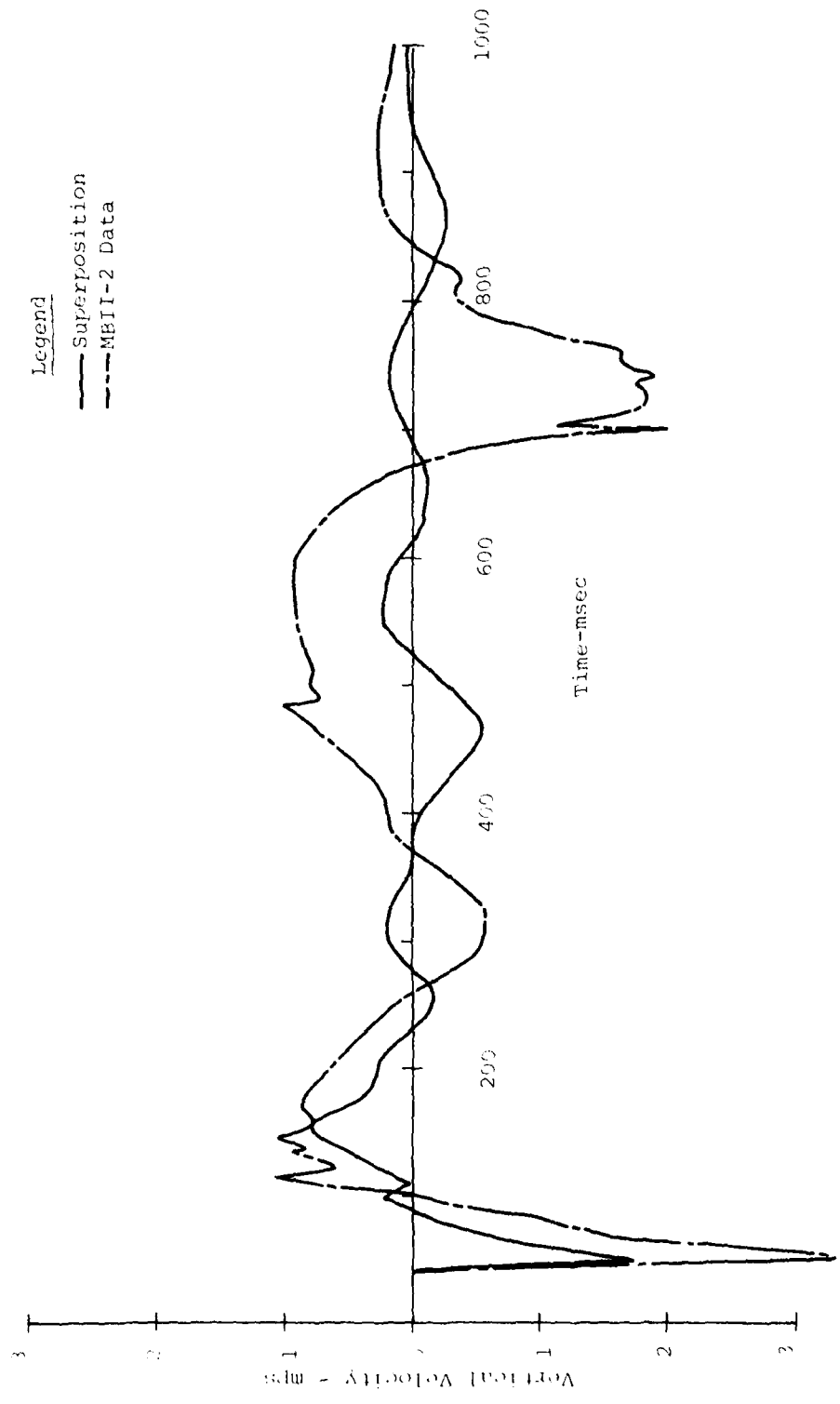


Figure A.29. Comparison of MBII-2 Data and Superimposed MBII-1 Data-@
 50-3-Bisector-Vertical Velocity

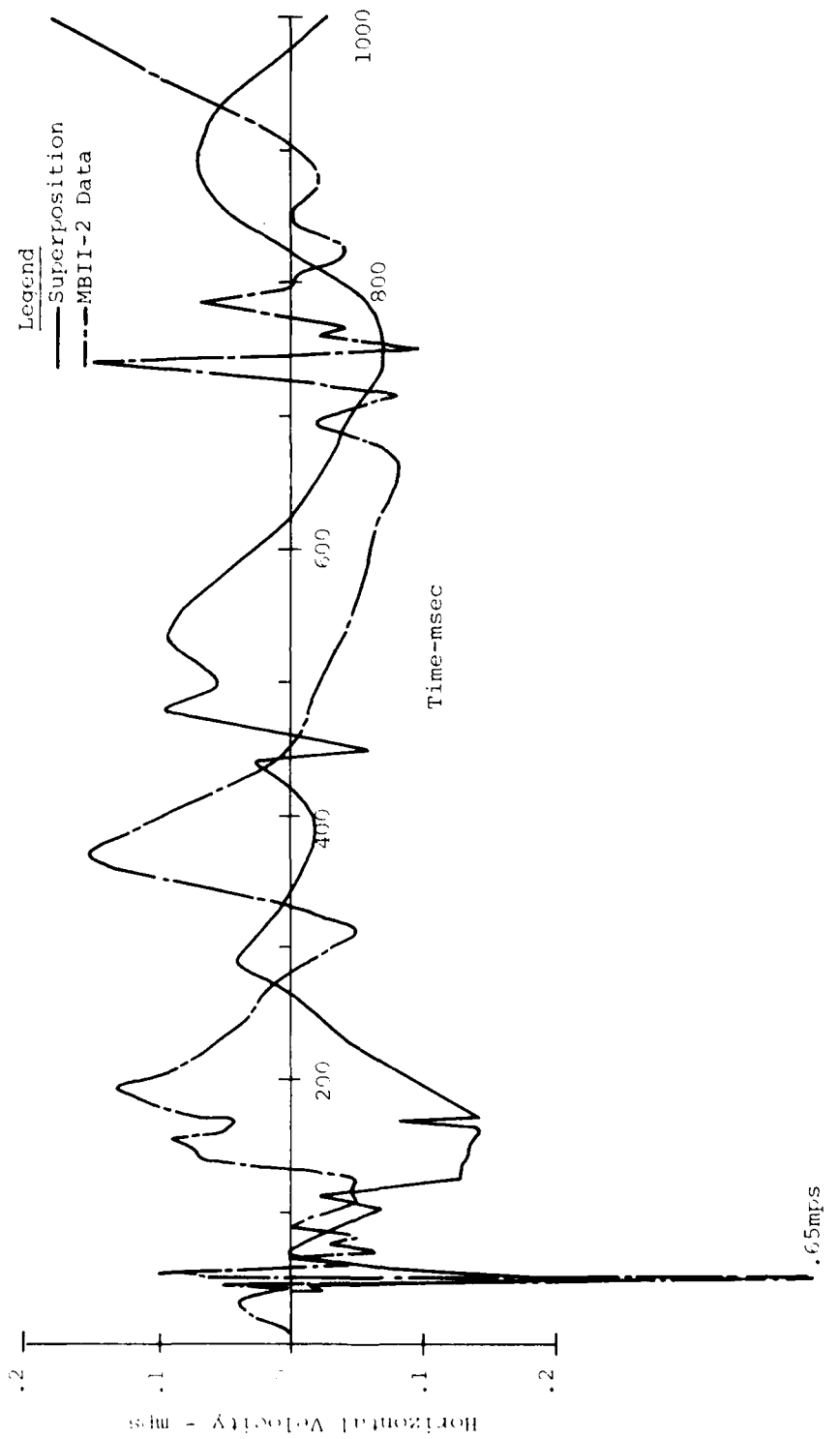


Figure A.30. Comparison of MBII-2 Data and Superimposed MBII-1 Data at 50-3-Bisector-Horizontal Velocity

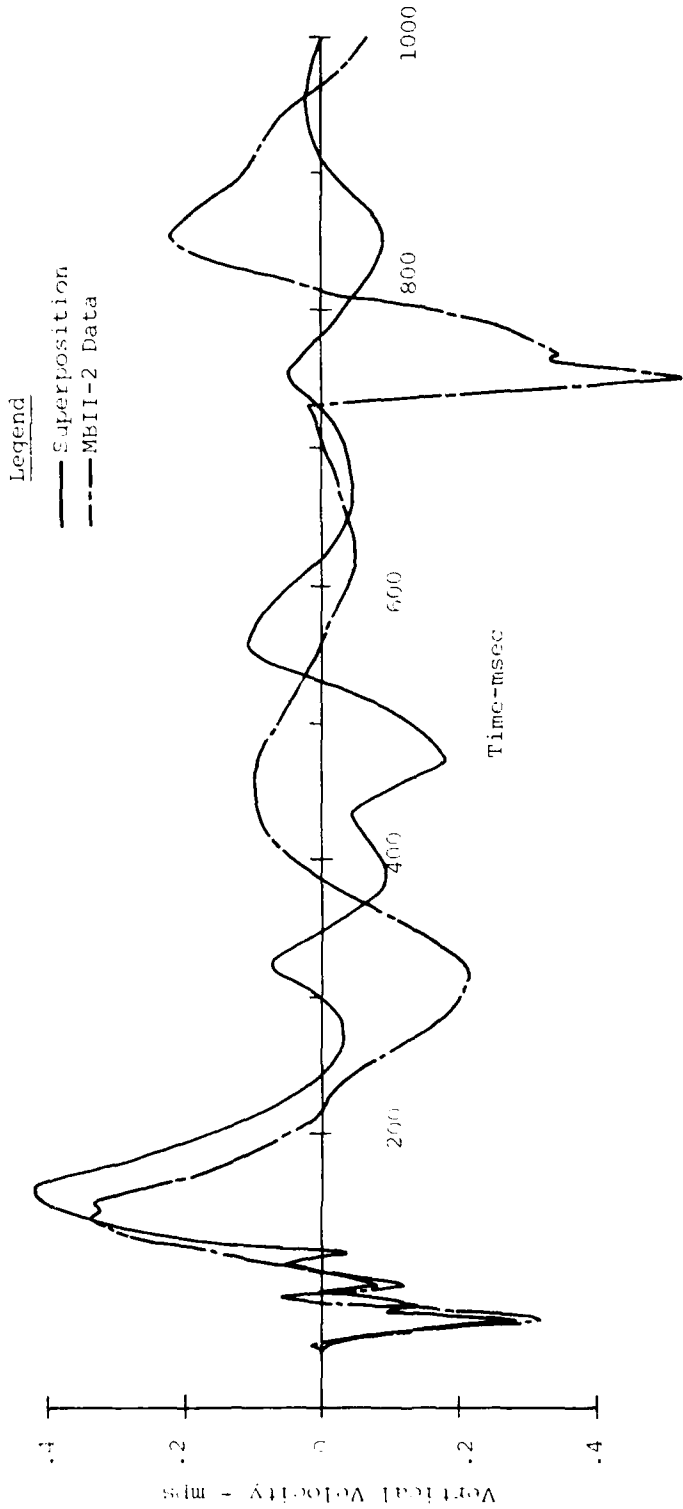


Figure A.31. Comparison of MBII-2 Data and Superimposed MBII-1 Data
a 50-9-Charge Line-Vertical Velocity

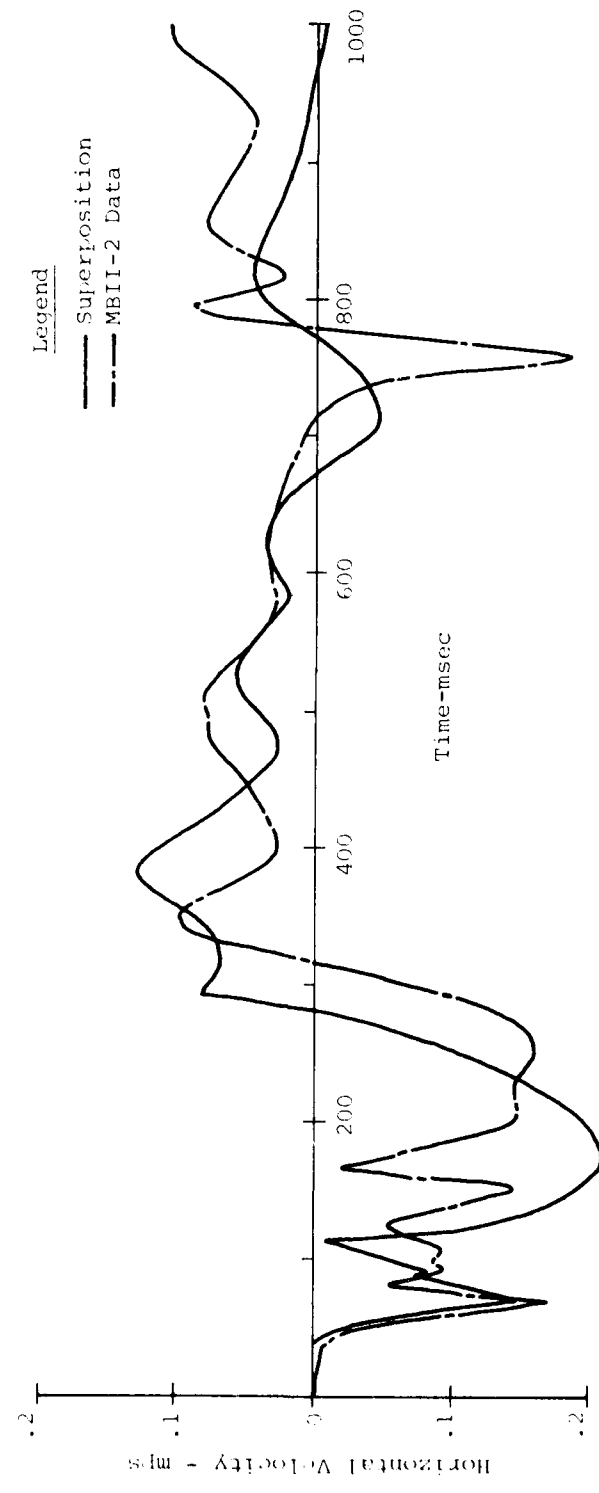


Figure A.32. Comparison of MBII-2 Data and Superimposed MBII-1 Data
a 50-9-Charge Line-Horizontal Velocity

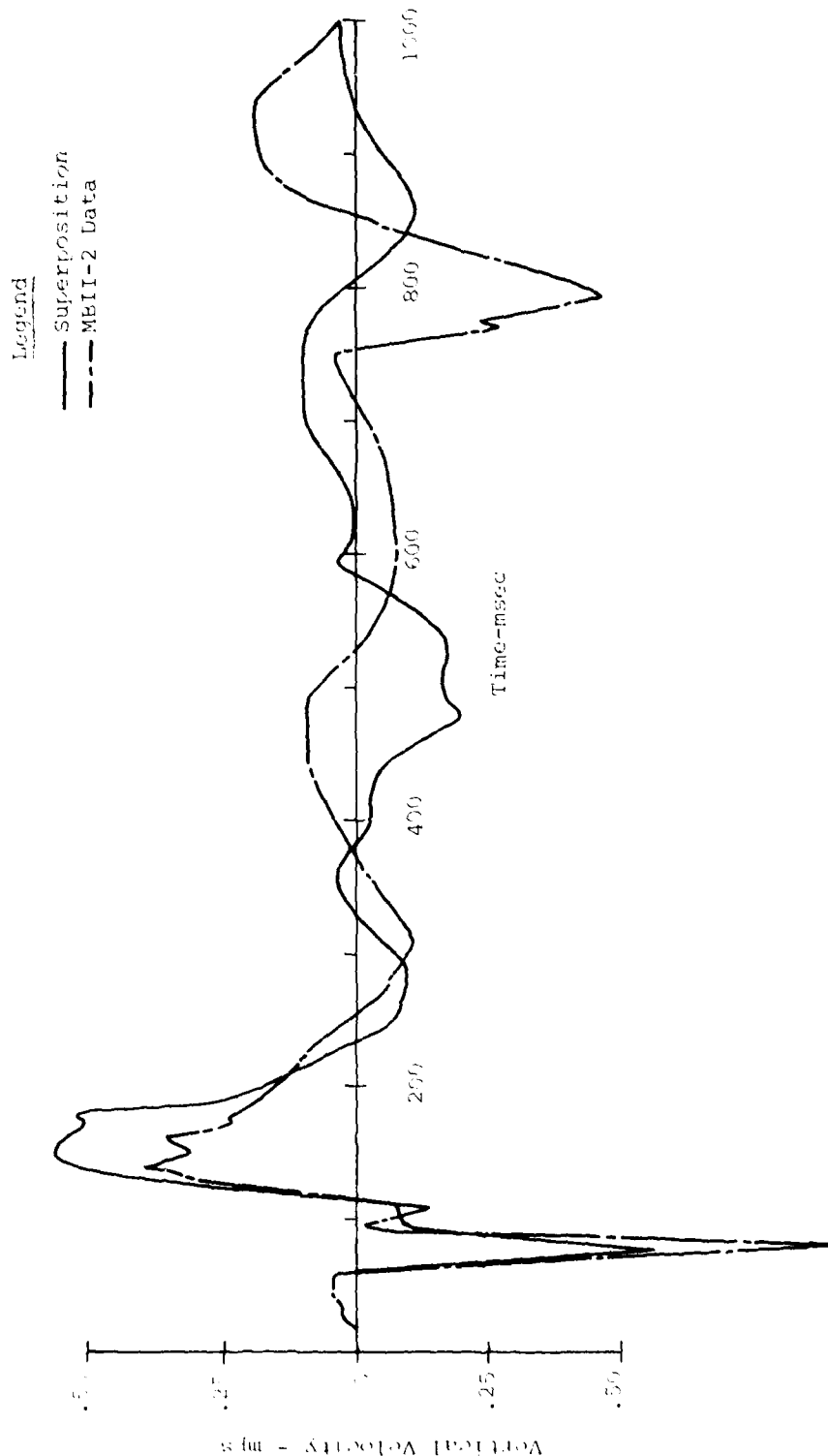


Figure A.33. Comparison of MBII-2 Data and Superimposed MBII-1 Data
a 50-9-Bisector-Vertical Velocity

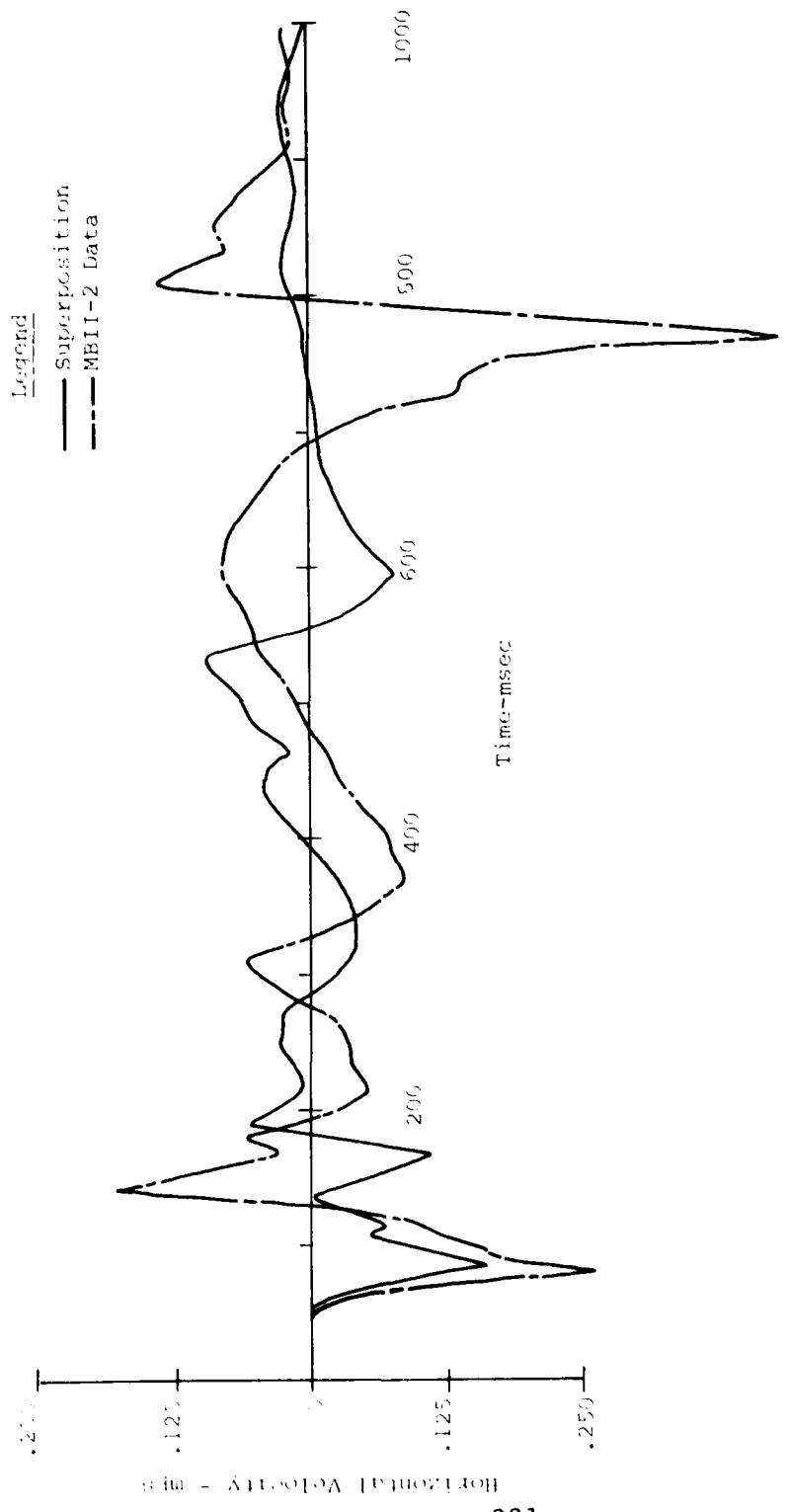


Figure A.34. Comparison of MBII-2 Data and Superimposed MBII-1 Data
at 50-9-Bisector-Hsector Velocity

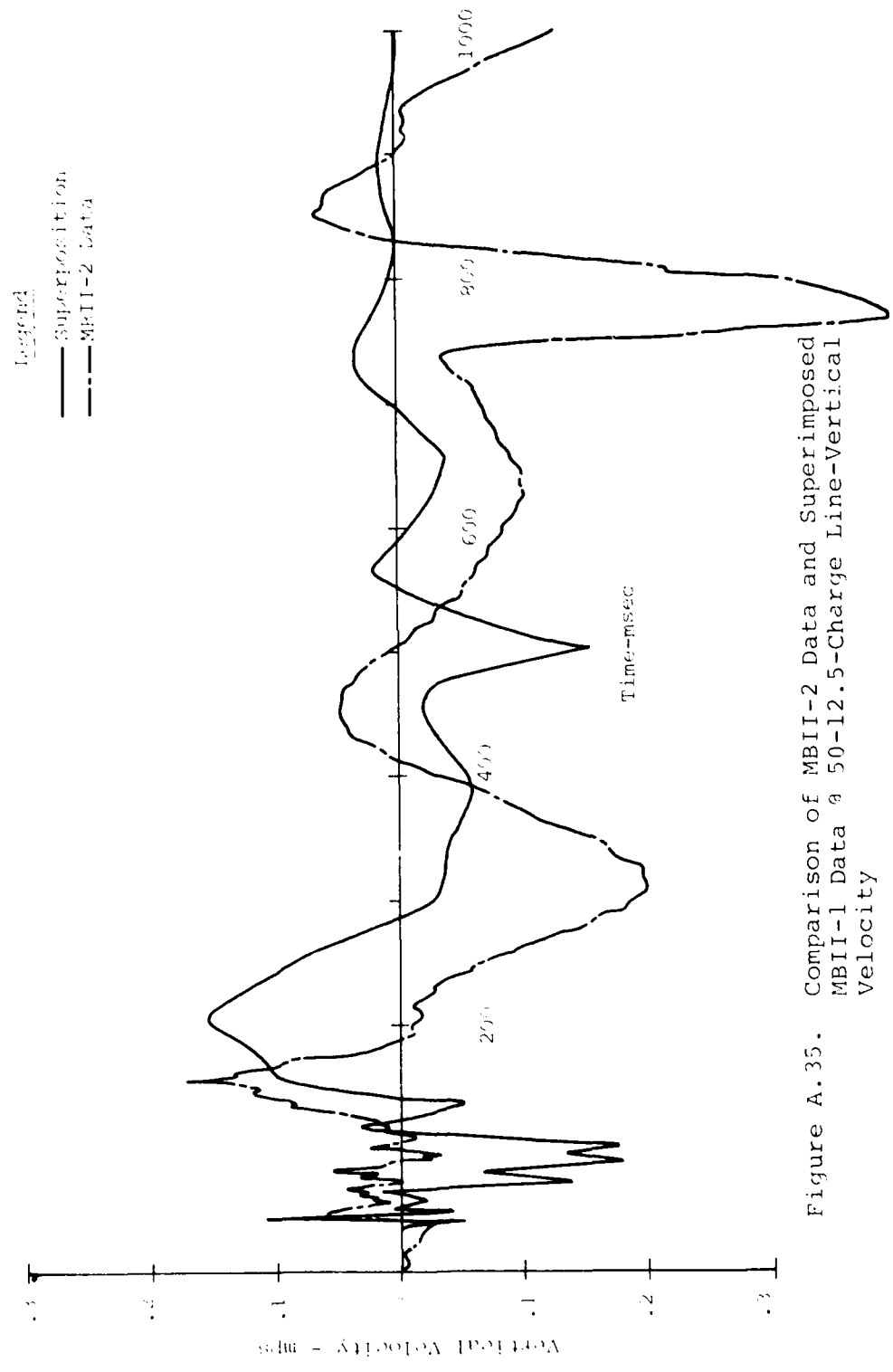


Figure A.35. Comparison of MBII-2 Data and Superimposed MBII-1 Data at 50-12.5-Charge Line-Vertical Velocity

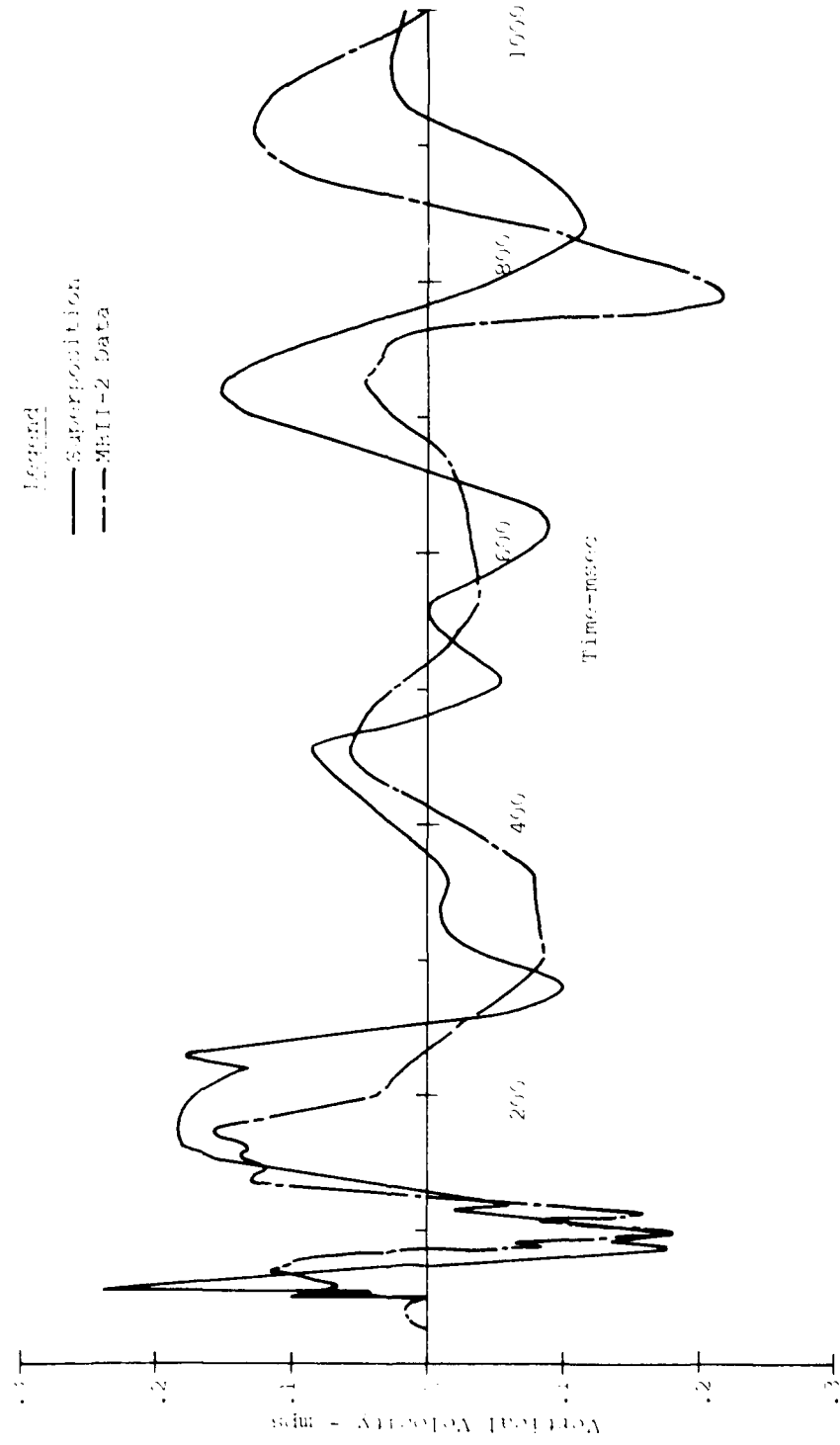


Figure K.36. Comparison of MBLI-2 Data and Superimposed MBLI-1 Data
a 50-12.5-Bisector-Vertical Velocity

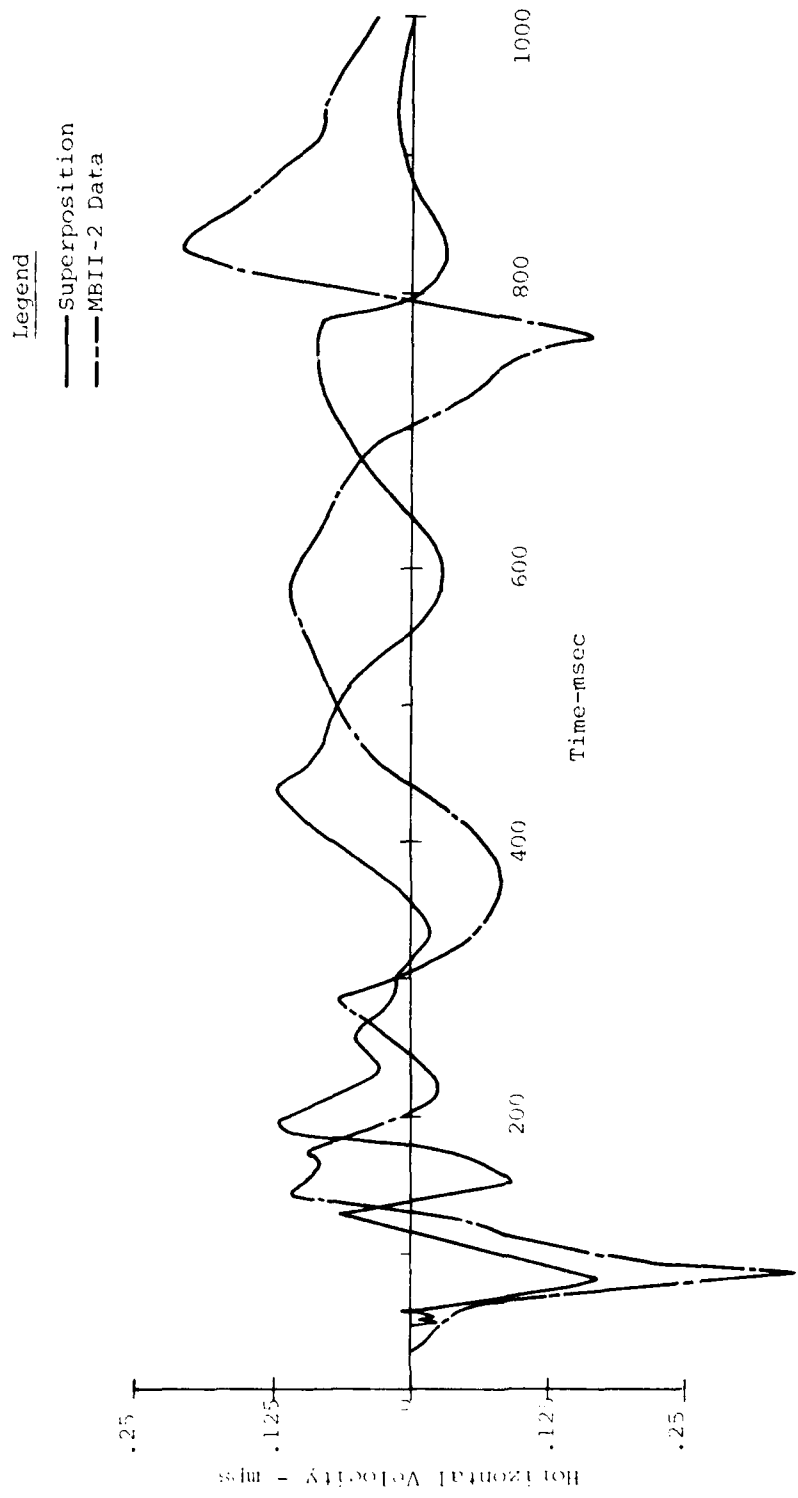


Figure A.37. Comparison of MBII-2 Data and Superimposed MBII-1 Data @ 50-12.5-Bisector-Horizonal Velocity

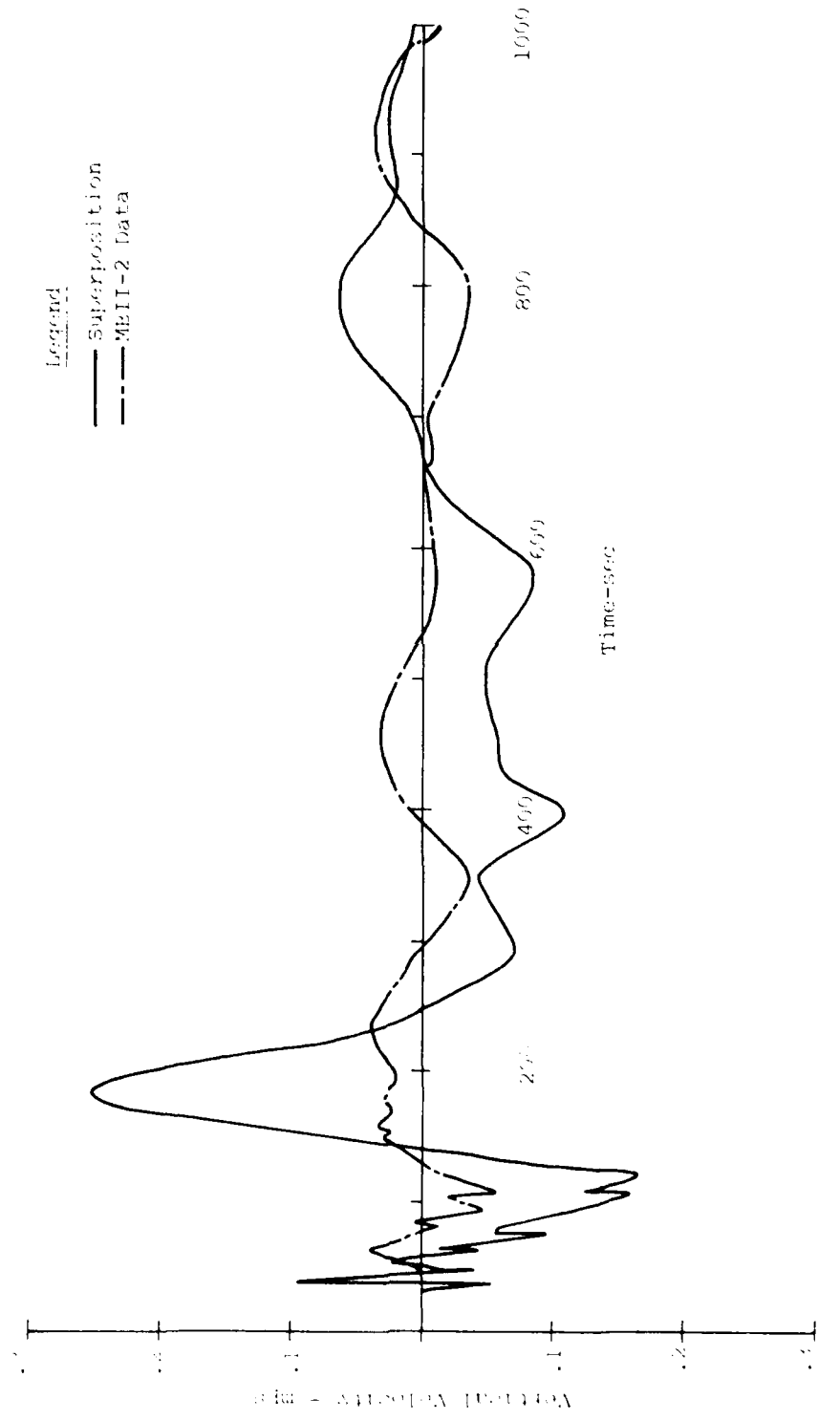


Figure A.38. Comparison of MBII-2 Data and Superimposed MBII-1 Data
a 50-25-Bisector-Vertical Velocity

AD-A092 874

CIVIL SYSTEMS INC ALBUQUERQUE NM
MISERS BLUFF PHASE II, GROUND SHOCK DATA ANALYSIS.(U)
OCT 79 J S PHILLIPS, L S MELZER, J L BRATTON DNA001-79-C-0168

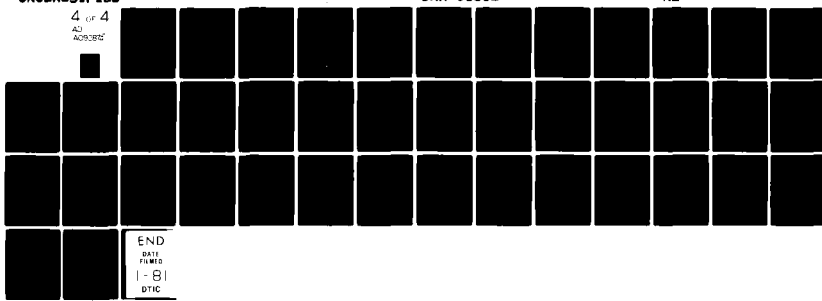
F/G 18/3

DNA-5135Z

NL

UNCLASSIFIED

4 of 4
AS
400002



END
DATE
FILED
I-81
DTIC

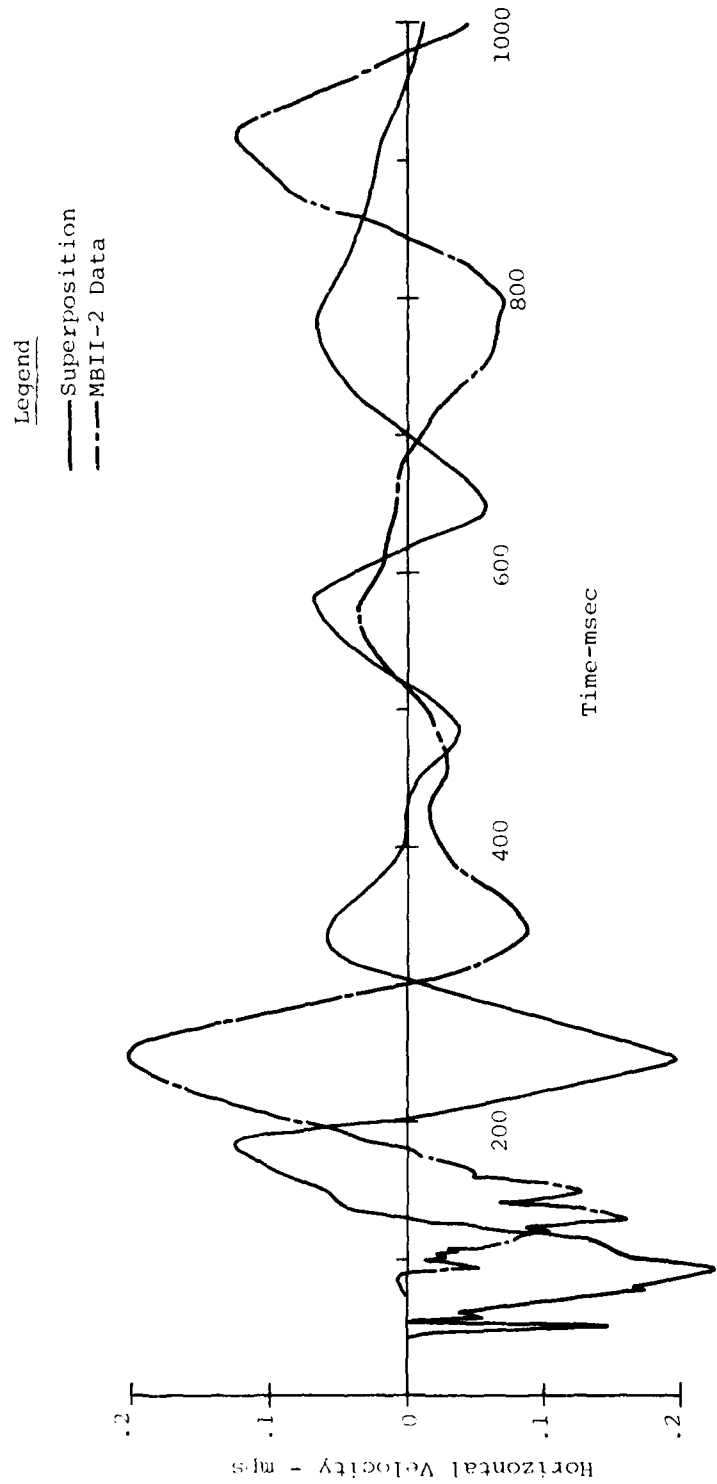


Figure A.39. Comparison of MBII-2 Data and Superimposed
MBII-1 Data @ 50-25-Bisector-Horizontal
Velocity

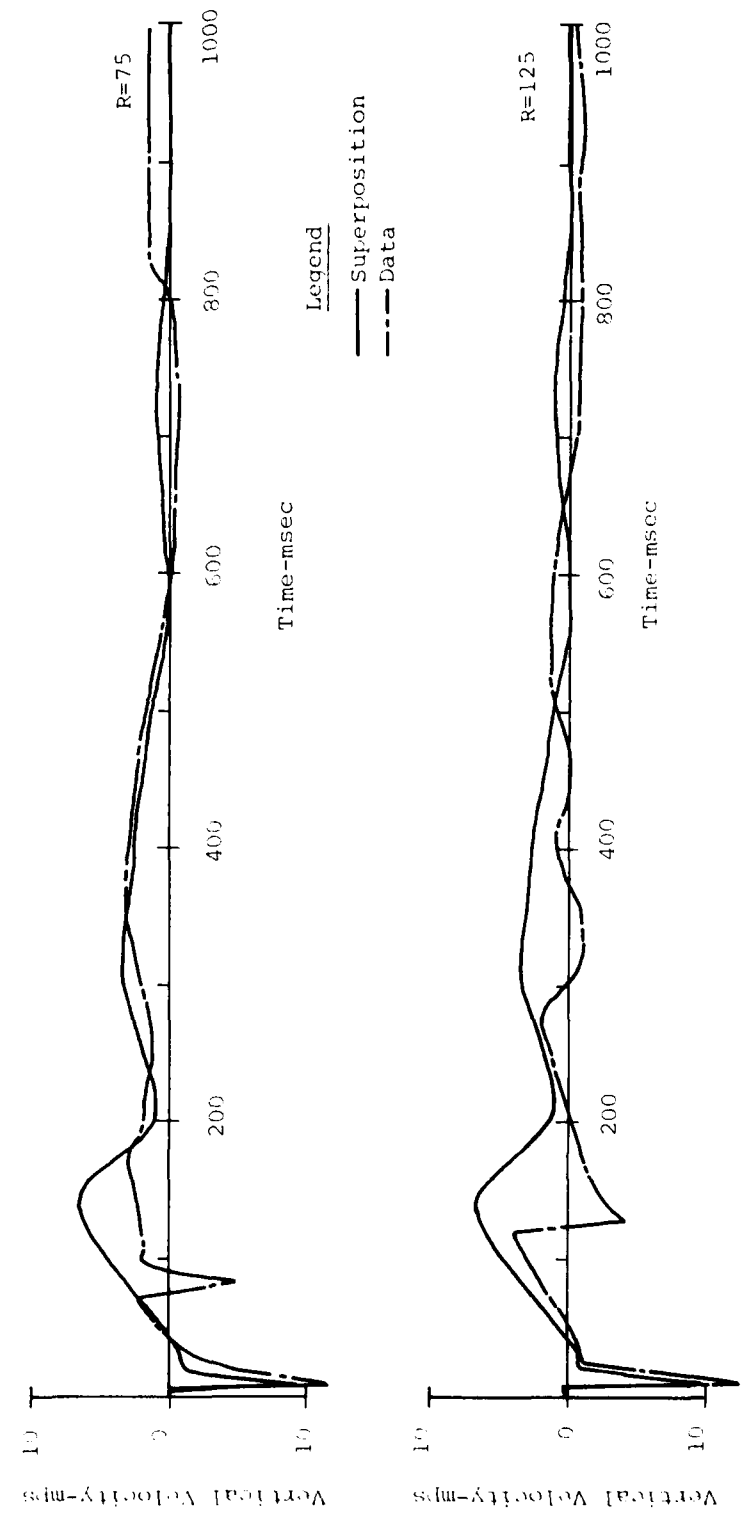


Figure A.40. Comparison of MBII-2 Data and Superimposed MBII-1 Data @ 75-0.5-Charge Line and 125-0.5-Charge Line Vertical Velocity

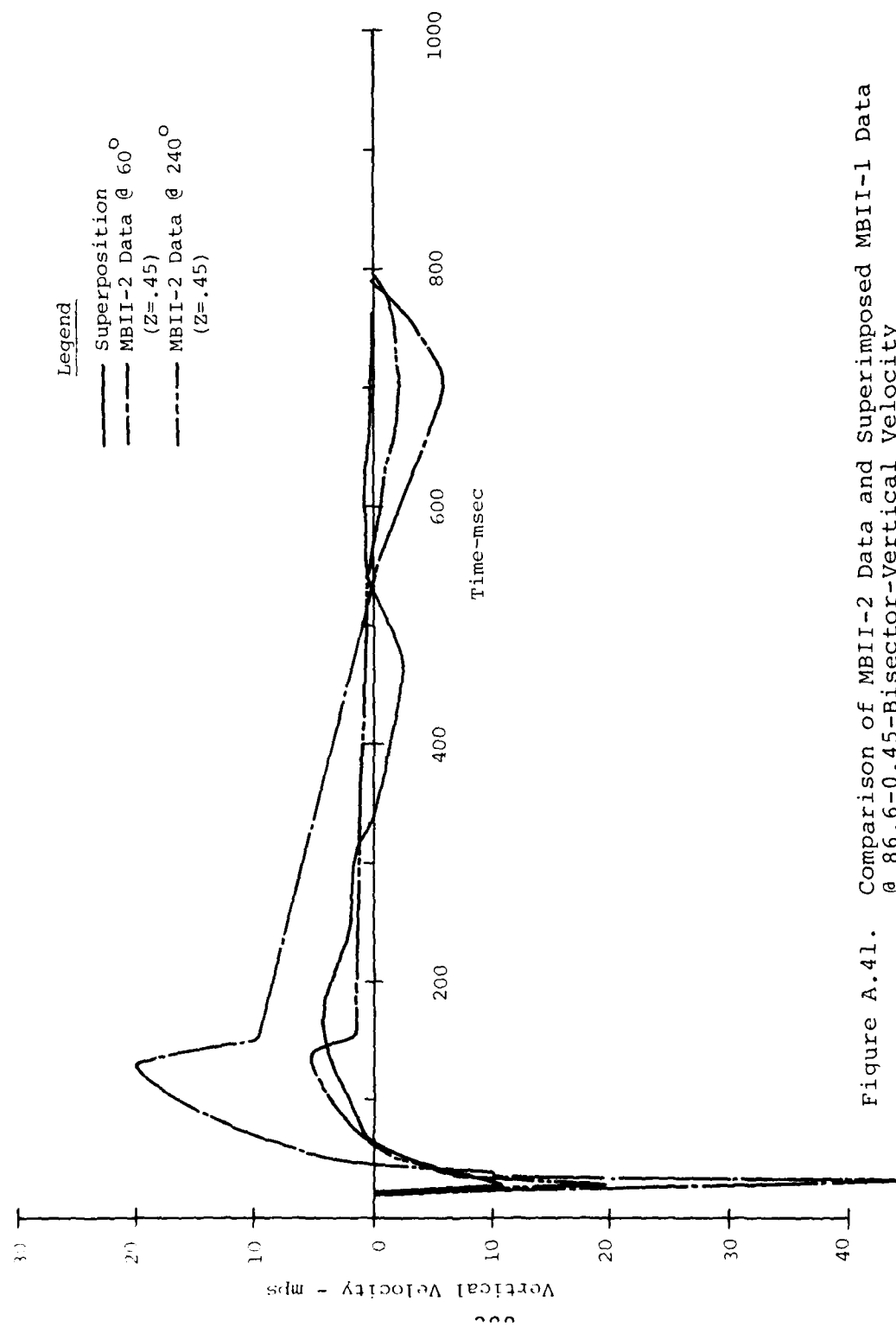


Figure A.41. Comparison of MBII-2 Data and Superimposed MBII-1 Data
@ 86.6-0.45-Bisector-Vertical Velocity

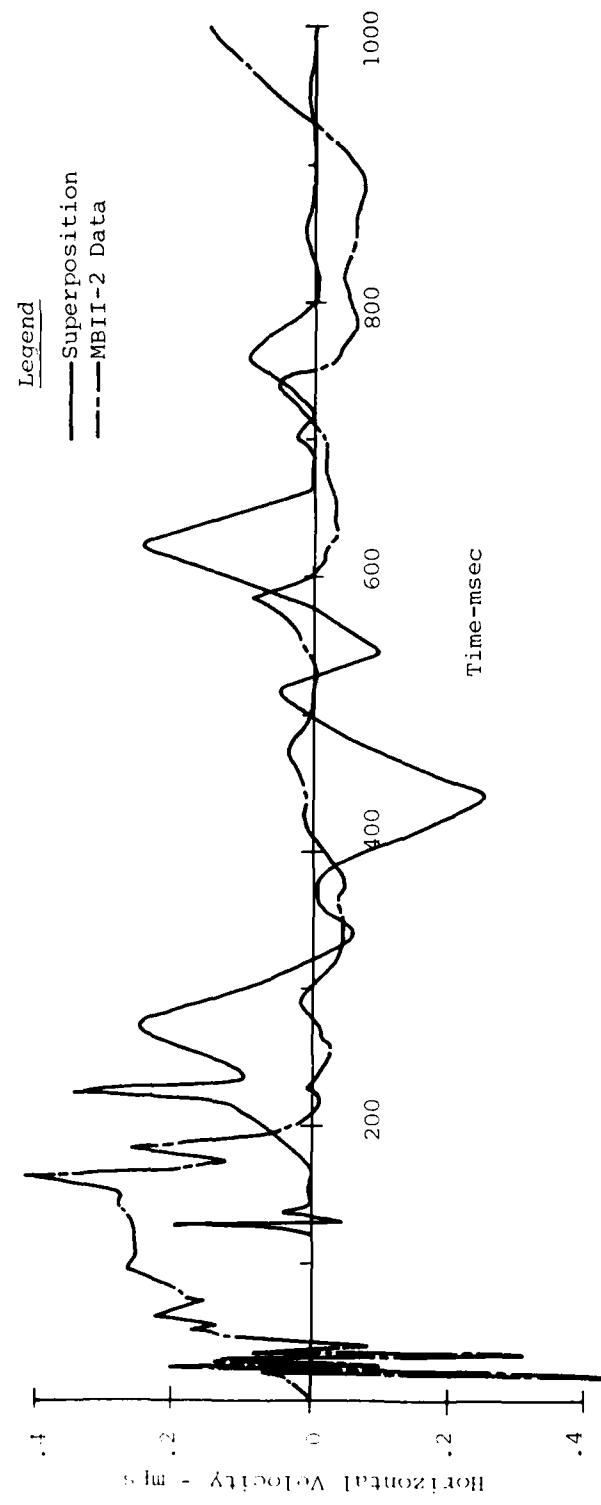
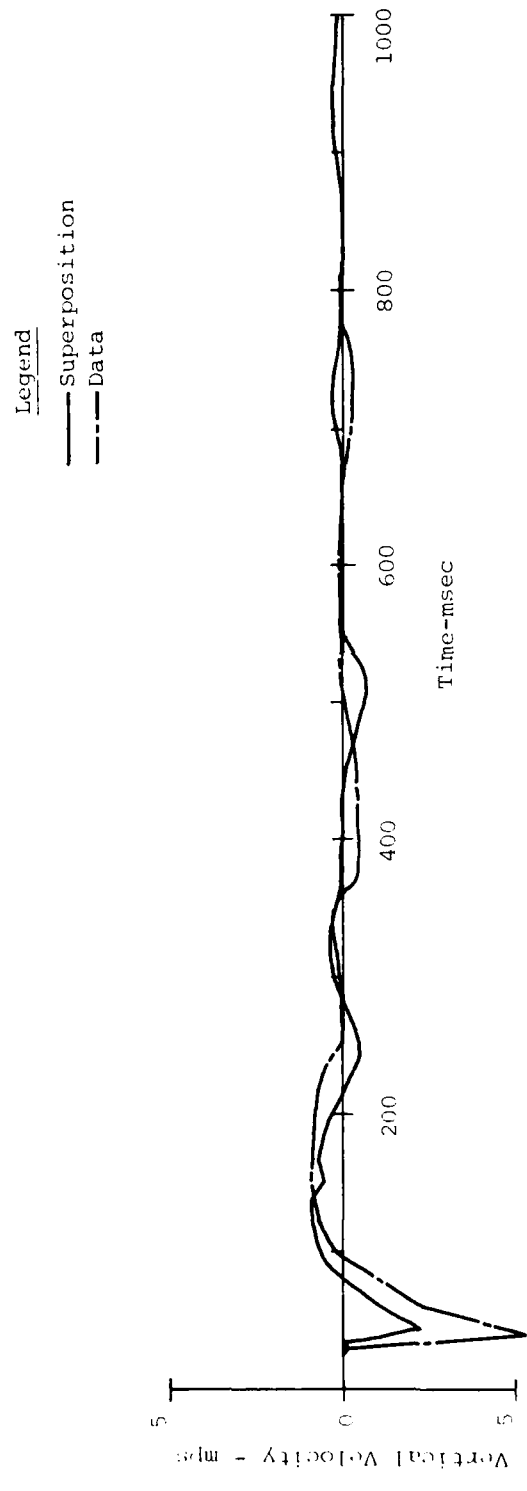


Figure A.42. Comparison of MBII-2 Data and Superimposed MBII-1 Data
@ 86.6-0.5-Bisector-Horizontal Velocity



290

Figure A.43. Comparison of MBII-2 Data and Superimposed of MBII-1 Data
at 86.6-3.0-Bisector-Vertical Velocity

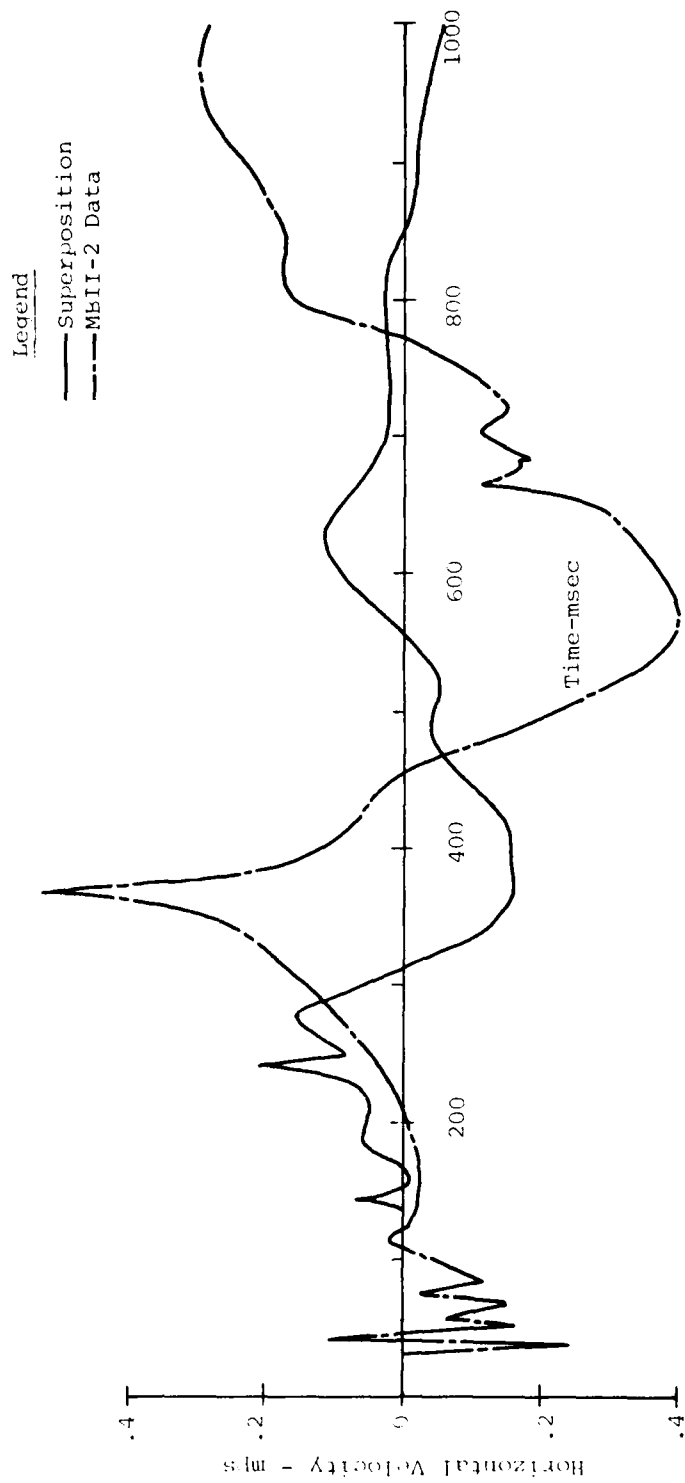


Figure A.44. Comparison of MBII-2 Data and Superimposed MBII-1 Data
@ 86.6-3-Bisection-Horizontal Velocity

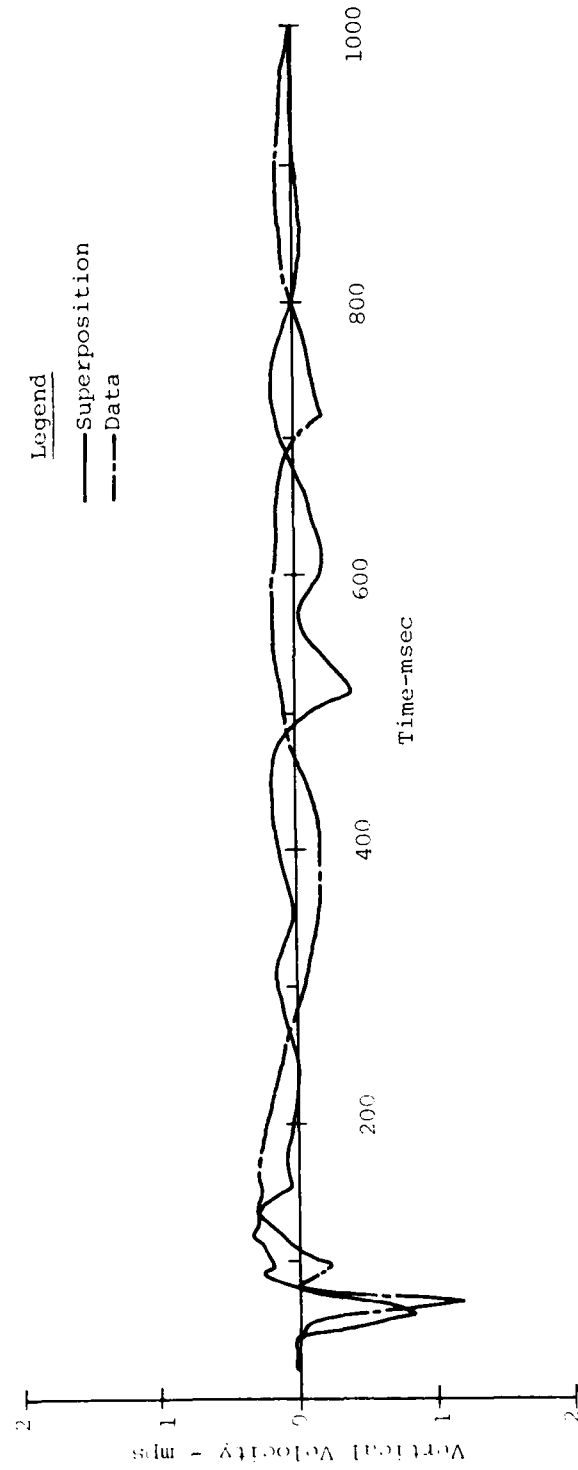


Figure A.45. Comparison of MBII-2 Data and Superimposed MBII-1 Data
a 86.6-9-Bisector-Vertical Velocity

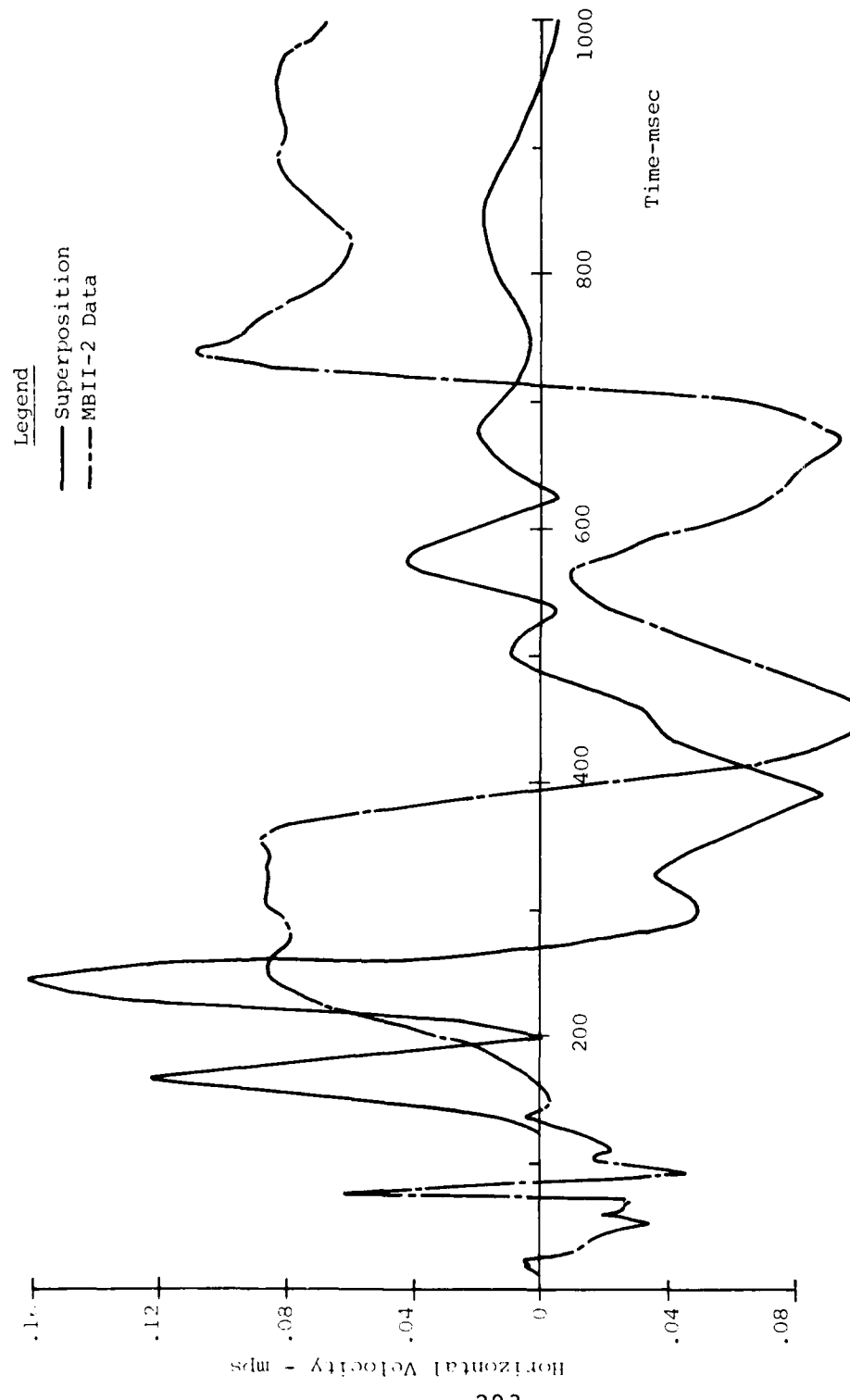


Figure A.46. Comparison of MBII-2 Data and Superimposed MBII-1 Data
at 86.6-9-Bisector-Horizontal Velocity

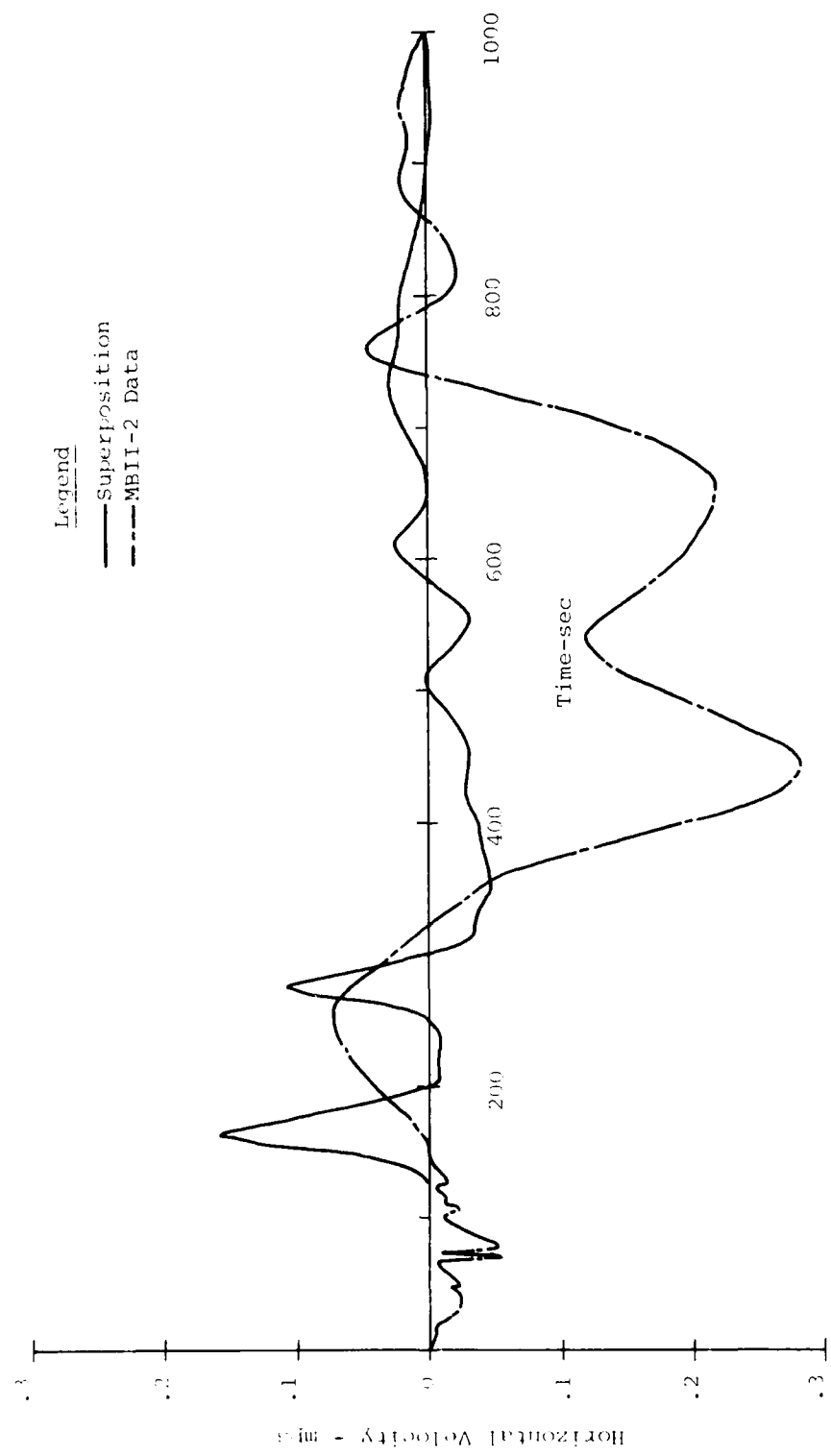


Figure A.47. Comparison of MBII-2 Data and Superimposed MBII-1 Data
at 86.6-12.5-Bisector-Horizontal Velocity

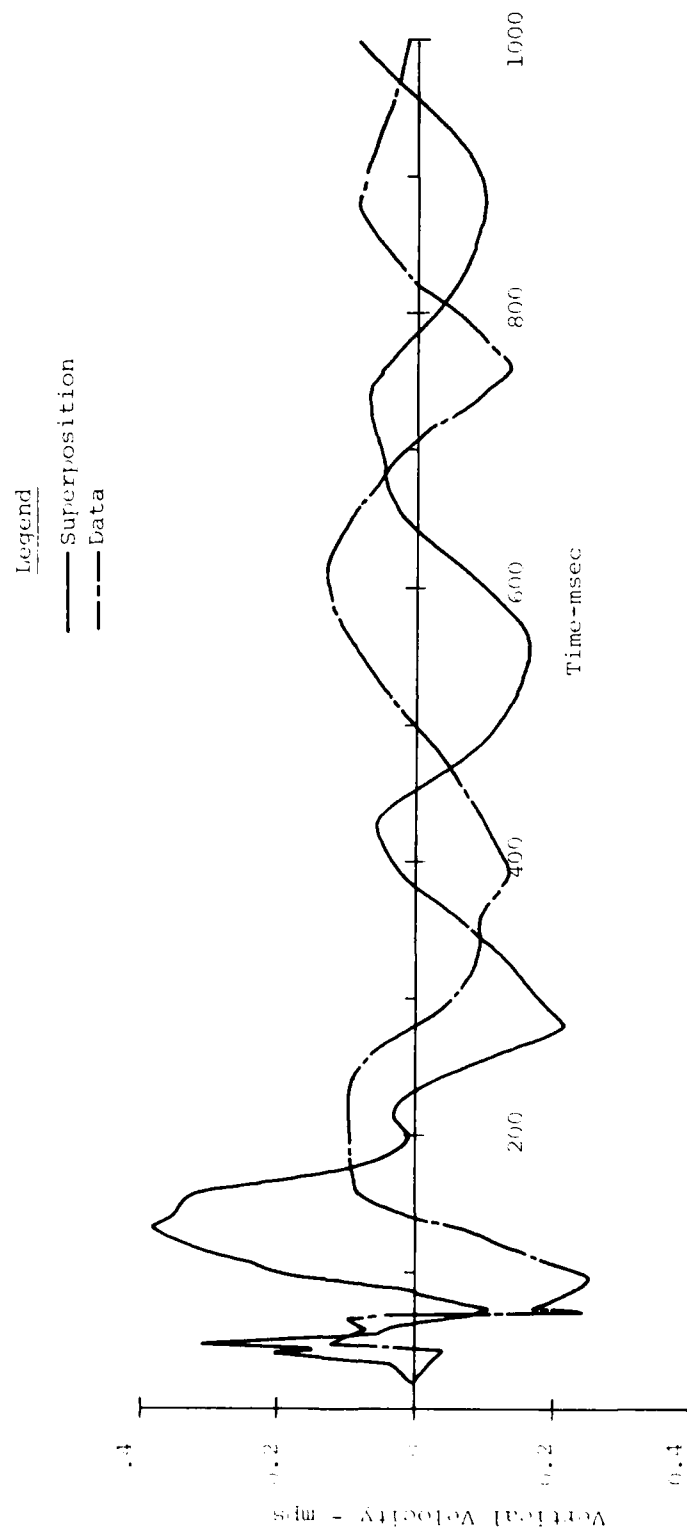


Figure A.48. Comparison of MBII-2 Data and Superimposed MBII-1 Data
at 86.6-12.5-Bisector-Vertical Velocity

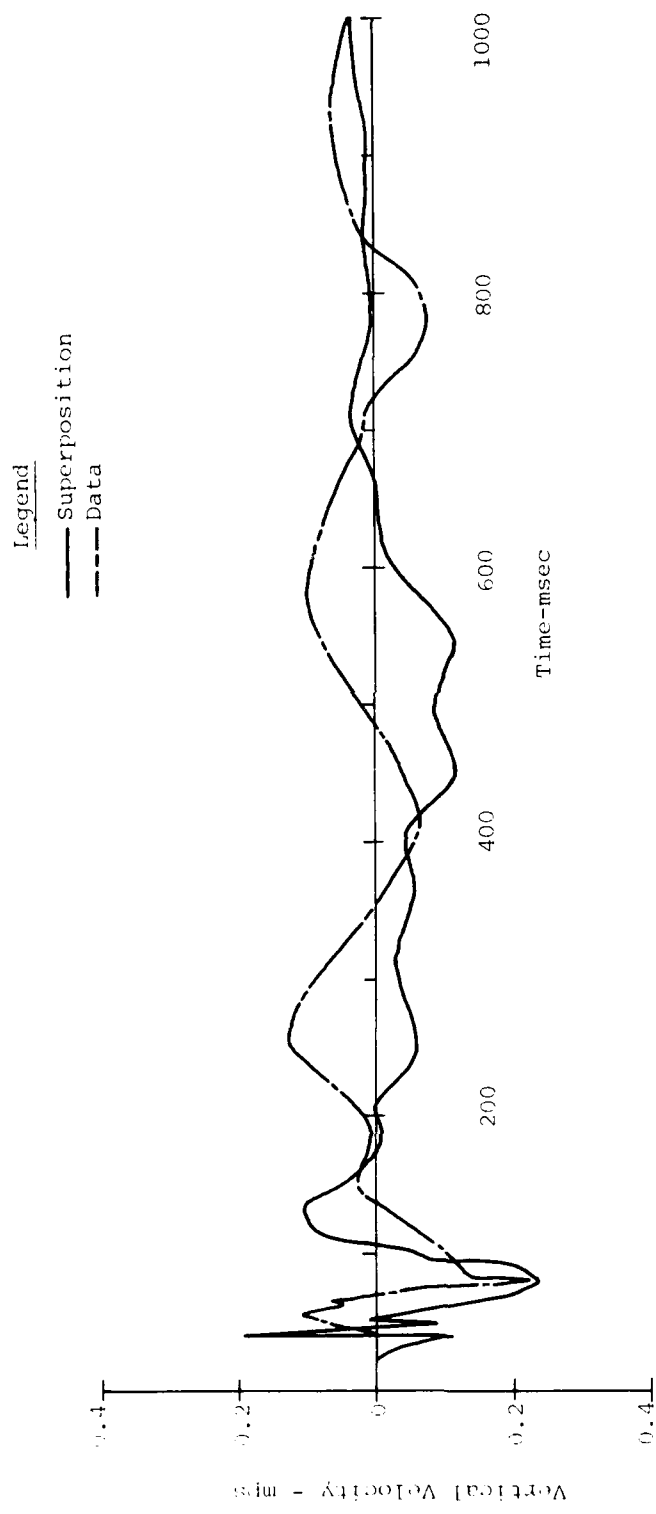


Figure A.49. Comparison of MBII-2 Data and Superimposed MBII-1 Data
at 86.6-25-Bisector-Vertical Velocity

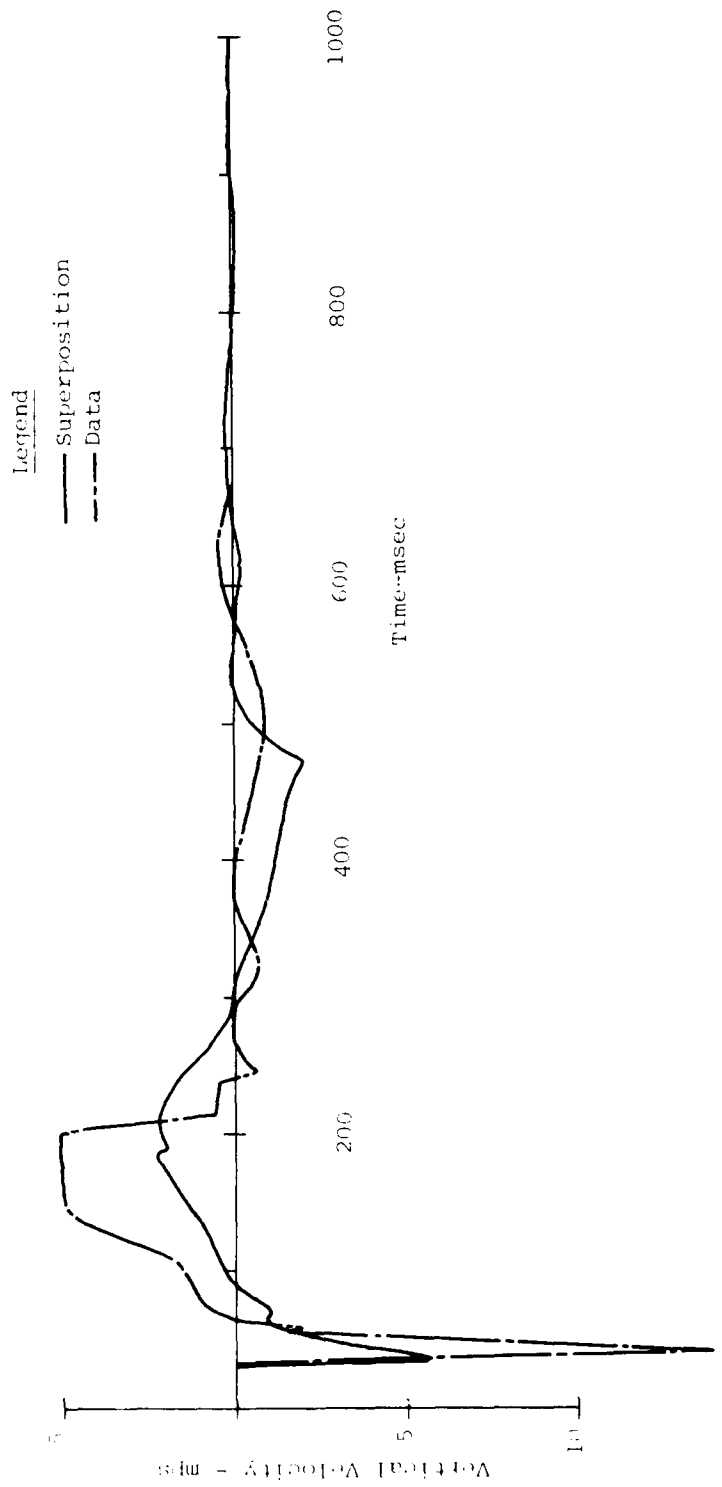


Figure A.50. Comparison of MBII-2 Data and Superimposed MBII-1 Data
at 129.9-0.5-Bisector-Vertical Velocity

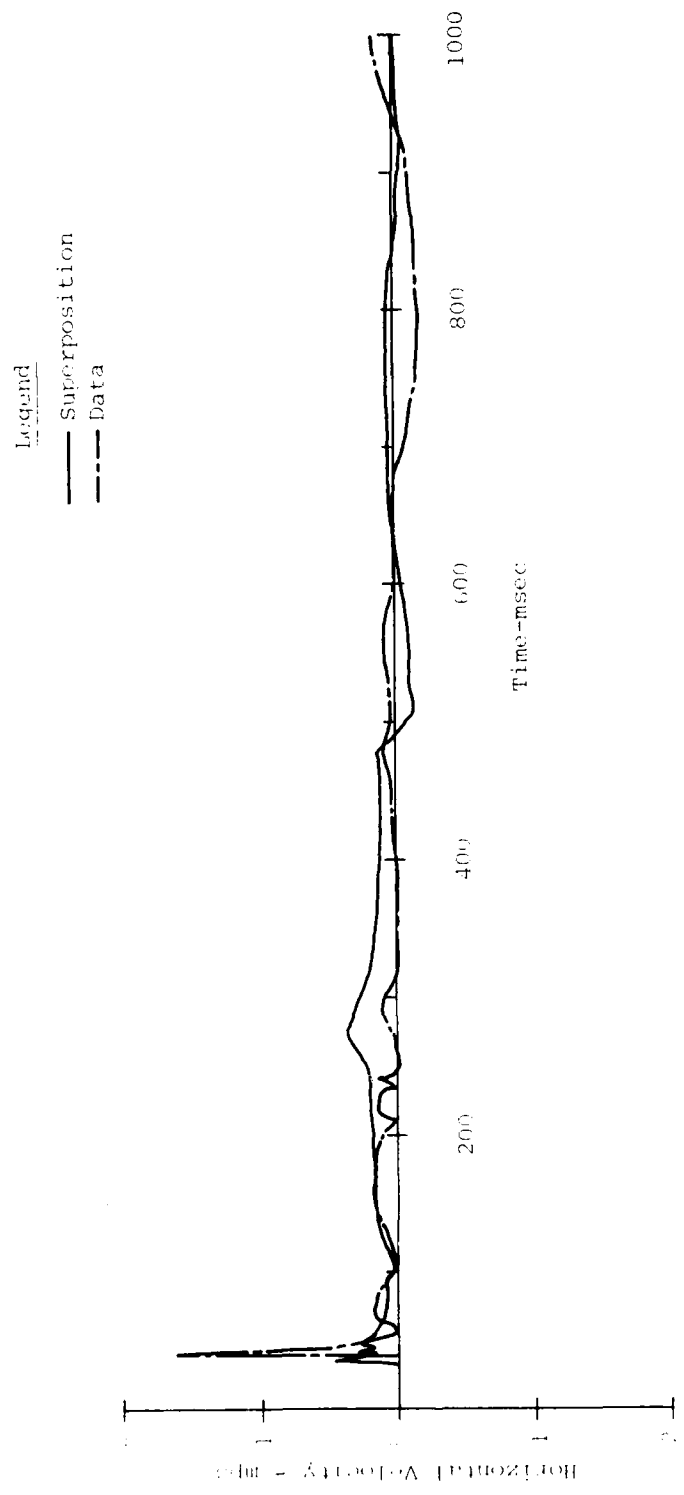


Figure A.51. Comparison of MBII-2 Data and Superimposed MBII-1 Data
at 129.9-0.5-Bisector-Horizonal Velocity

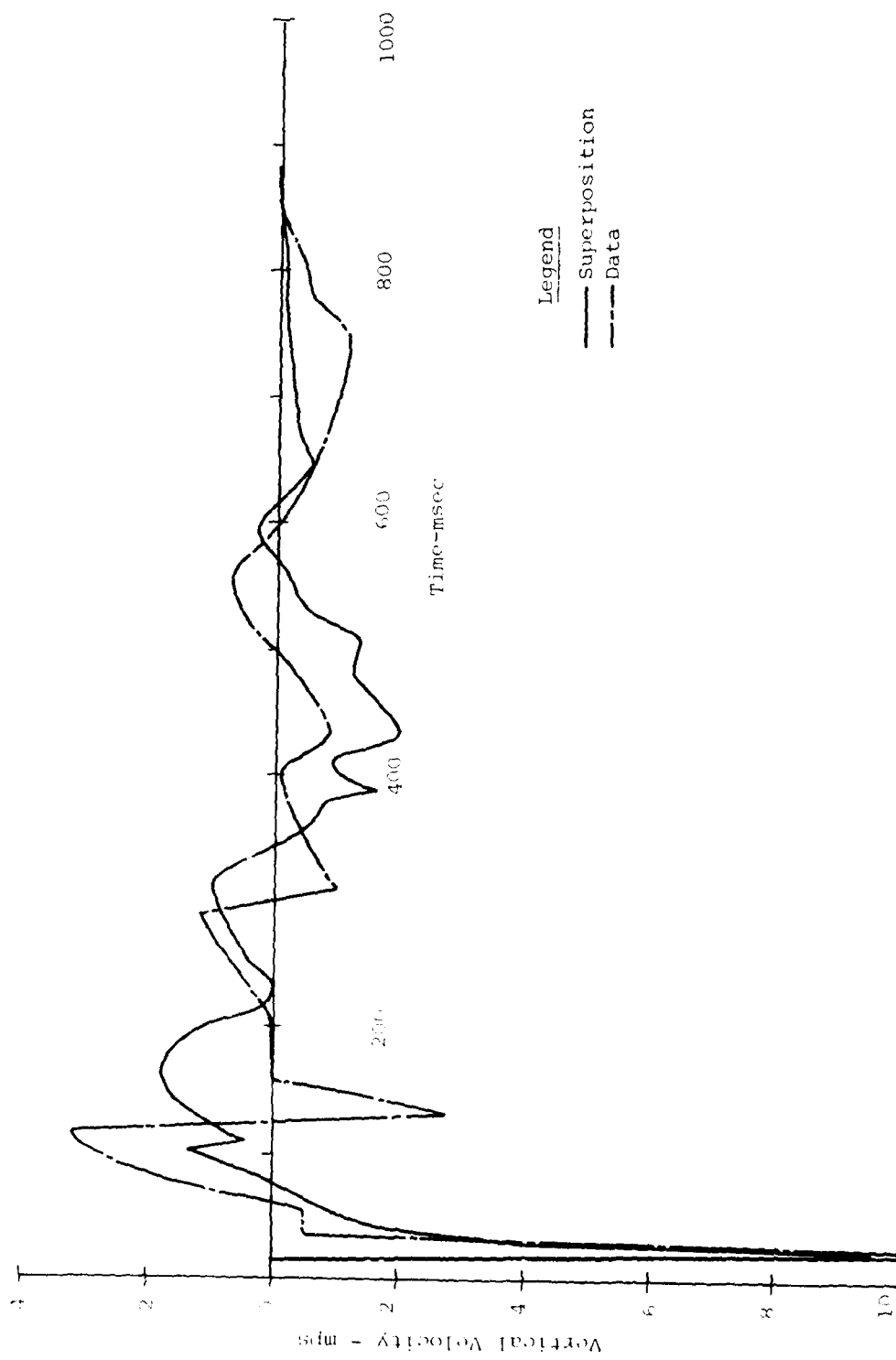


Figure A.52. Comparison of MBLI-2 Data and Superimposed MBLI-1 Data
at 133.5-0.5-Charge Line-Vertical Velocity

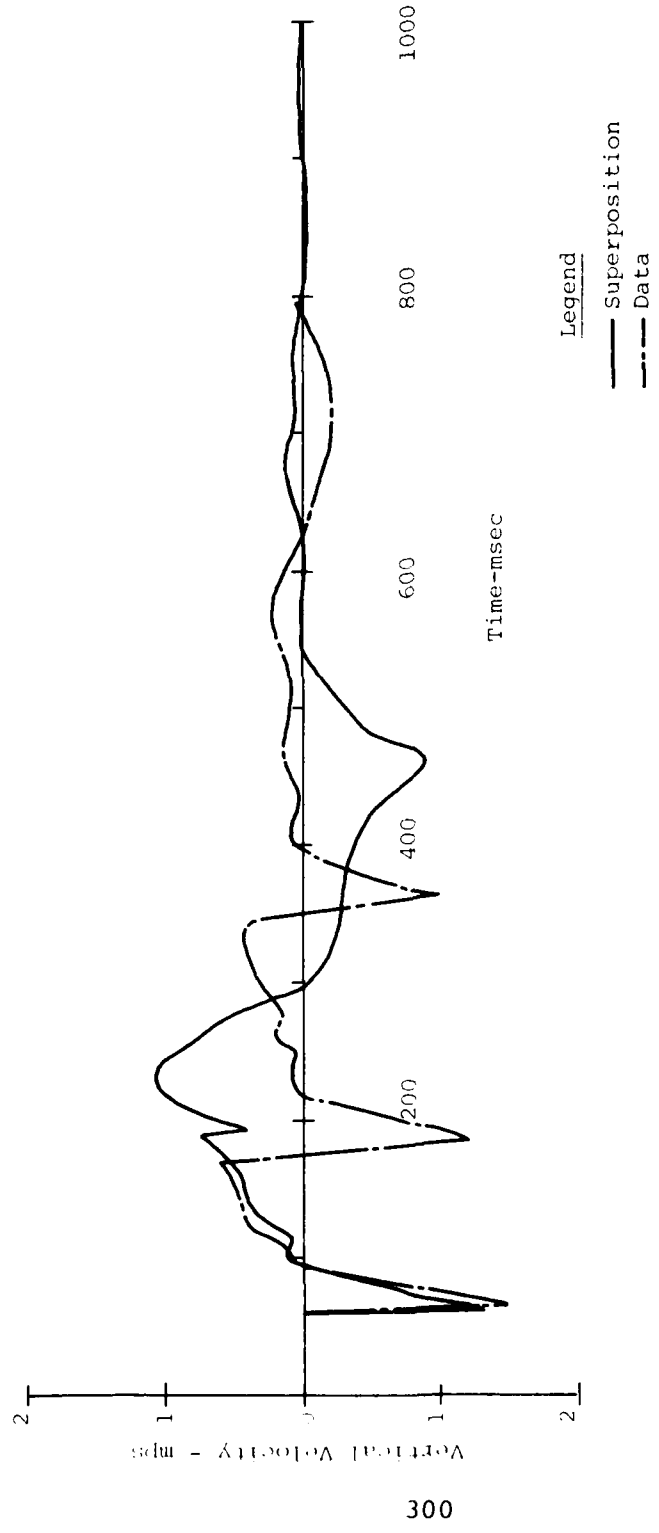


Figure A.53. Comparison of MBII-2 Data and Superimposed MBII-1 Data @ 188-0.5-Charge Line-Vertical Velocity

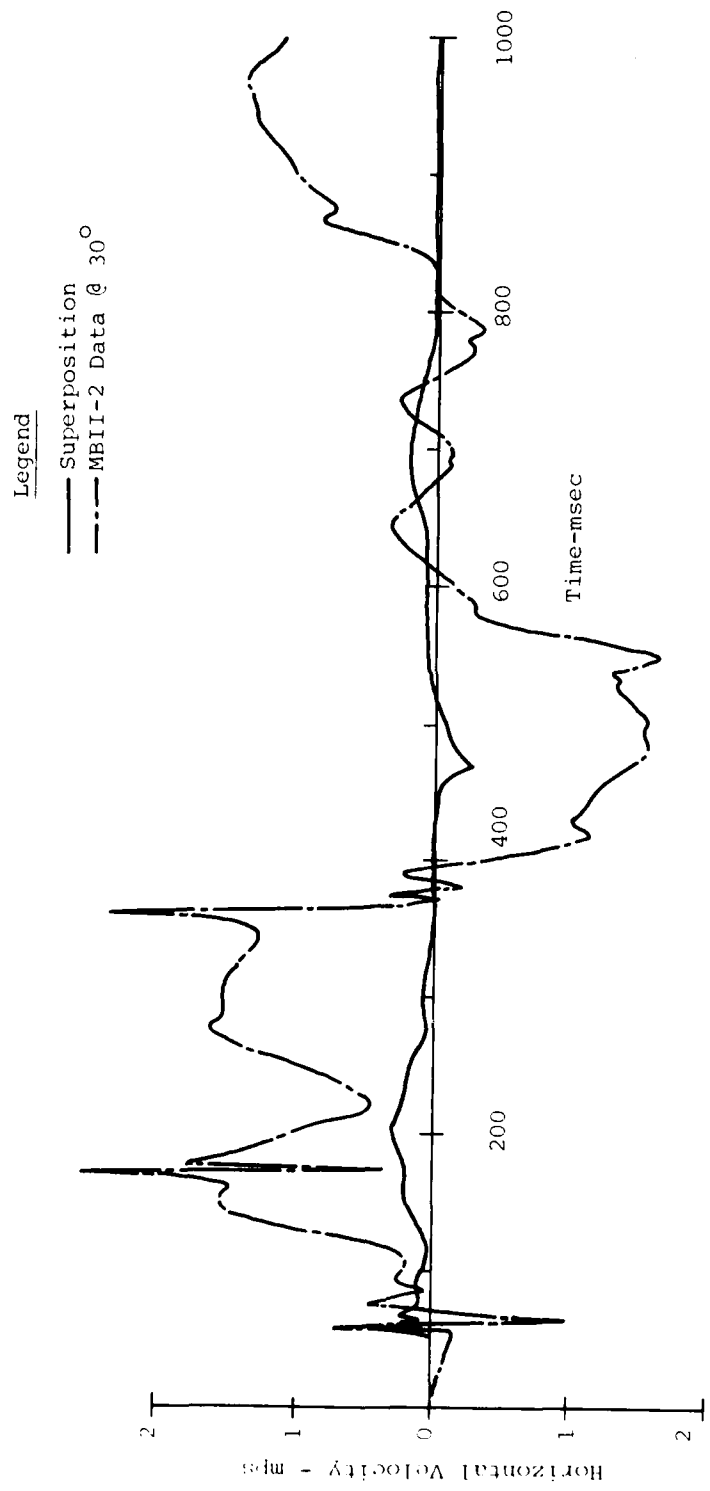


Figure A.54. Comparison of MBII-2 Data and Superimposed MBII-1 Data
 θ 188-0.5-Charge Line-Horizontal Velocity

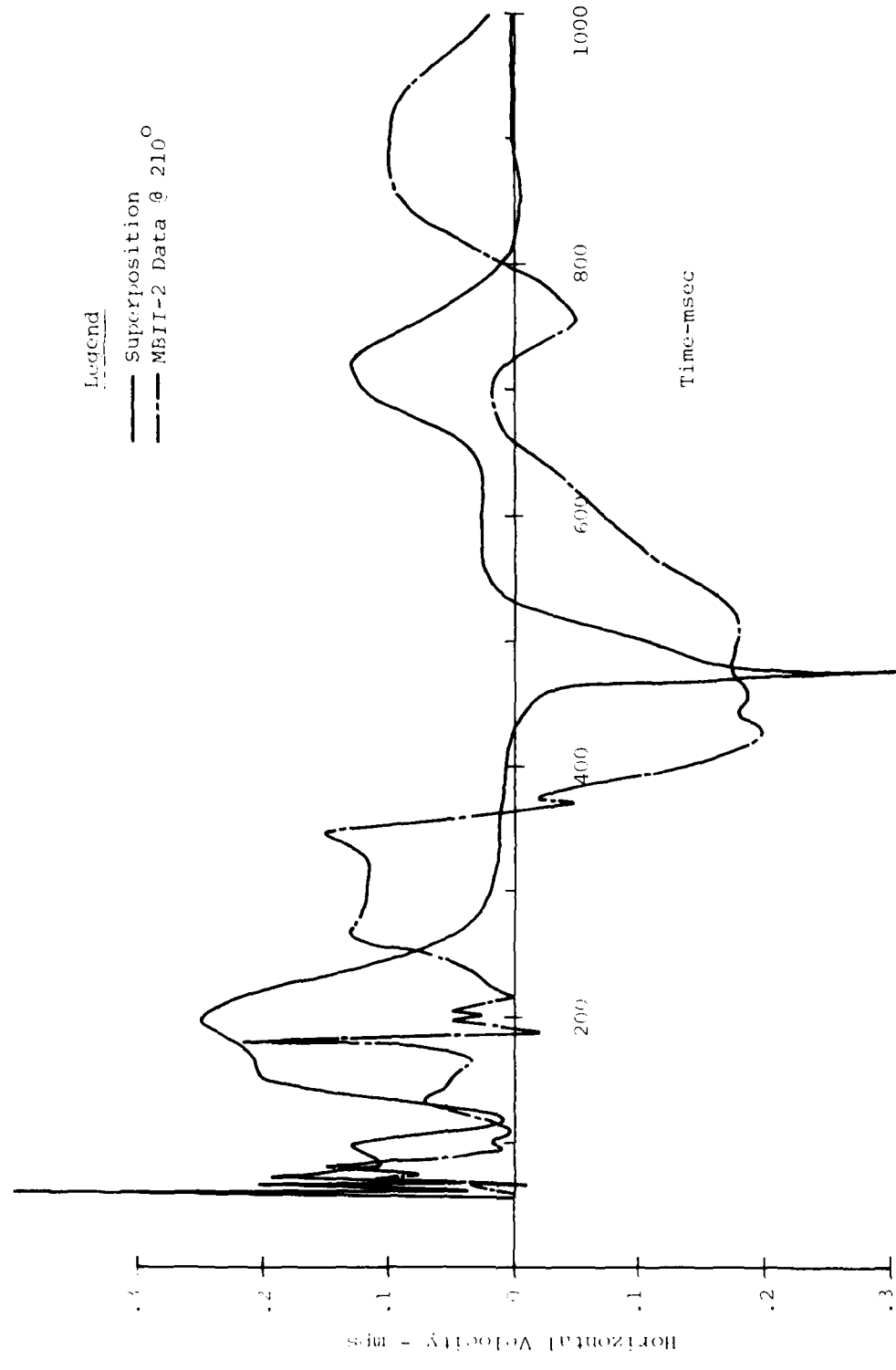


Figure A.55. Comparison of MBII-2 Data and Superimposed MBII-1 Data
at 188-0.5-Charge Line - Horizontal Velocity

APPENDIX B

Superposition vs Data
Shock Spectra Comparisons

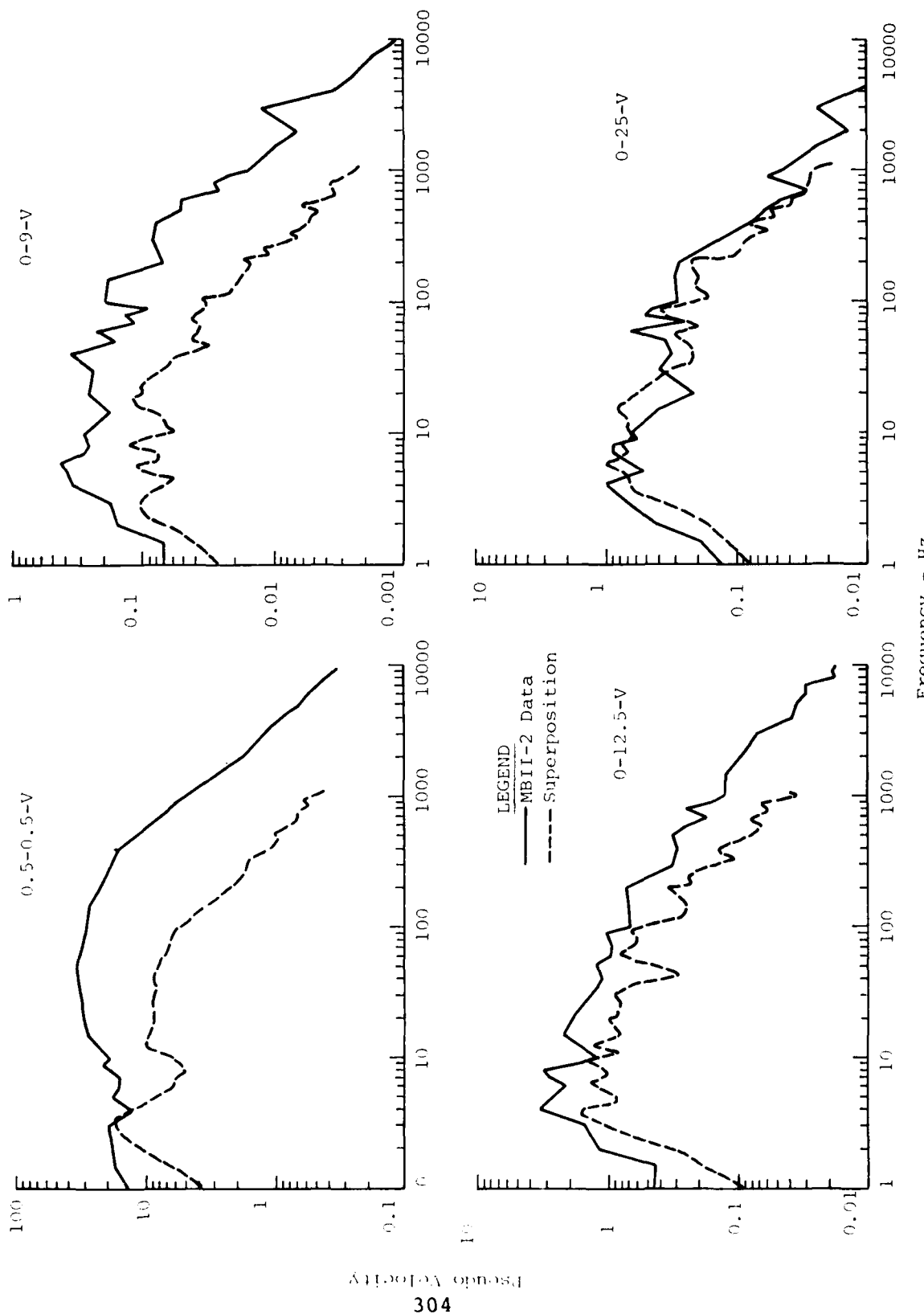


Figure B.1. Shock Spectra Comparisons of MBII-2 Data and Superposition
 $\oplus R=0$

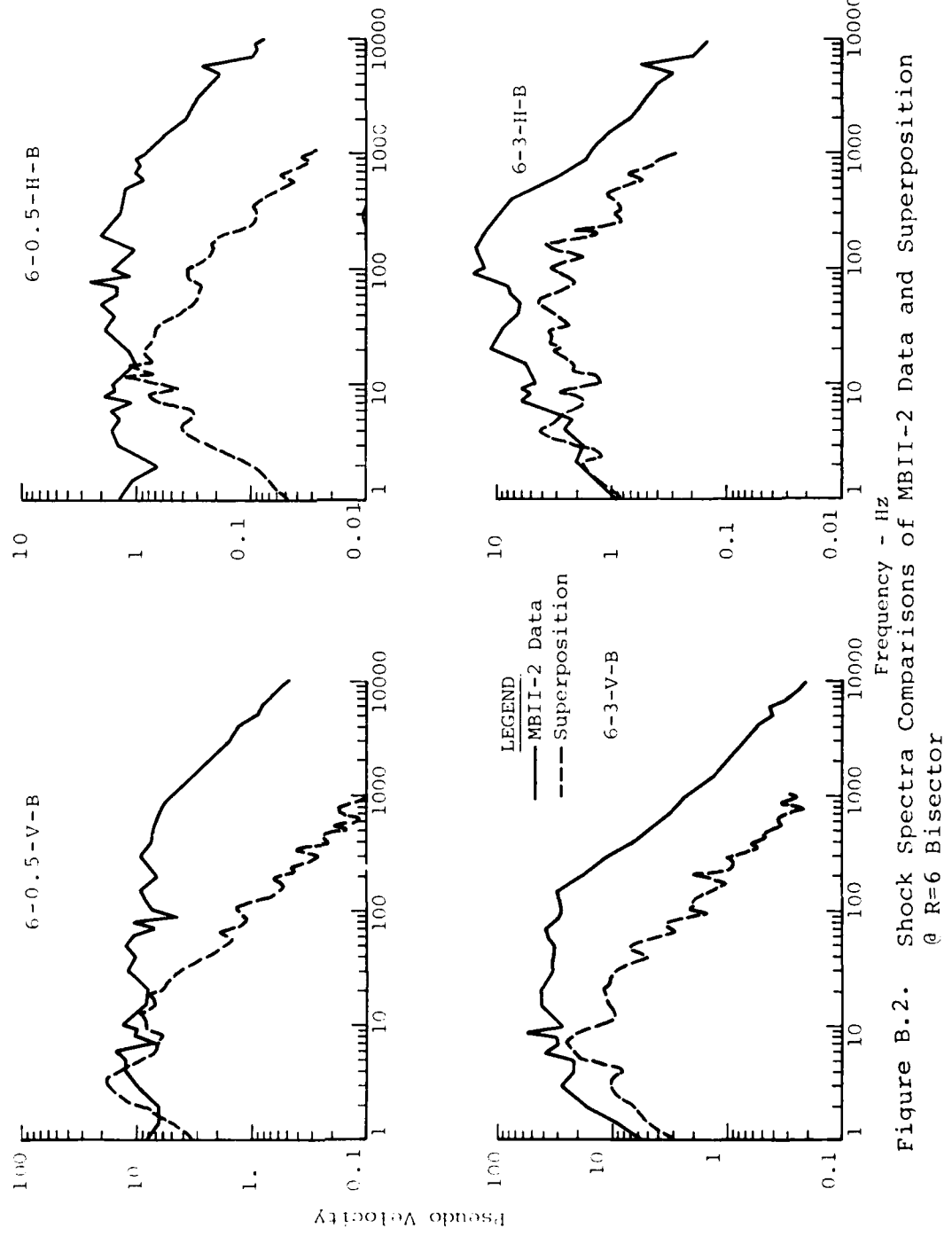


Figure B.2. Shock Spectra Comparisons of MBII-2 Data and Superposition
@ R=6 Bisector

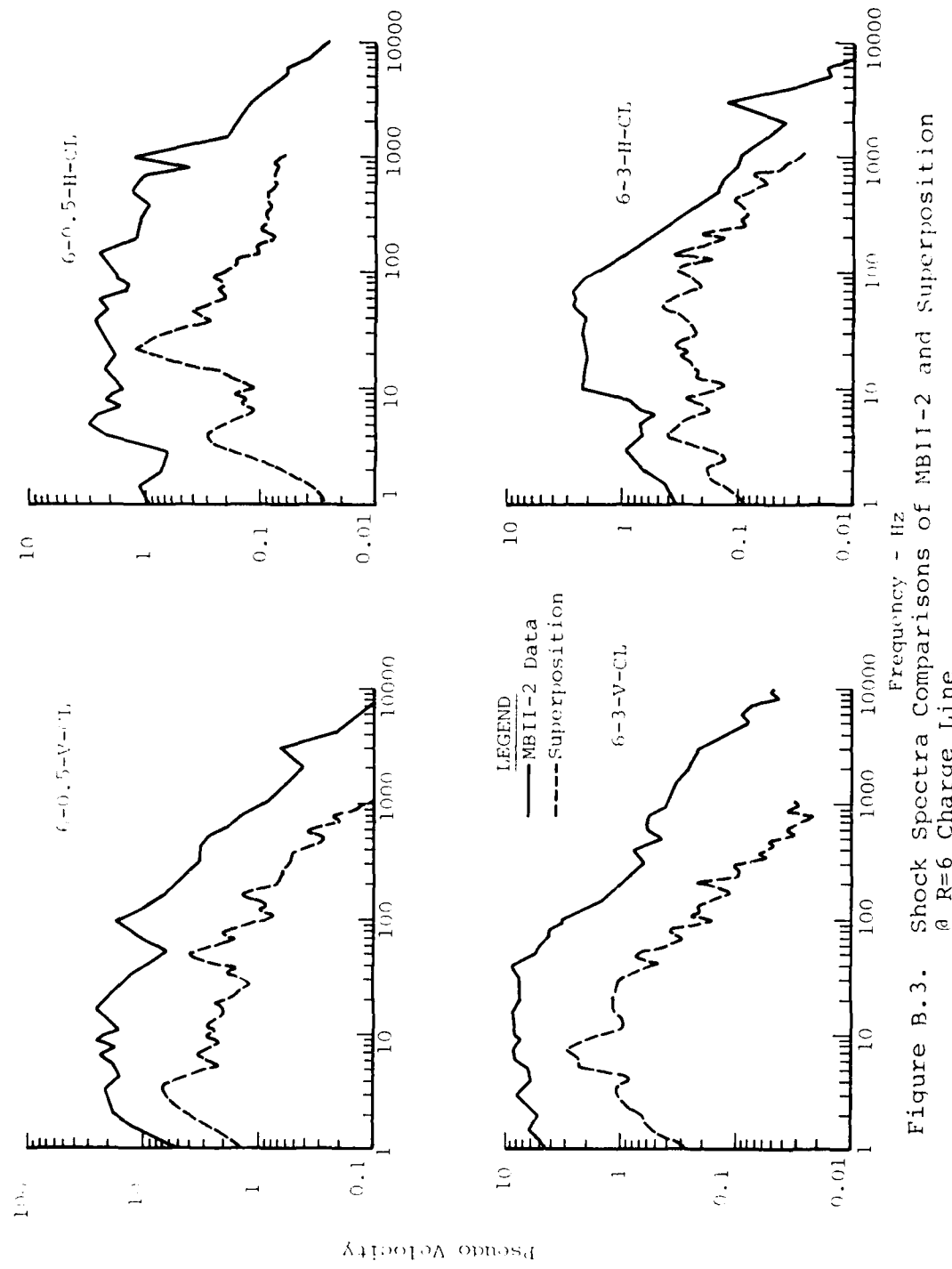


Figure B.3. Shock Spectra Comparisons of MBII-2 and Superposition
at R=6 Charge Line

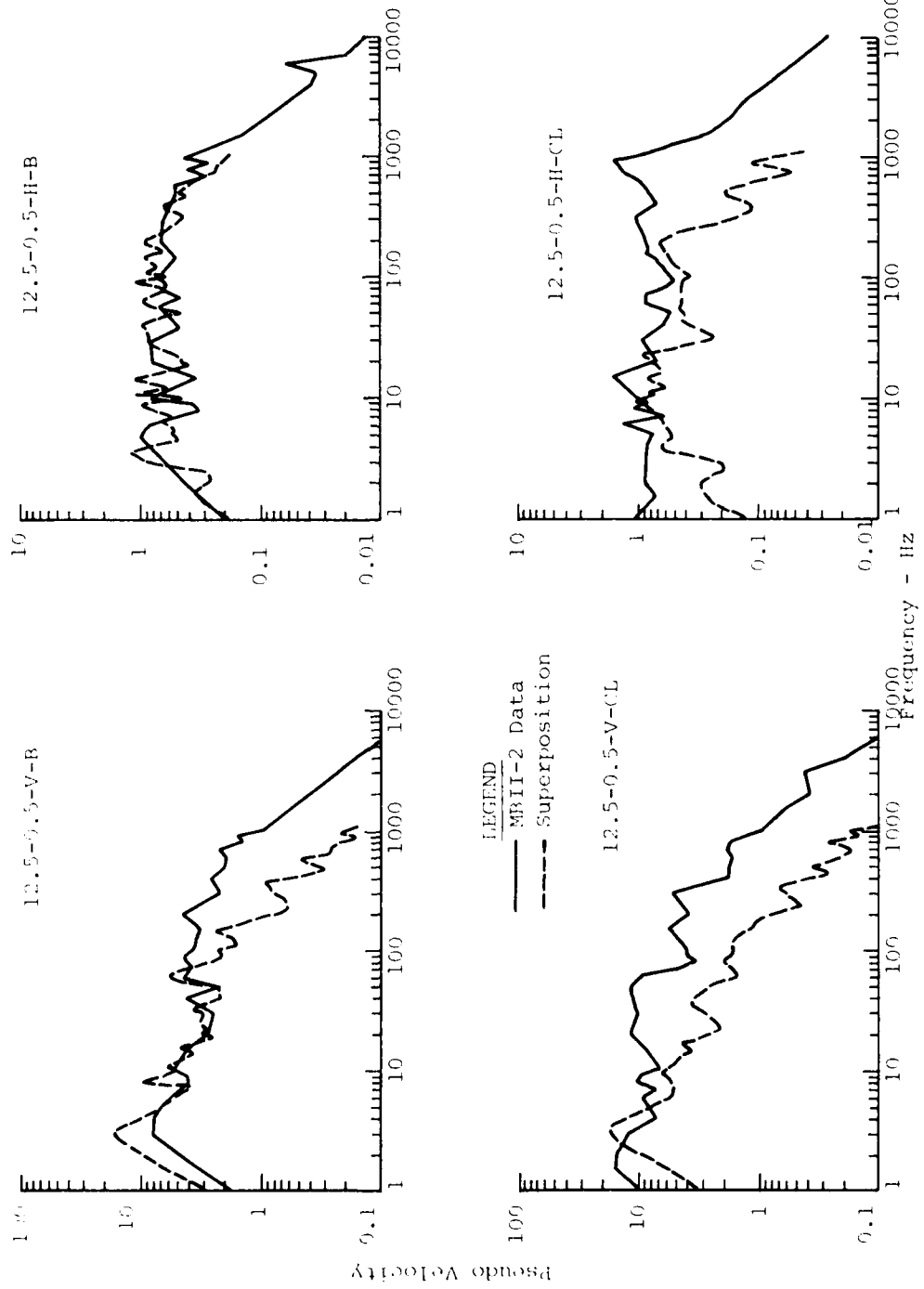


Figure B.4. Shock Spectra Comparisons of MBII-2 Data and Superposition
 \ominus R=12.5-0.5 - Bisector and Charge Line

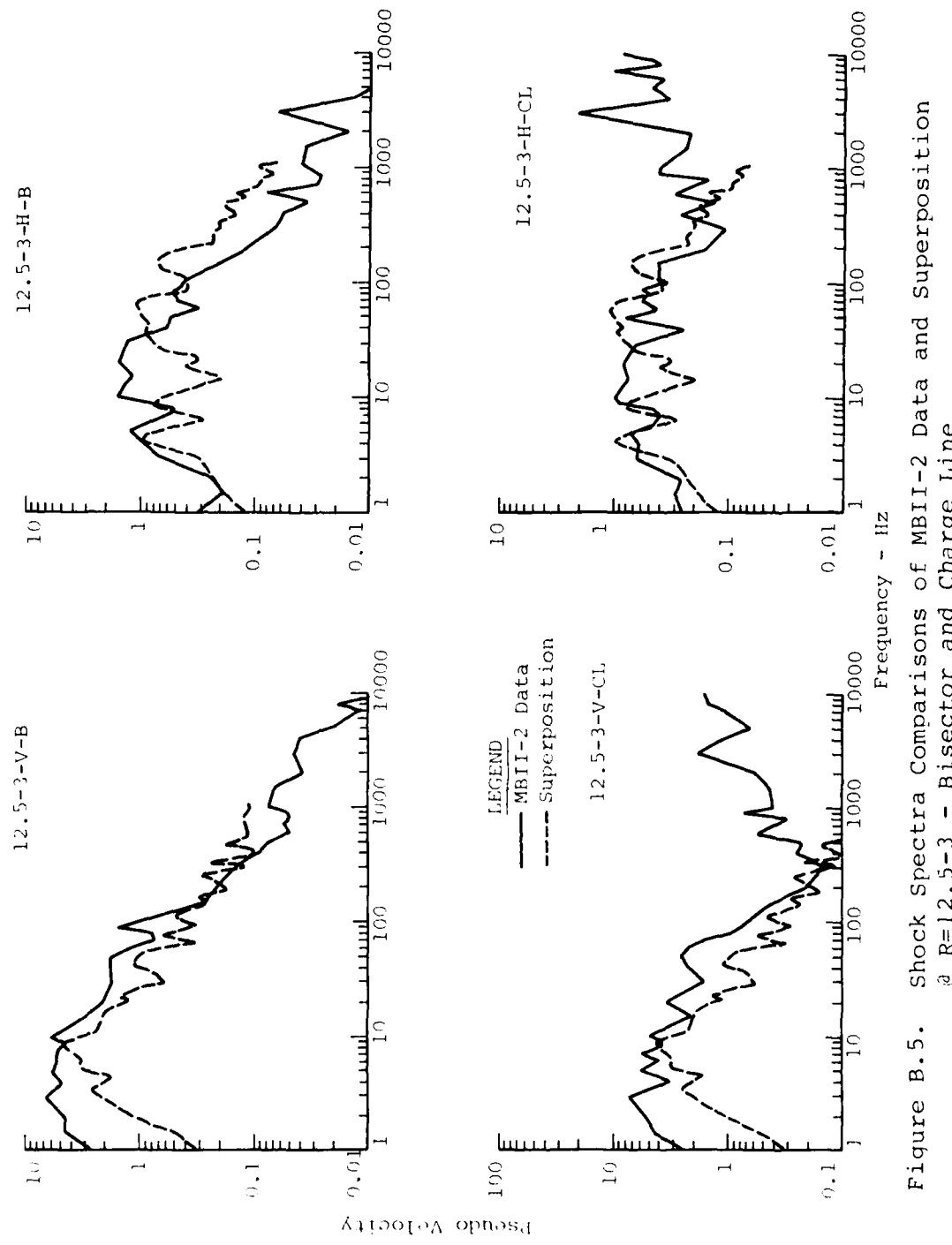


Figure B.5. Shock Spectra Comparisons of MBII-2 Data and Superposition
 ϑ R=12.5-3 - Bisector and Charge Line

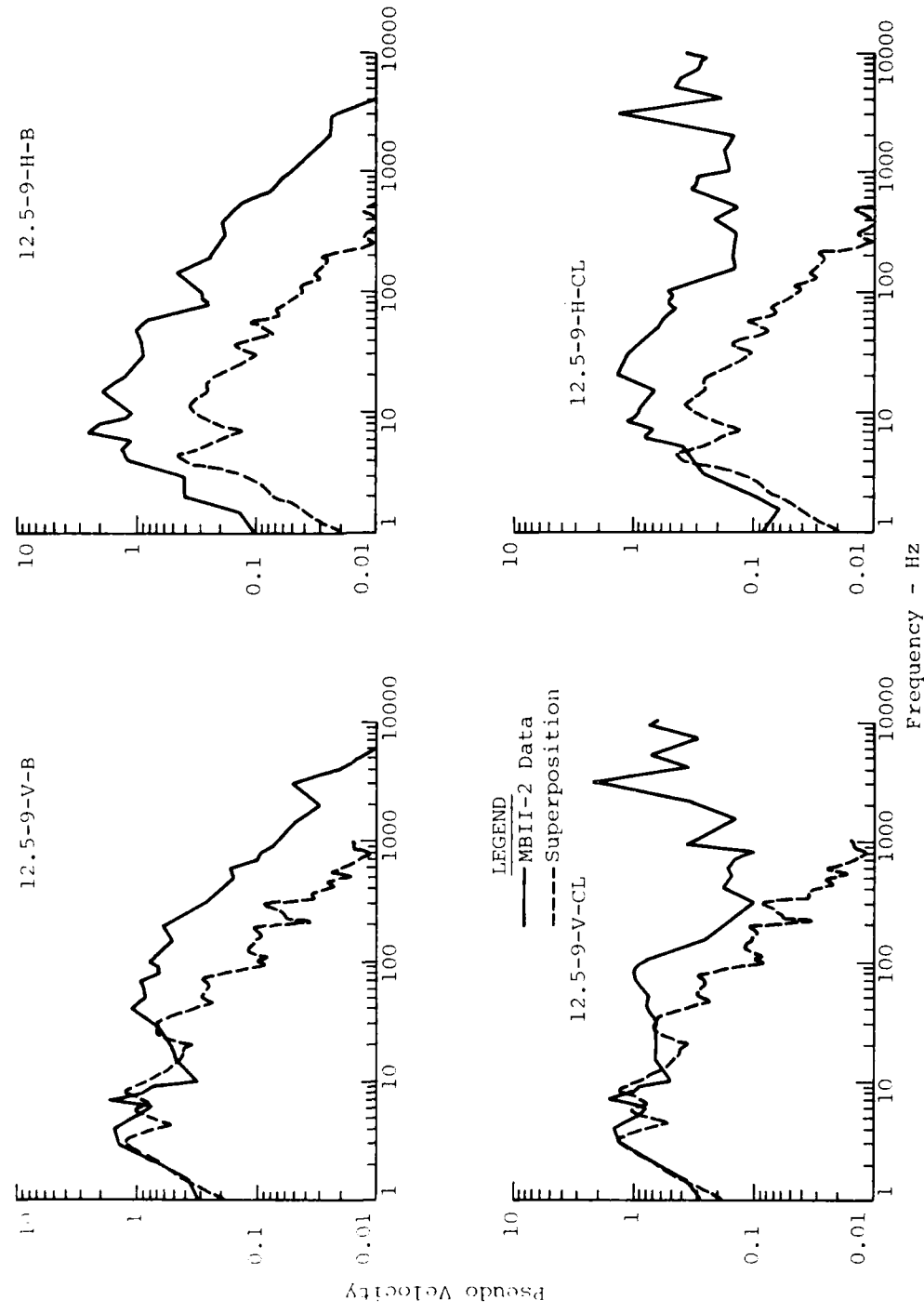


Figure B.6. Shock Spectra Comparisons of MBII-2 Data and Superposition
@ R=12.5-9 - Bisector and Charge Line

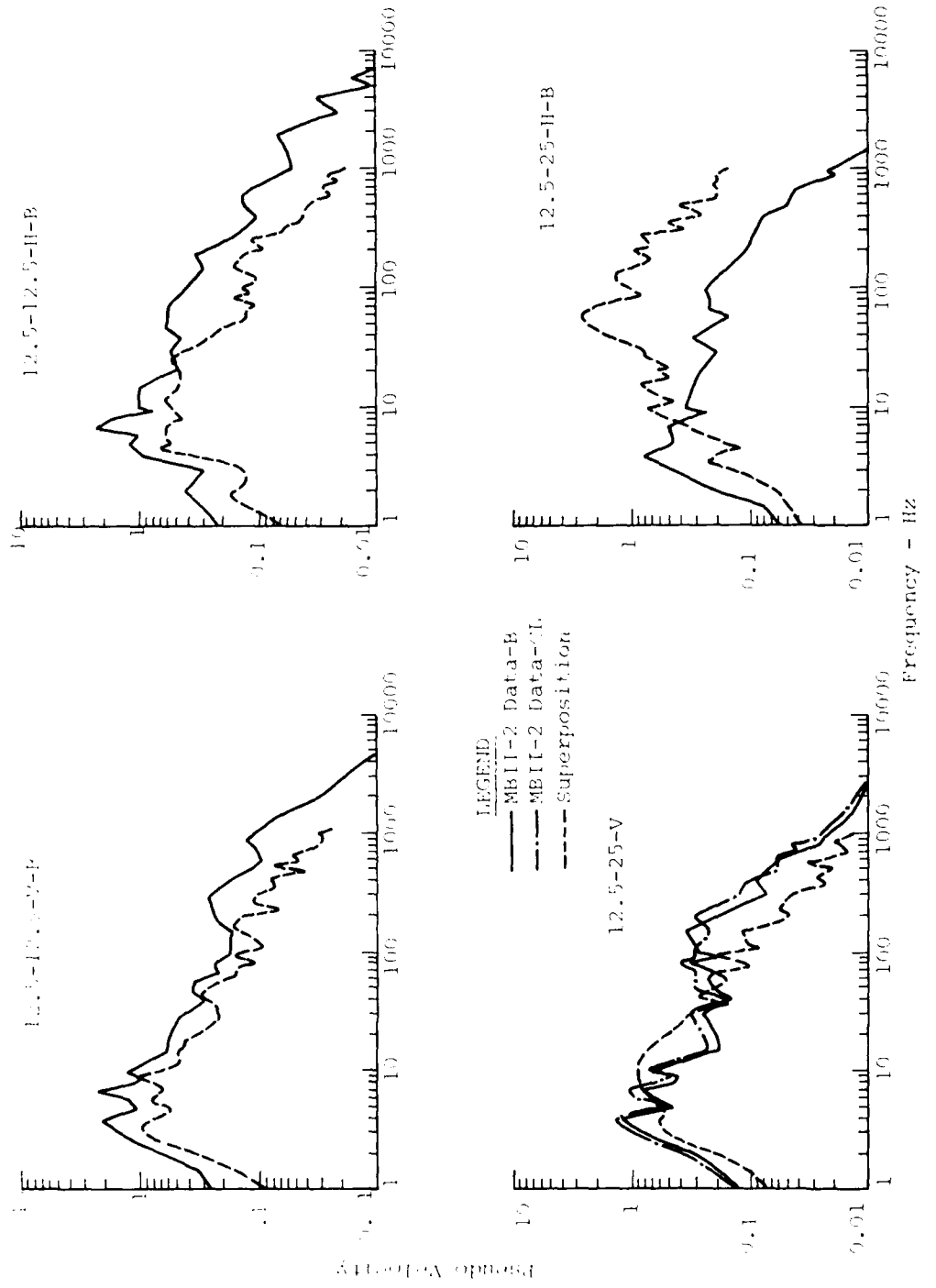


Figure B.7. Shock Spectra Comparisons of MBII-2 Data and Superposition
@ R=12.5-12.5 and 12.5-25 - Bisector and Charge Line

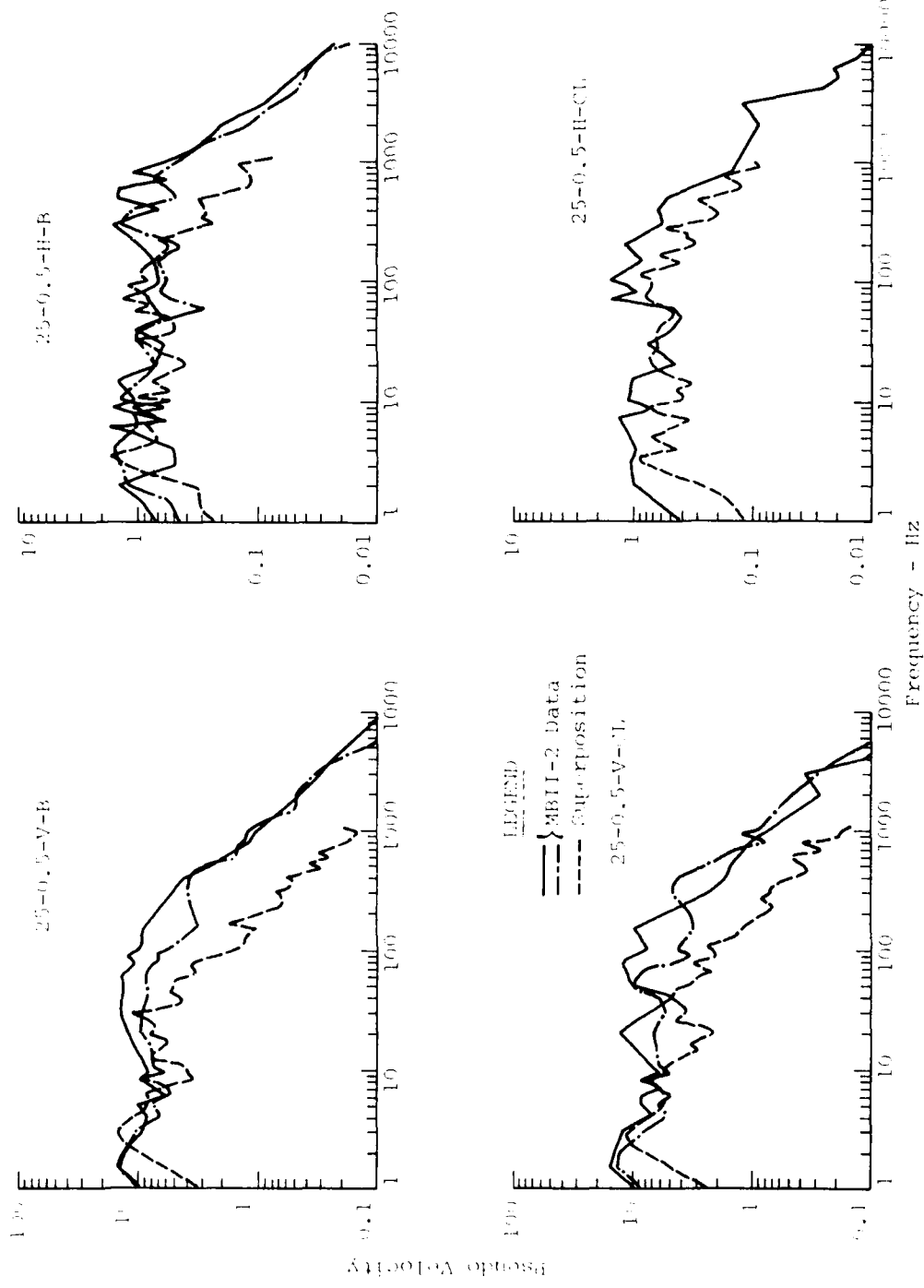


Figure B.8. Shock Spectra Comparisons of MBII-2 Data and Superposition
^a R=25-0.5 - B sector and Charge Line

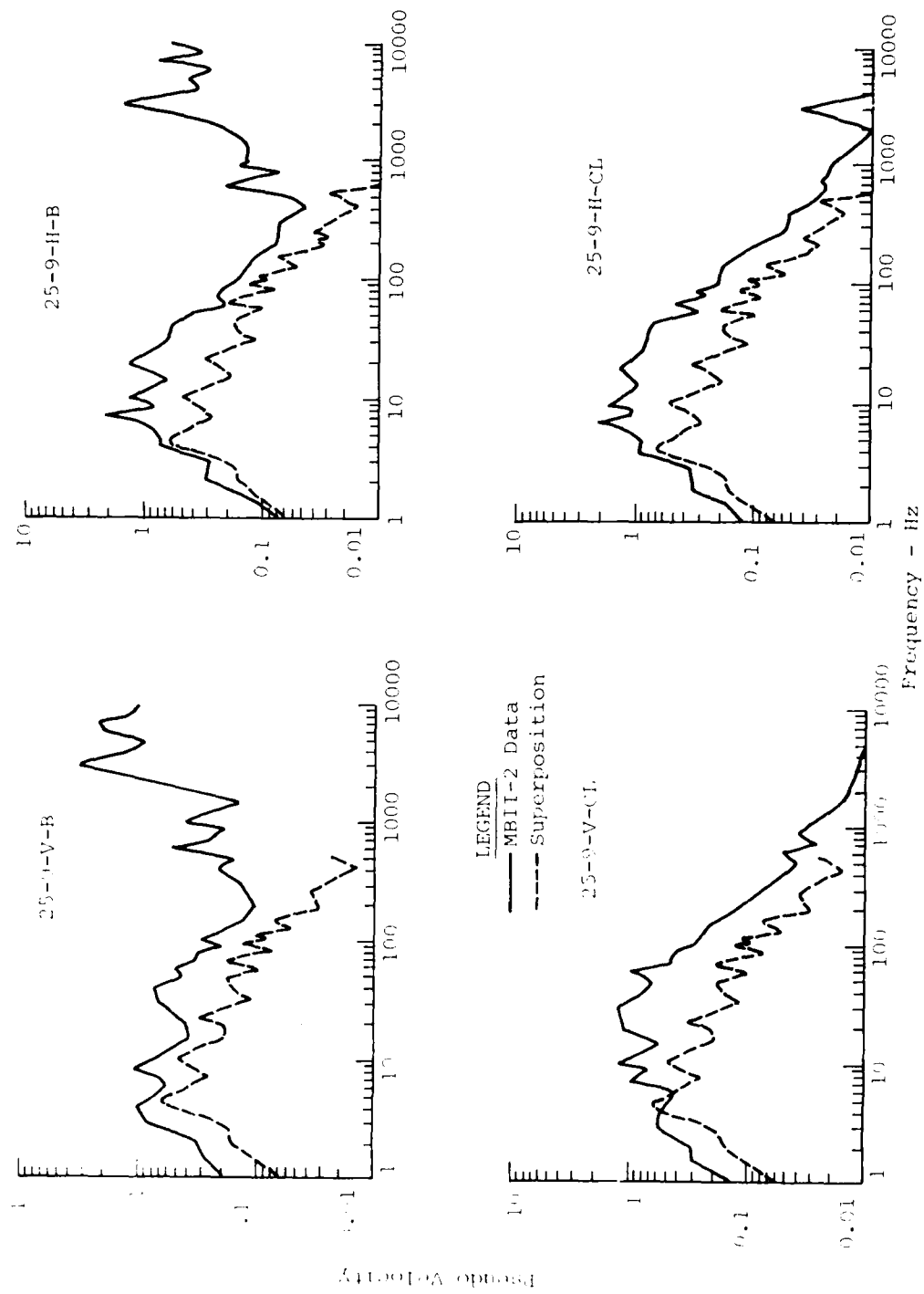


Figure B.9. Shock Spectra Comparisons of MBII-2 Data and Superposition
a R=25-9 - Bisector and Charge Line

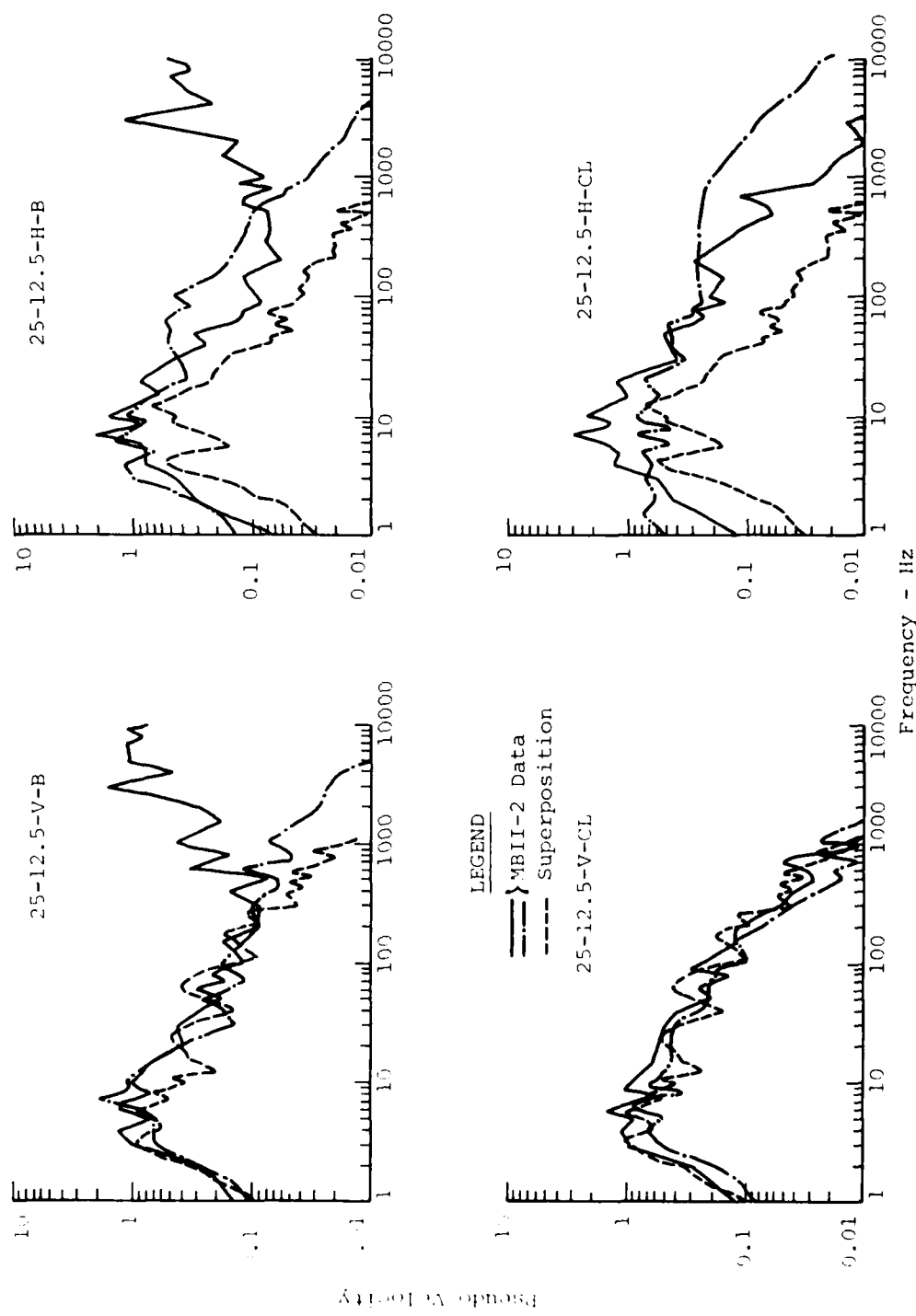


Figure B.10. Shock Spectra Comparisons of MBII-2 Data and Superposition
 @ R=12.5-12.5 - Bisector and Charge Line

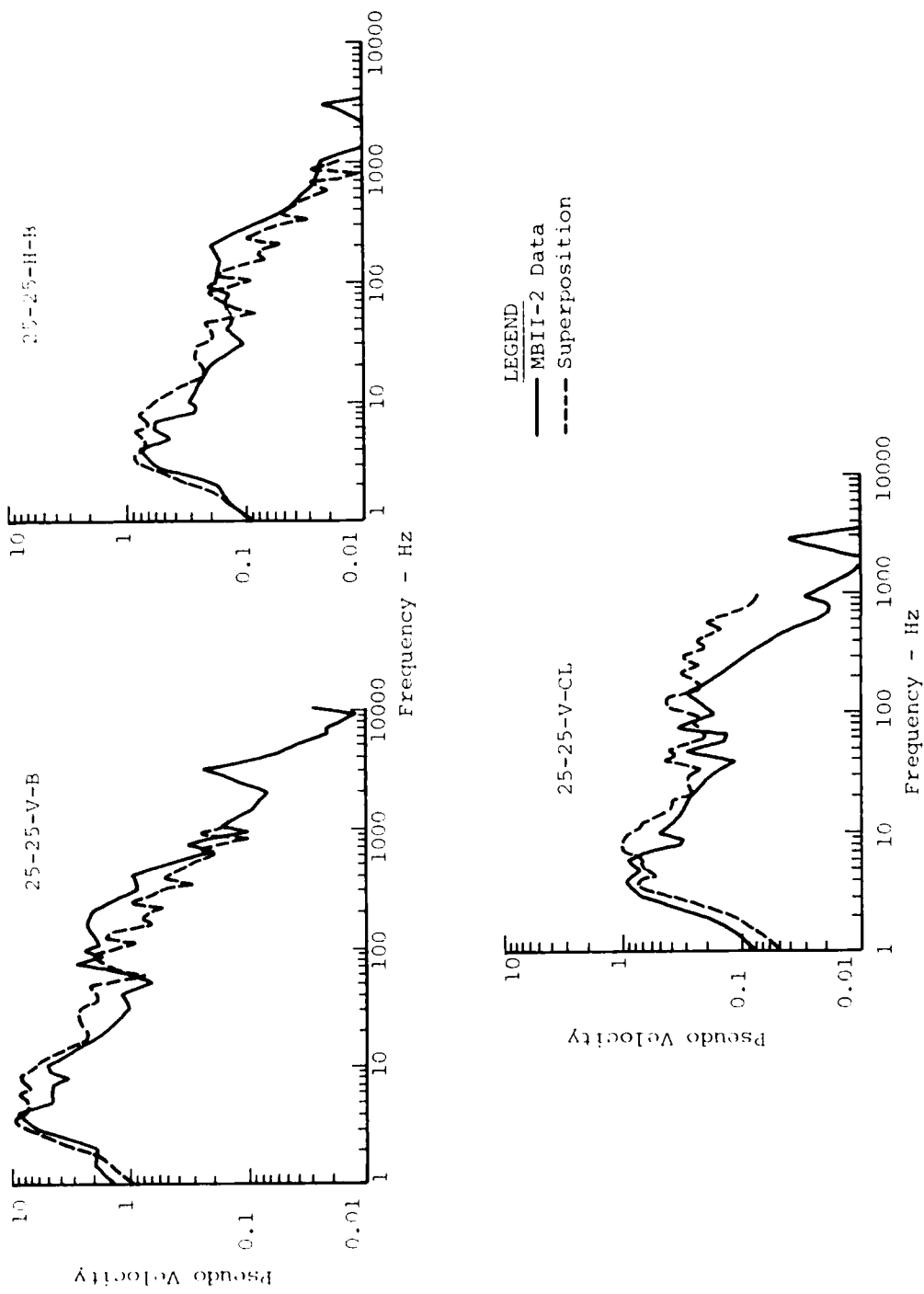


Figure B.11. Shock Spectra Comparisons of MBII-2 Data and Superposition
@ R=25-25 - Bisector and Charge Line

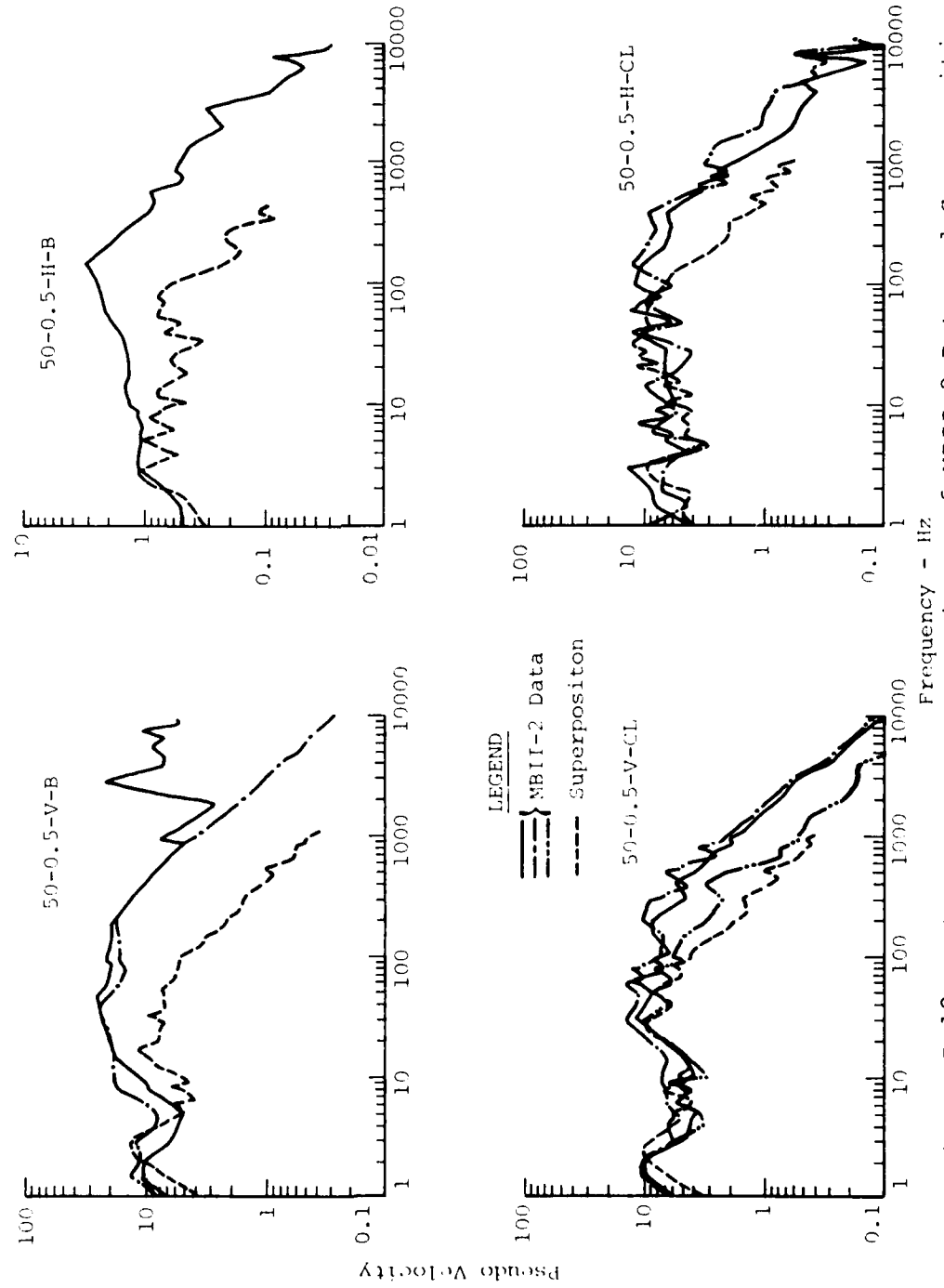


Figure B.12. Shock Spectra Comparisons of MBII-2 Data and Superposition
a R=50-0.5 - Bisector and Charge Line

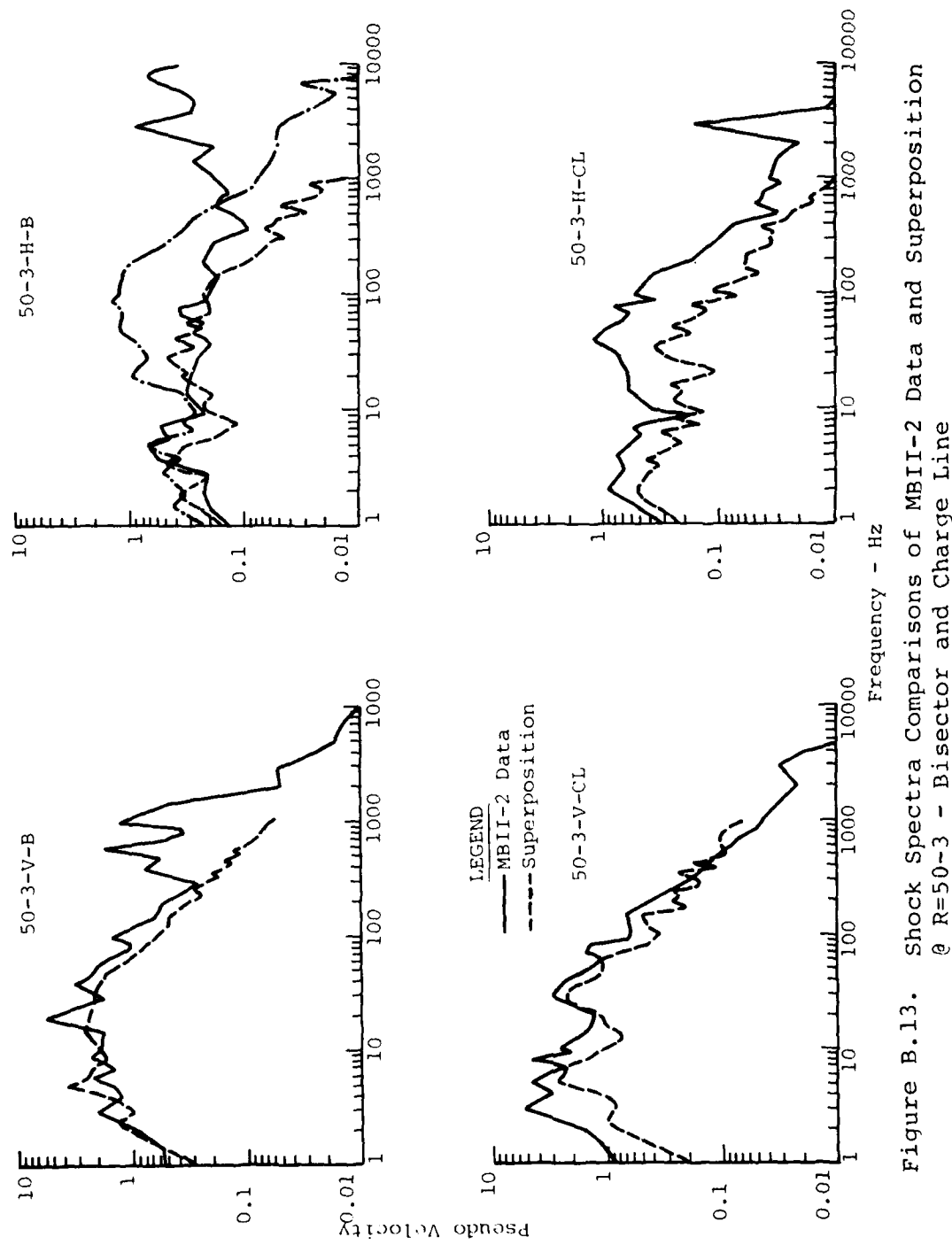


Figure B.13. Shock Spectra Comparisons of MBII-2 Data and Superposition
 @ R=50-3 - Bisector and Charge Line

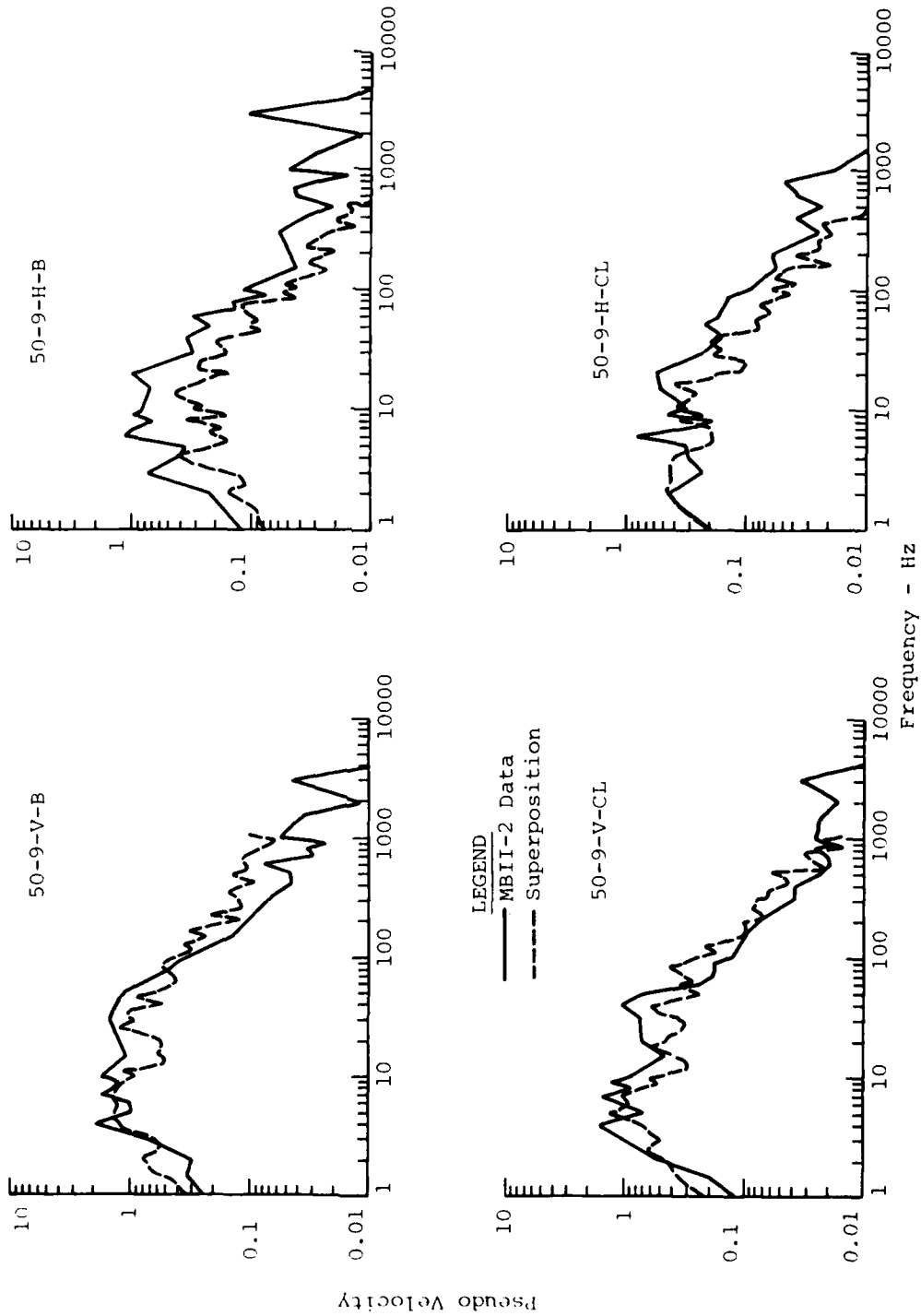


Figure B.14. Shock Spectra Comparisons of MBII-2 Data and Superposition
 \oplus R=50-9 - Bisector and Charge Line

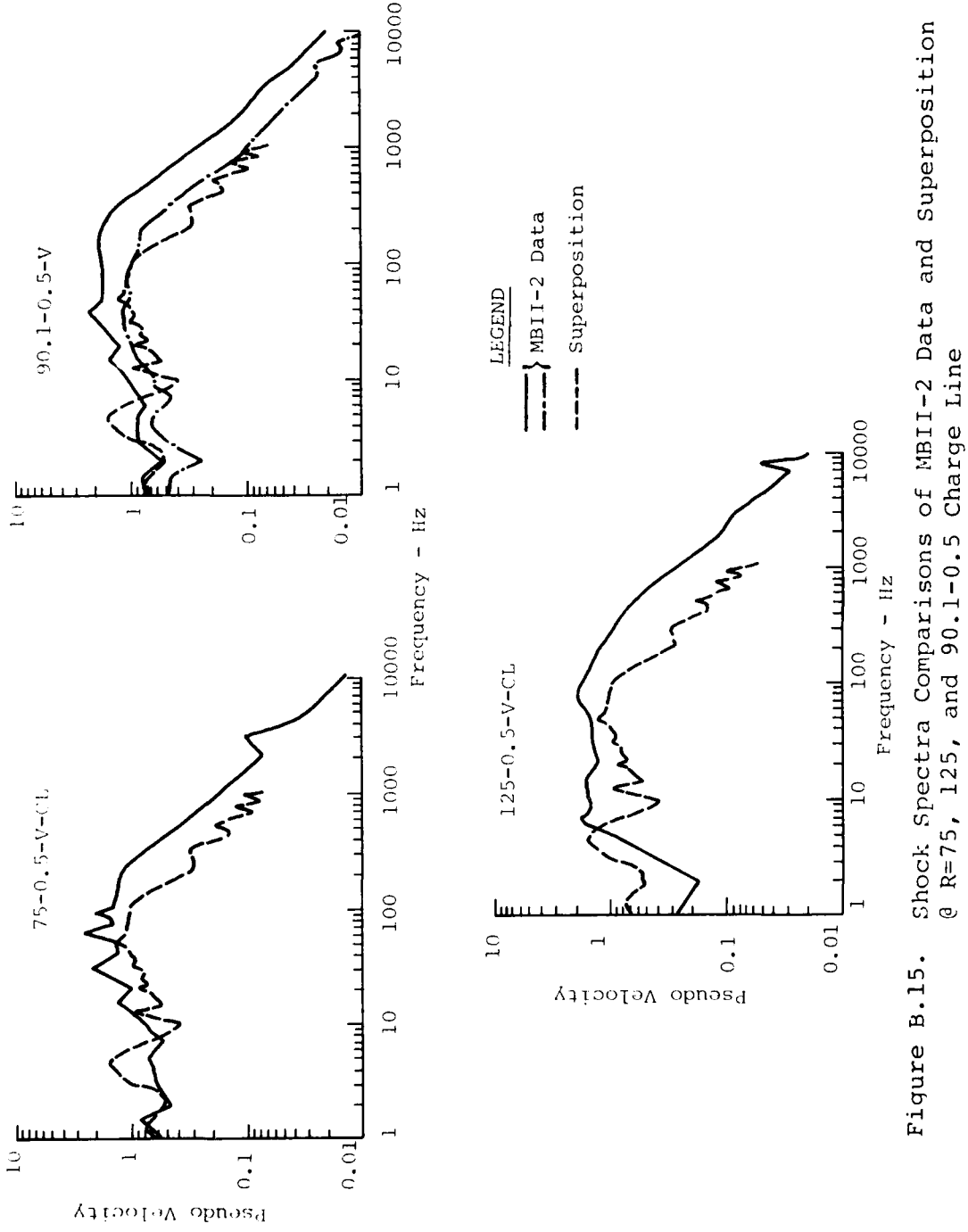


Figure B.15. Shock Spectra Comparisons of MBII-2 Data and Superposition
 ϱ R=75, 125, and 90.1-0.5 Charge Line

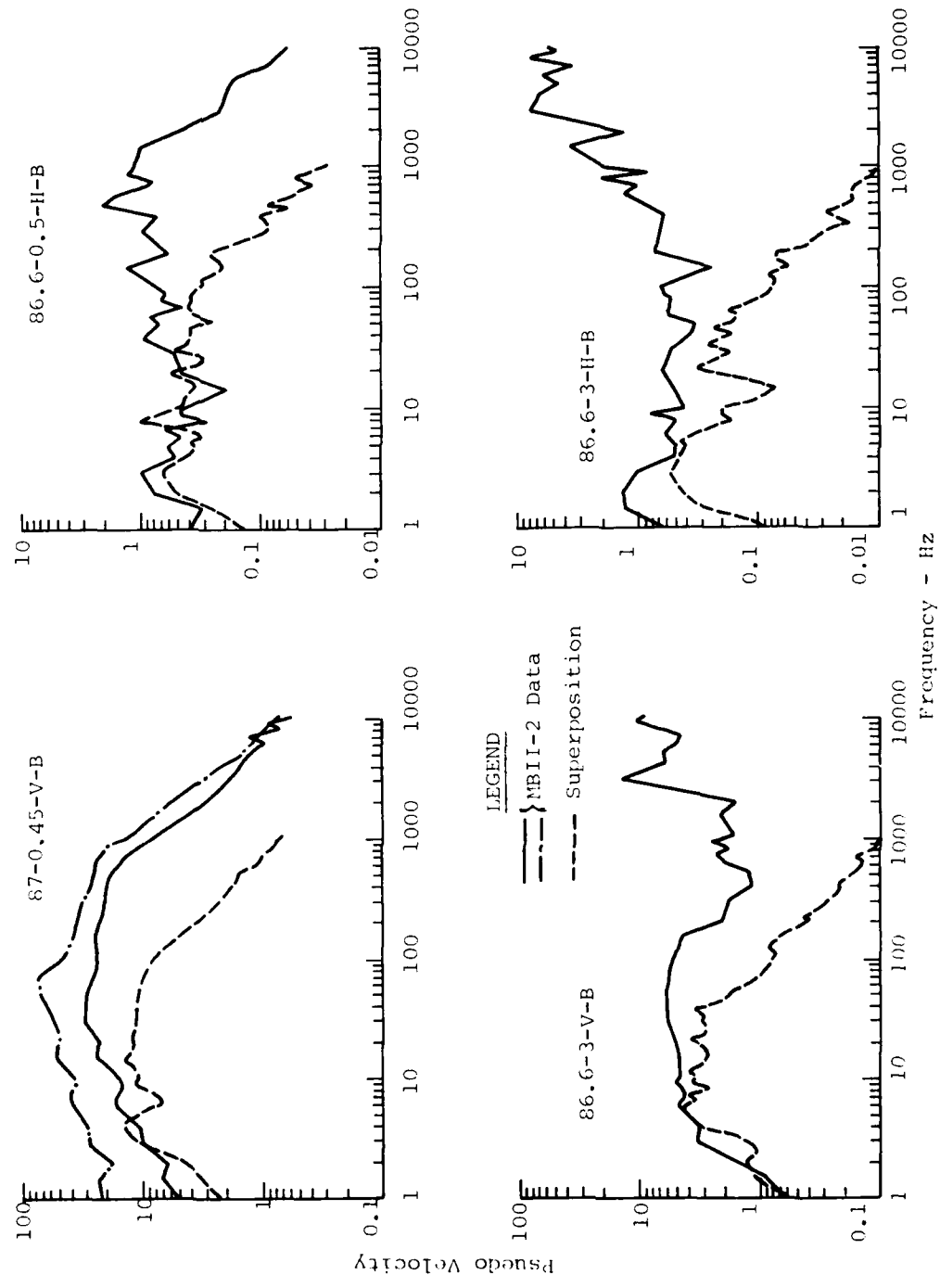


Figure B.16. Shock Spectra Comparisons of MBII-2 Data and Superposition
a R=86.6-0.5 and 3 - Bisector

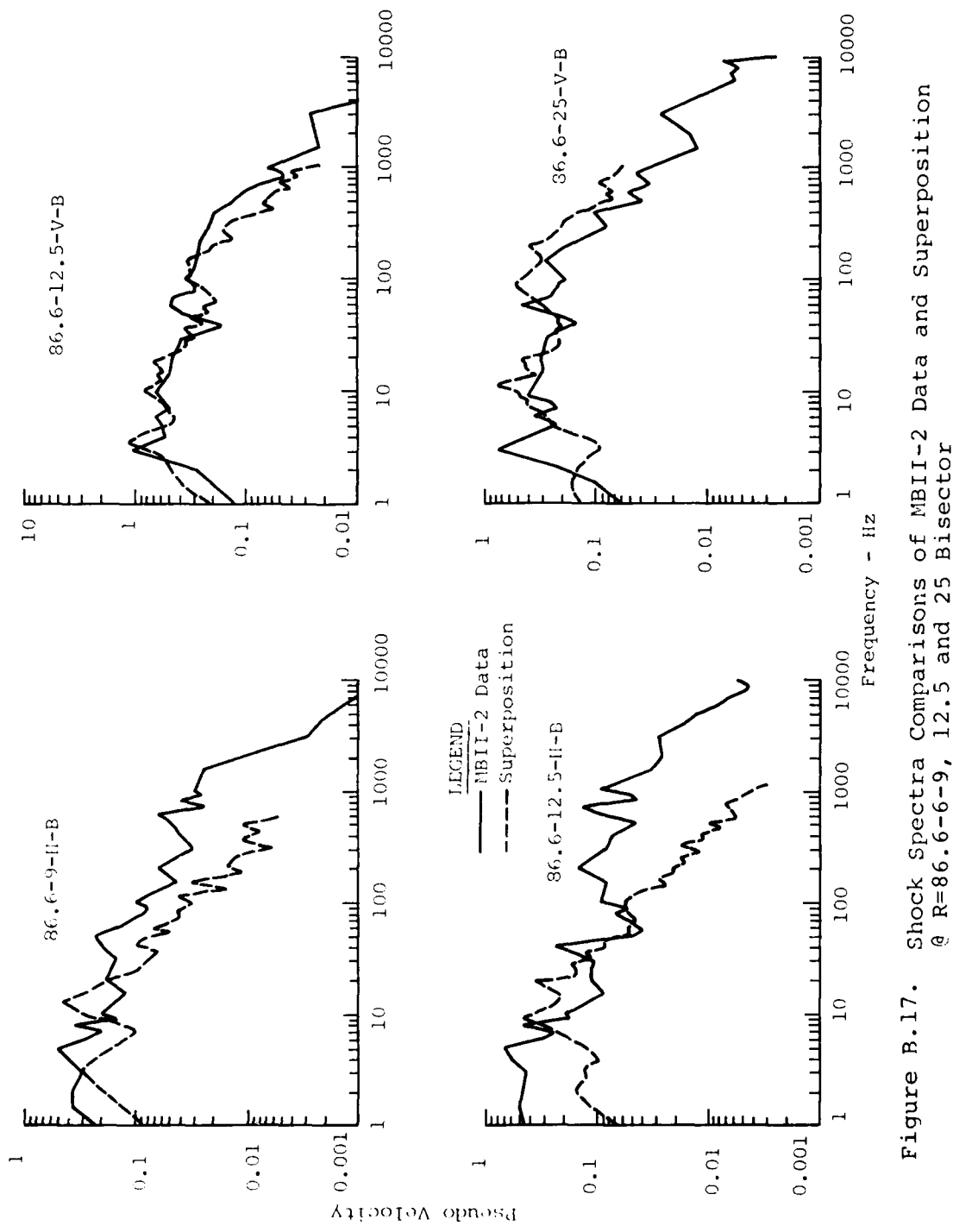


Figure B.17. Shock Spectra Comparisons of MBII-2 Data and Superposition
 $\oplus R=86.6-6-9$, 12.5 and 25 Bisector

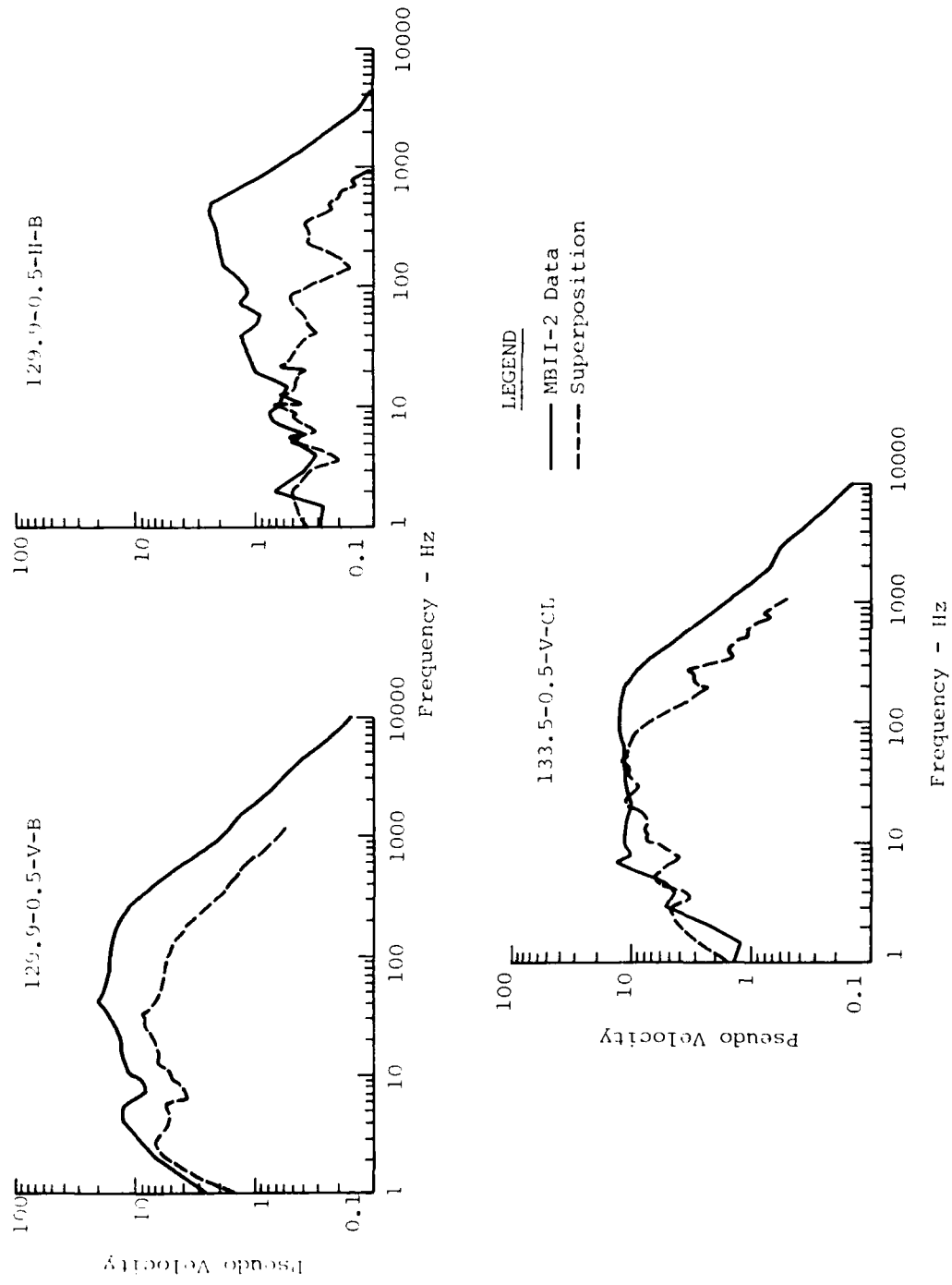


Figure B.18. Shock Spectra Comparisons of MBII-2 Data and Superposition
 @ R=129.9-0.5 Bisector and 133.5-0.5 Charge Line

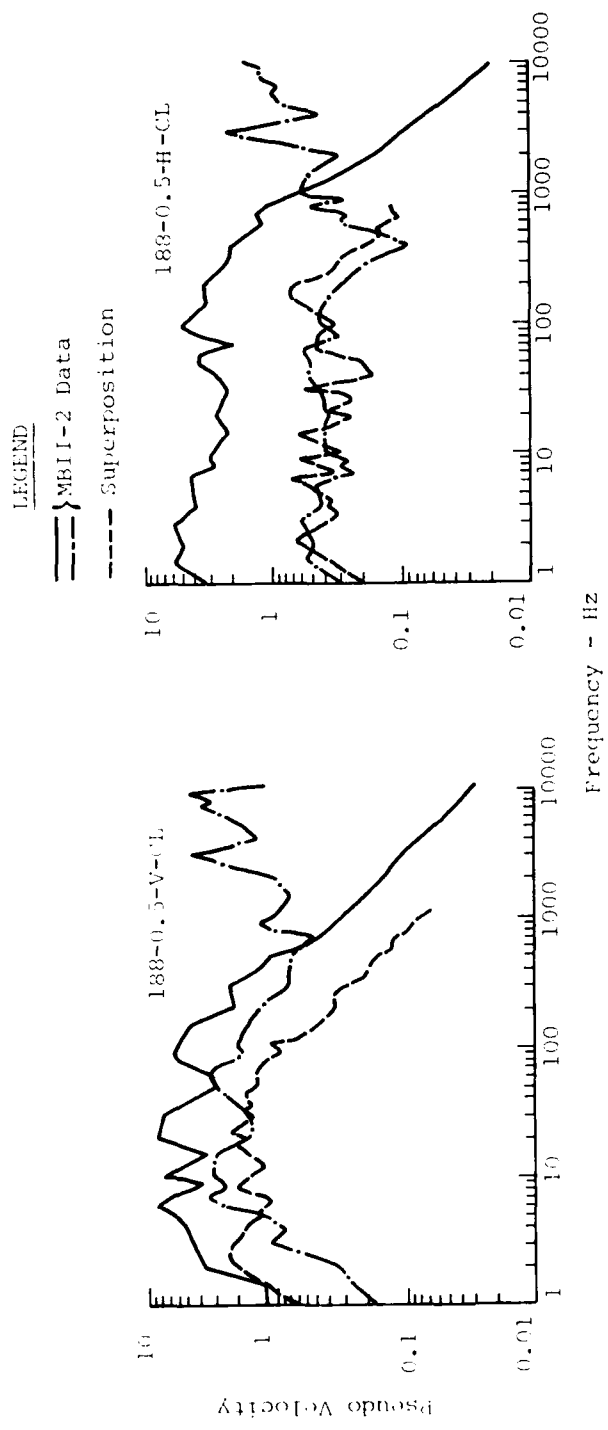


Figure B.19. Shock Spectra Comparisons of MBlI-2 Data and Superposition
 @ R=188-0.5 Charge Line

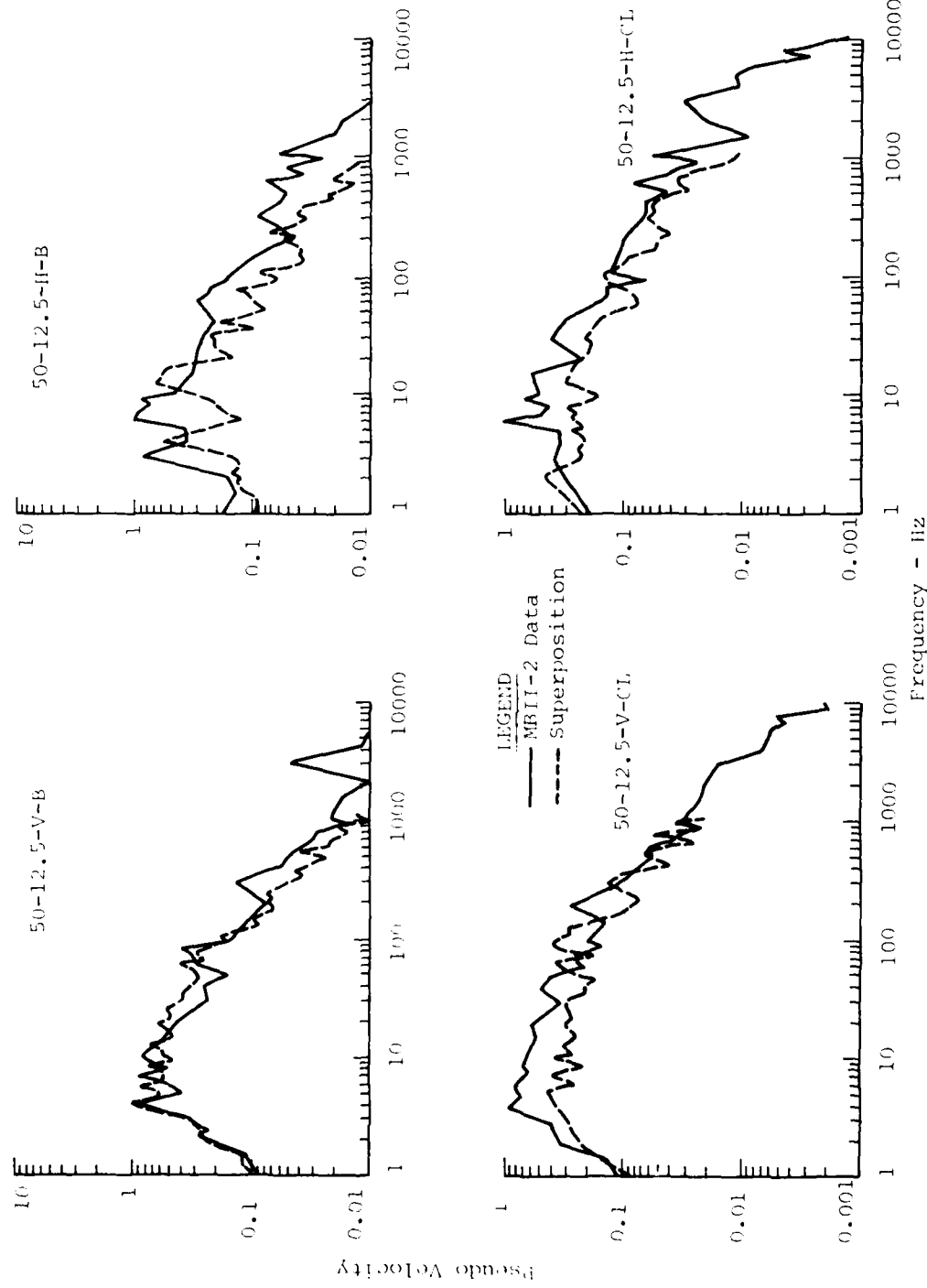


Figure R.20. Shock Spectra Comparisons of MBII-2 Data and Superposition
at $R=50-12.5$ Bisector and Charge Line

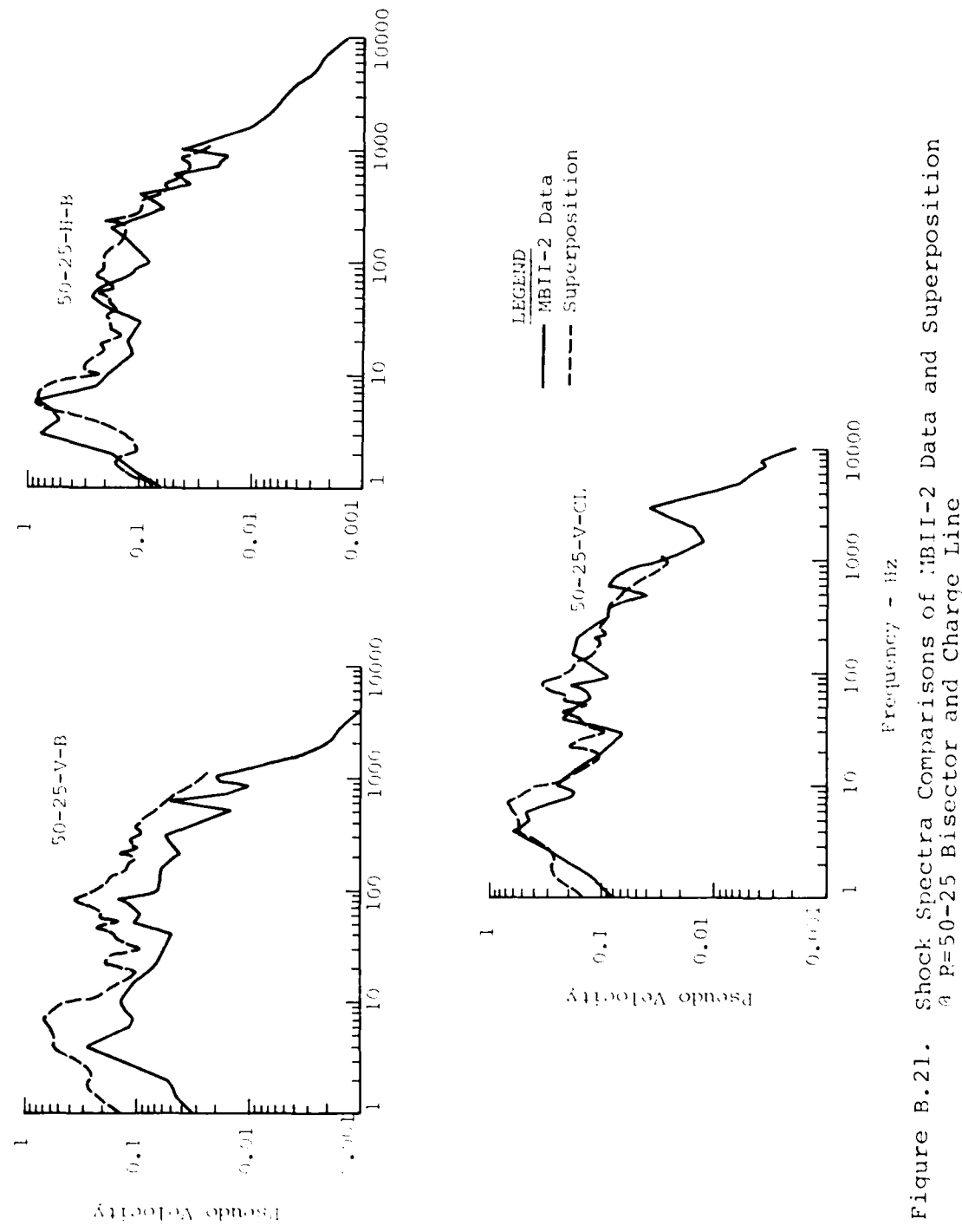


Figure B.21. Shock Spectra Comparisons of MBII-2 Data and Superposition
a R=50-25 Bisector and Charge Line

DISTRIBUTION LIST

DEPARTMENT OF DEFENSE

Assistant to the Secretary of Defense
Atomic Energy
ATTN: Executive Assistant

Defense Advanced Rsch Proj Agency
ATTN: TIO

Defense Intelligence Agency
ATTN: RDS-3A

Defense Nuclear Agency
ATTN: SPSS, C. Galloway
2 cy ATTN: SPSS, C. Ulrich
4 cy ATTN: TIE

Defense Technical Information Center
12 cy ATTN: DD

Field Command
Defense Nuclear Agency
ATTN: FCMD
ATTN: FCPR

Field Command
Defense Nuclear Agency
ATTN: FCPL

Joint Strat Tgt Planning Staff
ATTN: NRI-STIMFO Library
ATTN: XPF

Undersecretary of Def for Rsch & Engrg
ATTN: Strategic & Space Systems (OS)

DEPARTMENT OF THE ARMY

BMD Advanced Technology Center
Department of the Army
ATTN: ATC-T

BMD Systems Command
Department of the Army
ATTN: BMDSG-HW

Chief of Engineers
Department of the Army
ATTN: DAEN-AS1-L
ATTN: DAEN-RDM
ATTN: DAEN-MME-T, D. Reynolds
ATTN: DAEN-RDL

Harry Diamond Laboratories
Department of the Army
ATTN: DELHD-I-TL
ATTN: DELHD-N-P

U.S. Army Ballistic Research Labs
ATTN: DRDAR-TSB-S
ATTN: DRDAR-BLE, J. Keefer

U.S. Army Cold Region Res Engr Lab
ATTN: Library

U.S. Army Construction Engrg Res Lab
ATTN: Library

DEPARTMENT OF THE ARMY (Continued)

U.S. Army Engineer Center
ATTN: Technical Library

U.S. Army Engr Waterways Exper Station
ATTN: WESSA, W. Flathau
ATTN: WESSD, J. Jackson
ATTN: J. Zelasko
ATTN: Library

U.S. Army Material & Mechanics Rsch Ctr
ATTN: Technical Library

U.S. Army Materiel Dev & Readiness Cmd
ATTN: DRXAM-TL

U.S. Army Nuclear & Chemical Agency
ATTN: J. Simms
ATTN: Library

DEPARTMENT OF THE NAVY

Naval Construction Battalion Center
ATTN: Code 151, J. Crawford
ATTN: Code 10RA
ATTN: Code 153, J. Ferrest

Naval Facilities Engineering Command
ATTN: Code 09M22C

Naval Postgraduate School
ATTN: Code 0142 Library
ATTN: G. Lindsay

Naval Research Laboratory
ATTN: Code 2627

Naval Surface Weapons Center
ATTN: Code F31
ATTN: Code X211

Naval Surface Weapons Center
ATTN: Tech Library & Info Svcs Br

Office of Naval Research
ATTN: Code 715

DEPARTMENT OF THE AIR FORCE

Air Force Institute of Technology
ATTN: Library

Air Force Systems Command
ATTN: DLWM

Assistant Chief of Staff
Intelligence
Department of the Air Force
ATTN: IN

Assistant Secretary of the Air Force
Research, Development & Logistics
ATTN: SAFAR/R'DEP for Strat & Space Sys

DEPARTMENT OF THE AIR FORCE (Continued)

Air Force Weapons Laboratory
Air Force Systems Command
 ATTN: NTE, M. Plamondon
 ATTN: SUL
 ATTN: NT, D. Payton
 ATTN: NTED-I
 ATTN: NTED-A
 ATTN: DEY
 ATTN: NTES-S
 ATTN: NTES-G
 ATTN: NTEO

Ballistic Missile Office
Air Force Systems Command
 ATTN: MNXH, D. Gage
 ATTN: MNXN, W. Crabtree

Deputy Chief of Staff
Research, Development, & Acq
Department of the Air Force
 ATTN: AFRDQA
 ATTN: AFRDQSM
 ATTN: AFRDPN
 ATTN: AFRDQI, N. Alexandrow

Strategic Air Command
Department of the Air Force
 ATTN: MRI-STINFO Library
 ATTN: AFPS

Aerospace Technology Center
Department of the Air Force
 ATTN: G. Ulrich

DEPARTMENT OF ENERGY CONTRACTORS

Lawrence Livermore National Laboratory
 ATTN: D. Glenn

Los Alamos National Scientific Laboratory
 ATTN: J. Keller
 ATTN: R. Sanford

Sandia National Laboratories
 ATTN: A. Chabai
 ATTN: ORG 1250, W. Brown

DEPARTMENT OF DEFENSE CONTRACTORS

Aurex Corp
 ATTN: J. Stockton
 ATTN: K. Triebes
 ATTN: C. Wolf

Aerospace Corp
 ATTN: H. Mirels
 ATTN: Technical Information Services

Agbabian Associates
 ATTN: M. Agbabian

Applied Theory, Inc
 ATTN: J. Trulio

Artec Associates, Inc
 ATTN: J. Gill

Battelle Seattle Research Center
 ATTN: Technical Library
 ATTN: Track

DEPARTMENT OF DEFENSE CONTRACTORS (Continued)

California Research & Technology, Inc
 ATTN: M. Rosenblatt
 ATTN: Library

University of Denver
Space Science Lab
 ATTN: J. Wisotski

Eric H. Wang
Civil Engineering Rsch Fac
University of New Mexico
 ATTN: P. Lodde
 ATTN: J. Lamb
 ATTN: J. Kovarna

General Electric Company—TEMPO
 ATTN: DASIAC

H-Tech Labs, Inc
 ATTN: B. Hartenbaum

Higgins, Auld & Associates
 ATTN: N. Higgins
 ATTN: H. Auld
 ATTN: J. Bratton

IIT Research Institute
 ATTN: Documents Library

J. H. Wiggins Co, Inc
 ATTN: J. Collins

Kaman AviDyne
 ATTN: R. Ruetenik

Merritt CASES, Inc
 ATTN: Library

Mission Research Corp
 ATTN: G. McCarter
 ATTN: C. Longmire

Nathan M. Newmark Consult Eng Svcs
 ATTN: N. Newmark
 ATTN: W. Hall

Pacific-Sierra Research Corp
 ATTN: H. Brode

Pacifica Technology
 ATTN: Tech Library

Physics International Co
 ATTN: F. Sauer
 ATTN: Technical Library
 ATTN: J. Thomsen

R & D Associates
 ATTN: Technical Information Center
 ATTN: J. Carpenter
 ATTN: J. Lewis
 ATTN: C. MacDonald
 ATTN: A. Kuhl
 ATTN: R. Port
 ATTN: P. Haas

Science Applications, Inc
 ATTN: D. Hove

DEPARTMENT OF DEFENSE CONTRACTORS (Continued)

Science Applications, Inc
ATTN: H. Wilson
ATTN: Technical Library
ATTN: R. Schlaug

Science Applications, Inc
ATTN: B. Chambers III

SRI International
ATTN: G. Abrahamson
ATTN: D. Johnson
ATTN: J. Colton
ATTN: Library

Systems, Science & Software, Inc
ATTN: C. Needham

Systems, Science & Software, Inc
ATTN: J. Murphy

Systems, Science, & Software, Inc
ATTN: C. Hastings

DEPARTMENT OF DEFENSE CONTRACTORS (Continued)

Systems, Science & Software, Inc
ATTN: K. Pyatt
ATTN: J. Barthel
ATTN: Library

Terra Tek, Inc
ATTN: Library
ATTN: A. Abou-Sayed

TRW Defense & Space Sys Group
ATTN: Tech Info Center
ATTN: T. Mazzola
ATTN: N. Lipner

TRW Defense & Space Sys Group
ATTN: G. Hulcher

Weidlinger Assoc, Consulting Engineers
ATTN: I. Sandler

Weidlinger Assoc, Consulting Engineers
ATTN: J. Isenberg